Aalborg University

Department of Civil Engineering

Numerical predictions for centrifuge model tests of suction bucket foundation on liquefiable seabed

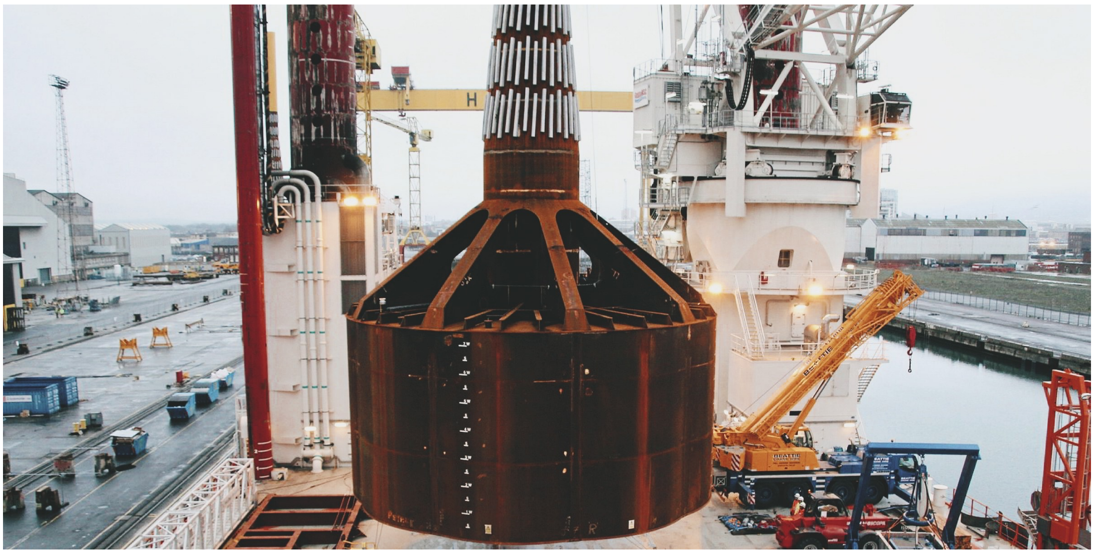

M.Sc. Structural and Civil Engineering

Master Thesis

Science Faculty
Department of Civil Engineering
Thomas Manns Vej 23
9220 Aalborg Øst

AALBORG UNIVERSITY
STUDENT REPORT

Title:
Numerical predictions for centrifuge model tests of suction bucket foundation on liquefiable seabed

Project:

Master thesis report

Project period:

February 2021 — June 2021

Authors:

Alfonso Estepa Palacios
Manh Duy Nguyen
Vladimir Markovic

Supervisors:

Amin Barari
Lars Bo Ibsen

Number of pages: 125
Including appendix: 200
Hand-in date:10/06/2021

Synopsis:

Offshore wind industry is rapidly growing, resulting in an immediate need of more innovative techniques and solutions for making this technology economically more reachable and suitable under different physical conditions.
Suction bucket foundations, primarily used in offshore oil platforms, is one of those techniques. However, its behaviour at seismic areas where the risk of liquefaction of the seabed exists has not been widely studied yet.
Thus, the aim of this report is the construction and validation of a numerical model, developed by the use of the software *OpenSees*, able to predict the outputs of a centrifuge test where a prototype of a wind turbine founded by the use of a suction bucket foundation on a liquefiable seabed is tested.
The constitutive models $PDMY01$ and $PM4Sand$ are used for the construction of the mentioned numerical model, whose correct performance is validated according to a provided experimental results.
Once the right behaviour of the mentioned numerical model is confirmed, some inputs such as the dynamic load induced or the characteristics of the original structure are modified in order to generate new predictions about the performance of the mentioned prototype under different conditions.

Preface

This Master Thesis has been developed by Alfonso Estepa Palacios, Manh Duy Nguyen and Vladimir Markovic, students of the M.Sc. Structural and Civil Engineering program in Aalborg University.

We would like to express our gratitude to our supervisors Lars Bo Ibsen and, specially, Amin Barari, for his guidance, passion for researching, and tireless work throughout the entire development of the present master thesis. Also, a special reference to the PhD student Sina Farahani and his immeasurable help, who provided us an extensive guidance about the development of the numerical model and contributed actively in the outcome of this research.

Last but not least, the bundle of sincere gratefulness would go for our families and classmates due to a ton of invisibly unlimited supports and encouragements from them. As young engineers, the vicious cycle of working with numbers, formulas, etc. could put much pressure on us, sometimes losing motivation or mental energy is the inevitable struggle, specially in the life of the international students. We hereby always respect every single touching moment of sharing and confiding in them during 2 years of tireless working in the master program of Aalborg University.

Overall, needless to say about the significant influences of up-mentioned people on becoming much more mature on the pathway of knowledge. We always honestly consider all of them as the good role models to look up to and the enormous source of inspiration on the way of being developed comprehensively.

Reading guide

A list of the sources and external references mentioned in the report are presented under the section "Bibliography" and are listed according to Harvard method (Author, Year). For internet sources without a release date, the date of the last visit is stated.

Figures, Tables and Equations are numbered by Chapter and number as shown in the following example: 'Figure 1.1', 'Table 1.2' and '(1.3)'. References are made in the same way for figures and tables, while equations are given by 'Equation 1.3'. For appendices, the above is assigned by a letter instead of chapter number, e.g. 'Figure A.1', 'Table B.2' and '(C.3)'.

In this report units are mentioned in the tables and decimals are separated with a period ".", where two digits are used.

Contents

Introduction 1

1.1 Abstract

Occurrence of liquefaction due to earthquake-imposed ground motion has shown to have a detrimental effect on the bearing capacity of the sandy soils and stability of the standing structure. During the last several decades, the liquefaction phenomenon was in the focus of research regarding the soil behaviour under seismic loading. Thorough understanding of the phenomena and the mechanisms that drive it, is of the great importance in order to provide safe and economically feasible structural design which would ensure proper response due to seismic loading. To achieve that, useful computational tools were developed in order to simulate the behaviour occurring in the real life setup. Employing these tools for design purposes can be very beneficial in terms of resources and time costs, avoiding engagement of laboratory testing facilities, problems with proper specimens extraction from the site, engagement of heavy machinery on site, etc.

Numerous numerical constitutive models were developed in the recent years in order to simulate the liquefaction occurring under seismic-induced ground shaking. Every of these developed models has its own advantages and flaws regarding the multiple parameters that affect the totality of the soil behaviour under such conditions. Still until today there is no such model developed being able to answer all sets of parameters that govern the soil behaviour crucial for various aspects related to the design process of the structure. Usually the models are able to capture many of the soil properties and performances but on the other hand fail to answer to the others.

In this report, two developed constitutive models are employed in software developed for simulation purposes in earthquake engineering called *OpenSees*. It is an open source software for earthquake engineering developed by researchers at University of California,Berkley (McKenna et al., 2000). The constitutive models used in the report are plasticity based *PressureDependMultiYield* (*PDMY*) (Parra-Colmenares, 1996),(Yang et al., 2000),(Yang, 2000) and *PM4SAND* (Boulanger and Ziotopuolou, 2017). Both models are able to simulate the nonlinear behaviour of the soil for undrained conditions under cyclic loading. Constitutive models are employed in simulation of the centrifuge test conducted by (Yu et al., 2014).

Configuration of the centrifuge test conducted includes the scaled model of the offshore wind turbine structure supported by a suction caisson foundation. Model of $PM4SAND$ is first calibrated according to the *Cyclic Direct Simple Shear Test CDSS*, which is not the case for $PDMY$. Both models are then calibrated according to the outputs of the prototype model conducted in the centrifuge test. The goal of the report is to see if the developed model following the finite element analysis in *OpenSees* software is able to provide reasonable results that would match with ones derived in the laboratory setup by (Yu et al., 2014), regarding the engaged constitutive models and its overall performance. Also general performance of the suction bucket

foundation of offshore wind turbine structure is analysed regarding the findings of (Yu et al., 2014) and in mitigation of the liquefaction occurrence.

After the mentioned process of calibration of the numerical model, the performance of this numerical simulation is tested under different input features such as the modification of the geometry of the suction bucket foundation or the testing by the use of different inputs motions.

1.2 Suction Bucket Foundation

Renewable energy has been emerging widely in developed countries in recent years and has been accepted as a more sustainable and ecological source of energy compared to the ones from fossil fuels. Important efforts have been invested to make it more available and affordable to the wider global population. Even though a research and employment of renewable energy are steadily on the rise, it is still a long way to go to make it as a leading source of energy. Wind energy has shown optimistic results as it is seen as a cost-effective solution, thus a lot of research in that field is generated nowadays. In the following years, it is expected that more wind farms will be constructed offshore as this offers multiple advantages compared to onshore. First, constructing offshore allows for larger turbine structures and farms, thus impacting on the environment in terms of noise and hurting the living world are reduced. Second, more energy can be generated offshore whether from the larger wind speeds or larger systems installed. Third, larger systems are easier for installation offshore than onshore, less infrastructure needs to be employed.

One of the major contributors to the cost of the offshore wind turbine structure is the foundation support that accounts around 20-25% of the total cost of the structure. Many times the cost can reach one third of all expenses, thus creating more affordable and cheaper solutions are imperative in order to combat the CO_2 emissions effectively. The more suitable answer can be deployed in the form of the suction caisson foundation which has been utilized in offshore oil and petroleum industry. The main advantages of suction caisson foundations compared to mono-piles and gravity based foundations lies in a much easier transportation and installation on site, less material usage, possible repeated use, and large bearing capacity.

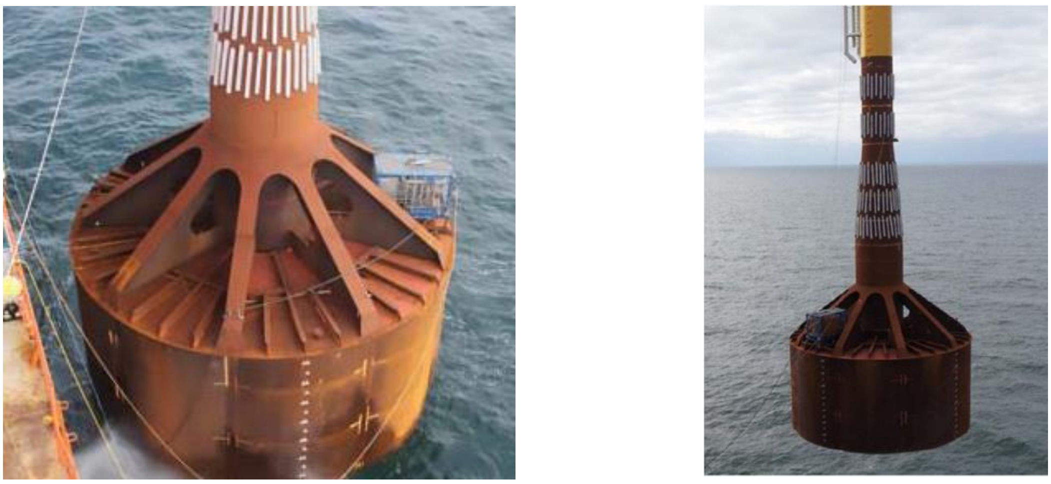

Figure 1.1. Installation of the suction caissons at Dodger Bank(Energy, 2013)

Suction caisson is usually constructed as a welded steel structure consisting on a circular lid that is connected at the edges to a thin vertical tubular skirt creating a bucket-like structure. The wind turbine tower is connected to the foundation via a tubular column that is welded with flange stiffeners to the lid of the bucket. One of the advantages of the suction bucket is that the structure is floated directly to a site where is embedded into the ground without the need of drilling or hammering the soil. Installation of the bucket foundation is obtained through the suction process enabled by self-weight penetration and difference pressure created by pumping water out within the skirts, Figure 1.2. Suction created allows for easier downward sliding of the foundation until the full contact between the lid and the surface ground has been attained. The bucket foundation confines the soil entrapped, which contributes to its stability. The foundation provides a coupled mechanism of contact pressure between the skirt and soil and vertical bearing capacity, which ends in good behaviour and stability to horizontal loading.

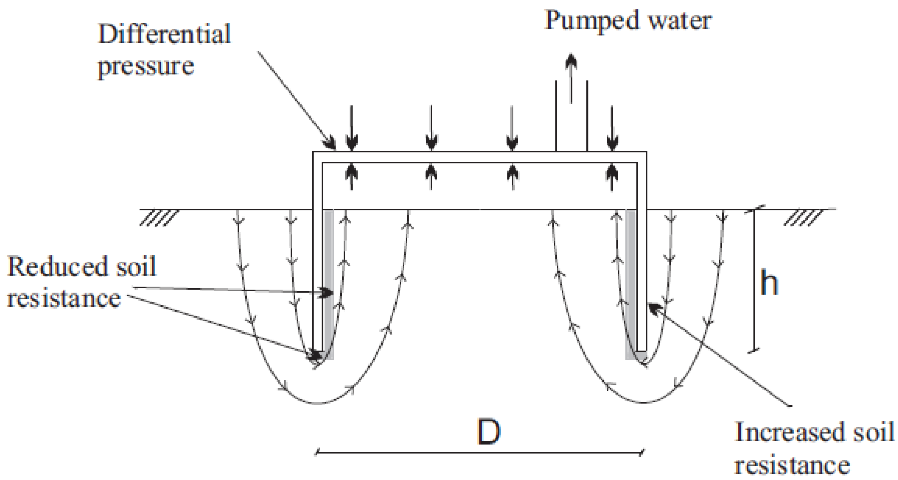

Figure 1.2. Scheme of skirt penetrating in dense sand soils (Koteras et al., 2016)

As the deployment of offshore wind energy rises globally so is the need for the appropriate sites for the installation of wind farms where energy could be generated efficiently. Many of these sites lies in regions where seismic activity presents a significant threat to a stability and normal functioning of the turbines. Soil prone to liquefaction due to earthquake excited ground motion could pose a certain risk to the bearing capacity of the foundation and the structure itself. More research has been mobilised to evaluate the behaviour of offshore wind turbines and its foundation under earthquake loads. Literature related to this topic is not as extensive as for the onshore turbines. Design practice relies mostly on the engineering assessment and empirical experience since codes of practice still do not incorporate any specific guidelines and methodology regarding the issue under seismic loading. A lot of experience generated from the conventional building structures, offshore oil and petrol industry helps in design practice until new codes and regulations come in to act. In the case of suction bucket support for offshore wind turbines, there are ongoing research on its performance under the seismic loading. These findings might discover which are the most important mechanisms and parameters that affect the behaviour of the structure under such loading which would then help establishing a set of rules for easier design practice. The key objective of this report is to assess the behaviour of the suction bucket supported wind turbine under earthquake loading and its resilience to liquefaction occurring. To achieve this goal, numerical tools for finite element analysis are deployed to simulate recorded outputs held by other researchers. In the following sections, mentions on the model created for the purposes of this report and current findings from ongoing research related to the Suction Bucket Foundation are introduced.

1.3 Seismic areas

The distribution of the seismic areas on the Earth's surface is closely related to the existence of tectonic plates in those areas. This hypothesis states that the Earth's surface is divided into large blocks which move respect to each other due to the convection currents in the mantle, induced by the requirement of thermo-mechanical equilibrium of the deeper layers.

The deformation of plates occurs along the boundaries between them. These deformations in general are continuous and slow but, sometimes, it can turn into a sudden process in which a large amount of energy is released. In that case, the process is called seismic deformation or earthquake. Hence, most of the seismic events are expected to occur along the borders of the plates. The Figure 1.3 shows the map of the most active countries in terms of development and installation of offshore wind energy and the locations of the boundaries of the tectonic plates together with the map of seismic hazard in terms of a peak ground acceleration (PGA) with probability of exceedance of 10% in 50 years. The blue lines on the map illustrate the subduction zones in which earthquakes of the magnitude M9-class megathrust can occur. From this map, it can be concluded that coasts of countries like USA, China, India and South-East Asia fall into these regions (Bhattacharya, 2019). These countries are among those investments in offshore wind energy so it is of great interest to investigate the potential setbacks regarding the design of these kind of structures.

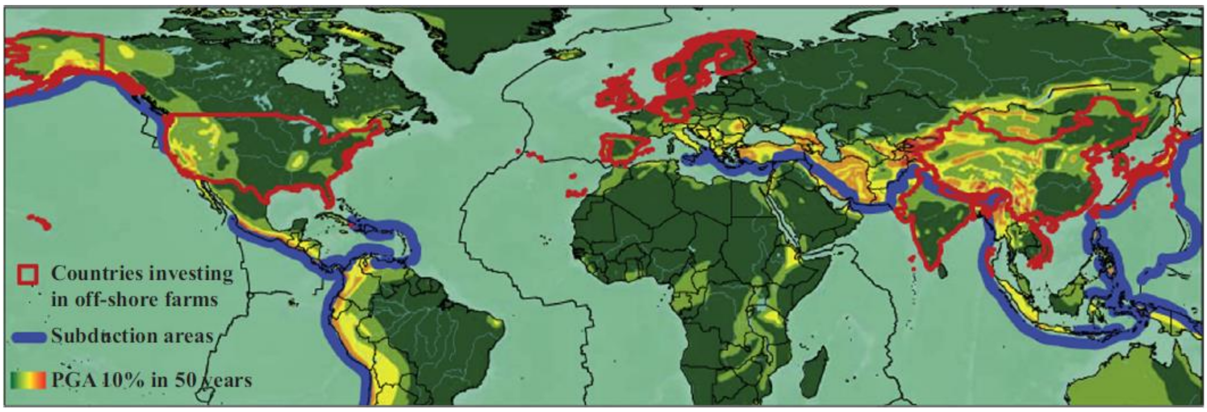

Figure 1.3. Map of countries investing in offshore wind energy (red mark), subduction trenches (blue line), seismic hazard map (Bhattacharya, 2019)

Design of the Offshore Wind Turbines (OWT) in seismic regions demands focus on various phenomena that might occur due the excitation of the ground motion, thus affecting the structure. The site has to be analyzed in terms of seismic hazard to evaluate the probable PGA during the lifetime of the structure as well as periods and frequency content that could alter the soil conditions during the excitation. The response of the structure excited due seismic loading is essential to be evaluated in order to avoid the effect of resonance resulting in the amplification of motion, which could be harmful to the stability and bearing capacity of the structure. The Figure 1.4 shows the normalized spectra with bands of frequency from external loads of wave, wind, and earthquake and also the frequency bands of the first mode together with higher ones of the vibration of the conventional wind turbine structure. Thus it is of great importance to avoid overlapping of the frequency content of the external loads and natural frequencies of the structure. Here it can be seen that the higher modes of structural vibration overlap with the spectrum of the earthquake loading, posing the potential detrimental effects on the overall stability of the structure.

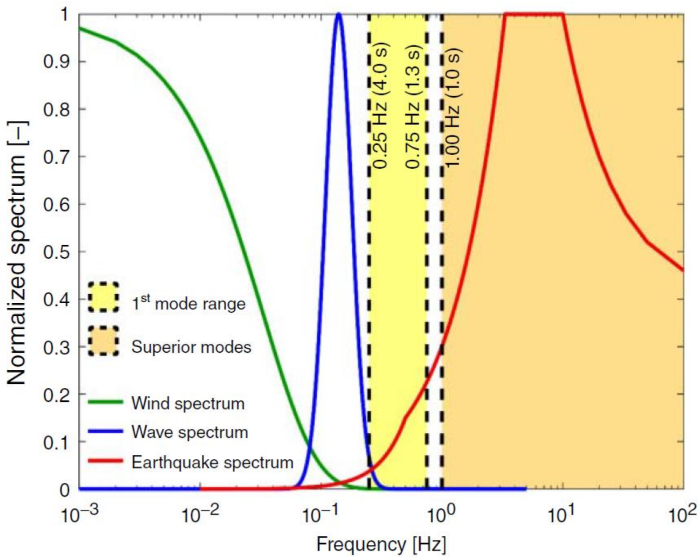

Figure 1.4. Normalized spectra of wind, wave and earthquake loads together with frequency content of first and higher modes of conventional OWT (Bhattacharya, 2019)

Other important factors that may affect the structural response are related to the characteristics of the site and soil itself. The relative distance from the fault rupture, seismo-tectonic in the area, faulting pattern, geological composition of the site, presence of liquefiable soil in the ground, the possibility of tsunami occurring after rupture in the ocean (Bhattacharya, 2019).The presence of liquefiable soils already proven to had harmful effects on soil bearing capacity. This phenomenon occurs in loose and medium-dense sands in saturated conditions. Due to the high shear forces imposed by earthquake loading, the generation of porewater pressure increases which leads to a decrement of the effective confining pressure and degradation of the soil shear strength. This loss of soil stiffness can lead to a failure of the bearing capacity of the soil, compromising the stability of the structure and its functioning. Another important aspect to account is the soil-structure interaction (*SSI*), which in design practice would often be overseen. Due to cyclic loading motion imposed on the structure interacts with the surrounding soil. This effect can result in increasing the stiffness of the soil or else it can end in degradation of soil stiffness. This change in soil stiffness can alter the vibration frequency of the structure, which can lead to potential resonance and amplification of motion. The effects of motion of the suction bucket foundation due to shaking are analyzed in this report and compared to those from the free-field. That is supposed to show the effect that *SSI* has on the total settlement in comparison to free-field, distincting between shear-induced and volumetric settlements. In subsequent chapters of the report, more detailed explanations to the mechanisms that govern the response of the *SSI* are analyzed.

1.4 State of the art

The technical and up-to-date advance methodologies for the development of renewable energy sources are investigated and researched on a daily basis. Regarding these new technologies, offshore wind energy has demonstrated to be an effective option to convert the wind's kinetic energy into electrical energy. However, as explained into detail in the introduction of the current report, one crucial fact is the characteristics of the location chosen for the installation of the wind farms regarding the seismic activity. This aspect becomes even more critical when more innovative options for foundation design of OWT such as suction bucket are considered due to the lack of designing codes or prescribed normative regulating its implementation, specially, under the conditions analyzed in the current report, where the possibility of liquefaction of the soil need to be accounted as well as the performance of such kind of foundation when seismic loads are considered.

Some standards related with the geotechnical design of the foundations and earthquake resistance of general structures need to be fulfilled (EN-1997, 2007)(EN-1998-5, 2004). As regards the design of offshore foundations, regulations like (API-RP-2A-LRFD, 1997) or (ISO-19900, 2019) can be considered, which contains mainly rules about the design of structures employed for the extraction of petroleum and gas, with special emphasis on piles, not being possible to find a wide amount of information about suction bucket foundations. Some requirements, specifically directed to the design of offshore wind turbines, can be found at (IEC-61400-1, 2005) but principally focused on the ensuring of the external structure and the safety measures against hazards during the planned lifetime of the wind turbine.

Lastly, with the role of a guideline and not like an official regulation, the documents contained at $Det\ Norske\ Veritas$ offer an extensive amount of recommendations in terms of assessment of loads and site conditions for wind turbines both onshore and offshore (DNVGL-ST-0437, 2016) (DNVGL-OS-C201, 2017) or information about construction, transportation, installation and inspection procedures (DNVGL-ST-0126, 2018). Also with the same role of guidelines, and overlooking the design of offshore wind turbines, design instructions and recommendations are found at (Lloyd, 2010) and (Dnv/Risø, 2002). Nevertheless, any specific regulation about the dimensioning of suction buckets foundations and its behaviour under dynamic loads on liquefiable sandy seabed is found.

Therefore, the main goal of this report is the development of a numerical model able to predict the performance of a suction bucket founded OWT prototype on liquefiable seabed under dynamic loads, with the intention of contributing to make wider the knowledge about this technique. Regarding the existing codes, it is obvious a lack of information and resources about the performance of offshore foundations on liquefiable soils and the complexities related with the interaction between soil and structure due to the slender characteristics of the tower or the characteristics of the induced motion. Thus, to achieve a better comprehending, a brief presentation of the state of art of such a researching topic is presented in this section.

The analysis of similar prototypes and the influence of their physical characteristics such as the skirt length or the diameter of the bucket on the development of pore water pressure and its influence on the vertical displacements of the structure has been already studied through the performance of centrifuge tests in several researches (K.Ueda et al., 2020) (T.Olalo et al., 2016). Particularly for the current report, the characteristics of the prototype considered and the experimental outputs used for the calibration and verification of the numerical model are gathered at (Yu et al., 2014) with the main sake of getting the approximately identical soil responses in the numerical analysis process in terms of generation of pore water pressure, accelerations and settlements.

Regarding the last feature, the induced vertical displacements of conventional building structures due to liquefaction, important findings are provided in scientific papers such as (Dashti, Bray, Pestana, Riemer and Wilson, 2010) or (Macedo Escudero, 2017). Moreover, not only its analysis but also techniques for achieving the mitigation of these settlements are studied at (Dashti, D.Bray, M.Pestana, Riemer and Wilson, 2010). Some mitigation techniques of liquefaction induced settlements of OWT are also studied and discussed in the current report, together with the influence of the input motion induced to the model and the modifications of the characteristics of the structure.

Similar procedures of comparison, as the ones mentioned above, between centrifuge laboratory tests and outputs received from numerical models have been also investigated before by the use of commercial software as *Abaqus* (Asheghabadi et al., 2019) or $FLIP$ computer code (K.Ueda et al., 2020). In the current report, the numerical simulation of the centrifuge test is carried using the open-source software *OpenSees* which is used for the construction of a 2D-model following the *.tcl* coding guidelines of (Mazzoni et al., 2007).

Another indispensable aspect concerning the definition of the numerical model simulation is the approaches followed for both applying the seismic loads and defining the boundary conditions of the prototype. Valuable information related with these features and a large number of practical examples are collected at (L.Kutter et al., 2017), where a series of collaborative research projects are presented with the aim of creating a powerful database of experimental and numerical examples which could be used for the validation and calibration of constitutive models for the analysis of soil liquefaction effects.

Following similar procedures but including the effects of SSI due to the presence of the offshore wind turbine prototype, the virtual model constructed in *OpenSees* for the current report is developed. In order to avoid spurious dynamic waves being reflected into the soil domain, absorbing boundary conditions are set which provide more reliable results (Zhang et al., 2018). A viscous material establishes the behaviour of these boundaries which are defined by a dashpot coefficient calculated according to (Joyner, 1975). Furthermore, the earthquake accelerations are implemented into the model by the calculation of equivalent forces applied to the bottom and lateral limits of the soil domain following the procedure described at (Joyner and Chen, 1975).

In addition, for verifying the reliability and identifying the possible limitations of the numerical model constructed before using it for obtaining predictions about the performance of the prototype, two kinds of constitutive models are employed in this report, $PressureDependMultiYield$ (Parra-Colmenares, 1996),(Yang et al., 2000),(Yang, 2000) and *PM4SAND* (Boulanger and Ziotopuolou, 2017).

Overall, all up-mentioned processes are conducted with the main aim of predicting the outputs of the experimental centrifuge test and verifying its correct behaviour in order to ensure that the numerical predictions obtained by its use provide accurate enough results. The problem statement is paraphrased in the following section presenting the principal objectives of this report.

1.5 Problem statement

- *Is the 2D plane strain model created in OpenSees finite element software code, separately employing the constitutive models of PressureDependMultiYield and PM4Sand able to predict the outputs obtained in the centrifuge test conducted by (Yu et al., 2014) in terms of excess pore water pressure generation, accelerations of the ground motion and settlements?*

- *If so, is it observed any changes on the total value of the settlements of the structure and the generation of pore water pressure within the soil domain of the OWT model constructed numerically when the physical characteristics of the structure such as the diameter or the length of the skirt of the suction bucket, and the weight of the prototype are modified?*

- *Is it also observed any change on the mentioned vertical displacements of the structure or the generation of pore water pressure underneath the prototype and at the free field when the dynamic input motion applied to the numerical model is modified?*

- *Could contribute the findings from the numerical analysis of the performance of a OWT prototype under dynamic loads carried in this report to a better understanding of the mechanisms implied on the development of settlements of suction bucket founded OWT due to the generation of excess pore water pressure on the liquefiable seabed?*

- *If so, could contribute the up-mentioned findings to an improvement of the current available standards about the needed requirements and proper dimensioning of suction bucket founded OWT on liquefiable soils regarding its performance under seismic loads by the use of more economical approaches like, for instance, the numerical test developed in the current report?*

Dynamic soil response 2

2.1 Seismic Hazards

The aim of the study of the earthquake phenomena is not only to analyze the social, political and economical consequences on people and their environment but also the finding of solutions for reducing the damaging effects. The hazards associated with earthquakes are commonly referred to as *Seismic Hazards*. The goal of this report involves the identification and mitigation of them regarding the performance of suction bucket founded offshore wind turbines undergone dynamic loads simulated, through the use of the numerical model presented in the previous section and validated later on through the comparison with the available experimental results.

Hence, the *Seismic Hazards* within the scope of this report are the ones which could influence directly on the behaviour of the seabed during the dynamic loading process, as the ground shaking and the liquefaction triggering. Nonetheless, the amount of them is much larger and, for wider investigations on earthquake engineering, they might need to be taken into consideration: structural hazards, landslides, failure of retaining structures, lifeline hazards, etc.

2.1.1 Ground shaking

Due to its great capacity of damaging, ground shaking can be considered to be the most important of all seismic hazards. When an earthquake occurs, the seismic waves radiate from the source through the body of the soil, then reaching eventually the surface. The shaking induced at this layer may last from a few seconds to minutes.

The last stage of this trip occurs through the soil layers which are closer to the surface so that its characteristics can greatly influence the performance of the shaking. Thus, it can be considered that the soil play the role of a filter which is able to reduce or amplify the motion frequencies.

Further information about the physical mechanisms of propagation of waves through the soil medium is collected in the Appendix A.

2.1.2 Liquefaction

This *Seismic Hazard* becomes specially relevant in some soil compositions. In general, this phenomena is more commonly observed in loose sandy soils but it can also occur in medium-dense and dense sands as explained in the following sections. The triggering of liquefaction implicates the lose of the strength of the soil deposits which start partially or totally to flow as fluids either due to static or dynamic forces. During this process, the soil might not be stable anymore and become unable to support structures.

One option to identify objectively this phenomena is through the comparison between the excess pore water pressure and the effective stress. Thus, it is considered that a certain soil has triggered liquefaction when the ratio between the excess pore water pressure Δu and the vertical effective stress σ'_v at that point is equal to the unit so that a not liquefied soil will show a value between 0 and 1. This ratio is known as excess pore water pressure ratio r_u and can be obtained through the Equation 2.1.

$$r_u = \frac{\Delta u}{\sigma'_v} \tag{2.1}$$

where,

Δu	Excess pore water pressure
σ'_v	Vertical effective stress

A great damaging failure mechanism of civil structures relates liquefaction with the development of large displacements. This mechanism could induce lateral spreading in the case of the supporting structures of bridges or, regarding the scope of the current thesis, settlements underneath the structure of a suction bucket founded offshore wind turbine. Detailed information about the liquefaction triggering phenomena is presented in Appendix A.

Figure 2.1. Bearing capacity failure due to liquefaction of the Kawagishi-cho apartment buildings after the 1964 Niigata earthquake. (Agaiby and Ahmed, 2016)

Figure 2.2. Lateral spreading of Showa Bridge pier foundations induced by liquefaction after 1964 Niigata Earthquake. (Agaiby and Ahmed, 2016)

2.2 Mechanisms of liquefaction-induced displacement

The risk of liquefaction occurring may pose a harmful effect to structure and its normal functioning, stability and bearing capacity. The detrimental effects it presents have been the focus of numerous researches for decades. To avoid potential hazardous scenarios and secure a satisfactory performance of a structure due to large shaking and liquefaction occurring, proper understanding of driving mechanisms the structure is exposed to under such a circumstances is of key importance. Here the findings of (Dashti, Bray, Pestana, Riemer and Wilson, 2010) on mechanisms influencing the liquefaction induced settlements of the buildings with shallow foundations are introduced. Although these are related to the shallow foundations of conventional buildings, it is considered that it can be of great use employing these findings in the case of the suction bucket foundation.

Mechanisms that govern the interaction between the conventional building structure and the soil may be conveyed to the purposes of this report. The behaviour of the liquefable soil in free-field differs from one near structure. The settlements near the structure are altered mainly due to *SSI* and imposed inertial effects of the structure to the surrounding soil, thus the settlements that occur are termed shear-induced or deviatoric settlements. On the other hand, settlements in the free-field occur as a result of post-liquefaction 1D consolidation after the dissipation of the porewater pressure generated and solidification and sedimentation, thus are termed volumetric. The Figure 2.3 illustrates some of the important mechanisms in building settlements due to seismic-induced ground shaking on liquefiable soil.

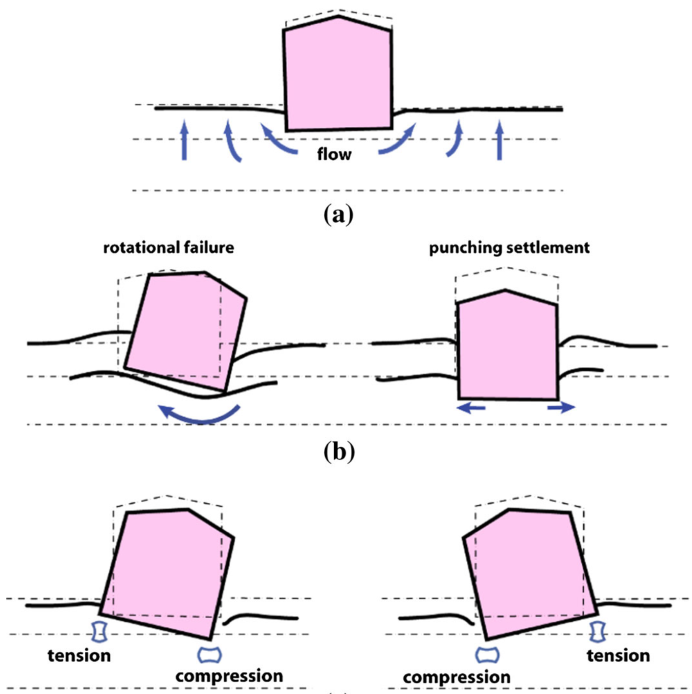

(c)

Figure 2.3. Liquefaction induced displacement mechanisms: a) Volumetric displacements triggered due to fluid outflow, b) Shear-induced displacements due to strength loss in the soil, c) Displacements induced due to effects of *SSI* (D.Bray and Dashti, 2014)

The mechanisms that govern the volumetric and shear-induced displacements are introduced by (Dashti, Bray, Pestana, Riemer and Wilson, 2010),(Bray and Dashti, 2010). Regarding the volumetric-induced displacements, following patterns are mentioned below:

- Localized volumetric strains during partially drained cyclic loading controlled by 3D transient hydraulic gradients (ε_{p-DR}), shown on Figure 2.3a
- Downward displacement due to sedimentation or solidification after liquefaction or soil structure break-down (ε_{p-SD})
- Consolidation induced volumetric strains due to dissipation of excess porewater pressure and increase in effective confining pressure (ε_{p-CON})

The primary shear-induced displacement mechanisms are following:

- Partial bearing failure under static loading of the structure due to strength loss in the foundation soil resulting in punching settlements or tilting of the structure (ε_{q-BC}), shown in Figure 2.3b
- Cumulative ratcheting foundation displacement due to cyclic loading induced by *SSI* near the edges of the foundation (ε_{q-SSI}), shown in Figure 2.3c

Localized volumetric strains ε_{p-DR} occurs even due to the assumption that during the cyclic loading caused by an earthquake, the undrained condition is in effect. This happens due to localized pore water migration as soon as excess porewater pressure builds up due to shaking. The phenomenon occurs mostly during the strong shaking period. The volumetric strains due to sedimentation ε_{p-SD} occur after the soil liquefied, due to the loss of strength dispersion of the soil fabric takes place. The settling particles accumulate at the bottom to form the solidified zone. This zone increases in time and consolidates under its own weight (Dashti, Bray, Pestana, Riemer and Wilson, 2010). Consolidation-induced strains ε_{p-CON} occurs as a result of dissipation of generated excess pore water pressure due to ground shaking. As the shaking stops, the generated excess pore pressure slowly starts to dissipate and the particles resettle again. The contact pressure between particles grows, leading to an increase of effective confining pressure as the excess pore water pressure drops to the levels of the hydrostatic again.

Deviatoric strains induced by partial bearing failure occurs as a result of strength loss and soil stiffness softening due to cyclic loading which for the consequence could lead to punching settlements or tilting. Shear-induced strains due to *SSI*, ε_{q-SSI}, occurs due to imposed inertial forces from an excited structure interacting with the surrounding ground in the form of rocking modes resulting in uplifting of the foundation opposite edges (Figure 2.3c) and horizontal punching modes. This mechanism leads to a loss of strength in the supporting soil and a voluminous accumulation of settlements during the strong shaking period (Dashti, Bray, Pestana, Riemer and Wilson, 2010).

2.2.1 Key Parameters of Liquefaction-Induced Settlement Mechanisms

Key factors that govern the mechanism behind the volumetric and shear-induced mechanisms are thoroughly explained according to the work of (Dashti, Bray, Pestana, Riemer and Wilson, 2010).

Peak Ground Acceleration (*PGA*) is one of the most important factors contributing the deformations induced by ground shaking motion. This parameter can give a good insight in terms of seismic demand on soil and structure. It is shown that increasing the *PGA* contributes to the progression of settlements regarding any of the previously mentioned mechanisms. Increasing seismic demand leads to an increase of all volumetric and deviatoric related deformation mechanisms. This progression in settlements reaches certain limits after which the increasing demand level-off.

Initial Relative Density of Sand D_R has considerable impact on the response of the soil and its resistance to liquefaction. Sands with higher initial relative density shows higher resistance against liquefaction and strength loss due to strong shaking. Lower void ratio counteracts the progression of volumetric settlements and provide higher soil stiffness. However, greater soil stiffness, on the other hand, triggers amplification of the ground motion, which could lead to higher shear-induced settlements provoked by *SSI* ε_{q-SSI}.

Thickness of liquefiable layer influences the progression of a volumetric induced settlements increasing with thickness growth. A thicker layer may deamplify the accelerations at the foundations level, thus reducing the effects of soil-structure interaction-induced settlements ε_{q-SSI}.

Foundation width affects the dissipation of the excess pore water pressure as its drainage path increases with increase in foundation width. Wider foundation could result in bigger post-liquefaction consolidation ε_{p-CON} and sedimentation ε_{p-SED} settlements. Localized volumetric strains ε_{p-DR} at edges of the wider structure are sparse. With increase of the width of the foundation the deviatoric component in settlement mechanism related to *SSI*, ε_{q-SSI}, reduces due to less rocking mechanism. Soil is harder to be pushed out laterally underneath the wider foundation so that also contributes to less settling. On the other hand, deviatoric induced ε_{q-BC} settlements increase with increase in foundation width.

Static Shear Stress Ratio if increased can help in overcoming the large seismic demand in form of large generation of pore water pressure so that the effective stresses do not fall to zero causing liquefaction to occur. Thus, contributing reducing the settlements due to consolidation ε_{p-CON}, partial drainage ε_{p-DR} and due to sedimentation ε_{p-SED} (at the perimeter of the foundation) while on the other hand increasing the shear stresses acting on the soil.

Structure Height/Width Ratio (H/B) has an effect on the amount of deviatoric-induced strains. By increasing the (H/B) ratio, the tendency to increase the strains induced by *SSI* ,ε_{q-SSI} is present, generated by the bigger demand in terms of inertial loads resulting in substantial *SSI*-induced soil disturbance and generation of pore water pressure. To a less extent, the increase in (H/B) ratio leads to increase in settlements of consolidation-induced ε_{p-CON}, sedimentation-induced, ε_{p-SED} and due to partial draining, ε_{p-DR}.

Structure Weight affects the contact pressure between soil and the foundation area. Increasing the structural weight for the same contact area induces the higher confinement of the soil below foundation increasing the strength of the soil, its resistance to pore water generation, and to liquefaction. Apart from the contribution of higher effective stress confinement in the soil, larger excess pore water pressures are generated below the structure foundation than in the free-field. However, even due to larger excess pore water pressures, higher confinement ensures that excess pore water ratio $r_u = \Delta u/\sigma'_{v0}$ do not reach value equal to 1. Sands with relative density higher than 30% tends to decrease in cyclic resistance ratio *(CRR)* and cyclic stress ratio *(CSR)* under higher confinement. According to (Macedo Escudero, 2017) increasing the weight of the structure proportionally leads to increase in settlements but after a certain point increase do not contribute any more to larger displacements, instead they plateau or even decrease.

3D Hydraulic Conductivity can alter the mechanisms of seismic-induced displacements. Higher hydraulic conductivity results in larger drainage rates, lowering the possibility of liquefaction , thus mitigating sedimentation. On the other hand, the faster fluid migration increases local volumetric strains due to partial drainage and due to shorter period of soil softening, the resistance to partial bearing capacity failure increases.

2.3 Laboratory tests

In order to evaluate the dynamic behaviour of the soil under laboratory conditions, several kind of tests are available which are chosen depending of the output needed. Although the execution of laboratory tests is out of the scope of this report, the outputs generated by a cyclic direct simple shear test and by a centrifuge test are received and used as a reference in order to calibrate the developed numerical model. Thus, a brief explanation is carried with the intention of giving the key features of both kind of tests.

2.3.1 Cyclic Direct Simple Shear Test (CDSS)

The outputs received from this test are used for estimating numerically an initial set of parameters of the constitutive model *PM4Sand* which is used later on, and together with the constitutive model *PDMY01*, for performing the numerical simulation of a centrifuge test.

Cyclic Direct Simple Shear Test belongs to the group of element tests and is able to reproduce the stress conditions of a liquefable soil during an earthquake. This test uses a cylindrical specimen whose lateral expansion is restrained by a rigid boundary as observed in Figure 2.4. During the performance, cyclic horizontal stress is applied to the bottom or the top of the specimen, simulating the propagation of s-waves.

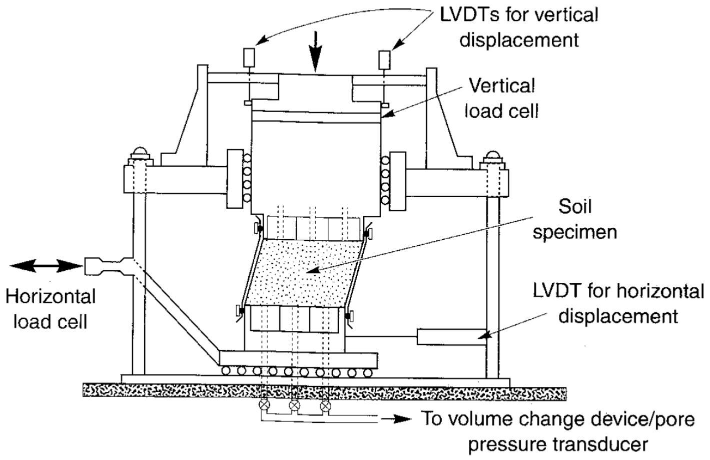

Figure 2.4. Cyclic Direct Simple Shear Test device. (Kramer, 1996)

2.3.2 Centrifuge test

The results cast by a centrifuge test are used in this report for calibrating the performance of a numerical prototype constructed by the use of the software *OpenSees*.

The centrifuge test is within the group of model tests which uses small-scale physical prototypes for reproducing the performance of full-scale structural or geothecnical problems. Due to this feature, the most challenging point is to reproduce the stress state of the real scenario. That is the reason why the testing process involves an increased gravitational field.

Thus, in a centrifuge test, a scaled model *1/N* located at a distance *d* from the axis, is spinned by the application of a rotational speed $V_r = (N/d)^{0.5}$ in order to simulate the stress conditions of the full-scale prototype. A diagram of the device used is represented in Figure 2.5.

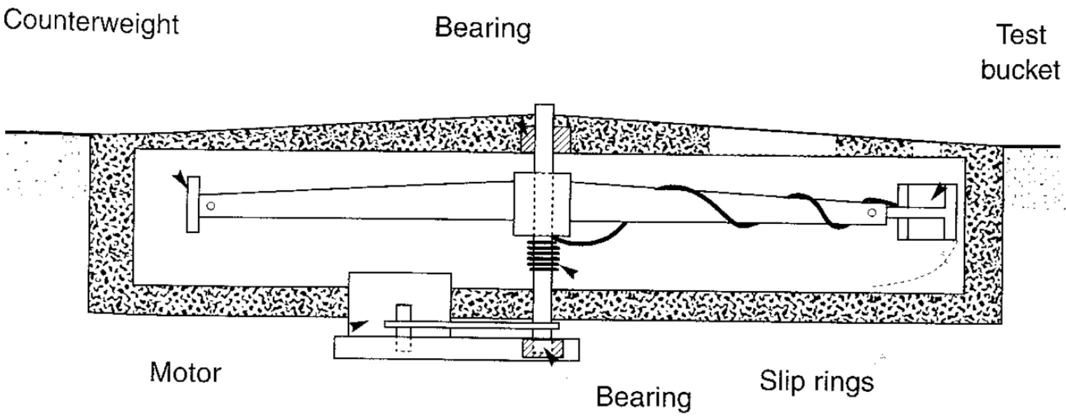

Figure 2.5. Geotechnical centrifuge equipment scheme. (Kramer, 1996)

Reference Test 3

In the previous section, the centrifuge test has been already characterized as a widely-used experiment in the laboratory. Among other applications, it can be used to simulate the behaviour of liquefiable soils undergone earthquake motion.

In this section, the test configuration and the outputs obtained from a centrifuge test performed on a sand box to simulate a scaled prototype of an offshore wind turbine are presented (Yu et al., 2014), under regulated conditions of gravitational acceleration. These model characteristics and outputs are used in following sections for the validation and calibration of the numerical model proposed in the current report.

A general overview of the conducted experiment procedure as well as the results obtained in terms of pore water pressure generation, nodal accelerations and settlement, are depicted thoroughly in this chapter.

3.1 Test facilities

Firstly, the general information of the experimental utilities and researched soil features are introduced. As far as the facilities of the centrifuge test are concerned, a scaled wind turbine model is set into a sand-box rigid container, with dimensions 53.3cm x 24.1cm x 17.7cm length, width and height respectively. The container together with the scaled prototype of the wind turbine is set up in a dual platform located at one of the ends of the centrifuge device beams which counts with a radius of 1.37 m respect to the center, similar to the illustration at the Figure 2.5.

The carrying payload capacity of such device is up to 182kg, however, the gravitational acceleration can be modified up to 200g for static analysis and 100g for dynamic analysis by the use of the centrifuge spinning flight. This centrifuge acceleration, in the case of the current test equivalent to 50g, allows to set to the reduced scaled prototype the same value of stresses at the soil domain and weight of the structure than the actual prototype, which is also scaled to 1/10 of the full size construction. Once the acceleration reaches the desired value, the dynamic loads are applied to the prototype by the use of a shaking platform simulating thus the 1-D earthquake during the spinning flight of the sand container.

3.2 Model configuration

Describing the model constructed in prototype scale, its main dimensions are observed at Figure 3.1. During the test, the water table level remains unchanged at 1.5m above the surface of sand layer for modelling the real conditions of the offshore construction. On the other hand, in order to simulate the weight of the nacelle, the blades and the rotor, a lumped mass equal to 10.6 *tons* (W) is set at the tip of the wind turbine prototype as shown in the Figure 3.1.

As regard the soil properties, the rigid container is filled out by well graded Toyoura sand with $D_{50} = 0.17mm$, poured from a level of $80cm$ for ensuring a value of relative density equal to $D_r = 68\%$. The saturation process is conducted by using de-aired water system and a vacuum device for at least 24 hours for getting the simulation as realistic as possible.

A fundamental aspect for achieving the centrifuge test success is the setting-up of the record instrumented sensor devices in the sand container. In the case of the presented centrifuge test, 9 primary sensors of different typologies are equipped inside the sandbox, see Figure 3.1, three accelerometers (ACC), four pore pressure transducers (PPT) and two linear variable differential transducers ($LDVT_s$) with the aim of measuring accelerations, pore water pressure and settlements and rotations respectively. However, the outputs received about the rotation of the structure are not considered for the current report. By using the same setting described in the previous paragraphs, four different tests with variable geometrical characteristics of the wind turbine prototype are taken into consideration whose features are shown in the Table 3.1.

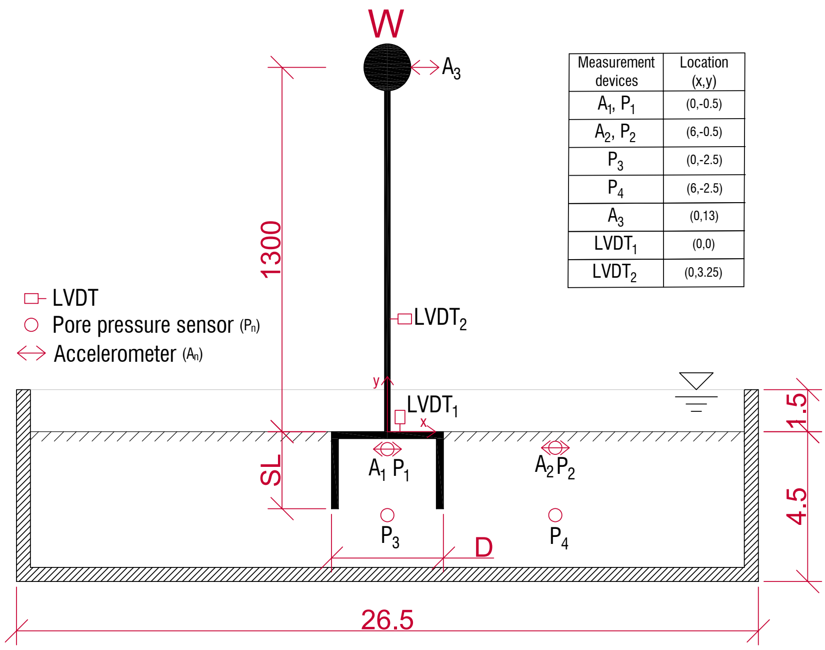

Figure 3.1. Model configuration of a centrifuge test,(Yu et al., 2014).

	Diameter (m)	Skirt length (m)	Weight-T(ton)	Lumped mass-W (ton)
Test 1	4	1.75	18.7	10.6
Test 2	6	1.75	18.7	10.6
Test 3	4	2.5	18.7	10.6
Test 4	4	1.75	28.2	10.6

Table 3.1. Technical specifications of the structure of the prototype in the 4 different laboratory tests performed (Yu et al., 2014)

Regarding the artificial 1-D earthquake motion applied to the prototype, its acceleration time-history is shown in the Figure 3.2a.

In this report, the output results of Test 1 according to the table 3.1 are used for the verification and calibration of the results obtained from the numerical model. Nonetheless, the time histories from the remaining tests are also employed for comparing the predictions cast by the numerical model and the experimental model.

3.3 Centrifuge test output results

After applying the input motion to the test model, the above-mentioned 9 sensors are responsible for recording 3 kinds of phenomena occurring in the prototype: accelerations, pore water pressure, and settlements and rotations. The experimental nodal acceleration values obtained from the 3 accelerometers: A1, A2, and A3, are shown in the Figures 3.2b, c and d.

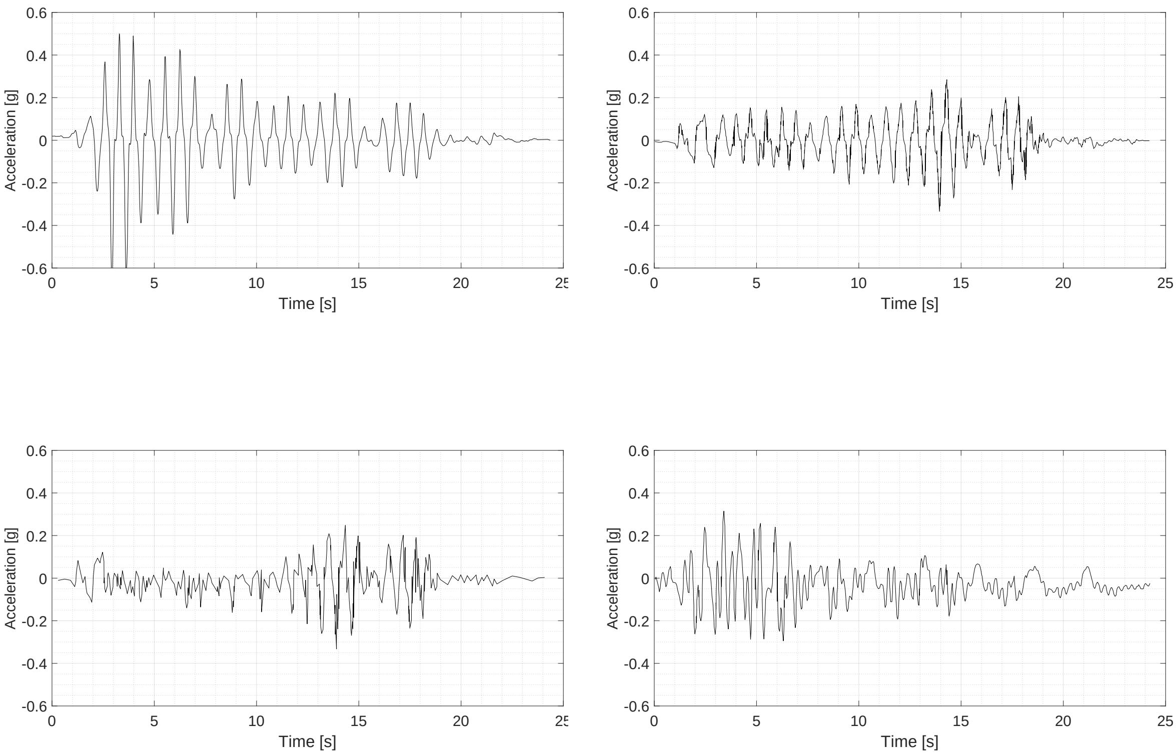

Figure 3.2. Input motion applied to the model and outputs from acceleration recorders (Yu et al., 2014), from left to right: (a) Input motion applied to the prototype (b) Nodal accelerations at sensor A1 (c) Accelerations at sensor A2 (d) Accelerations at sensor A3.

By the use of the software *SeismoSignal*, from the provided nodal accelerations, the acceleration spectral of the input motion and the mentioned accelerometers are obtained, see Figure 3.3.

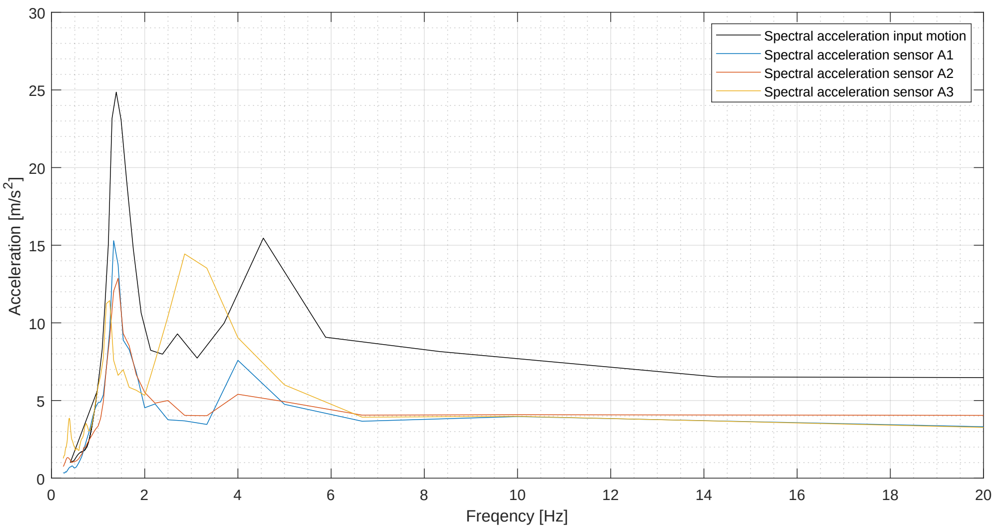

Figure 3.3. Frequency spectrum of received acceleration time history

Taking a look at the sensors A1 and A2, see Figure 3.2b and c, it is observed that the trends of acceleration time history of the soil nodes at these locations differs to the recorded time history at the tip of the structure obtained at the location A3 3.2d. The peak nodal accelerations during approximately the first 10 seconds is smaller than the measured at the tip of the structure by A3. This fact can be explained regarding the increment of the pore water pressure after few seconds of applying the seismic loading at the model base, which results in a reduction of the soil stiffness and a deamplification of the soil nodal accelerations due to the inability of the water for transmitting shearing waves.

Having said that, it is also noticed that after the first 10 seconds, the period corresponding to the strongest shaking, see Figure 3.2a, the liquefaction phenomenon most likely mitigates, which culminates in a re-consolidation of the particles of the soil and, subsequently, a regaining of soil stiffness. Consequently, the peak ground accelerations at the soil domain are amplified at the end of the shaking period. In contrast to these behaviours, the structure seems to show a similar trend than the input motion applied so that the pattern recorded by the sensor A3 located at the top of the prototype registers higher peaks on the acceleration during the strong shaking period, becoming smaller after 10 seconds, see Figure 3.2d.

These different trends can be also analyzed in terms of frequencies. Taking a look at the figure 3.3, the peak value of accelerations of the two sensors located at the soil domain (A1 and A2) is found at the same range of frequencies, around 1 Hz, which also correspond to the predominant frequency of the input motion. However, it is also noticed the important deamplification of the peak accelerations at these sensors in comparison with the dynamic time history.

On the other hand, the spectrum acceleration obtained from the accelerometer A3 looks different than the ones measured at the soil. Thus, it is noticeable that a predominant value of the frequency of the tower is also found at the value of 1 Hz but the highest peak is obtained at higher frequencies, specifically at $3Hz$. This second peak replicates also the spectrum profile of the input motion which shows also a local maximum at higher frequencies than 1 Hz.

Regarding the pore water pressure generation, the value of the pore water pressure ratio r_u at the 4 previously mentioned locations (sensors P1, P2, P3 and P4) is showed in order to discuss the differences between the trends observed at different locations and the possible factors responsible of the liquefaction triggering in some of the cases, see Figure 3.4a, b, c and d.

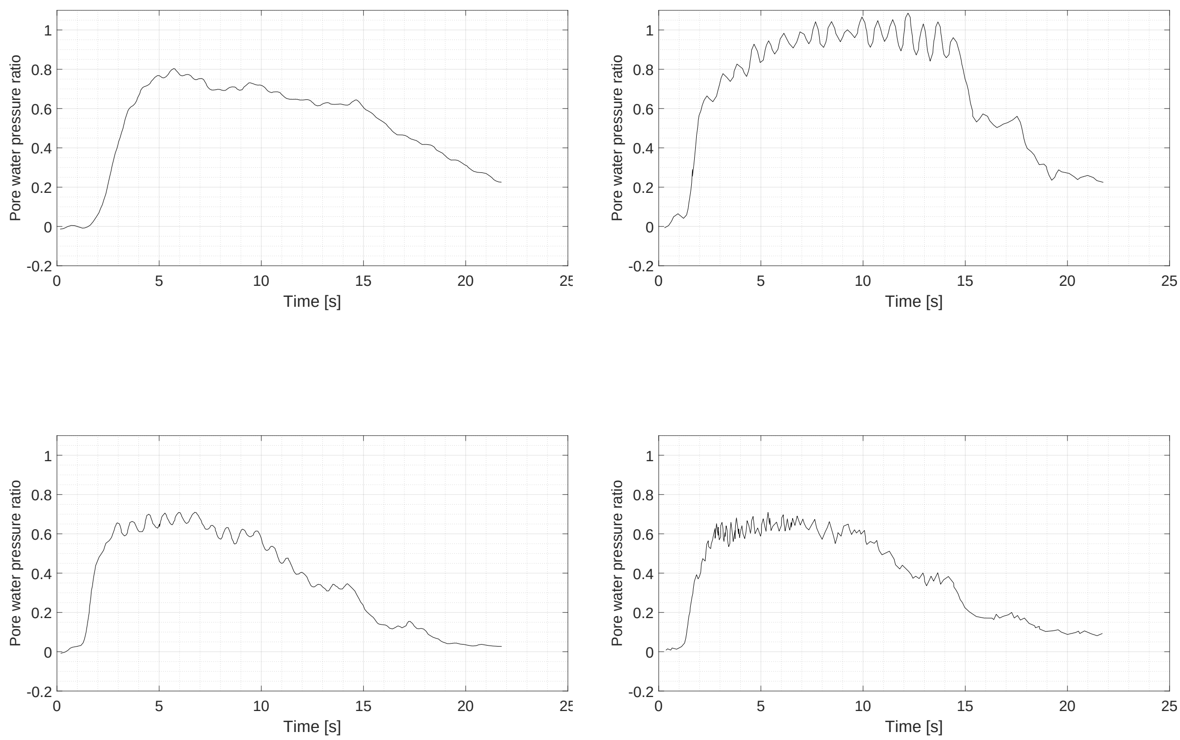

Figure 3.4. Pore water pressure ratio-time history r_u at different locations (Yu et al., 2014), from left to right: (a) Pore water pressure ratio at P1 (b) Pore water pressure ratio at P2 (c) Pore water pressure ratio at P3 (d) Pore water pressure ratio at P4

Taking a look at the 4 up-illustrated figures, the liquefaction phenomenon is only experienced at the location of sensor P2 which is located at the free field, x=6 m and y=-0.5, since the pore water pressure ratio reaches a value equal 1 during several stages of the shaking. The difference between this recorder and the sensor located at P1 is the presence of the structure since the depth in both cases is the same. Thus, it can be concluded that increment on the vertical pressures due to the presence of the wind turbine prototype, makes more difficult the triggering of liquefaction due to the larger value of vertical effective stresses at that point, see Equation 2.1. Regarding the sensors at deeper layers, liquefaction phenomenon is not triggered there, a fact that can be explained again taking into account the larger value of effective stresses at these points.

Moreover, it is observed that the pore water pressure obtained by the 4 sensors starts to be dissipated at different time. Thus, the sensor P2 is the one showing a later dissipation, whereas the dissipation is observed after approximately 8 second in the rest of the sensors being slower at P1, presumably due to a longer drainage because of the presence of the suction bucket.

When it comes to the settlements of the prototype of the OWT, the results are obtained from the linear variable differential transducer $LVDT_1$, see Figure 3.5.

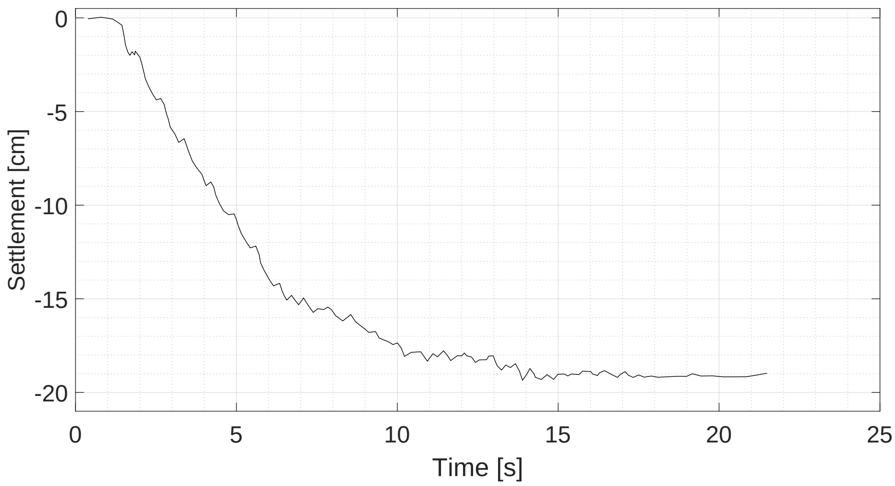

Figure 3.5. Settlement obtained by transducer $LVDT_1$(Yu et al., 2014)

As observed, the settlements generated follow a non-linear pattern which can be explained observing the variation of the intensity of the seismic acceleration along the time. In addition, it is observed that most of the vertical displacements occur during the first seconds of shaking, when the intensity is larger, see Figure 3.2a. Thus, a dramatic increment of 16 cm is witnessed after the first 8 seconds, remaining this value almost unchanged until the end of the dynamic event, presumably, due to the re-consolidation of the soil.

Construction of the numerical model 4

The numerical simulation of the centrifuge test described in the previous section is carried by the use of the software *OpenSees*, an open source program which allow the construction and analysis of structural and geotechnical finite element models under dynamic loads.

The programming language used by this software is *.tcl*. In order to simplify the tasks of construction and manipulation of the code, the software *GID+Opensees* is used for the definition of the geometry of the model. In the current section, all of the information needed for achieving the task of constructing mentioned numerical model is presented.

4.1 Simplified model proposed

Based on the prototype tested during the performance of the centrifuge test described in the previous chapter, see Figure 3.1, simplified models are built for running the numerical simulation. As far as the characteristics of the structure and the size of the bucket are concerned, they correspond to the ones showed at Table 3.1 for "Test 1".

The models constructed are showed at Figure 4.1 and Figure 4.2 for the constitutive models *Pressure Dependent Multiyield 01 (PDMY01)* (Parra-Colmenares, 1996)(Yang et al., 2000)(Yang, 2000) and *Plasticity Model for Sand (PM4Sand)* (Boulanger and Ziotopuolou, 2017) respectively. Two different models are built since the soil domain counts with different mesh refinement in every case and a small adjustment of the dimensions respect to the physical prototype presented at Figure 3.1 need to be made in the case of *PM4Sand* for ensuring the right position of the bucket and recorders respect to the soil nodes.

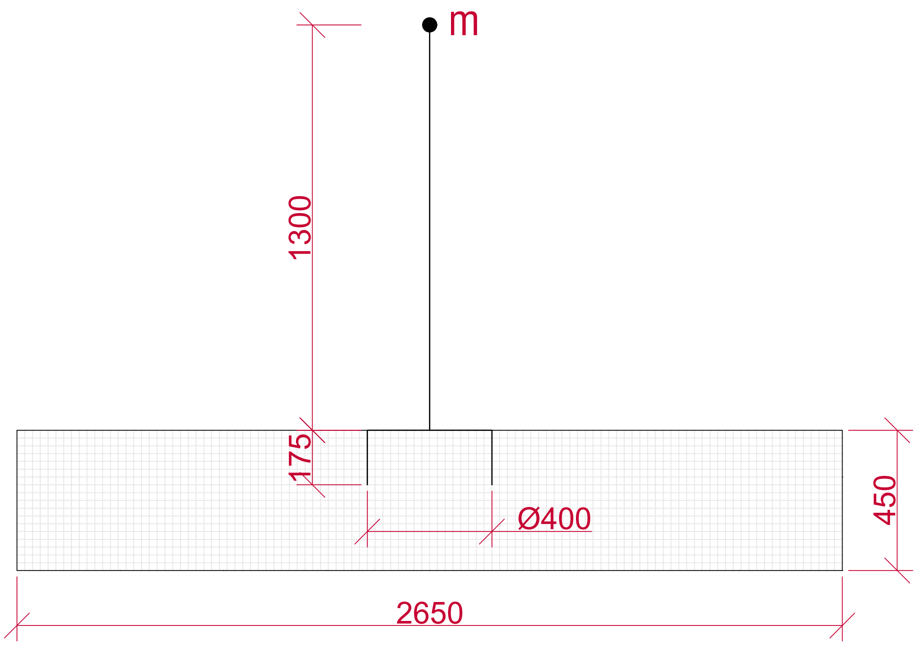

Figure 4.1. Simplified model proposed for numerical simulation with *PDMY01* constitutive model

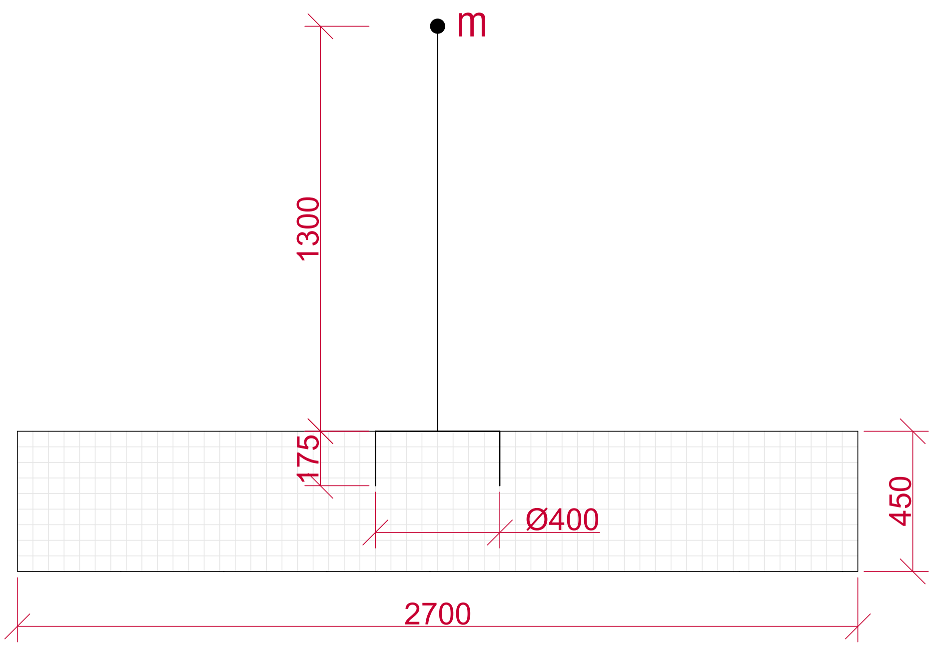

Figure 4.2. Simplified model proposed for numerical simulation with *PM4Sand* constitutive model

The "Test 1" of the real prototype counts with a concentrated mass at the tip of the tower of 10.6 tons simulating the weight of the rotor, blades, gearbox and nacelle of the wind turbine, and a second mass located at the foundation of 18.6 tons, see Table 3.1. This mass configuration is simplified in the numerical tests as a single mass m located at the tip of the tower equal to the sum of the above mentioned ones. This decision is made in order to improve the results of the generation of pore water pressure underneath the foundation since setting a mass at the foundation level introduce spurious dynamic waves within the nodes inside the bucket.

As far as the soil domain is concerned, two different constitutive models are used which are explained in detail in following paragraphs, *Pressure Dependent Multiyield 01 (PDMY01)* and *Plasticity Model for Sand (PM4Sand)*. Depending on the constitutive model used, the soil is modelled with a different refinement of mesh since the computational time is higher in the case of *PM4Sand*. Thus, the soil domain is modelled using a mesh of 106 x 18 *quadUP elements* with a size of 0.25m x 0.25m in the case of *PDMY01*, while regarding *PM4Sand*, the computational domain of the soil is constructed with a mesh of 53 x 9 *quadUP elements* (Mazzoni et al., 2007) with a size of 0.50m x 0.50 m.

In the case of the structure, *Elastic Beam Column elements* (Mazzoni et al., 2007) are used. The connection between bucket foundation and soil domain is accomplished invoking the command *equalDOF* between their nodes and the nodes of the soil, considering the soil as *master nodes* and structure as *slave nodes*. Further details are presented during the current section.

4.2 Mesh definition

4.2.1 Soil domain

In order to simulate properly the soil domain, *QuadUP* elements are chosen since they bring the possibility of simulating the generation of pore water pressure in saturated soil. *QuadUP* element is a four-node plane strain element suitable for 2D simulations. Each of its nodes count with 3 degrees of freedom, 1 and 2 for translations along x and y respectively, and the third one for the generation of fluid pressure, see Figure 4.3. This kind of element is specially recommended for carrying dynamic simulations of solid-fluid materials (Theocharis, 2020).

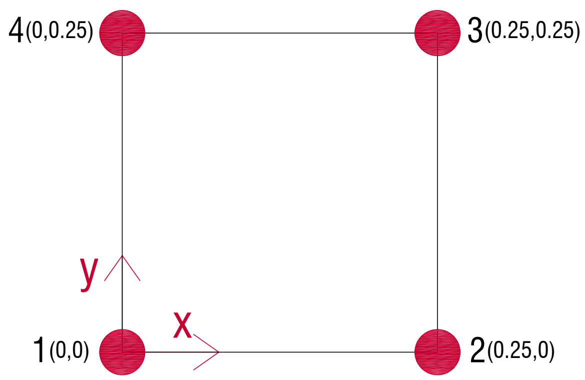

Figure 4.3. Four-node QuadUP soil element.

Nonetheless, not only the kind of element but also the size of them plays a key role in the obtaining of accurate results. The maximum dimension of the elements located at the soil domain must be limited to be smaller than the value of one-eighth to one-fifth of the shortest wavelength considered in the analysis (Zhang et al., 2018). The wave length λ can be calculated following the Equation 4.1:

$$\lambda = \frac{v_s}{f_p} \tag{4.1}$$

v_s	Velocity propagation of S-waves following Equation A.2
f_p	Predominant frequency of the input motion

Since the element size need to be set before starting the calibration process, the values of the shear modulus G and density of the soil ρ are still unknown. However, for carrying out the shear velocity calculation v_s, typical values of these parameters for medium sand according to (Mazzoni et al., 2007) are considered knowing that the values received from the centrifuge test were obtained for a relative density of $Dr = 68\%$, see Chapter 3.

Regarding the predominant frequency of the input motion f_p, a value of 1.5 Hz is used according to the results observed at Figure 3.3. A summary of the values considered for all the mentioned parameters are collected in the Table 4.1.

Description	Symbol	Value	Units
Shear modulus	G	7.50e4	kPa
Soil density	ρ	1.90	$tons/m^3$
Shear wave velocity	v_s	198.68	m/s
Predominant frequency	f_p	1.50	Hz
Wave length	λ	132.45	m

Table 4.1. Parameters considered for wave length calculation

Following the most conservative procedure, the value of one-eighth of the wave length gives a result of approximately 16.5 m. For the construction of this model, meshes composed by *quadUP elements* with a size of 0.25m x 0.25m and 0.50m x 0.50m are considered, so enough refinement in both cases is achieved.

Regarding the behaviour of the soil under real conditions, it is expected that the value of the permeability were not the same in all the tested domain since it is related with the depth and the position of a certain point respect to the structure. Therefore, the soil mesh is divided into four different domains with the intention of having a higher control of the permeability. Thus, by setting separate values of hydraulic conductivity for the different soil domains, a higher control of the possible inaccuracies of the numerical model related with this issue is achieved. The configuration followed is shown at Figure 4.4 and Figure 4.5 for the case of *PDMY01* and *PM4Sand* respectively. The value of permeability in each domain is obtained after the calibration process but it is already shown at Table 4.2.

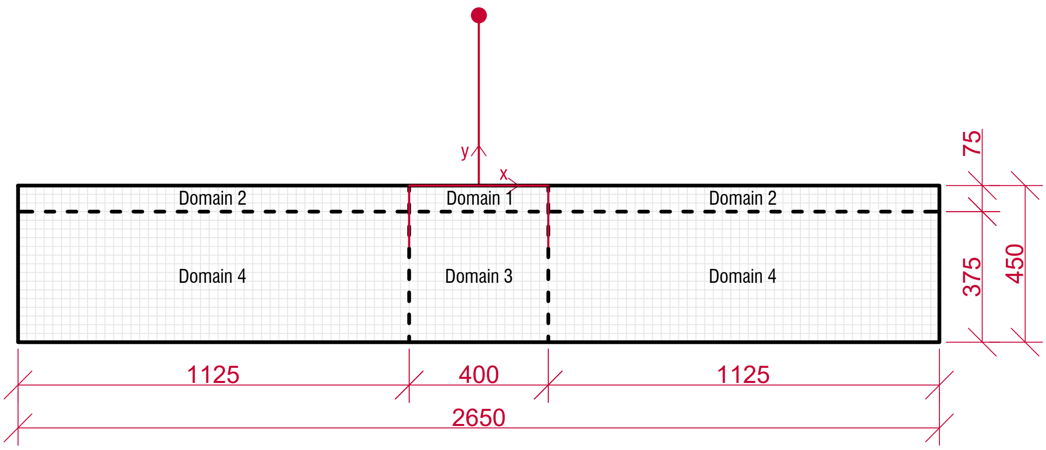

Figure 4.4. Domains distribution of mesh of the soil for *PDMY01* material

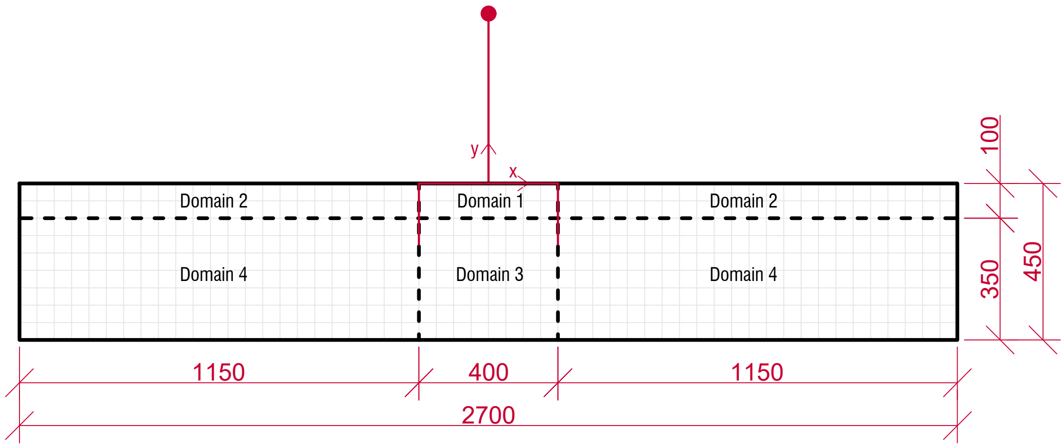

Figure 4.5. Domains distribution of mesh of the soil for *PM4Sand* material

	PDMY01		PM4Sand	
	nº elements	Permeability $[cm/s]$	nº elements	Permeability $[cm/s]$
Domain 1	16 x 3	2.00e-4	16 x 2	1.00e-4
Domain 2	45 x 3	3.50e-5	46 x 2	2.00e-5
Domain 3	16 x 15	2.50e-4	16 x 14	1.00e-4
Domain 4	45 x 15	1.00e-4	46 x 14	2.00e-4

Table 4.2. Size and permeabilities considered for the soil domain for PDMY01 and PM4Sand materials

4.2.2 Structure domain

When it comes to the definition of the structure of the wind turbine, *elastic beam column elements* available in *OpenSees* are used. This element consists of 2 nodes, in which each of them has 3 degrees of freedom, two translation, along x and y directions, and one rotation (Theocharis, 2020), see Figure 4.6.

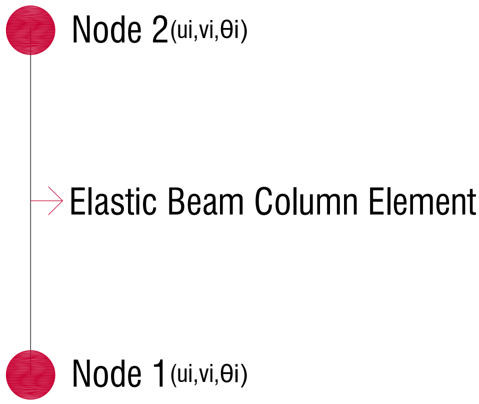

Figure 4.6. Elastic beam column defined for structure element.

Young's modulus E is used to set the stiffness of this type of element, a characteristic which define the transmission of the loads coming from the masses of the structure to the soil domain.

4.3 Soil-foundation interface

Once having completed the definition of the soil and the structure domain, the interface between structure and soil is modelled by using the *equalDOF* command. Thus, the displacement of the nodes of the bucket, *slave nodes*, are restrained to follow the same displacements than the soil, *master nodes*. With the purpose of carrying a most accurate analysis, the lid of the bucket is tied to the soil by the use of *EqualDOF* just along y direction while the skirts are tied following x direction following the setting observed at Figure 4.7.

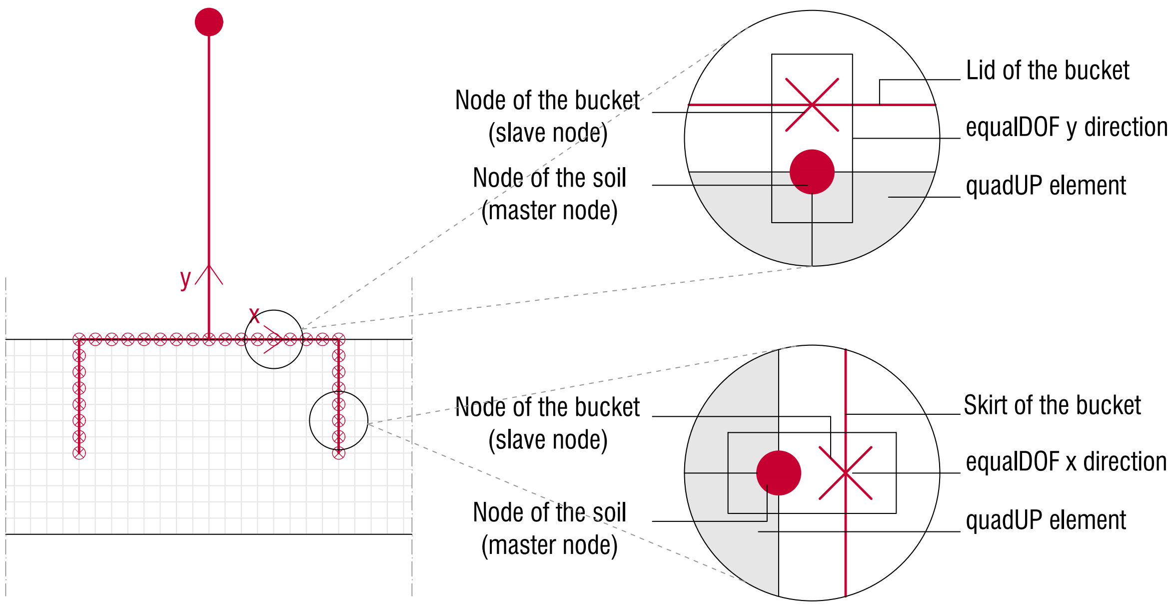

Figure 4.7. Interface between soil and bucket foundation

Moreover, with the purpose of simulating the confinement capacity of the skirts of the bucket foundation, the command *equalDOF* is invoked once again so as to tie together along x direction the nodes of the skirts which share the same y coordinate.

4.4 Constitutive models

Numerical model is the well-known method to simulate the dynamic analysis concept with many remarkable characteristics in comparison with the experiment. Specially, such method is a widely employed technique to research complex geotechnical issues by the numerically computational simulation of the considered model, which brings out another standpoint of outputs evaluation. Moreover, the saving of time working can also be the significant advantage in the analysis strategy. In order to make full use of the numerical method efficacy, the proper constitutive models need to be taken into consideration thoroughly, in terms of the geotechnical features in each of them.

Constitutive soil model is a fundamental factor regarding the quality of the performance of the numerical model. It is not possible the use of an unique constitutive model suitable for all of the geotechnical applications and soil conditions: drained or undrained conditions, static or dynamic loads, etc. Hence, the users need to take charge of choosing the proper constitutive model depending on the desired characteristics being simulated. In this report, the *Plasticity Model for Sand* ($PM4Sand$) (Boulanger and Ziotopuolou, 2017) and $PressureDepend\ Multi-Yield\ 01$ ($PDMY01$) (Parra-Colmenares, 1996)(Yang et al., 2000)(Yang, 2000) are the constitutive model chosen to for simulating the current numerical dynamic analysis. Further information about *PM4Sand* and *PDMY01* models is explained thoroughly in the proceeding section.

The command codes used for setting the mentioned constitutive models and its detailed definition are explained in the Appendix B.

4.4.1 PM4Sand constitutive model

PM4Sand model is developed to be such that the engineering design relations are approximated to estimate the stress-strain behaviors, which are crucial to predict liquefaction phenomenon induced by ground shaking during earthquakes. This improvement process is conducted based on the experimental data correlation and also the historically inherent designing. In this model, the fabric formation of the soil is depended on plastic shear strain, which provides more control of volumetric contraction (Boulanger and Ziotopuolou, 2017).

PM4Sand model follows the basic framework of stress-ratio controlled, critical state compatible, plane strain bounding surface plasticity model for sand presented by (Dafalias and Manzari, 2004). Model is improved in order to better predict the stress-strain relations due to liquefaction-induced deformations during earthquake loading which would be of use in engineering practice(Boulanger and Ziotopuolou, 2017). The model counts with a narrow stress-ratio based elastic cone and three other key surfaces: bounding, dilation and critical state surface (Ziotopoulou, 2018).

Regarding the critical state approach, it is incorporated in the model via relative sate parameter index ζ_R which stands for the difference between the current value of the relative density D_R and value of relative density at critical state $D_{R,cs}$. This allows model to adapt to the changes in void ratio, mean effective stresses exhibited in soil during the loading conditions.

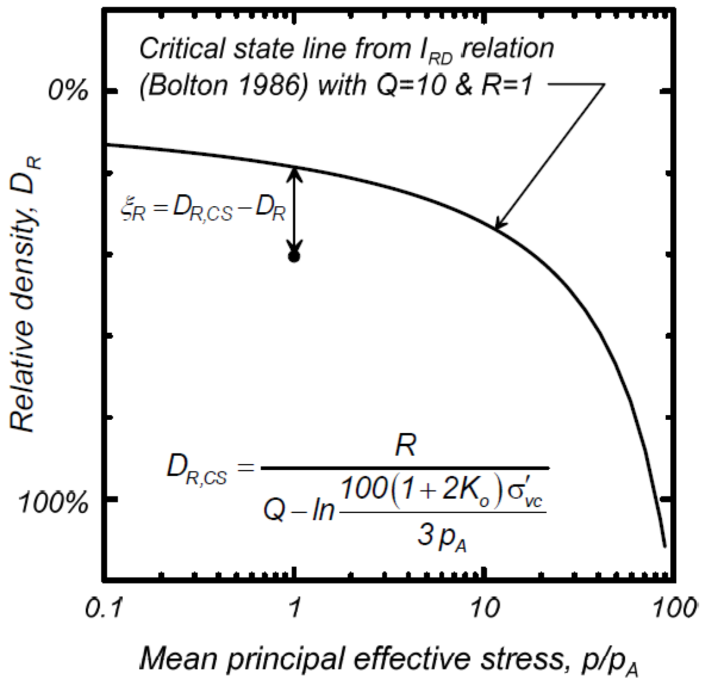

Figure 4.8. Relative state parameter index ζ_R in terms of relative density D_R and mean effective stress (Boulanger and Ziotopuolou, 2017)

Bounding and dilatancy surfaces are closely related to the value of the relative state parameter index ζ_R as it governs the position of the surfaces according to the critical state line. Due to shearing that approaches critical state of soil, bounding and dilatancy surfaces move together until they coincide with each other with critical state surface. The critical state surface is determined by the friction angle at constant volume ϕ_{cv}. The bounding surface cannot be exceeded. Dilatancy surface serves as a distinction boundary between the phases in terms of contractive or dilative behaviour of the soil during shearing. The model also accounts for incorporating the fabric changes.

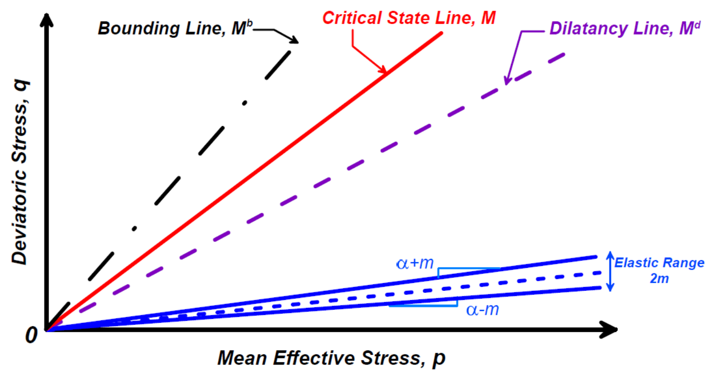

Figure 4.9. Bounding, critical, yield and dilatancy surface in $p - q$ space (Boulanger and Ziotopuolou, 2017)

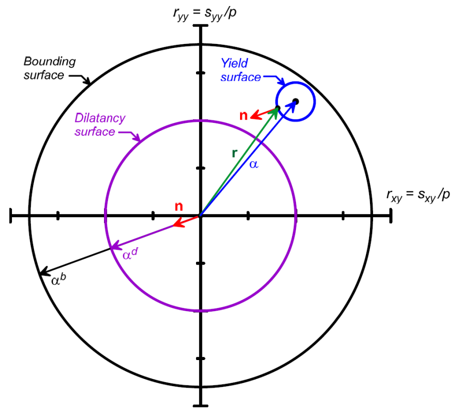

Figure 4.10. Bounding, yield and dilatancy surface in $r_{xx} - r_{xy}$ space (Boulanger and Ziotopuolou, 2017)

PM4Sand model consists of 22 input parameters in total that are specifically divided into 2 parts, such as a primary combination of 3 parameters and a set of secondary parameters. One of the advantages of *PM4Sand* is that it is supposed that calibration of the model can be achieved by focusing on the primary set of parameters according to (Boulanger and Ziotopuolou, 2017). Contrary, all of the secondary parameters are set as default values. Depending on cases, if calibration process demand additional effort extra set of secondary parameters can be adjusted to fit the targeted values. Subsequently, model parameters are introduced in the proceeding section.

Primary model parameters

Three up-mentioned primary input model parameters are relative density D_R, the shear modulus coefficient G_o and the contraction rate parameter h_{po}. These are the main parameters in order to achieve the calibration of the model so that it is assumed that this process can be completed by manipulating only these parameters. A brief overview of each parameter characteristics are mentioned below.

Relative density (D_R)

Relative density is supposed to be responsible for controlling dilatancy and stress-strain response characteristics. Initial value determines the contractive/dilative behaviour of the soil and proximity to the phase transformation surface herein model termed dilatancy surface. The value of this parameter can be estimated based on 2 kinds of experimental in-situ test, such as standard penetration test (SPT) and cone penetration test (CPT). However, in the numerical model simulation, this parameter is calibrated according to the relative density of medium dense sands recommended values 5.32.

Shear modulus coefficient (G_0)

Shear modulus coefficient is used to control the small strain or the elastic shear modulus, according to the Equation 4.2 . Taking a look at the Figure 4.11, it is observed how the value of the normalized elastic shear modulus G over the shear modulus coefficient G_0 is reduced as the shear strains become larger. Thus, the shear stiffness of the soil is considered almost unchanged when very small strains occur.

$$G = G_0\, p_A \left(\frac{p}{p_A}\right) \tag{4.2}$$

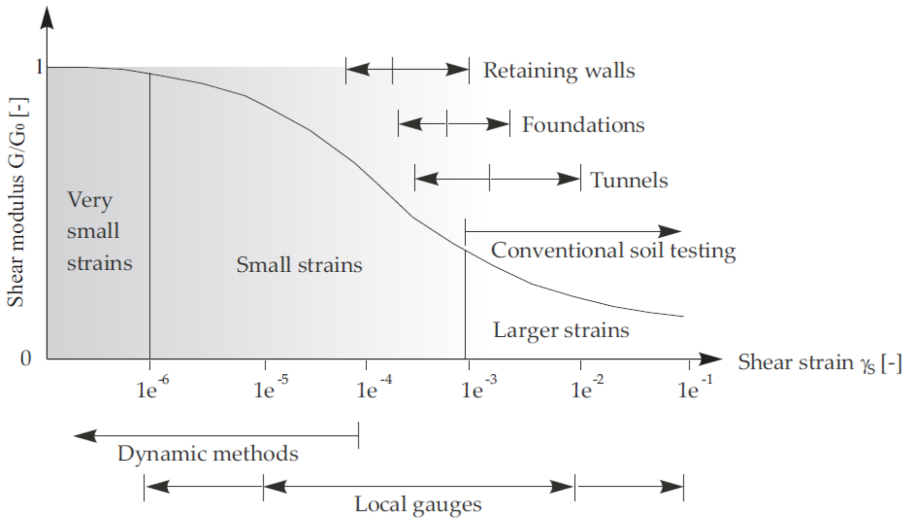

Figure 4.11. Characteristic stiffness-strain behaviour of soil with typical strain ranges for laboratory tests and structures(Plaxis 2D Reference Manual, 2020)

An initial value for the elastic shear modulus can be calculated if the shear wave velocity V_s is known, following the expression $G = \rho V_s$, being ρ the soil density. Alternatively, elastic shear modulus coefficient G_0 can be estimated based on the following relation with relative density D_r, see Equation 4.3 .

$$G_0 = 167\sqrt{46\, D_R^2 + 2.5} \tag{4.3}$$

Contraction rate parameter (h_{po})

The third primary input parameter is a fundamental factor for target cyclic resistance ratio (CRR) and control of the contraction rate due cyclic loading. Thus, the contraction state of the soil element is also controlled by adjusting the values of contraction rate parameter. The calibration process of (h_{po}) is totally depended on the defined values of the other two primary input parameters, which means that this procedure is totally iterative once a proper combination D_r and G_0 is set.

Secondary input parameters

$PM4Sand$ plasticity constitutive model also counts with a set of 19 secondary parameters that can be calibrated. Nevertheless, they can be set up with the default values, which are already set for providing appropriate results in term of the typical design relation. However, in some particular occasions, they might need to be adjusted to bring out more accurate results. These parameters are presented in the Table 4.3 together with its recommended default values(Boulanger and Ziotopuolou, 2017).

Parameter [OpenSees Name]	Explanation
h_o [h0]	Variable that adjusts the ratio of plastic modulus to elastic modulus. The default value of $ho = (0.25 + DR)/2$, with a minimum value of 0.30, was chosen to provide reasonable G/G_{max} and damping relationships for the default value of G_o. This variable may require adjustment in combination with any adjustments to G_o.
e_{max} and e_{min} [emax], [emin]	The maximum and minimum void ratios affect the computation of density, and affect how volumetric strains translate into changes in relative state. Default values of 0.8 and 0.5, respectively, were adopted. Refinements in these parameters for a practical problem may not be necessary, as the calibration of other parameters will have a stronger effect on monotonic or cyclic strengths.
n^b [nb]	Default value is 0.50. Controls dilatancy and thus also the peak effective friction angles. Note that M_b for loose of critical states is computed using $n^b/4$.
n^d [nd]	Default value is 0.10. Controls the stress-ratio at which contraction transitions to dilation, which is often referred to as phase transformation. A value of 0.10 produces a phase transformation angle slightly smaller than ϕ_{cv}, which is consistent with experimental data. Note that M_d for loose of critical states is computed using $4n^d$.
A_{do} [Ado]	Default value is computed based on Bolton's dilatancy relationship at the time of initialization; typical values will be between 1.2 and 1.5.
z_{max} [zmax]	Default value is computed at the time of initialization as, $zmax = 0.70exp(-6.120\xi_{Ro}) \leq 20$ This returns 0.7 if ξ_{Ro} is initially 0.0, and increases to its maximum value of 20 with increasing dense-of-critical states. May require varying if the relationship between D_R and cyclic strength is significantly different from that implied by the liquefaction correlations of Idriss and Boulanger (2008).
c_z [cz]	Default value is 250. Controls strain levels at which fabric affects become important.
c_ϵ [ce]	Default value varies with D_R. The value is 5.0 for D_R less than 35%, and linearly decreases to its minimum value of 1.0 at $D_R = 75\%$. Can be used to adjust the rate of strain accumulation in undrained cyclic loading.
ϕ_{cv} [phicv]	Default value is 33 degrees.
ν_o []	Default value is 0.30. For 1-D consolidation of an elastic material, the value of K_o would correspond to, $K_o = \nu/1/nu$ The default value for ν results in a K_o value of 0.43 in 1-D consolidation.
C_{GD} [Cgd]	Default value is 2.0. The small-strain elastic modulus degrades with increasing cumulative plastic deviator strains (z_{cum}). The maximum degradation approaches a factor of $1/C_{GD}$.
$C_{k\alpha f}$ [ckaf]	Default value varies with DR. as, $C_{k\alpha f} = 5 + 220(\mathrm{D}_{Ro}\text{-}0.26)^3 \in [4.0; 35.0]$ The value is 4.0 for D_R less than 10%, and increases to its maximum value of 35.0 at $D_R = 77\%$. This variable controls the effect that sustained static shear stresses have on plastic modulus.

Parameter [OpenSees Name]	Explanation
Q [Q]	Default value is 10. Default value is for quartzitic sands per recommendations of Bolton (1986).
R [R]	Default value is 1.5. Default value for quartzitic sands would be 1.0 per recommendations of Bolton (1986); a slight increase in R is used to lower the critical state line to better approximate typical results for direct simple shear loading.
m [m_m]	Default value is 0.01. Default value provides reasonable modeling and numerical stability.
$F_{sed,min}$ [Fsed_min]	Default value is. computed at the time of initialization as a function of relative density: $F_{sed,min} = 0.03exp(2.6\text{D\_\{R\}}) \leq 0.99$ Controls the minimum value the reduction factor of the elastic moduli can attain during reconsolidation (used when Post_Shake=1.0).
$p'_{sed,o}$ [p_sedo]	Default value is $-P_{atm}/5$. It is the mean effective stress up to which re-consolidation strains are enhanced when Post_Shake=1.0

Table 4.3. Secondary input parameters according to (Boulanger and Ziotopuolou, 2017)

4.4.2 Pressure Depend MultiYield01 constitutive model

The constitutive material model *PressureDependMultiYield01* is an elasto-plastic material which accounts for the characteristics of pressure sensitive soils in general loading situations. For this model emphasis is placed on controlling the magnitude of cycle-by-cycle permanent shear strain accumulation in clean medium to dense sands (Parra-Colmenares, 1996), (Yang, 2000). Furthermore, appropriate loading–unloading flow rules were devised to reproduce the strong dilation tendency, which results in increased cyclic shear stiffness and strength.

The model basis is original multi-surface plasticity framework established by (Prevost, 1985) , that includes a non-associative flow rule and strain space mechanism so to reasonably simulate cyclic mobility response (Elgamal et al., 2003),(Yang et al., 2000). Besides that, this constitutive material is widely used to simulate the numerical models in terms of elasto-plastic soil behaviors regarding both the deviatoric stress-strain response and the volumetric stress-strain response. Such features lead to the capturing of dilatancy induced by shear wave and non-flow liquefaction (cyclic mobility).

Moreover, this constitutive model works with kinematic hardening based on multiple criteria, which is interpreted by a range of open conical-shaped yield surfaces. On the other hand, such characteristic brings out the disadvantage in capturing volumetric plasticity under the specific stress ratio, which results in the difficulty of total dilation intensity and geotechnical deformation records during the liquefaction phenomenon.

This model adjustment is hereby implemented in parallel with *PM4Sand* constitutive model for the comparison and evaluation of each model performances regarding the output results with respect to experimental results.

Yield function

The yield surface of the model is multi-surface cone in the stress space with the common apex in $-p_0'$ point located along the hydrostatic axis. The outermost surface defines the yielding criterion while a number of similar different size surfaces within the bounds having the common apex form hardening zone (Mróz, 1967),(Iwan, 1967), (Prevost, 1985). It is assumed that material elasticity is linear and isotropic and that nonlinearity and anisotropy accounts for plasticity (Hill, 1950).

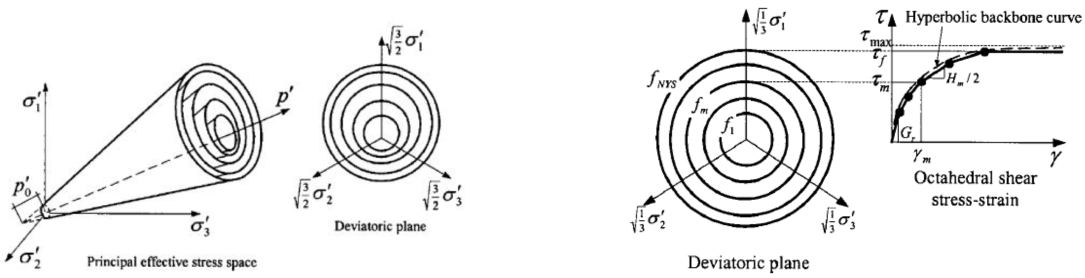

Figure 4.12. Conical multiyield surface in principal stresses space and deviatoric plane (Prevost, 1985),(Parra-Colmenares, 1996), (Yang, 2000).

Hardening rule

Hardening follows purely deviatoric kinematic hardening (Prevost, 1985), so the generation of the hysteretic response under cyclic shear loading occurs. This rule dictates that all yield surfaces may translate within the stress space bounded by failure envelope (Hill, 1950), shown in the Figure 4.13. Kinematic hardening is hereby effective for modelling unloading and strain reversals, early on especially for predicting plasticity behaviours under cyclic loading.

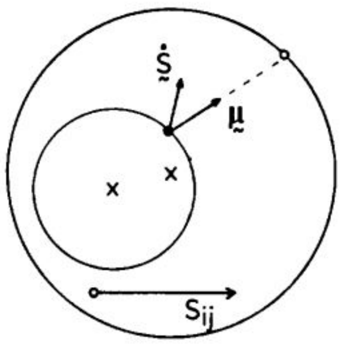

Figure 4.13. Yield surface translation by the stress point in deviatoric stress space according to (Prevost, 1985).

Flow rule

The flow rule that govern the contractive/dilative soil behaviour due to shear loading is non-associative flow rule (Parra-Colmenares, 1996) in order to achieve satisfactory interaction between deviatoric and volumetric response. Plastic strain increments are defined using the outer normal tensors to the yield surface $\tilde{\mathbf{Q}}$ and plastic potential surface $\tilde{\mathbf{P}}$. These normal tensors are deconstructed in two major components of volumetric and deviatoric nature giving $\tilde{\mathbf{Q}} = \tilde{\mathbf{Q}}' + \mathrm{Q}''\tilde{\mathbf{I}}$ and $\tilde{\mathbf{P}} = \tilde{\mathbf{P}}' + \mathrm{P}''\tilde{\mathbf{I}}$ where $\tilde{\mathbf{Q}}'$ and $\tilde{\mathbf{P}}'$ stands for deviatoric components while $\mathrm{Q}''\tilde{\mathbf{I}}$ and $\mathrm{P}''\tilde{\mathbf{I}}$ for volumetric. Plastic strain increments follows the associate flow rule in case of deviatoric components $\tilde{\mathbf{Q}}' = \tilde{\mathbf{P}}'$ while in the case of volumetric component follows the nonassociative flow rule $\mathrm{Q}'' \neq \mathrm{P}''$, (Khosravifar et al., 2018). P'' is defined depending on the location of the stress state with respect to the *Phase transformation surface* PT, thus following that several scenarios are possible:

1. The stress state lies inside the PT surface, phase 0-1 in Figure 4.14, resulting in contractive behavior.
2. The stress state lies outside the PT surface, phase 2-3 in Figure 4.14 resulting in dilative behavior.
3. The stress state is initially outside the PT surface provoking dilative behaviour and aftewards is turned inside, phase 3-4 in Figure 4.14, resulting in contractive behaviour during unloading.

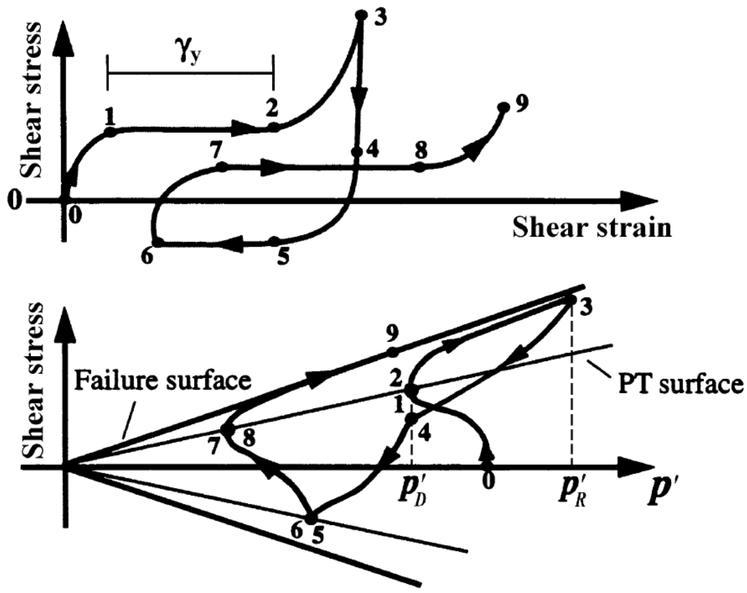

Figure 4.14. Scheme of model response in terms of octahedral stress τ,effective confinement $p\prime$, and octahedral strain γ relationship, (Parra-Colmenares, 1996).

For lower values of effective confining pressure when stress state reaches the PT surface due to shear loading, significant accumulation of the shear strains occurs even though further increment of shear stress does not develop, phase 1-2 Figure 4.14. This happens when the stress state approaches perfectly-plastic zone, before the dilation initiation outside the PT surface phase 2-3, Figure 4.14. Model can control the level of accumulation of shear strains and perfectly-plastic zone by adjusting the parameter of octahedral shear strain γ_y shown on the Figure 4.14. This way calibration of deformations induced by cyclic mobility in stress-strain space is more controllable.

Model parameters

The model parameters that governs the model functioning are presented in the Table 4.4.

Parameter	Description
ρ	Saturated soil mass density
$p_r^{'}$	Reference mean effective pressure at which small-strain shear modulus G_r and bulk modulus K_r are specified
G_r	Small-strain shear modulus at the reference mean effective pressure $p_r^{'}$ at 101 [kPa] (1 atm)
$\gamma_{max,r}$	The octahedral shear strain at failure at reference mean effective stress $p_r^{'}$ at 101 [kPa]
K_r	Bulk modulus at reference mean effective pressure derived from the small strain-shear modulus
d	The pressure dependency coefficient defines the dependency of the small-strain shear modulus and the shape of the modulus reduction curves to the effective confining stress
ϕ	Friction angle defines the size of the outermost yield surface
ϕ_{pt}	Phase transformation angle defines the angle at which soil from contractive turn to dilative behaviour
c_1	The contraction rate parameter controls the contraction rate and the porewater generation rate
d_1	The non-negative parameter accounts for the controlling the dilation rate
d_2	The non-negative parameter accounts for the controlling the dilation rate
l_1	Parameter controlling the mechanism of liquefaction-induced perfectly plastic shear strain accumulation, cyclic mobility. Defines the effective confining pressure below which the mechanism is in effect.
l_2	Parameter controlling the mechanism of liquefaction-induced perfectly plastic shear strain accumulation, cyclic mobility. Defines the maximum amount of perfectly plastic shear strain developed at zero effective confinement during each loading phase.
l_3	Parameter controlling the mechanism of liquefaction-induced perfectly plastic shear strain accumulation, cyclic mobility. Defines the maximum amount of biased perfectly plastic shear strain γ_b accumulated at each loading phase under biased shear loading conditions
k_h	The parameter accounts for horizontal hydraulic conductivity, coefficient of permeability
k_v	The parameter accounts for vertical hydraulic conductivity, coefficient of permeability
NYS	Number of yield surfaces
e	Parameters defining a straight critical-state line in e-$p^{'}$ space.
c_{s1},c_{s2}, c_{s3}	Initial void ratio

Table 4.4. PressureDependMultiYield constitutive model parameters (Yang et al., 2000)

4.5 Boundary conditions and input loads

Boundary conditions play a fundamental role in the correct definition of the numerical model, specially when the analysis of dynamic loads is involved. The performance of real structures undergone seismic forces is subjected to a condition of infinite boundaries in which the dynamic waves generated dissipate from the epicenter toward the free field. Nevertheless, this condition can not be strictly simulated numerically. As an alternative, boundaries able to dissipate the spurious reflections generated within the computational soil domain are needed.

Soil modeling based on fixed boundary conditions does not provide accurate outputs since it does not take into account this fact (Zhang et al., 2018). However, fixed boundaries are needed in order to ensure the confinement of the soil domain during analysis. Therefore, two different sets of boundaries are used during the calculation process, depending on either the gravity loads are applied or the dynamic forces. The procedure follows the steps presented below:

- *First step.* The bottom boundaries of the model domain are restricted for translations along x and y directions, allowing the generation of pore water pressure. Regarding the lateral boundaries, only the displacements along x direction are restrained. By last, the generation of pore water pressure at the nodes located at the surface is restricted. See Figure 4.15.

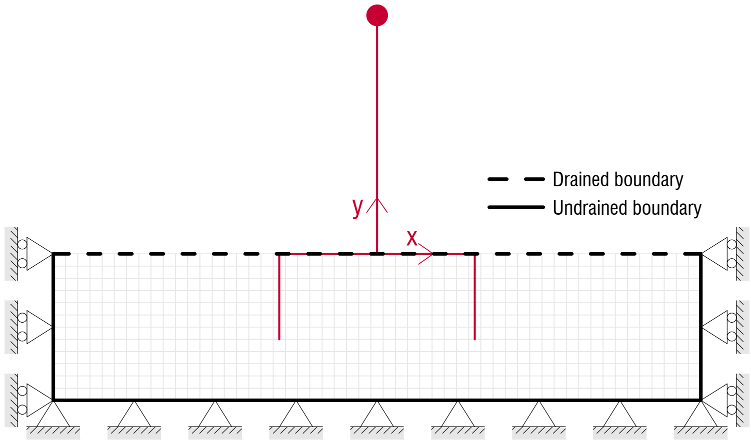

Figure 4.15. Diagram of boundaries used for gravity analysis stage

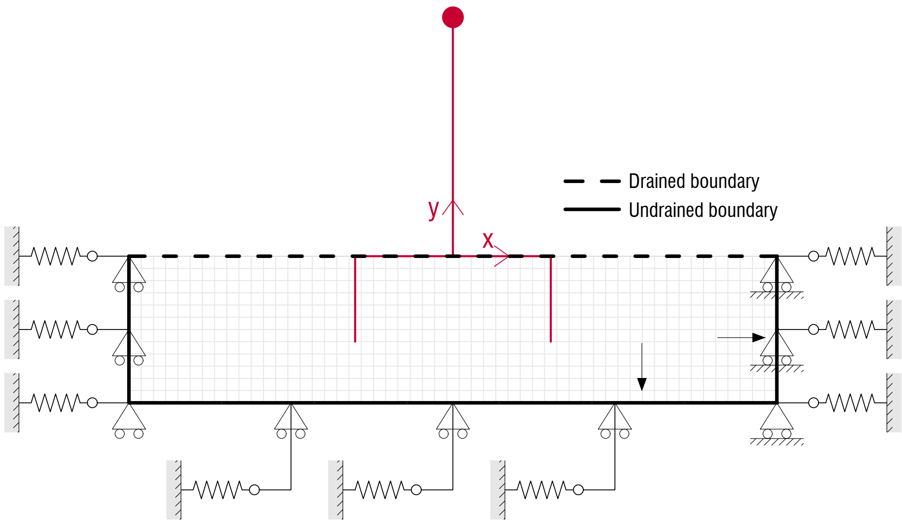

Figure 4.16. Diagram of boundaries used for dynamic analysis stage

- *Second step.* The gravity analysis is performed by the use of the mentioned set of boundaries. Then, the horizontal nodal reaction forces generated along the lateral and the bottom boundaries are recorded from the model. This step is carried as a transient analysis with a large time step following the recommendations of (Theocharis, 2020).

- *Third step.* Prior to carry the dynamic analysis, the horizontal restraints are removed and substituted by horizontal dashpots at every single node of both the lateral and the bottom boundary (Lysmer and Kuhlemeyer, 1969), see Figure 4.16. These dashpots are defined using viscous elements invoking the command *element ZeroLength* available in *OpenSees* following the configuration observed at Figure 4.17.

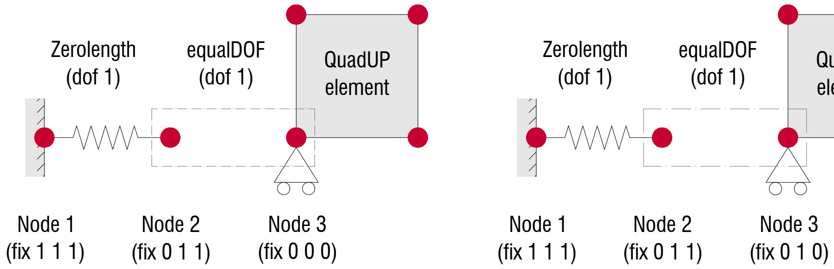

Figure 4.17. (a) Dashpot configuration of lateral boundaries (b) Dashpot configuration of bottom boundaries

Thus, the energy of the dynamic waves generated within the computational domain spreading through the boundaries is absorbed. The damping coefficient c set to these viscous elements is calculated assuming an elastic rock medium out of the computational domain. Its value at each node can be obtained following the Equation 4.4 or 4.5 (Zhang et al., 2018), depending on either the node is located at the lateral boundary or the bottom.

$$c_s = A\, \rho\, \nu_s \tag{4.4}$$

$$c_p = A\, \rho\, \nu_p \tag{4.5}$$

where,

A	Tributary area of each node
ρ	Density of the rock medium
v_s	Shear wave velocity of the rock medium
v_p	Compressive wave velocity of the rock medium

Since the targeted values come from the performance of a centrifuge test, see Chapter 3, the values of shear wave velocity, compressive wave velocity and density of the considered elastic rock medium are unknown. Nonetheless, values within the common ranges of these parameters are taken and calibrated based on the output obtained from the numerical simulation. The values considered for this numerical model are collected in the Table 4.5.

Description	Symbol	Value	Units
Rock density	ρ	3	$tons/m^3$
Shear wave velocity	v_s	1000	m/s
Compressive wave velocity	v_p	1000	m/s

Table 4.5. Characteristics of elastic rock medium considered for the numerical simulation

- *Fourth step.* Once the boundary conditions are switched to viscous before the implementation of the dynamic loads, the horizontal reactions of all the nodes located at the boundaries and recorded during the *Secondstep* are included in the model with the aim of keeping the confinement induced by the fixed boundaries.

- *Fifth step.* An artificial earthquake is induced to the computational model follows the time history of accelerations showed at Figure 3.2. This input motion is applied to the model by the use of equivalent forces acting along both lateral and bottom boundaries (Joyner, 1975) (Ayala and Aranda, 1977). In contrast to other approaches, the equivalent forces in this case are not applied only to the bottom of the model simulating the performance of a real earthquake. This fact is explained taking into account that the input motion received does not correspond to a time history recorded at the surface of the free field that can be deconvoluted and applied to a chosen depth. The time history received is applied to the rigid box used for the performance of the centrifuge test described in the Chapter 3.

  Thus, mentioned equivalent forces are calculated applying the Equation 4.6 in the case of the bottom boundaries F_{e_s} or the Equation 4.7 in the case of lateral boundaries F_{e_c}. The obtaining procedure of these expressions is explained in detail in Appendix C.

$$F_{e_s} = V_t \, v_s \, \rho \, A \tag{4.6}$$

$$F_{e_p} = V_t \, v_p \, \rho \, A \tag{4.7}$$

where,

V_t	Velocity time history
A	Tributary area of each node
ρ	Density of the rock medium
v_s	Shear wave velocity of the rock medium
v_p	Compressive wave velocity of the rock medium

As observed in the expressions above, the input motion provided needs to be transformed from acceleration time history to the equivalent velocity time history. This tasks is carried by the use of the software *SeismoSignal*. The output received is shown in Figure 4.18. The values of the rest of the parameters needed are showed in the Table 4.5.

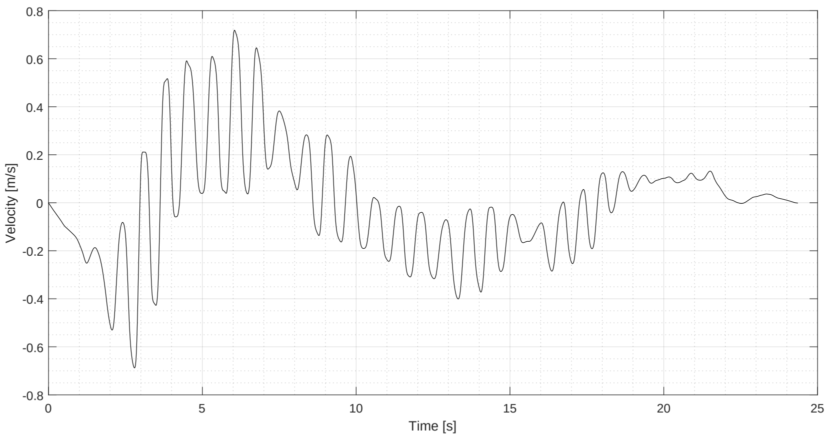

Figure 4.18. Equivalent velocity time history

4.6 Rayleigh damping

In order to control the damping of the numerical simulations, Rayleigh damping is used and implemented in the *OpenSees* code. Rayleigh damping counts with a viscous behaviour and it is built proportionally to the damping provoked by the mass of the element and its stiffness according to Equation 4.8 (K.Chopra and McKenna, 2015). Figure 4.19 shows a scheme of how Rayleigh Damping is obtained.

$$\zeta_n = \frac{a_o}{2}\frac{1}{\omega_n} + \frac{a_1}{2}\omega_n \tag{4.8}$$

where a_o and a_1 can be obtained from ith and jth modes respectively following the Equation 4.9(K.Chopra and McKenna, 2015):

$$\frac{1}{2}\begin{bmatrix} 1/\omega_i & \omega_i \\ 1/\omega_j & \omega_j \end{bmatrix}\begin{Bmatrix} a_o \\ a_1 \end{Bmatrix} = \begin{Bmatrix} \zeta_i \\ \zeta_j \end{Bmatrix} \tag{4.9}$$

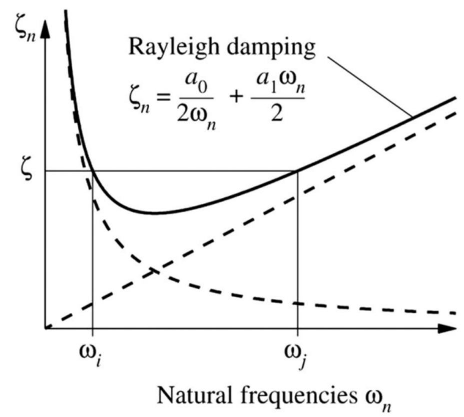

Figure 4.19. Construction of Rayleigh damping, (K.Chopra and McKenna, 2015).

Theoretically, in order to choose the proper value of viscous damping, the natural frequencies of the earthquake input motion corresponding to the different considered modes needs to be accounted. Moreover, to achieve the approximately precise value of such frequencies, the mass participation is also necessary to be investigated thoroughly in every single mode analysis. However, due to the limited time, such tasks are not carried in the current report.

Therefore, the chosen option for obtaining an appropriate value of viscous damping considered for the numerical model follows the findings of (Hashash and Park, 2002). There, a constant strain viscous damping applied for non-linear model is recommended within the range of 1.5 - 4 % for almost all of soils. Although implementing the numerical model with viscous damping factor among the up-mentioned bound values, high fluctuations of r_u at the vicinity of the structure was still received during all the shaking period.

Thus, the value of viscous damping (ζ) is set to 5 % with the main intention of reducing the mentioned noise of the output plots and getting more fitted results respect to the experimental results. Regarding the coefficients a_1 and a_0, needed for assigning the value of Rayleigh damping in the *OpenSees* code, these factors are also depended on the natural frequencies corresponding to the different modes analysis, according to the Equation 4.8.To simplify this calculation process, the value of the first two natural frequencies ω_i and ω_j corresponding to the first two modes are taken from the example *Dynamic 2D Effective Stress Analysis of Slope* found at the virtual *OpenSees* library (McKenna et al., 2000). Thus, these are calculated based on the Equations 4.10 and 4.11 and the coefficients a_1 and a_0, by applying the Equations 4.12 and 4.13.

$$\omega_i = 2\,\pi\,0.2 \tag{4.10}$$

$$\omega_j = 2\,\pi\,20 \tag{4.11}$$

$$a_0 = \frac{2\,\zeta\omega_i\,\omega_j}{\omega_i + \omega_j} \tag{4.12}$$

$$a_1 = \frac{2\,\zeta}{\omega_i + \omega_j} \tag{4.13}$$

ω_i	Natural frequency corresponding to the i^{th} mode
ω_j	Natural frequency corresponding to the j^{th} mode
a_0	The mass-proportional damping coefficient which is constant and has unit of sec^{-1}
a_1	The stiffness-proportional damping coefficient which is constant and has unit of sec

The calculated values of such coefficients corresponding to the desired Rayleigh damping ratio are collected in the Table 4.6:

Definition	Symbol	Value
Damping ratio	ζ	0.05
Coefficient $a1$	a_1	0.000787895
Coefficient $a0$	a_0	0.124419511

Table 4.6. Values of Rayleigh damping ratio and a_n coefficients used.

Model calibration 5

The calibration and validation of the numerical model constructed in the previous section, Chapter 4, is carried in the following pages through the comparison of the outputs received from the software *OpenSees* and the ones received from the centrifuge test shown at Chapter 3 (Yu et al., 2014). The outputs available from the experiment correspond to the nodal accelerations within the soil domain and at the tip of the structure and, the pore water pressure ratio r_u-time history and the settlements time-history. Equation 2.1 is used in order to transform the pore water pressure recorded at the numerical model to r_u.

Mentioned calibration process is carried according to the two different constitutive models previously presented, *PM4Sand* and *PDMY01*. The influence of the inputs parameters of both models is also analyzed as well as the deviation of the results obtained between them.

5.1 Calibration based on *PDMY01*

The current section explains the process followed for calibrating the model according to *PDMY01* material. The different subsections that compose this section are arranged according to the same order than the actual process followed. An analysis of the parameters with largest influence in every section is carried in order to compare the influence of them on the results. The influence of other parameters is collected at Appendix E.

5.1.1 Generation of pore water pressure at the free field

The first calibration step correspond to the fitting of the curves of r_u generated by the numerical model with the ones received from the centrifuge test at the free field, locations P2 and P4 at Figure 3.1 and curves observed at Figure 3.2b and 3.2d.

Regarding the up-mentioned purpose, four different parameters are observed to count with a larger influence on the fitting process of r_u curves at the free field, shear modulus G_r, bulk modulus K_r, friction angle ϕ and phase transformation angle ϕ_{ph}. In this subsection, the affects of such four parameter respect to the earthquake motion induced are characterized and assessed graphically.

Reference bulk modulus K_r

Reference bulk modulus is the numerical parameter controlling the volumetric stiffness of the soil. Thus, the volumetric strains of the material can be reduced with higher values of bulk modulus. Theoretically, the generation of pore water pressure is inversely proportional to the value of bulk modulus so that the soil shows a larger contractive behaviour with small values of bulk modulus. The excess pore water pressure ratio outputs in the free field according to P2 and P4 sensors are hereby shown in the two Figures 5.1 and 5.2.

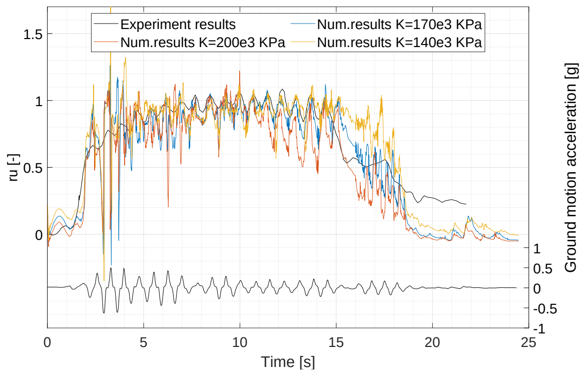

Figure 5.1. Pore water pressure ratio of sensor P2 at the location of x=6m and y=-0.5m.

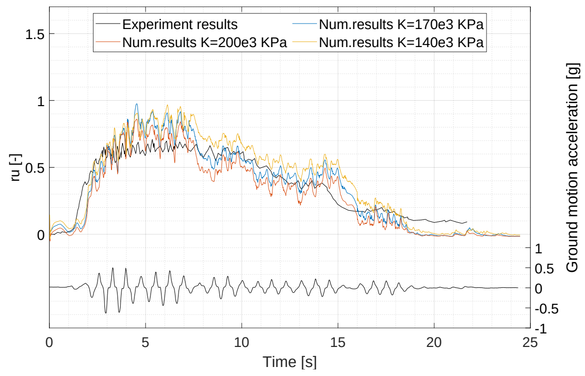

Figure 5.2. Pore water pressure ratio of sensor P4 at the location of x=6m and y=-2.5m.

Taking a look at 2 Figures above, it is noticeable that the excess pore water pressure ratio is increased by decreasing the value of bulk modulus from $170e3\ kPa$ to $140e3\ kPa$. The reversed way is witnessed by increasing the bulk modulus to $200e3\ kPa$. Hence, it can be concluded that the behavior of the soil for different values of K_r follows the theoretical statement mentioned before. Overall, the modification of bulk modulus value brings out significant influence on the task of catching fitted the numerical outputs versus experimental results regarding the generation of excess pore water pressure.

Reference shear modulus G_r

Reference shear modulus is the parameter representing the elastic shear stiffness of the soil. Thus, it plays a central role describing the soil's shear strain response to the deviatoric stresses.

This parameter brings out an affect on the soil behaviour significantly when the frictional sliding phenomenon inside the soil domain occurs due to the presence of the structure. Hence, the adjustment of the reference shear modulus needs to be taken into consideration. Such task is shown graphically in the two Figures 5.3 and 5.4.

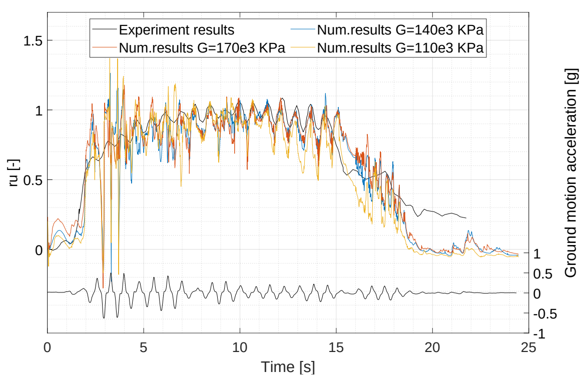

Figure 5.3. Pore water pressure ratio of sensor P2 at the location of x=6m and y=-0.5m.

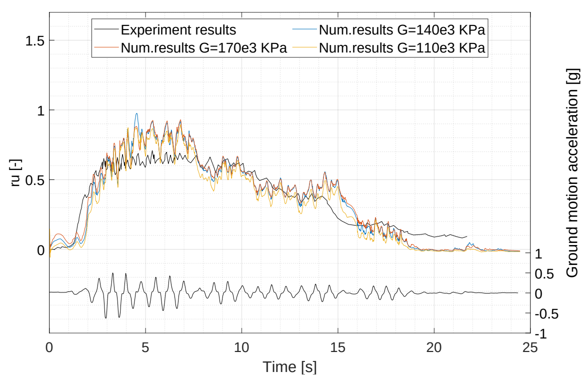

Figure 5.4. Pore water pressure ratio of sensor P4 at the location of x=6m and y=-2.5m.

Taking a look at the 2 Figures above, apparently, the increasing of pore water pressure ratio is proportional to the magnitude of shear modulus. However, the fact is that the adjustment of shear modulus brings out a slightly changing of r_u time histories. Overall, it can be concluded that the process of modification of the value of G_r does not provide great changes in terms of catching well-fitted numerical excess pore water pressure results in the free field.

This might be explained regarding the location of the structure. The presence of shearing forces is more critical at the vicinity of the foundation so that most of the deformations registered at the free field are volumetric strains and no shear strains.

Friction angle ϕ

If $PDMY01$ model is regarded, friction angle is the parameter defining the position of the outermost yield surface of the material. In addition, friction angle is depended on the friction coefficient governing the taken-place sliding phenomenon among the working surfaces inside the soil domain. With such characteristics, theoretically, the changing of this parameter is predicted to bring out the significant affect on the pore water pressure that is clarified by taking a look at the two Figures 5.5 and 5.6.

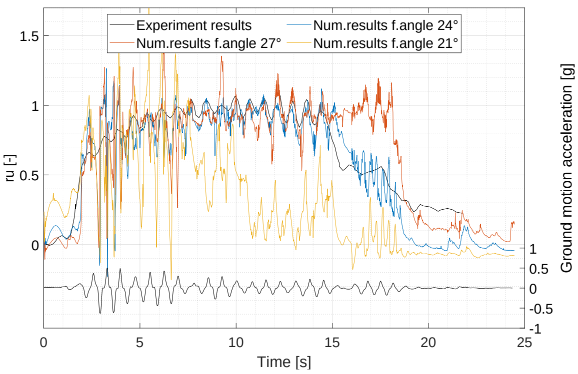

Figure 5.5. Pore water pressure ratio of sensor P2 at the location of x=6m and y=-0.5m.

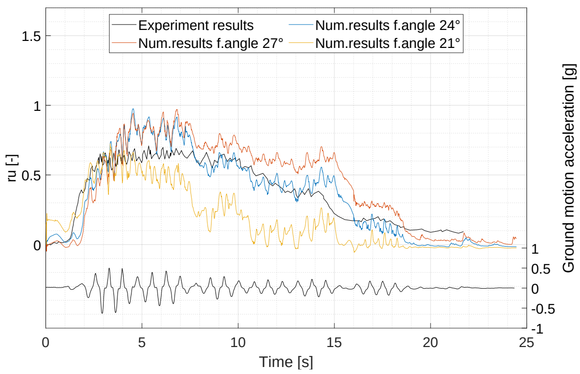

Figure 5.6. Pore water pressure ratio of sensor P4 at the location of x=6m and y=-2.5m.

Overall, it is noticeable that the excess pore water pressure generation experiences an earlier dissipation by decreasing the friction angle, while the reversed trend is measured when it is increased. Besides, the procedure of reducing friction angle also restrains the liquefaction phenomenon occurring.

This trend might seem not to be realistic since a higher value of friction angle is a characteristic of denser soils in which the possibility of liquefaction is smaller. Nevertheless, if the soil is softer, larger deamplification of the acceleration are experienced. Thus, it seems that the increment of the friction angle also enlarge the level of shear stresses induced to the soil since it becomes stiffer.

Phase transformation angle ϕ_{ph}

Phase transformation angle is the parameter which controls the change of phase of the soil, from contractive to dilative responses when it is being sheared. Theoretically, the contractive phase is smaller with the smaller values of the phase angle, which results in that the soil is more dilative during shear loading. The excess pore water pressure is hereby decreased according to such theory. In order to get the precise clarifying assessment, the excess pore water pressure ratio with respect to time interval are plotted as the two Figures 5.7 and 5.8.

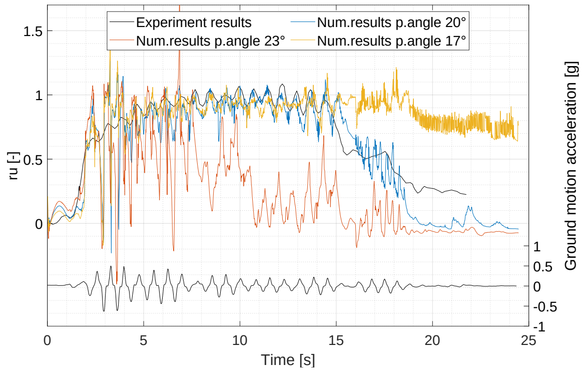

Figure 5.7. Pore water pressure ratio of sensor P2 at the location of x=6m and y=-0.5m.

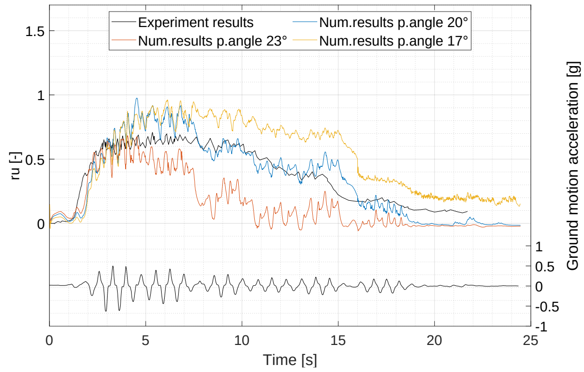

Figure 5.8. Pore water pressure ratio of sensor P4 at the location of x=6m and y=-2.5m.

Taking a look at the two Figures above, it is evident that the trend of numerical curves is opposite to the theoretical comment above. The fact is that the excess pore water pressure ratio increases by reducing the phase angle. On the other hand, regarding the increment of phase angle, the excess pore water pressure shown to plummet, specially after the first five seconds of the given period.

Nevertheless, a smaller value of phase angle is a characteristic of less dense soil, whose tendency to liquefy is higher. This fact could explain the behaviour observed in the previous curves.

However, the adjustment of phase angle needs to be associated with the calibration of the friction angle. In the case presented, the value of the friction angle is set equal to 24^o but, if it is set larger and some trials of phase angle are carried, the behaviour observed is different to the one observed.

5.1.2 Settlements of the structure

Once the generation of excess pore water pressure is caught at the free field, theoretically, the settlements of the structure are also almost calibrated. The settlements received from the centrifuge test are measured at the base of the tower, see Figure 3.1, and its changing along the time is presented at Figure 3.5.

The calibration of settlement is carried by adjusting mainly 4 different parameters: reference bulk modulus, phase transformation angle, contraction rate and permeability coefficient. However, the pattern trend of the settlement always remains unchanged under the affect of shaking motion. Thus, the soil surface starts to be settled down rapidly in the first 10 seconds of the dynamic event, when the shaking is stronger. After that, a slight increment is observed until the end of the shaking motion time series.

Reference bulk modulus K_r

As regards settlements, bulk modulus plays an indispensable role in controlling the output values of these vertical displacements. The fact is that the bearing capacity of the soil under the compression loading is theoretically depended on the bulk modulus a parameter that, as mentioned previously, controls the volumetric stiffness of the material. In order to clarify such statement, the results of settlement corresponding to different values of K_r are depicted at Figure 5.9.

Taking a look at that Figure, it is obvious that the bulk modulus magnitude is inversely proportional to the settlements. The fact is that when bulk modulus was decreased from $170e3kPa$ to $140ekPa$, a significant increment is measured in the curve and vice versa.

When K_r is increased, the soil is volumetrically stiffer and, as observed in the previous section, the values of excess pore water pressure decrease. These facts makes the settlements smaller.

Phase transformation angle ϕ_{ph}

Phase transformation angle explained briefly in the section 5.1.1 is also a parameter with high influence in settlement controlling standpoint. Theoretically, the contractive phase in terms of soil response behaviours is governed by the calibration of phase transformation angle. In order to take an overview of such influence, 3 different values of phase angle were applied and plotted in the figure 5.10.

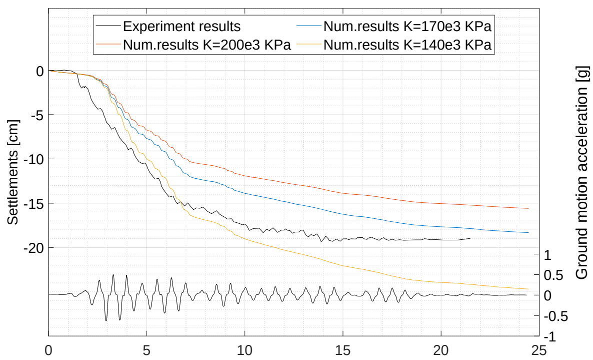

Figure 5.9. Settlement with the regulation of bulk modulus.

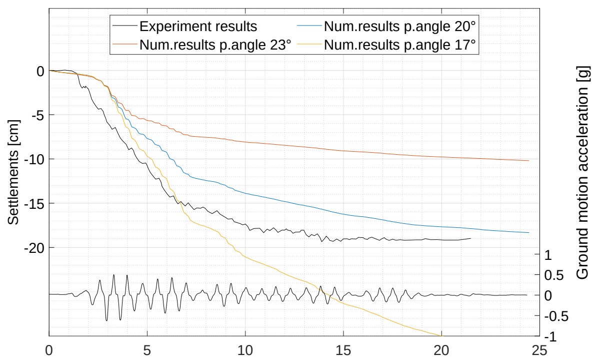

Figure 5.10. Settlement with the regulation of phase transformation angle.

A sharp difference occurs after a slight modification of phase transformation angle, particularly, the small adjustment from 20 to 17 leads to the significant increment in settlement as shown in the Figure 5.10. As demonstrated in the previous section, a decrement on the value of phase transformation angle makes the r_u to be closer to liquefaction. This fact provides higher values of settlements due to a temporary loosing of the bearing capacity of the soil.

However, it must be mentioned again that the calibration process of this parameter is sensitively associated with the value of friction angle. For the plotted curves, the value of the friction angle is equal to 24^o but should be expected that for higher values of this parameter, the difference between phase angle and friction angle cast different trends.

Contraction parameter c

Contraction parameter is an input value controlling the rate of shear-induced volume decrement and the excess pore water pressure generation rate subsequently. In this sub-subsection, the influence of such parameter is illustrated through the numerical output data plotting in the Figure 5.11.

Taking a look at the Figure 5.11, the lowest output data of settlement is witnessed by using the smallest value of contraction parameter. On the other hand, in the reversed side, the highest settlements is shown by the numerical curve when the biggest value of contraction parameter is used.

As mentioned, this parameter controls the trend of the soil to contract during shearing. A more contractive soil leads to a higher generation of pore water pressure which provokes higher settlements due to a larger loss of bearing capacity of the soil.

However, the influence of contraction parameter on the settlement standpoint is not as significant as other input parameters.

Permeability

Permeability a crucial coefficient in terms of governing the hydraulic conductivity of the soil during the dynamic loading process. Thus, high influence on the value of settlements is expected when this parameter is modified. In order to go deeply into this statement, 3 numerical output-data plots with different values of permeability of the domain 1 are shown in the Figure 5.12 for getting the proper assessment.

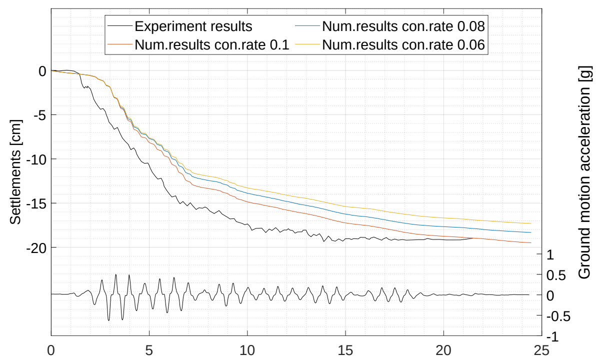

Figure 5.11. Settlement with the regulation of contraction parameter.

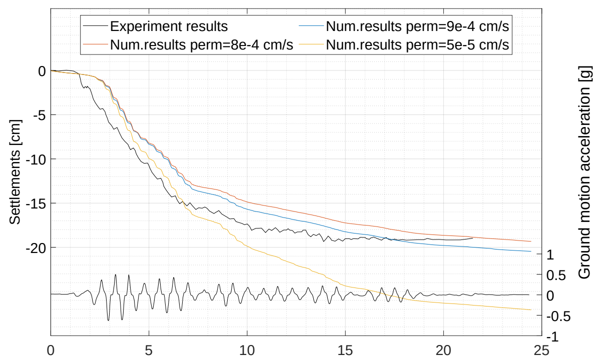

Figure 5.12. Settlement with the regulation of permeability in the domain number one.

It is noticed that the changing of permeability is negative proportional to the settlements, therefore, the smaller the permeability, the larger are the settlements measured. Once again, it is concluded that when the excess of pore water pressure is increased by the modification of any parameter, the settlements received from the numerical model are larger due to a higher loss of bearing capacity of the soil.

5.1.3 Generation of excess pore water pressure in the vicinity of the structure

Once the curves corresponding to the generation of excess pore water pressure ratio are fitted at the free field, an extra adjustment is required for fitting also those curves at the vicinity of the foundation. The sensors at those locations are $P1$ and $P3$ as observed at the Figure 3.1, and the curves generated by them are observed at Figures 3.4a and b.

All the parameters analyzed during the calibration of the curves corresponding to the generation of excess pore water pressure at the free field play an important role also on the calibration of the curves at the vicinity of the structure. Nevertheless, the effects observed on the graphs are the same than the ones observed in the previous section so they are not going to be shown again.

The main adjustment needed by the excess pore water pressure generation curves close the bucket after having calibrated the free field recorders is related with the calibration of the contraction parameter c, the hydraulic conductivity of the elements or permeabilities *perm* and the density of the soil ρ.

Contraction parameter c

The contraction parameter included at *PDMY01* material is a non-negative constant defining the rate of shear-induced volume decrease, in other words, the contraction of the soil domain (Mazzoni et al., 2007). A faster contraction rate is induced to the model if larger values of this parameter are set. Thus, higher generation of excess pore water pressure and slower dissipation is expected for when its value is higher.

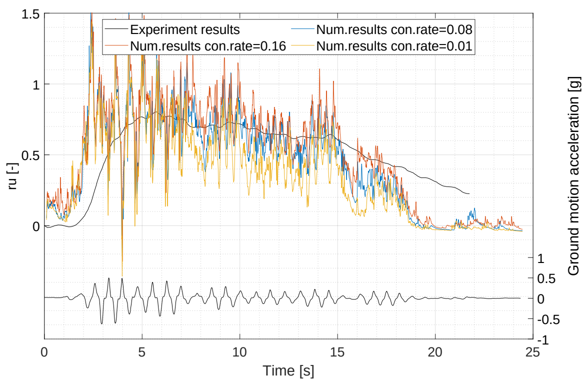

Figure 5.13. Pore water pressure ratio of sensor P1 at the location x=6m and y=-0.5m.

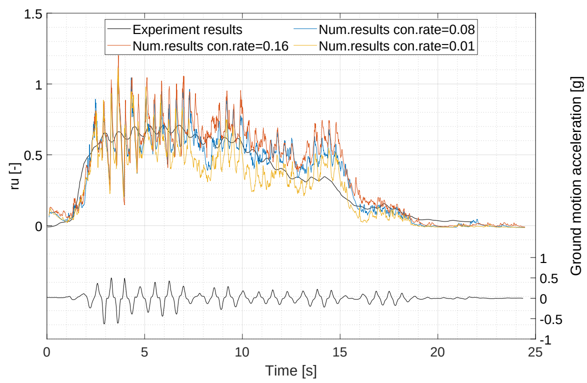

Figure 5.14. Pore water pressure ratio of sensor P3 at the location x=6m and y=-2.5m.

If the Figures 5.13 and 5.14 are checked, the behaviour observed agrees with the expectations. Hence, a higher value of r_u is observed when the value of the contraction parameter is set higher. On the other hand, if these graphs are compared with the ones received from the free field, see previous section, it is easily noticeable that the fluctuations of r_u are larger in the vicinity of the foundation. These fluctuations are observed to be increased for lower values of contraction parameter so it is important to set a relatively high value of this variable in the case of the current research respect to the input recommended for medium dense sand at (Mazzoni et al., 2007).

Density ρ

Another parameter which is observed to count with a high relevance during the calibration process of the generation of pore water around the foundation is the value of the density ρ. As mentioned at the Chapter 3, the tested sand during the centrifuge test is considered as medium-dense with a relative density of $D_r = 68\%$. The value of ρ for this kind of sand is around 2 $tons/m^3$ (Mazzoni et al., 2007), so this value is considered as a reference for carrying the calibration process.

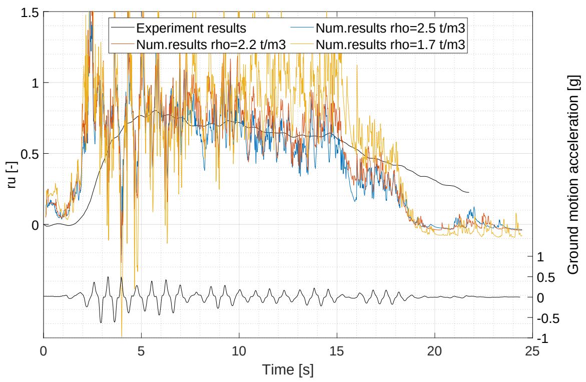

Figure 5.15. Pore water pressure ratio of sensor P1 at the location x=6m y=-0.5m.

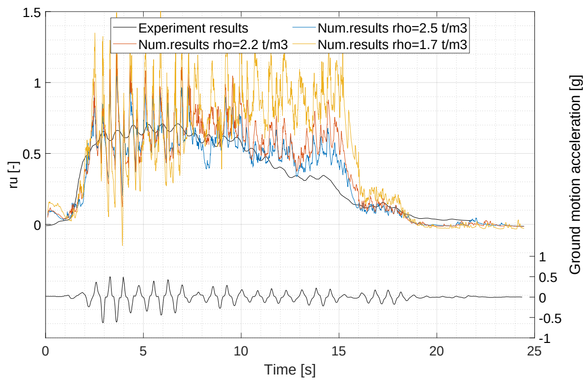

Figure 5.16. Pore water pressure ratio of sensor P3 at the location x=6m y=-2.5m.

As expected, an increased value of density reduce the value of r_u making more difficult the generation of excess pore water pressure and therefore, the triggering of liquefaction within the soil domain due to a higher value of vertical effective stresses. However, another important feature observed during the current calibration process is the reduction of the fluctuations of r_u observed when larger values of soil density are used.

As experienced during the adjustment of the input parameters of *PDMY01*, one of the more complicated task is to achieve mentioned reduction. Thus, it is found that the increasing of the density of the soil is an effective way as can be observed at Figures 5.15 and 5.16.

In this case, the higher the value of density, the more reduction is experienced regarding mentioned fluctuations. Nonetheless, the value of 2.5 $tons/m^3$ is just observed at very dense sands, not being likely to find values above that amount in real life. Therefore, values above that density are not used in the simulation of the current numerical model.

Permeability

The generation and the dissipation of excess pore water pressure is strongly related with the hydraulic conductivity of the soil. As far as the numerical model is concerned, this feature can be controlled by adjusting the horizontal and vertical permeability of the *quadUP* elements which compose the soil domain.

According to (Mazzoni et al., 2007), common values of permeability of sands are within the range of $1.0 \cdot 10^{-3}$ and $1.0 \cdot 10^{-1}$ cm/s. Nevertheless, for the particular case of this numerical model, those values are decreased since the mentioned ones do not provide good results. That reduction places the soil simulated in the range of silty sands according to the mentioned resource. In order to show the influence of permeability on the outputs, only the value of this parameter in the domain 1 is modified, see Figure 4.4.

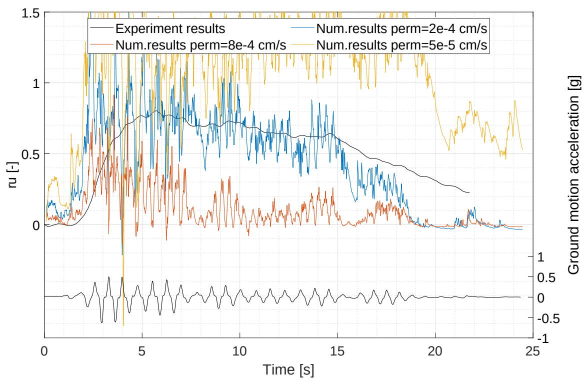

Figure 5.17. Pore water pressure ratio of sensor P1 at the location x=6m y=-0.5m.

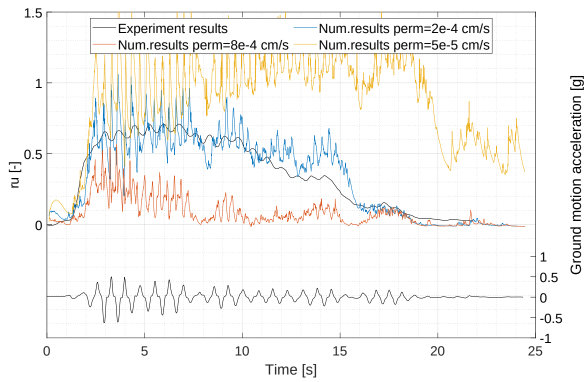

Figure 5.18. Pore water pressure ratio of sensor P3 at the location x=6m y=-2.5m.

As observed in the Figures 5.17 and 5.18, the hydraulic conductivity of the soil plays a relevant role on the obtained values of r_u. When the permeability at the domain 1 is set higher, the generation of excess pore water pressure is closer to zero along all the shaking. In other words, the variation of the pore water pressure respect to the hydrostatic pressure is less pronounced. On the other hand, when the permeabilities are set with a low value, the value of r_u in the numerical model increases even above the theoretical upper bound considered for liquefaction triggering $r_u = 1$.

Moreover, it is also noticed the influence of this parameter on the excess pore water pressure dissipation. As expected, this phenomenon occurs slower in the numerical model when the hydraulic conductivity is smaller and vice versa.

Once again, the fluctuations of the value of r_u at the recorders located close to the foundation, i.e., P1 and P3, need to be mentioned since this feature can be also controlled with the adjustment of the permeability of the soil. As observed in the graphs, these fluctuations become more pronounced when the hydraulic conductivity is set smaller. Therefore, is more convenient to set a relatively high value of permeabilities and, if it is needed to raise the curve of r_u generated by the numerical model, increase the above mentioned contraction parameter in order to carry the fitting process.

5.1.4 Acceleration recorders

Other recorders used for verifying the right behaviour of the numerical model correspond to the ones received from the accelerometers located within the soil and the tip of the structure of the prototype tested during the performance of the centrifuge test.

Accelerations at the soil domain

Regarding the accelerations registered within the soil domain, two accelerometers are set up in the prototype for this purpose, the first one located in the interior of the bucket and tagged as A1, and the second one located at the free field, tagged as A2, see Figure 3.1. By the use of recorders located at the same locations than the accelerometers of the prototype, the accelerations generated by the numerical model are also recorded.

Even though all the soil parameters influence the accelerations recorded, only the ones with more important effects observed are presented in this section. The rest of the results are collected in the Appendix E.1.4.

Phase angle ϕ_{ph}

As illustrated at Figure 4.14, a phase transformation surface can be defined at $p' - \tau$ space. This surface defines the boundary between contractive and dilative behaviour of the soil when it is already at steady state of deformation. Looser sands usually show lower values of phase angle.

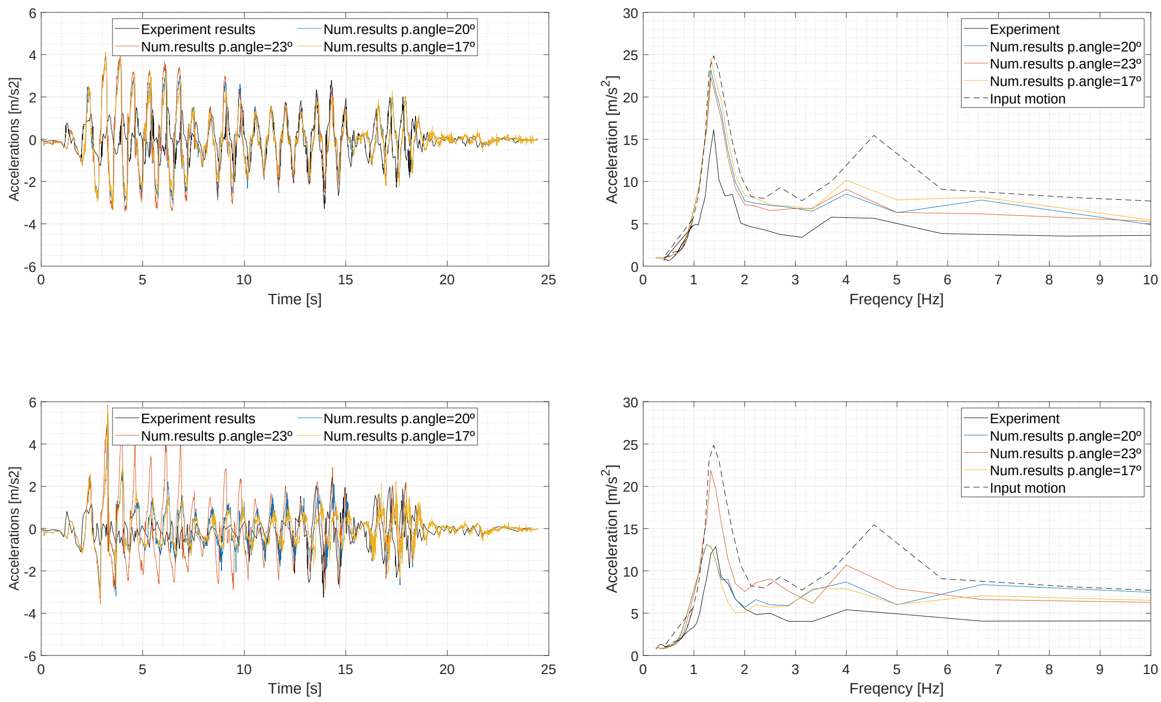

Figure 5.19. Nodal accelerations and acceleration spectra at soil domain, from left to right: (a) Nodal accelerations sensor A1 x=0m y=-0.5m. (b) Accelerations spectra, sensor A1 x=0m y=-0.5m. (c) Nodal accelerations sensor A2 x=6m y=-0.5m. (d) Accelerations spectra sensor A2 x=6m y=-0.5m.

If the acceleration spectra under the bucket, Figure 5.19b, is compared with the one generated at the free field, Figure 5.19d, it is observed that the influence of modifying the phase angle is more noticeable when there is not presence of structure since the values remain almost unchanged when measures at sensor A1 are compared. This phenomenon might be occurring due to the higher confinement of the soil within the bucket, which controls the generation of pore water pressure making the soil less dependent of this parameter.

As observed at Figures 5.19c and 5.19d, the reduction of the phase angle is able to reduce the accelerations drastically, being able to match the values registered during the experiment when it is small enough. Nonetheless, it is almost observed that this reduction is limited since the same outputs are received for phase angle equal to 20º and 17º.

Checking the Figures 5.7 and 5.8, when the value of phase angle is reduced, the generation of excess pore water pressure increases drastically. Since the water is not able to transmit shear waves, a great drop of the value of accelerations is observed at the free field when ϕ_{ph} is decreased.

Contraction parameter c

As explained in the previous section, the contraction parameter is a constant which regulates the rate of excess pore water pressure build up (Elgamal et al., 2003). Besides, it is observed that a larger value of this variable brings a higher generation of excess pore water pressure since the dilation capacity of the soil is restricted.

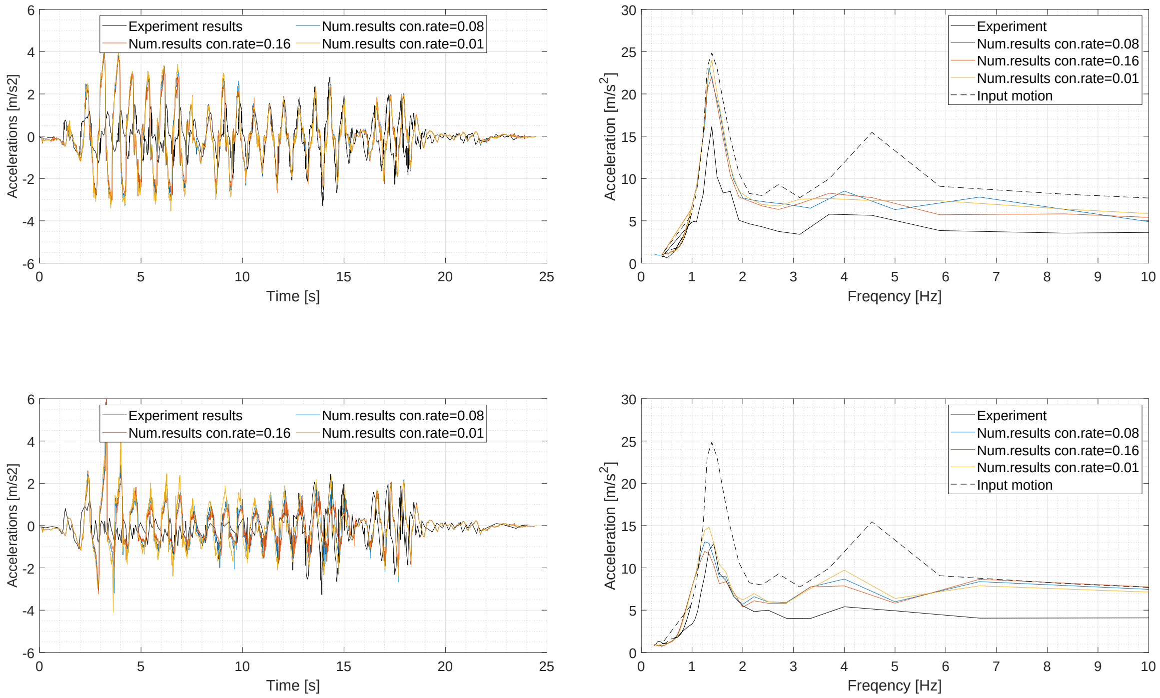

Figure 5.20. Nodal accelerations and acceleration spectra at soil domain, from left to right: (a) Nodal accelerations sensor A1 x=0m y=-0.5m. (b) Accelerations spectra sensor A1 x=0m y=-0.5m. (c) Nodal accelerations sensor A2 x=6m y=-0.5m. (d) Accelerations spectra sensor A2 x=6m y=-0.5m.

In contrast to the differences observed in the generation of excess pore water pressure when several values of the contraction parameter are tested, see Figures 5.13 and 5.14, the differences observed in terms of nodal accelerations and acceleration spectra both at the vicinity of the structure and at the free field are not quite important, see Figure 5.20.

However, the behaviour obtained follows the expectation. As observed in the Figures 5.13 and 5.14, an increment of the value of the contraction parameter supposes a higher generation of excess pore water pressure. Since the water does not have the capacity of transmitting shear waves, a higher presence of pore water pressure is directly related with a decreasing of the value of accelerations. Exactly this trend is the one observed in the Figures above. Thus, a higher value of the contraction parameter contributes to a lower value of accelerations.

Permeability

The permeability of the soil is another key parameter regulating the nodal accelerations within this domain since, as mentioned previously, it regulates the capacity and the velocity of the sand to dissipate and generate pore water pressure.

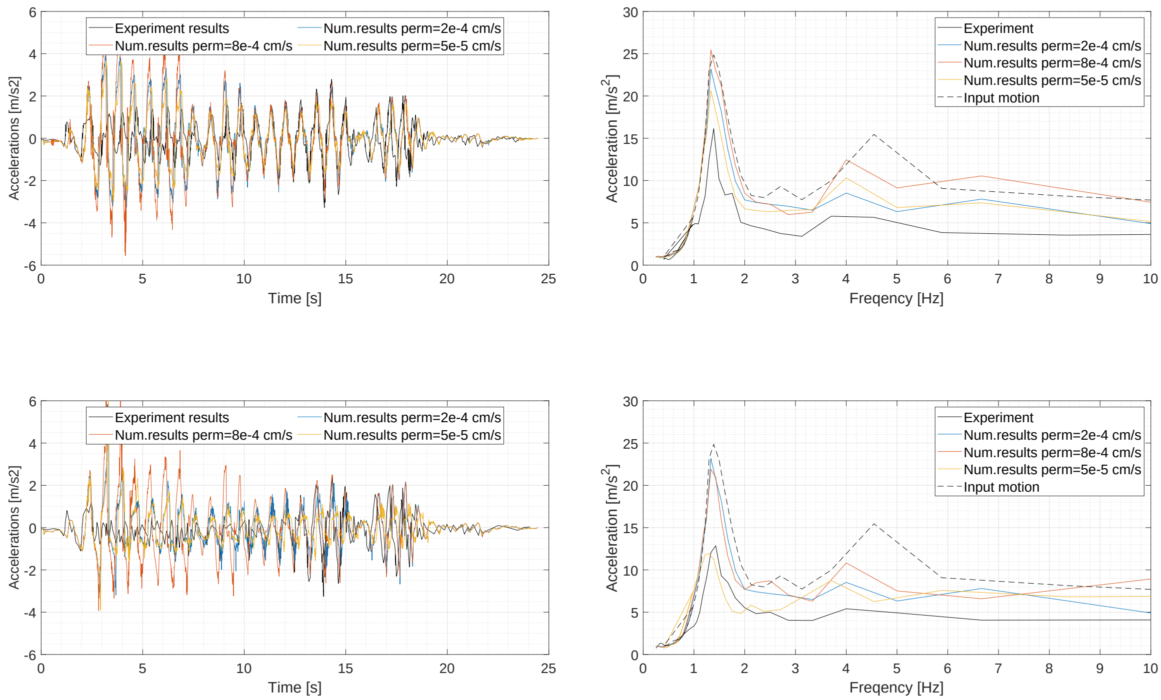

Figure 5.21. Nodal accelerations and acceleration spectra at soil domain, from left to right: (a) Nodal accelerations sensor A1 x=0m y=-0.5m. (b) Accelerations spectra sensor A1 x=0m y=-0.5m. (c) Nodal accelerations sensor A2 x=6m y=-0.5m. (d) Accelerations spectra sensor A2 x=6m y=-0.5m.

Taking an overview of the Figure 5.21, it can be observed that small changes in this parameter provoke important modifications of the acceleration trends.

Once again, the graphs behave as expected. A small value of permeability makes the generation of excess pore water pressure larger. Moreover, the velocity of dissipation becomes slower, see Figures 5.17 and 5.18. As mentioned before, a higher presence of pore water pressure leads to a decreasing of the accelerations since the water is not able to transmit shear waves. This tendency is the observed in graphs. When the value of hydraulic conductivity is increased, the generation of pore water pressure is smaller and the accelerations increase. On the other hand, when the permeability is decreased, the presence of water makes the acceleration to drop.

Another characteristic observed is that these changes become more important at the free field, Figures 5.21c, d, than at the vicinity of the structure, Figures 5.21a, b. The presence of the structure makes the values of acceleration to drop in a smaller scale when the values of permeability are decreased. Nonetheless, an important drop is observed in the recordings at the free field when lower values of permeability are set.

Accelerations at the tip of the structure

All the input parameters which define the behaviour of *PDMY01* constitutive model have their influence on the acceleration time history registered at the tip of the structure, sensor tagged as A3 in the Figure 3.1. However, the features with a more important observed influence on these recordings are the ones related with the characteristics of the structure.

Therefore, during the current section, the effects induced by the modification of the stiffness of the tower and foundation, and the effects provoked by the modification on the distribution and the magnitude of the masses are studied.

In contrast to the characteristics of the soil, any parameter defining the characteristics of the structure such as stiffness, moment of inertia of the section or material is not available at the reference centrifuge test (Yu et al., 2014). Therefore, larger deviations should be expected between the outputs from the numerical centrifuge test and the actual one.

Stiffness of the foundation

The Young's modulus value of the *elasticBeamColumn* elements used for defining the foundation of the numerically simulated wind turbine is modified in order to analyze its influence on acceleration recorders at the tip of the structure.

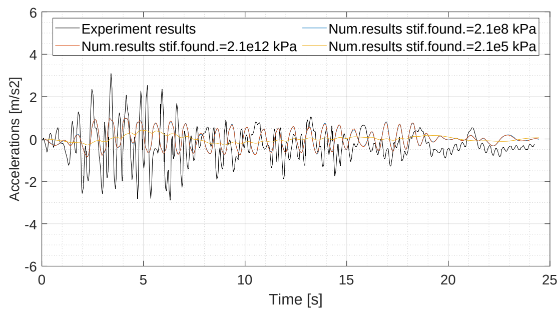

Figure 5.22. Analysis nodal accelerations sensor A3 x=0m y=13m.

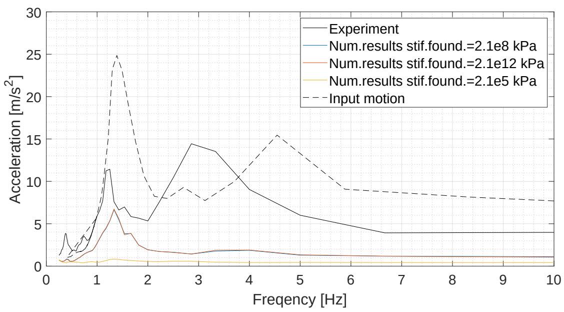

Figure 5.23. Analysis spectral accelerations sensor A3 x=0m y=13m.

As observed in the Figures 5.22 and 5.23, the influence of the stiffness of the foundation on the accelerations at the tip of the tower is negligible unless a small enough value is set. In this case, the nodal accelerations and the spectral accelerations are virtually the same for the values 2.1e8 and 2.1e15 kPa. Nonetheless, when this stiffness is set small enough, the values of acceleration are almost zero.

It seems that a low stiffness of the foundation makes this region of the structure to work as a damper. Possibly, this small value makes the foundation to plastify not allowing the elastic respond of the wind turbine to be transmitted toward the top of the tower.

Stiffness of the tower

Following the same procedure than in the case of the stiffness of the foundation, the value of the stiffness of the *elastic Beam Column* elements of the tower of the wind turbine is modified and compared in order to analyze the influence of this parameter on the accelerations at the tip of the tower.

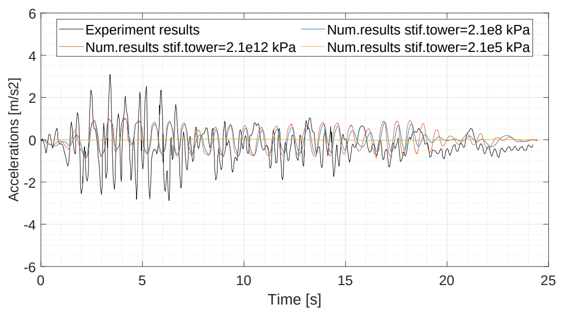

Figure 5.24. Analysis nodal accelerations sensor A3 x=0m y=13m.

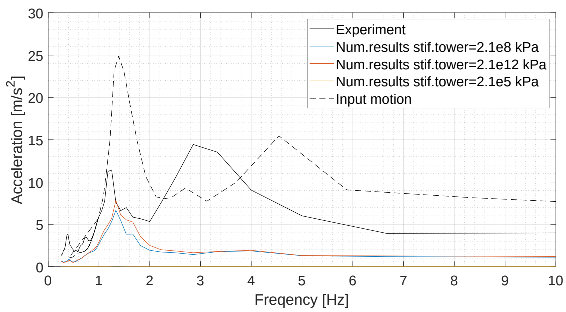

Figure 5.25. Analysis spectral accelerations sensor A3 x=0m y=13m.

The responses registered follow the expectation. Thus, when the value of the stiffness of the tower is increased, an increment of the acceleration is observed and vice versa, see Figures 5.24 and 5.25.

Nonetheless, this fact occurs within a certain range of values of the Young's modulus. As observed in the graphs above, when this parameter is set with a small enough value, the accelerations registered are zero or close to zero at the top of the tower. Due to the small value of stiffness of the body of the structure, the elements which compose it reach the plastic region before being able to transmit thus any accelerations from the foundation to the tip of the structure.

Magnitude and distribution of masses of the tower

Another important feature governing the accelerations recorded at the tip of the prototype of the wind turbine is the magnitude and the distribution of the masses of the tower. As observed at the reference centrifuge test, see Chapter 3, the masses uses for the $Test1$ are set equal to 10.6 *tons* at the tip of the tower and equal to 18.7 *tons* at the foundation. Nonetheless, this distribution and magnitude of masses is modified for constructing the numerical model with the purpose of improving the outputs received. As explained in the Chapter 4, both mentioned masses are lumped at the tip of the tower, considering the foundation as massless.

However, different distributions and magnitude of masses are tested during the current section in order to analyze the influence of them on the behaviour of the numerical model and justifying the final configuration used.

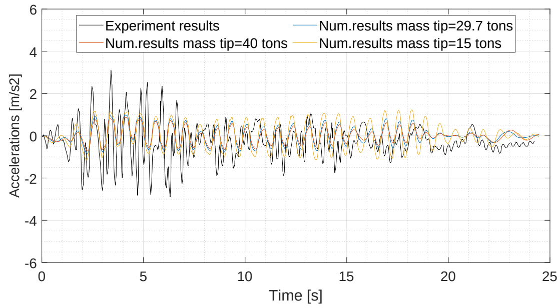

Figure 5.26. Analysis nodal accelerations sensor A3 x=0m y=13m.

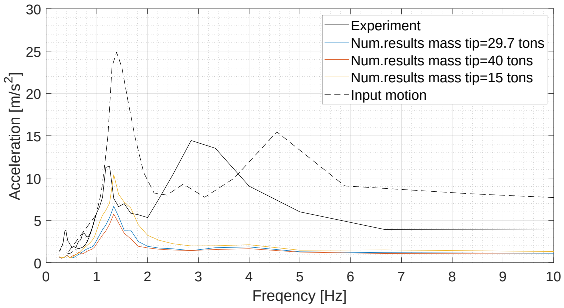

Figure 5.27. Analysis spectral accelerations sensor A3 x=0m y=13m.

The Figures 5.26 and 5.27 show the comparison between tests carried out for studying the influence of the mass magnitude at the tip of the tower, considering a mass equal to zero at the foundation level.

The model response observed shows an expected behaviour. When the mass of the tower is increased, the frequency of the vibration becomes smaller and, consequently, the accelerations are decreased. The opposite outputs are received when the mass is reduced, the accelerations increase at the position of the sensor A3.

Another option studied for modelling the distribution of the masses on the tower were following the same way proposed at the physical centrifuge test, i.e. setting 10.6 *tons* at the tip and 18.7 *tons* at the foundation. Moreover, in order to cover all the possible options, a third test is ran setting a lumped mass equivalent to the value of the two mentioned masses at the foundation. The results obtained are showed at Figures 5.28 and 5.29.

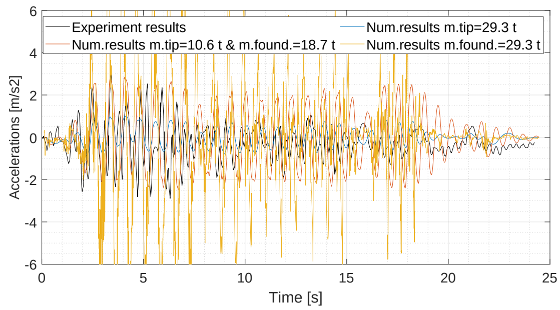

Figure 5.28. Analysis nodal accelerations sensor A3 x=0m y=13m.

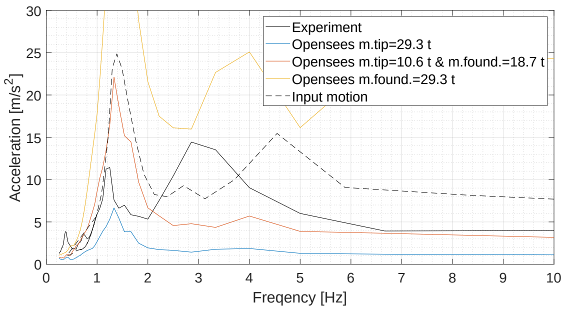

Figure 5.29. Analysis spectral accelerations sensor A3 x=0m y=13m.

As observed in the Figures above, the relevancy of the masses distribution along the structure is very high. If Figure 5.29 is checked, it can be concluded that the lighter is the foundation, the smaller are the accelerations recorded at the tip of the structure. When all the mass is concentrated at the foundation level, the accelerations are even amplified respect to the input motion induced to the numerical model.

If the distribution of masses followed is set according to the one proposed by the reference centrifuge test, i.e. setting masses both at the tip and at the foundation, the spectra is reduced respect to the previous case but the accelerations registered are more less the same than the ones corresponding to the input motion, dashed line at Figure 5.29. Therefore, any damping is induced by the structure.

At last, it is observed that the lower values of accelerations are registered when all the masses are lumped at the tip of the tower. Moreover, the spectra recorded is closer to the one obtained after the experiment although a second peak at a value of frequency equal to 3 Hz is missed.

Furthermore, the option of concentrating all the masses of the model at the tip of the tower is the solution which provides better results in terms of fluctuation of excess pore water pressure at the recorders located close to the structure, P1 and P3, see Figures 5.30 and 5.31. Therefore, that is the option chosen for obtaining the final calibration of the model as can be seen at Chapter 4.

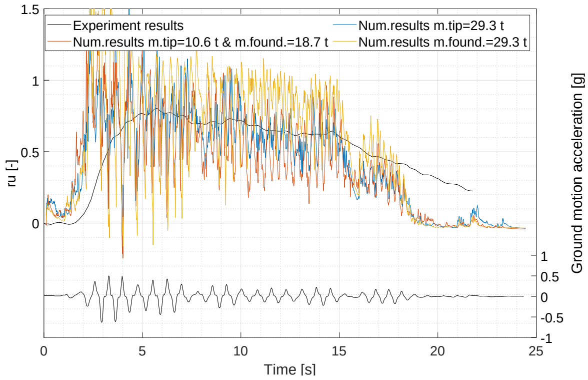

Figure 5.30. Pore water pressure ratio sensor P1 x=0m y=-0.5m.

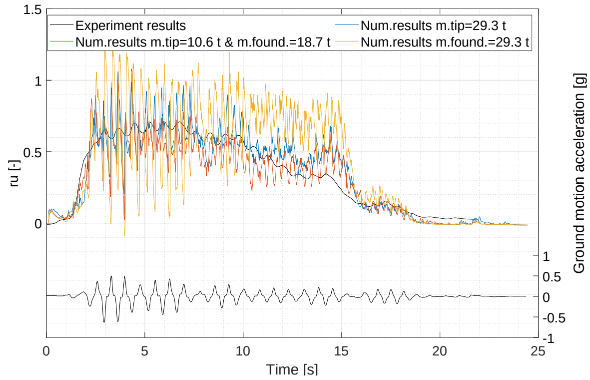

Figure 5.31. Pore water pressure ratio sensor P3 x=0m y=-2.5m.

5.2 Calibration based on *PM4Sand*

5.2.1 Initial set of parameters

As mentioned before, during the Section 3, the available outputs of the centrifuge test which are used for comparison with the numerical model constructed in this report comes from a performance which uses Toyoura sand with a relative density $D_r = 68\%$ (Yu et al., 2014).

Knowing this information, a first set of parameters for *PM4Sand* can be obtained by conducting a numerical simulation of a *Cyclic Direct Simple Shear Test* using the mentioned constitutive model in *OpenSees*. In order to achieve this task, the *CSR-Ncycles curves* corresponding to Toyoura Sand $D_r = 75 - 81\%$ from (Ishihara and Yamazaki, 1984) are used for the calibration of the element test.

The available results come from the performance of *Circular Shear Tests, Cyclic Triaxial Shear Tests* and *Cyclic Torsional Shear Tests*. Thus, although the ones from *Cyclic Direct Shear Simple Test* are not found, an equivalence between the *Cyclic Shear Ratio (CSR)* obtained from the *Cyclic Triaxial Shear Test* and the *Cyclic Direct Shear Test* can by calculated following the Equation 5.1 (Kramer, 1996).

$$(CSR)_{SS} = C_r\,(CSR)_{tx} \tag{5.1}$$

where

$$C_r = (1 + K_0)/2 \quad \text{for} \quad K_0 = 0.5 \tag{5.2}$$

$(CSR)_{SS}$	Cyclic Shear Ratio for Simple Shear Test
$(CSR)_{tx}$	Cyclic Shear Ratio for Triaxial Test
C_r	Correction factor
K_o	At-rest coefficient showing the ratio of horizontal to vertical effective stress

For the sake of accomplishing this numerical element test, the four-noded quadrilateral element *SSPquadUP* is used. This element counts with three degree of freedom, 1 and 2 accounting for the translation along x and y axis, and 3 for the generation of pore water pressure, see Figure 5.32. The threshold considered for triggering liquefaction is determined in terms of shear strains and equal to $\gamma = 2.5\%$ in the case of Toyoura Sand as recommended by (Huang et al., 2015), see Figure 5.33 . Further details about the numerical performance of the *Cyclic Direct Shear Simple Test* can be found in the Appendix D.

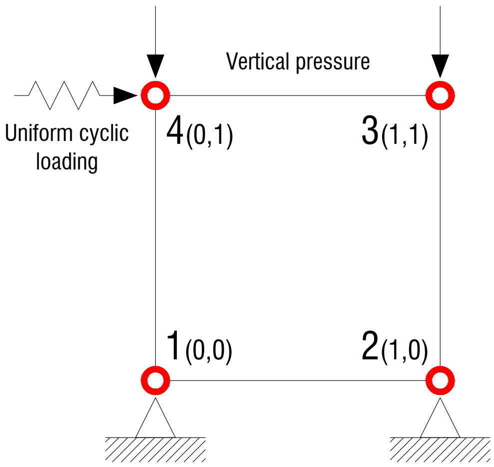

Figure 5.32. Diagram of *SSPquadUP* element during *CDSS* test.

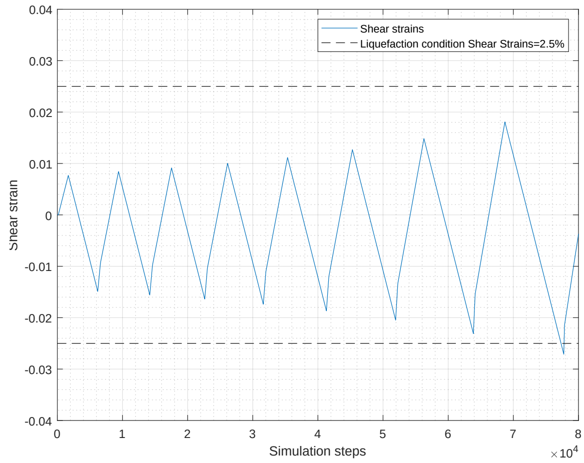

Figure 5.33. Shear strains development during *CDSS* test for medium dense Toyoura Sand

The authors of the current report carried out the calibration of this numerical element test in previous stages of the present researching process. Therefore, the influence of the different parameters of *PM4Sand* constitutive model is not presented again since it is out of the scope of this report. Nevertheless, the calibrated set of parameters of the mentioned constitutive model respect to the available ones (Ishihara and Yamazaki, 1984) is showed at Table 5.1. These values are used as a first approach for the calibration process of the centrifuge test whose performance is presented in the next section.

Parameter	Toyoura medium dense sand
D_r	0.75
G_o	107
h_{po}	0.16
h_o	0.500
e_{max}	0.987
e_{min}	0.589
e_{init}	0.689
n_b	0.01
n_d	0.1
z_{max}	5
A_{do}	1.3
c_z	250
c_ϵ	1.7
ϕ_{cv}	33
C_{Gd}	2
C_{Dr}	10
$C_{k\alpha f}$	30.88
Q	10
R	1.5
m	0.01
$F_{sed,min}$	-1
p_{sed}	-1

Table 5.1. Calibrated parameters of *PM4Sand* model for Toyoura medium dense sand

As observed in the Figure 5.34, the fitting between the experimental values and the obtained from the numerical *CDSS* is quite accurate. The Table 5.2 compares the number of cycles to liquefaction of both approaches. The graph includes also the calibration of medium dense Nevada Sand but those values are not going to be used on the current report, they belong to the previous stage of this research process.

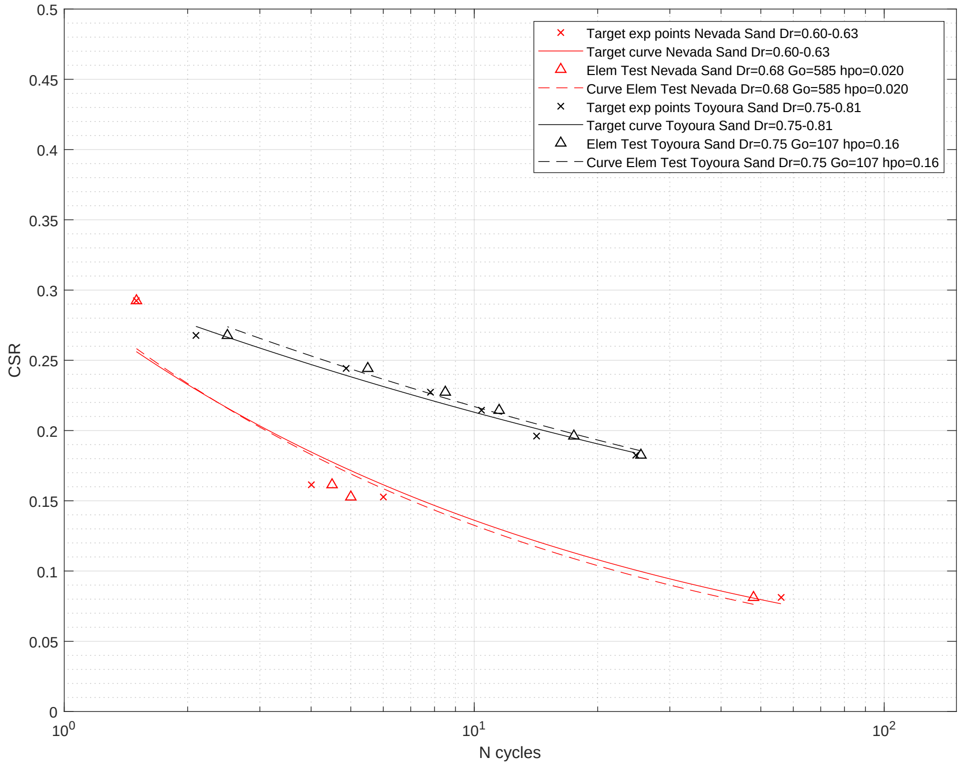

Figure 5.34. Calibrated and available $CSR - N_{cycles}$ *curves* for medium dense Toyoura and Nevada sand

	Toyoura medium dense sand					
CSR	0.2677	0.2442	0.2273	0.2144	0.1961	0.1825
$Ncyctargetted$	2.1	4.9	7.8	10.4	14.2	24.8
$Ncycsimulated$	2.5	5.5	8.5	11.5	17.5	25.5

Table 5.2. Comparison of number of cycles from experiment and number of cycles obtained in numerical simulation

5.2.2 Generation of excess pore water pressure at the free field

To assess the calibration process for *PM4Sand* constitutive model, the captured outputs of pore water pressure ratio in the free field are taken into consideration as the first aspect of such evaluation process. In this subsection, the effects of 3 primary parameters on the pore water pressure ratio of the sensors P2 and P4 are investigated and characterized thoroughly.

Relative density D_R

Relative density is the parameter responsible of controlling the response of the volumetric strains in soil domain. The dilatancy is hereby governed by the adjustment of relative density that leads to a significant influence on the pore water pressure ratio as shown on the Figures 5.35 and 5.36.

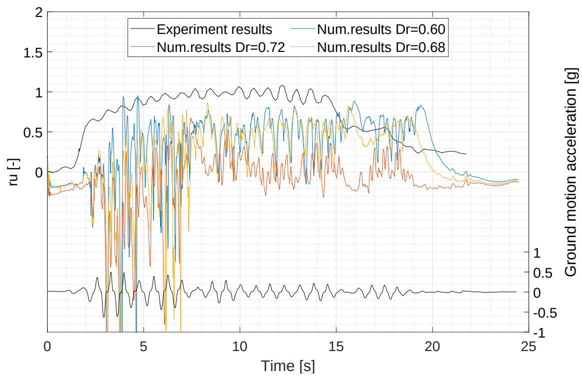

Figure 5.35. Pore water pressure ratio of sensor P2 at the location of x=6m and y=-0.5m.

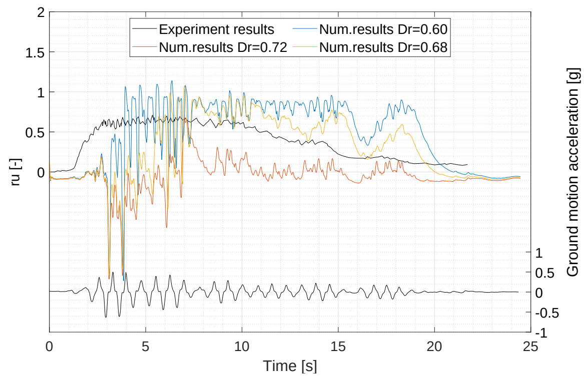

Figure 5.36. Pore water pressure ratio of sensor P4 at the location of x=6m and y=-2.5m.

Taking a look at the two figures above, apparently, the effect on dilatancy of the soil is changed substantially by calibrating the relative density D_R. Particularly, regarding the highest considered value of relative density as 72 %, the soil is more dense. In other words, more dilative compared to the rest ones, causing the generation of negative excess pore water pressure during the imposed shaking due to the vacuum effect, in both P2 and P4. It is evident that the curve trend of pore water pressure ratio is lifted up when the decrements of relative density D_R are implemented, which leads to the reduction of dilative soil behaviour, inducing more contractive response instead.

Thus, it can be concluded that the increment of relative density is related with a decrement of the values of pore water pressure. That assessment is also in accordance with the theoretical soil behaviors.

Shear modulus coefficient G_0

Shear modulus coefficient G_0 is calibrated mainly for controlling the elastic behaviour of the soil under shearing, especially in small strain region, approximately from $1e-6$ to $1e-3$ in shear strain according to the Figure 4.11. Its associated effects on the calibration of the model regarding the generation of pore water pressure at the free field are analyzed graphically through the numerical output data plotted on the Figure 5.37 and 5.38.

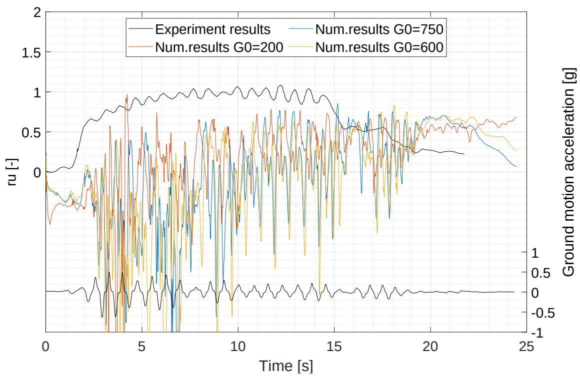

Figure 5.37. Pore water pressure ratio of sensor P2 at the location of x=6m and y=-0.5m.

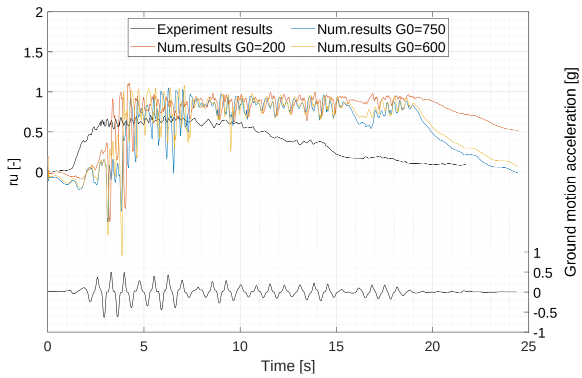

Figure 5.38. Pore water pressure ratio of sensor P4 at the location of x=6m and y=-2.5m.

Taking an look at the two Figures, it is observed that the curves of r_u-time history are uplifted when the shear modulus coefficient is reduced, in both sensors P2 and P4. Moreover, such parameter modification also brings out effects on the excess pore water pressure dissipation. In particular, regarding for instance the sensor P4 located at the depth of 2.5 m from the ground surface, a slower dissipation is noticed.

The up-mentioned evidences follow the expected soil response, since the elastic soil stiffness to shearing is reduced by decreasing the shear modulus coefficient and therefore, making the soil more susceptible to be liquefied.

Contraction rate parameter h_{po}

Once the values of D_R and G_0 are calibrated, the adjustment of the contraction rate parameter need to be carried with the main sake of controlling the contractive soil response, which also counts with an important influence on the r_u values. Here, 3 different values of contraction rate parameter are used for the analysis of the influence of this parameter on the excess pore water pressure generation at the free field, see Figures 5.39 and 5.40.

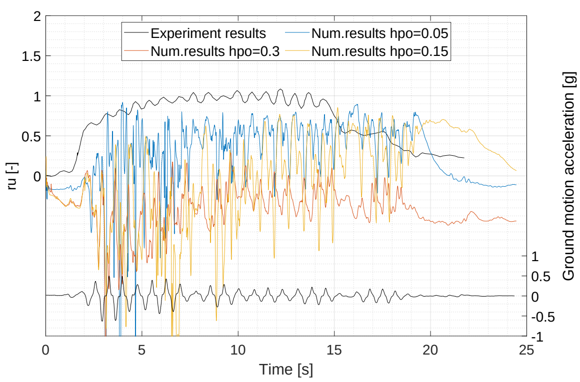

Figure 5.39. Pore water pressure ratio of sensor P2 at the location of x=6m and y=-0.5m.

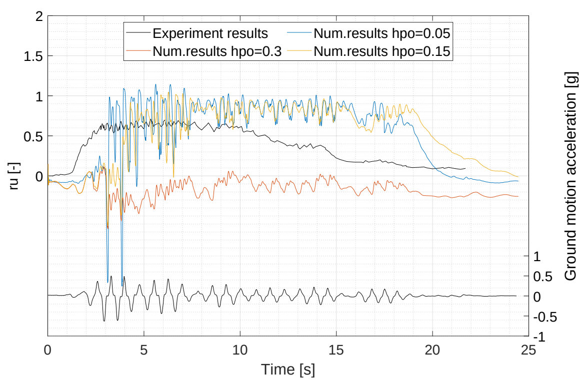

Figure 5.40. Pore water pressure ratio of sensor P4 at the location of x=6m and y=-2.5m.

Taking a look at the two Figures above, apparently, the pore water pressure ratio is reduced by increasing the contraction rate parameter. Thus, the curves trends of the pore water pressure ratio are witnessed to plummet and fluctuate around zero when the value of $h_{po} = 0.3$ in both sensors P2 and P4 is tested. In addition, the adjustment of contraction rate parameter can also bring out the up-lifting in the curve trend by decreasing its value.

By adjusting h_{p0}, the dissipation process can also be modified but it does not show a clear trend. For instance, it is observed that the dissipation is quicker for $h_{po} = 0.05$ than for $h_{po} = 0.15$, but if the value is increased to $h_{po} = 0.30$, excess pore water pressure is almost not generated.

5.2.3 Settlement of the structure

Once captured the fitted results of excess pore water pressure ratio at the free field according to the experimental results, the adjustment of settlement is the next step of the calibration process. Apart from the 3 primary parameters, the secondary parameter Z_{max} - is also considered since it is demonstrated to have a significant impact on fabric-dilatancy associated to the soil, and important feature regarding the total value of the settlements.

Relative density D_R

Volumetric strain governed by relative density is a crucial factor leading to the settlement of the structure indeed. With such statement, 3 different values of relative density are tested in *OpenSees* for carrying a graphical evaluation of the influence of this primary parameter, see Figure 5.41.

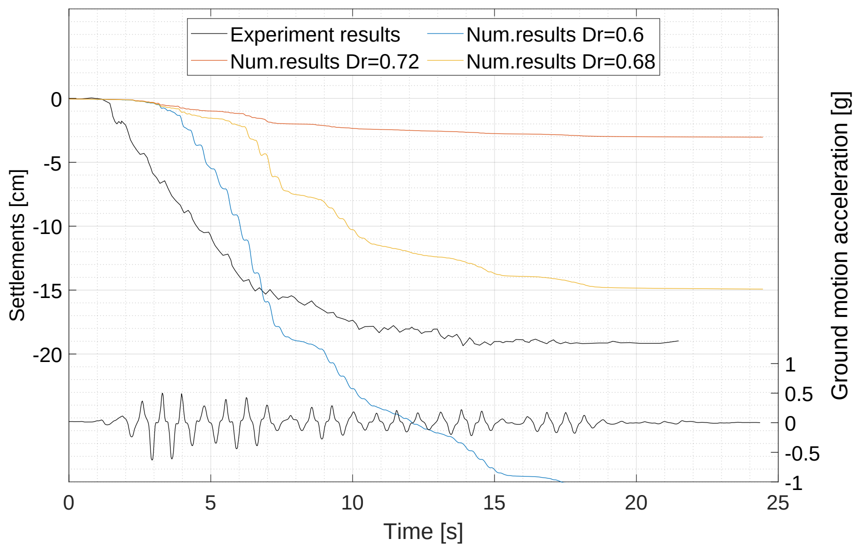

Figure 5.41. Settlement with the regulation of relative density

Taking a look at the figure above, it is obvious that the relative density is inversely correlated to the value of the settlements. In addition to a higher resistance to pore water pressure generation, see Figures 5.35 and Figures 5.36, a denser sand counts with a smaller void space for volumetric densification, a greater stiffness and a more dilative tendency, leading to a sooner arresting of the shear strains. Nevertheless, this fact might not occur in all the cases since structures with large height/width ratios may provide greater seismic response due to amplified ground oscillations (Dashti, D.Bray, M.Pestana, Riemer and Wilson, 2010).

According to such hypothesis, for the case of the current numerical model, the largest values of vertical displacements are witnessed for the smallest value of relative density $D_R = 60\%$, whereas the opposite trend is observed by using the highest value of relative density $D_R = 72\%$.

Shear modulus coefficient G_0

As previously mentioned, shear modulus coefficient plays an important role regarding the small shear strain development and the elastic shear modulus of the model. Thus, the calibration of G_0 needs to be taken carefully into consideration with the main sake of getting better fitted results regarding vertical displacements. In this sub-subsection, the influence of the shear modulus coefficient regulation is characterized graphically, by assigning 3 different values of G_0 to the numerical model , see Figure 5.41.

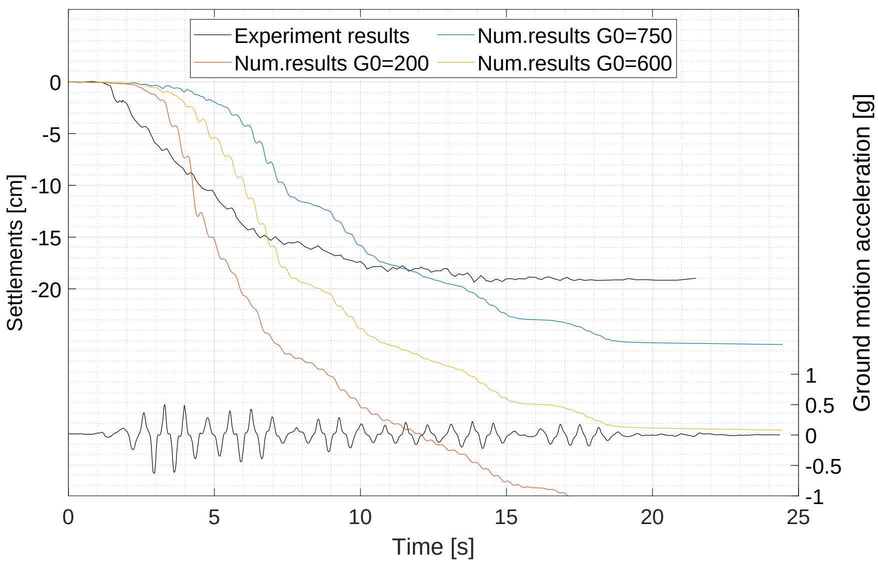

Figure 5.42. Settlement with the regulation of shear modulus coefficient

Theoretically, the increment of G_0 leads also to an increment of the soil stiffness according to the relation between G_0 and elastic shear modulus presented in the Equation 4.2 (Boulanger and Ziotopuolou, 2017). Thus, it is expected that the highest considered value of $G_0 = 750$ provides lowest results compared with the rest of the cases since the shear strength of the soil is larger, reducing the tendency of the soil to liquefy.

Contraction rate parameter h_{po}

Contraction rate parameter is an important factor governing the target cyclic resistance ratio *(CRR)* (Boulanger and Ziotopuolou, 2017). It hereby means that the liquefaction phenomenon is also controlled by calibrating such parameter. Therefore, by the adjustment of h_{po}, the settlements of the super structure can be controlled.

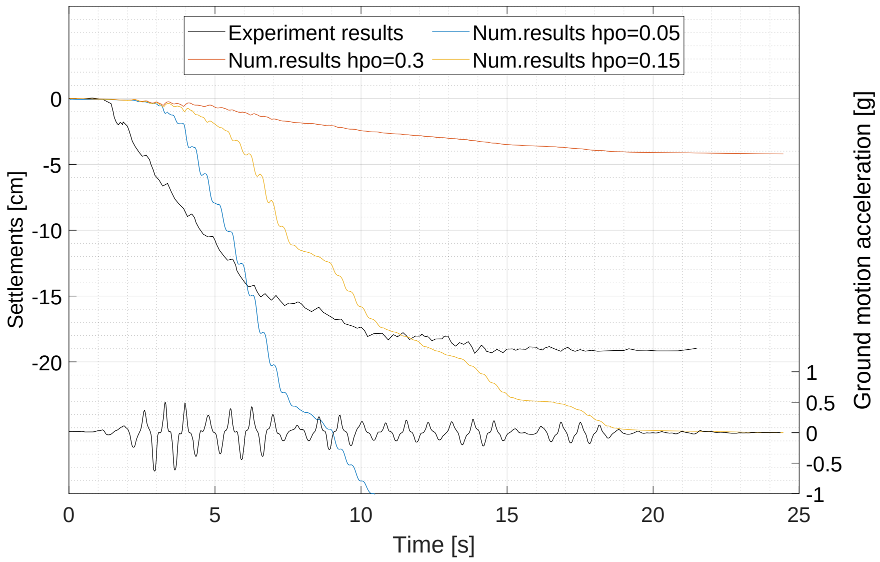

Figure 5.43. Settlement with the regulation of contraction rate parameter

By checking the effects of the different values of h_{po} at the Figure 5.43, a inverse correlation is observed respect to the vertical displacements measured. Besides, the influence of contraction rate calibration on the settlement seems to be very significant. As noticed, the settlements increased around 70 % when h_{po} decreased from 0.3 to 0.15. Thus, the blue curve experiences a higher settlement rate from the fourth second when h_{po} is reduced to 0.05, as illustrated in the Figure 5.43.

Overall, to get the fitted results of settlement compared with experimental results, calibration of the contraction parameter is crucial to be implemented.

Z_{max} coefficient

Parameter Z_{max} is a coefficient which governs the relation between the relative density D_R and cyclic strength of the soil (Boulanger and Ziotopuolou, 2017). Thus, the task of adjusting this parameter affects dramatically the settlement measured as experienced during the current calibration process. Here, two different values of Z_{max} are tested in the model, with the main purpose of showing visually the influence of this parameter in terms of settlement.

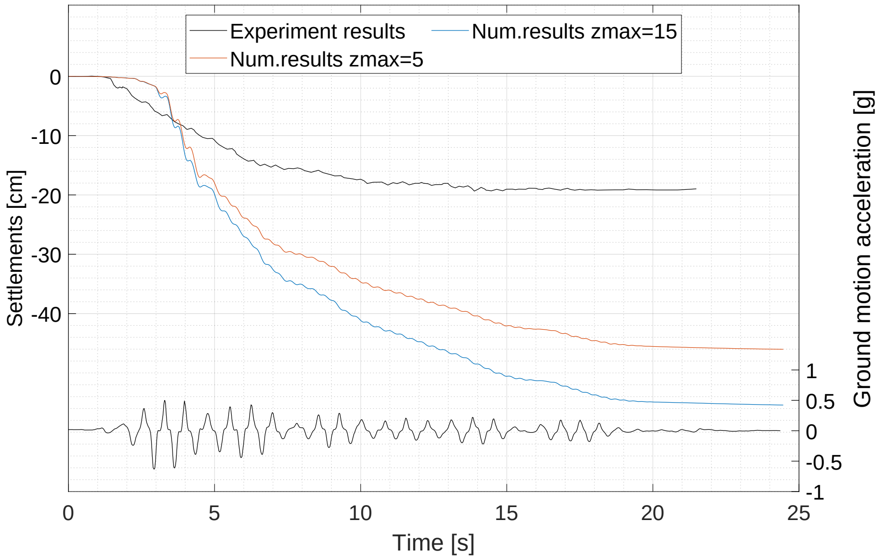

Figure 5.44. Settlement with the regulation of Z_{max} coefficient

Taking a look to the Figure 5.44, it is evidenced that the increment of Z_{max} leads to an increment of settlement so it might mean that an a larger value of Z_{max} implies a smaller resistance of the soil to cyclic loading according to its definition (Boulanger and Ziotopuolou, 2017). Thus, the increment of Z_{max} coefficient brings a larger value of settlements.

However, the adjustment of this coefficient within the recommended values proposed by (Boulanger and Ziotopuolou, 2017) does not bring out such large changes in comparison with the modification of the primary parameter h_{po}. Therefore, this parameter may be modified respect to its recommended values for small adjustments and after a rigorous analysis of its influence in the performance of the model since the variation of the value of the secondary parameters is only suggested when enough information about the soil is available.

5.2.4 Generation of excess pore water pressure in the vicinity of the structure

Regarding the influence of the three primary input parameters of *PM4Sand* (D_R,G_0,h_{po}) on generation of excess pore water pressure recorded by sensors below the structure, the general finding confirms the trends seen in the free field showing similar patterns as for the calibration of sensors P2, P4. Despite some differences, merely influenced by the presence of the structure and its contribution in terms of higher effective confinement of the soil as well as the higher deviatoric contribution driven by inertial effects, the effect of the parameters on the generation trends remains unchanged. Thus, a more detailed elaboration on the parameter influences on the sensors P1, P3 located below the suction bucket foundation can be seen in section in the Appendix E.2.

5.2.5 Acceleration recorders

The last records employed for evaluating the influences of the primary parameters of *PM4Sand* model comes from the accelerometers A1, A2, and A3. Thus, the acceleration records measured at the soil domain and at the tip of the wind turbine prototype are taken into consideration in this subsection.

To implement the assessment process mentioned above, three different values of the three primary parameters are assigned to the model simulations, with the main purpose of getting visual evidences of their effects regarding both the nodal acceleration and the acceleration spectra, in comparison with the provided experimental results.

Relative density D_R

The adjustment of the relative density brings changes at the soil stiffness by reducing the void ratio. Thus, it is predicted that the acceleration records were affected by such parameter calibration since the dynamic response of a soil system is closely related with its associated stiffness. Therefore, the outputs from the three accelerometer A1, A2, and A3 are compared according to three different numerical models, corresponding to 3 distinctive values of relative density. First of all, the recordings from the soil domain, sensors A1 and A2, are considered analyzed.

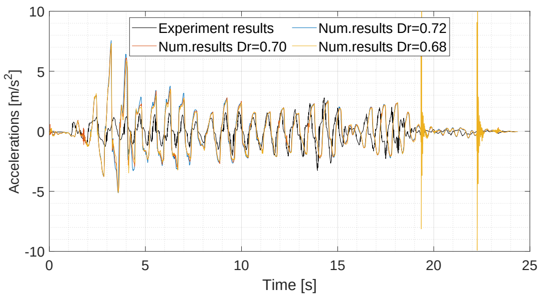

Figure 5.45. A1 acceleration records with the regulation of relative density.

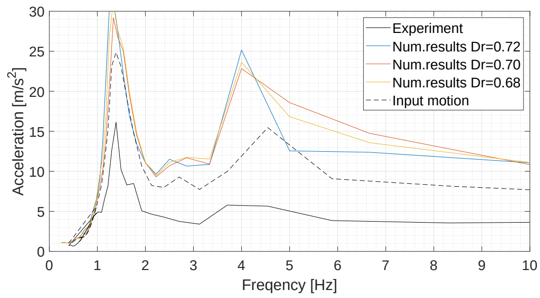

Figure 5.46. Analysis spectral accelerations sensor A1.

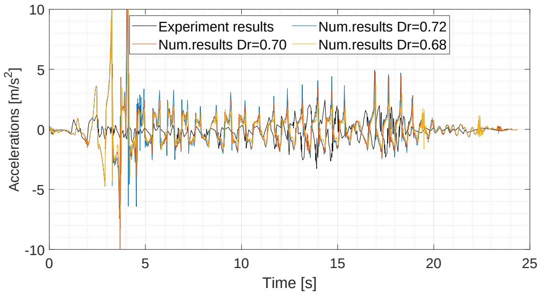

Figure 5.47. A2 acceleration records with the regulation of relative density.

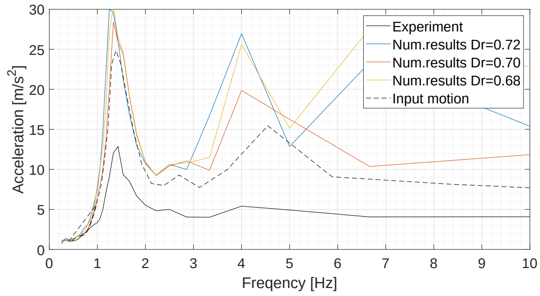

Figure 5.48. Analysis spectral accelerations sensor A2.

Taking an overview at the Figures 5.45 and 5.47, the changes of the acceleration graph follow the theoretical expectation. The fact is that the excess pore water pressure generation is increased with the decreasing of relative density according to the Figures 5.35 and 5.36. This phenomenon leads to the reducing of the dynamic response due to the incapacity of water generated to transmit shear waves and therefore, a reduction of the peak accelerations regarding the spectra. As a result, with the highest considered value of D_R as 0.72, the blue curves in the Figures 5.45 and 5.47 are witnessed higher amplitudes than the other cases. However, the stiffness overestimation of the numerical model specially during the first second is not overcame in both sensors A1 and A2, irrespective of what magnitude the relative density is used.

In regard to the analysis of the acceleration spectra, shown in the Figures 5.46 and 5.48, the same issue is evidenced. Thus, the peak accelerations of the three D_R studied occur at a frequency of 1.3 Hz, replicating the predominant frequencies of the input motion, but any de-amplification is observed since the peaks are even larger than the dynamic motion induced. Regarding the second peak, accelerations witnessed are also observed at a frequency of 4 Hz, being once again these results are much higher than the second peak of the input motion curve. Such occurrence observed depicts an enlarged soil response mechanism undergone the applied shaking motion which might be compromising the outputs received from the rest of the recorders.

Despite of the mentioned issue, if the records under the bucket A1 are compared with the ones at the free field A2, the curves obtained under the bucket seem to show more similar shapes, while the ones at the free field depicts more different trends. This fact might be explained considering the presence of the suction bucket, which makes the accelerations to be more dependent on the acceleration of the structure.

Regarding the accelerometer at the tip of the superstructure, an identical analyze process is carried, see Figures 5.49 and 5.50.

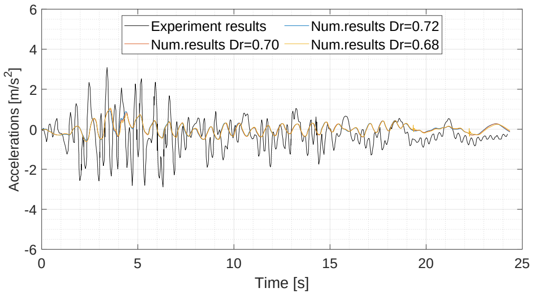

Figure 5.49. A3 acceleration records with the regulation of relative density.

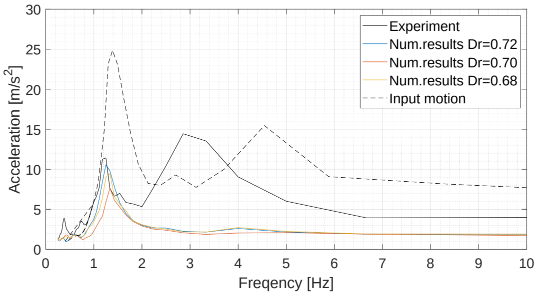

Figure 5.50. Analysis spectral accelerations sensor A3.

Checking visually the two figures above, apparently, the same trend of acceleration recorded in the soil domain is shown at the tip of the wind turbine so that the seismic response is increased by increasing the relative density. However, in all of three considered cases, the acceleration amplitudes of numerical models are much smaller than the experimental results regardless of any value of D_R. As mentioned previously, this is a consequence of the way of modelling the masses of the structure which, in the case of the numerical model, are lumped at the tip of the tower which results in structural oscillations with smaller frequencies.

As regards to the analysis of the spectra, the magnitude of the peak acceleration matches with one of the predominant frequencies of the tower tested during the physical centrifuge test. Nevertheless, any value of D_R is able to replicate the second peak observed.

Shear modulus coefficient G_0

It is expected that the acceleration records were affected by adjusting G_0 due to the influence of this parameter on the elastic shear stiffness of the soil. For studying its effect, three different values used in the previous section are tested, with the main purpose of providing a visual overview of the calibration process.

First of all, the two acceleration sensors in the soil domain, A1 and A2, are taken into account, see Figures 5.51 and 5.53. Apparently, by increasing the value of G_0, the amplification of acceleration is increased correspondingly. That phenomenon can be justified by the soil response mechanism mentioned in the previously. Particularly, the excess pore water pressure generation is reduced by increasing the shear modulus coefficient that leads to an easier transmission of shear waves from earthquake motion. Therefore, the acceleration amplitudes are increased due to a more vigorous soil response. Taking a look at the Figures 5.51 and 5.53 to achieve a visual comprehending, with the highest considered value of G_0 as 750, the blue curves are witnessed higher amplitudes than the rest cases.

Once again, an overestimation of model stiffness is observed. The fact is that the magnitudes of accelerations in both sensors A1 and A2 are over amplified as opposed to the experimental results in the up-mentioned period of time. However, after the period of strong shaking, the numerical results are approximately fitted to the experimental outputs.

When it comes to the analysis of the acceleration spectra of the sensors in the soil domain, Figures 5.52 and 5.52, the overestimation of the stiffness of the soil is again evidenced. Thus, the acceleration values around the two predominant frequencies of the input motion, 1.3 Hz and 4 Hz are surpasses by the peak accelerations of the soil, proving then that the model is amplifying the seismic motion.

As a summary, it can be concluded that the dynamic soil response can be reduced by reducing the magnitude of G_0, although this is not sufficient for matching proper values of accelerations.

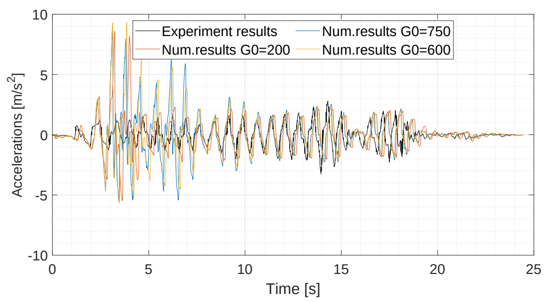

Figure 5.51. A1 acceleration records with the regulation of shear modulus coefficient.

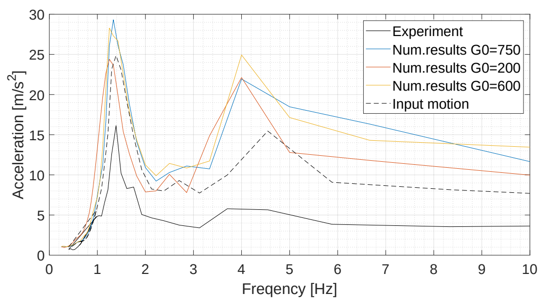

Figure 5.52. Analysis spectral accelerations sensor A1.

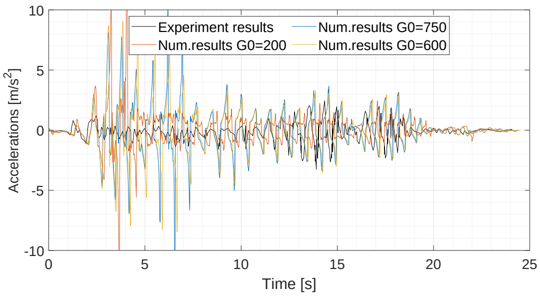

Figure 5.53. A2 acceleration records with the regulation of shear modulus coefficient.

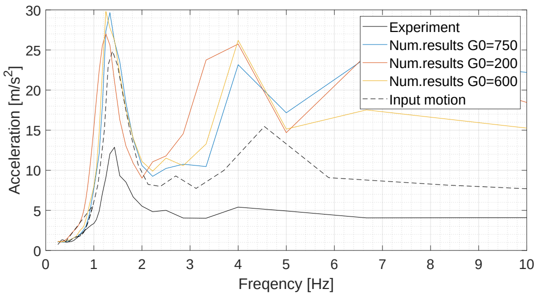

Figure 5.54. Analysis spectral accelerations sensor A2.

As far as the sensor A3 located at the tip of the wind turbine prototype is concerned, the magnitudes of the numerical acceleration record are lower than the experimental results due to the way of modelling the masses as explained previously. Interestingly, such issue can be modified slightly by adjusting the value of G_0 assigned for numerical model. Taking a look at the blue curve with the highest considered $G_0 = 750$, Figure 5.55, the curve of the outputs is lifted compared to the rest ones.

Analyzing the acceleration spectra, Figure 5.56, the peak acceleration corresponding to the predominant frequency at the tip of wind turbine is also lifted moderately by increasing the value of shear modulus coefficient. However, the values of peak acceleration of 3 cases captured are much smaller than the input motion peak acceleration.

Overall, it seems that the calibration process of G_0 can be used for adjusting also the values of accelerations at the tip of the structure. Nevertheless, other options like adjusting the stiffness, the section parameters of the tower or the way of modelling the masses are demonstrated to be more influential on the output results of the sensor A3 as showed during the calibration of $PDMY01$.

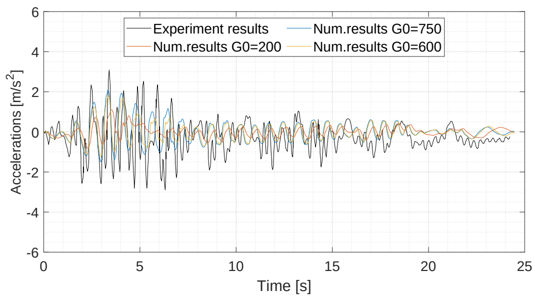

Figure 5.55. A3 acceleration records with the regulation of shear modulus coefficient.

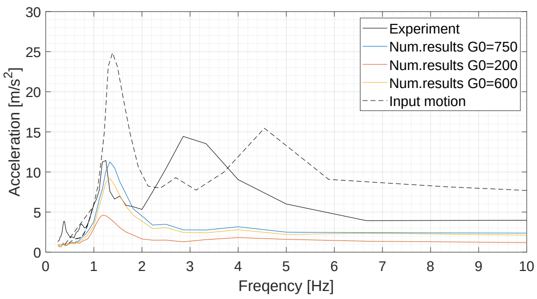

Figure 5.56. Analysis spectral accelerations sensor A3.

Contraction rate parameter h_{po}

As mentioned in the previous subsection, the contraction rate parameter is able to control the triggering of liquefaction phenomenon by governing the target cyclic resistance ratio. Considering this, the acceleration records could be affected significantly by calibrating such parameter. Therefore, 3 different values of h_{po} are tested, with the main sake of getting a visual comparison about the affect of h_{po} on the acceleration records.

Firstly, the two accelerometers in the soil domain A1 and A2 are analyzed according and compared with the experimental result in terms of nodal accelerations and acceleration spectra, as shown in the Figures 5.57, 5.58, 5.59 and 5.60.

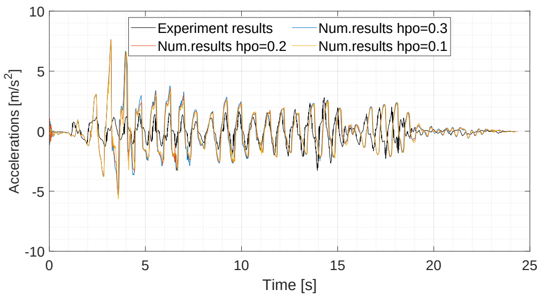

Figure 5.57. A1 acceleration records with the regulation of contraction rate parameter.

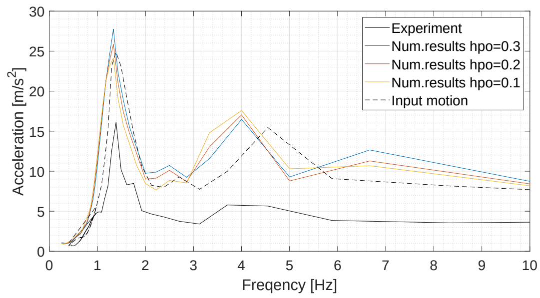

Figure 5.58. Analysis spectral accelerations sensor A1.

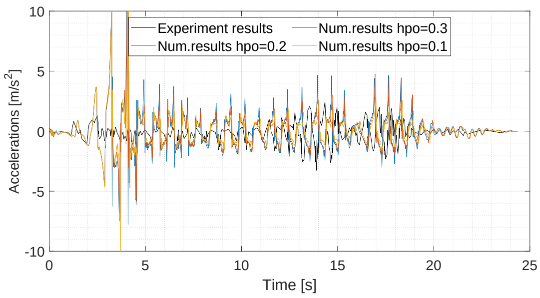

Figure 5.59. A2 acceleration records with the regulation of contraction rate parameter.

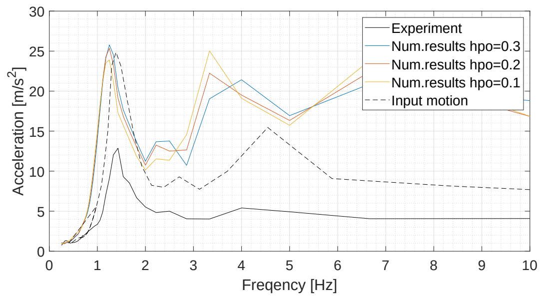

Figure 5.60. Analysis spectral accelerations sensor A2.

It is obvious that the overestimation of the soil stiffness is still witnessed for the three values of h_{po} tested. Particularly, in the first 7 seconds, the numerical acceleration outputs are greatly over amplified compared with the experimental results. However, after the period of strong shaking, a better fitting of the numerical model respect to the experiment is achieved specially at A1. Although small changes on the trends prediction of h_{po} are registered, it can be noticed that the acceleration records are decreased slightly by reducing the magnitude of contraction rate parameter.

Regarding the analysis of spectral acceleration, the high peaks acceleration phenomenon continues to be captured at the predominant frequencies of 1.3 Hz and 4 Hz, take a look to Figures 5.58 and 5.60. The profile depicted by the input motion is virtually replicated by the numerical model at A1, and amplified by the curves cast by the sensor A2. Hence, it is observed that the soil is not inducing any damping to the induced input motion, something that does not fit with the real conditions.

The last evaluated feature of h_{po} calibration process regarding acceleration output is the sensor A3 located at the top of the wind turbine prototype. Once again, the comparison with experimental results and acceleration spectral is carried, as shown in the Figures 5.61 and 5.62.

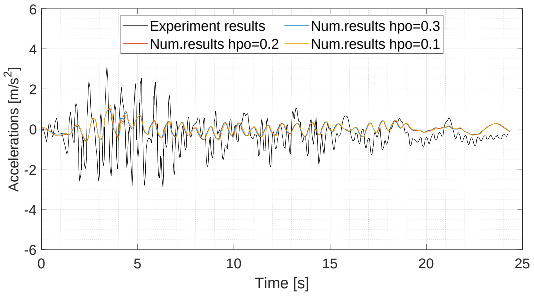

Figure 5.61. A3 acceleration records with the regulation of contraction rate parameter.

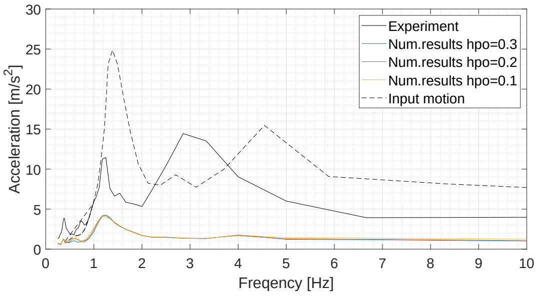

Figure 5.62. Analysis spectral accelerations sensor A3.

Apparently, at sensor A3, the effect of h_{po} adjustment is not substantially significant. Consequently, the three numerical models tested with 3 values of h_{po} provide almost the same output curves.

Regarding the analysis of spectral acceleration, the inconsiderable influence of h_{po} calibration is proved again. Thus, the value of peak accelerations corresponding to the predominant frequency of the input motion at 1.3 Hz almost remains constant by iterating the value of h_{po} from 0.1 to 0.3. In addition, the values of such peak accelerations at A3 are always smaller than the input motion and experimental ones, no matter what the magnitude of h_{po} is.

To summarize, the task of calibrating contraction rate parameter can be applied for adjusting better acceleration outputs in soil domain versus experimental results. Nevertheless, the mentioned parameter brings negligible changes of the records of accelerations at A3.

5.3 Calibrated parameters

Once having studied the effects of the selected input parameters on the numerical models, both for $PDMY01$ and $PM4Sand$, the sets of parameters which provide the best fit with respect to the output received from the centrifuge test (Yu et al., 2014) are collected in the Table 5.3 and in the Table 5.4.

Name	Code	Value	Units
Density	$\$rho$	2.5	$tons/m3$
Reference shear modulus	$\$refShearModul$	140 000	kPa
Reference bulk modulus	$\$refBulkModul$	170 000	kPa
Friction angle	$\$frictionAng$	24	^{o}
Peak shear strain	$\$peakShearStra$	0.1	m
Reference mean effective confining pressure	$\$refPress$	80	kPa
Pressure dependent coefficient	$\$PressDependCoe$	0.5	$-$
Phase transformation angle	$\$PTAng$	20	^{o}
Contraction parameter	$\$contrac$	0.08	$-$
Dilation coefficient 1	$\$dilat1$	0	$-$
Dilation coefficient 2	$\$dilat2$	0	$-$
Liquefaction coefficient 1	$\$liquefac1$	10	$-$
Liquefaction coefficient 2	$\$liquefac2$	0.02	$-$
Liquefaction coefficient 3	$\$liquefac3$	1	$-$
Number of yielding surfaces	$\$noYieldSurf$	20	$-$
Initial void ratio	$\$e$	0.55	$-$
Parameter straight critical state 1	$\$cs1$	0.9	$-$
Parameter straight critical state 2	$\$cs2$	0.02	$-$
Parameter straight critical state 3	$\$cs3$	0.7	$-$
Atmospheric pressure for normalization	$\$pa$	101	kPa
Numerical constant	$\$c$	0.3	$-$

Table 5.3. Calibrated set of parameter of $PDMY01$ material

Name	Code	Value	Units
Density	$\$rho$	2.20	$tons/m^3$
Apparent relative density	$\$Dr$	0.68	-
Shear modulus coefficient	$\$G0$	195	-
Contraction rate parameter	$\$hpo$	0.26	-
Atmospheric pressure	$\$Patm$	101.3	kPa
h_o	$\$h0$	0.465	-
Maximum void ratio	$\$emin$	0.47	-
Minimum void ratio	$\$emax$	0.75	-
n^b	$\$nb$	0.70	-
n^d	$\$nd$	0.10	-
A_{do}	$\$Ado$	1.30	-
z_{max}	$\$zmax$	5.00	-
c_z	$\$cz$	150	-
c_ε	$\$ce$	1.70	-
phi'_{cv}	$\$phicv$	26.00	-
Poisson's ratio	$\$nu$	0.33	-
C_{GD}	$\$Cgd$	2.00	-
C_{DR}	$\$Cdr$	13.25	-
$C_{k\alpha f}$	$\$ckaf$	21.30	-
Q	$\$Q$	10.00	-
R	$\$R$	1.00	-
m	$\$m\_m$	0.01	-
$F_{sed,min}$	$\$Fsed\_min$	0.04	-
$p'_{sed,o}$	$\$p\_sedo$	-20.26	-

Table 5.4. Calibrated set of parameter of $PM4Sand$ material

Regarding the values needed for the calibration of the model by the use of $PDMY01$ material, it is relevant to point out the relative high value of density used, as well as the low values of friction angle and phase angle respect to the recommended set of parameters for medium-dense sands for the material $PDMY01$ presented at (Mazzoni et al., 2007). However, these deviations allow to control the fluctuations of r_u at the recorders of pore water pressure at the vicinity of the structure which is the main issue showed by the numerical model as evidenced in the previous paragraphs.

As far as the values of the input parameters used for the calibration of $PM4Sand$ are concerned, the parameters applied deviate from the ones applied in the element test but in general the deviation is not drastic since similar ranges of parameters are used , see Table 5.1. Thus, the value of G_o shows an important deviation with respect to the value proposed by the Equation 4.3, being necessary to apply an important decrement for fitting the experimental curves provided.

5.3.1 Excess pore water pressure ratio

The outputs generated by both numerical models, $PDMY01$ and $PM4Sand$, constructed in *OpenSees* corresponding to the excess pore water pressure ratio r_u are compared with the results received from the reference centrifuge test presented at Chapter 3. The sensors are tagged as P1, P2, P3 and P4 and their locations are showed at Figure 3.1.

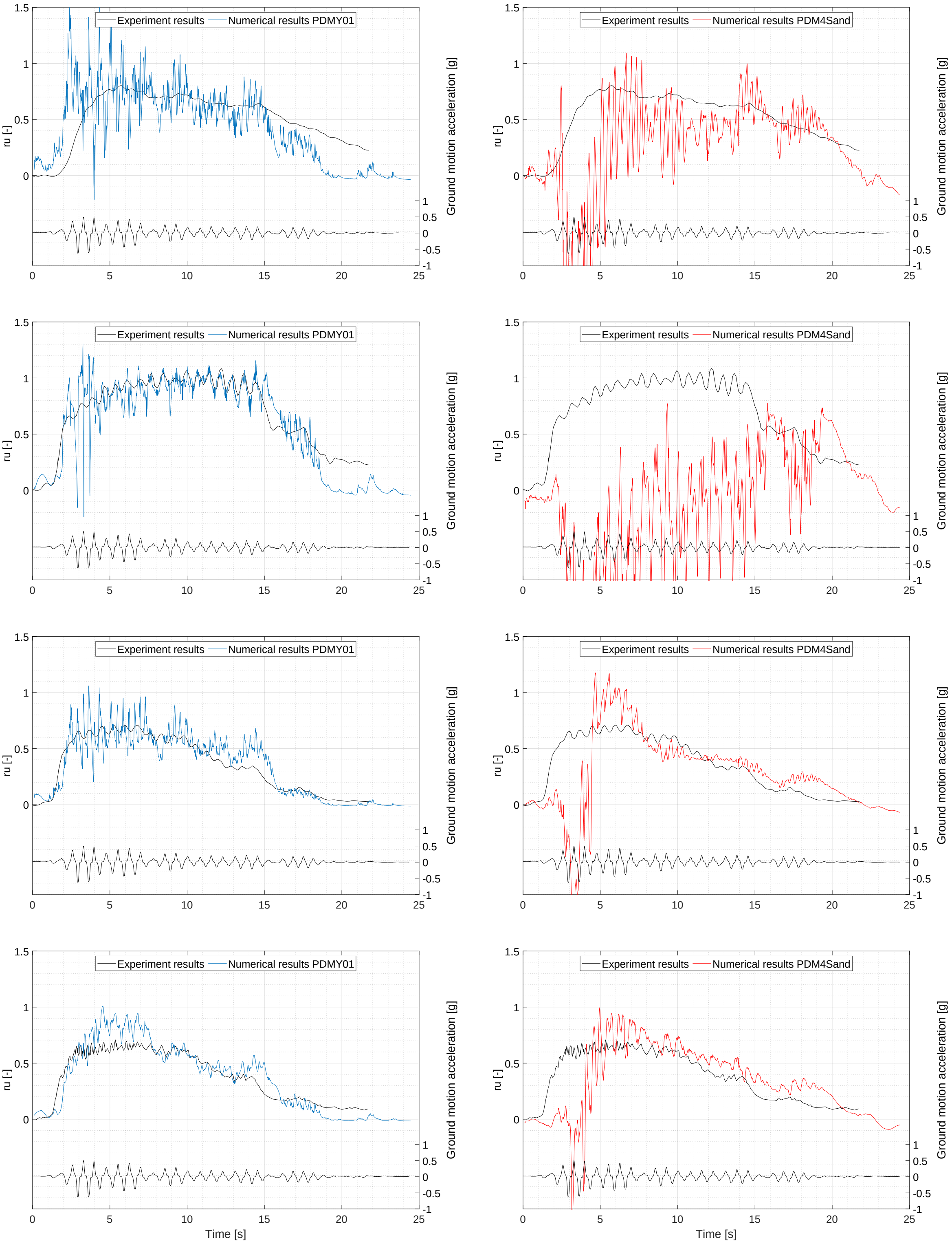

Figure 5.63. Comparison between experimental and numerical results of pore water pressure ratio r_u time histories, from left to right: (a) r_u P1 x=0m y=-0.5m $PDMY01$. (b) r_u P1 x=0m y=-0.5m $PM4Sand$. (c) r_u sensor P2 x=6m y=-0.5m $PDMY01$. (d) r_u sensor P2 x=6m y=-0.5m $PM3Sand$. (e) r_u sensor P3 x=0m y=-2.5m $PDMY01$. (f) r_u sensor P3 x=0m y=-2.5m $PM4Sand$. (g) r_u sensor P4 x=6m y=-2.5m $PDMY01$. (h) r_u sensor P4 x=6m y=-2.5m $PM4Sand$.

Taking a general overview at Figure 5.63, it can be concluded that the numerical model constructed with $PDMY01$ material is able to catch the trend of all the recorders received from the experiment. However, it is also observed that the accuracy of the outputs generated by *OpenSees* respect to the actual centrifuge test is different depending on the location of the record. This fact is different if the results received from $PM4Sand$ are studied. In this case, there are some locations at which the model is totally unable to match the curves from the experiment.

The curves corresponding to the sensor P4 in both numerical models, Figure 5.63g and h, are the most precise. Regarding $PDMY01$, higher values than the experimental results are observed during the period of strongest shaking, between 2 and 8 seconds, although the deviation of r_u is not larger than 0.3 points. The same happens if the plot of $PM4Sand$ is observed at the range 5 to 8 seconds. However, in the last case, the generation of pore water pressure is delayed respect to the experiment not registering any increment, or even decrement, from 0s to 5s. This behaviour is evidenced in all the recorders and it is one of the causes of the inaccuracies showed by $PM4Sand$ model.

The better accuracy at this location might be explained regarding the location of the recorders. This point is located at the free field where the disturbances generated by the structure have smaller effects. Moreover, it is usual to experience some inaccuracies when the outputs obtained are closer to the surface due to the limitations of the numerical models to simulate the sedimentation process occurring after liquefaction of saturated soils. However, this problem is less common at deeper layers like in this case.

As can be checked in the Figures 5.63e and 5.63g, the value of r_u obtained from the experiment at the location of the sensors P3 and P4 is virtually the same. Nevertheless, the curves generated by the numerical models differ each other. In the case of the recorders located at P3, the fluctuations of the value of r_u become more evident, being specially critical the case of $PM4Sand$ where a great dilation and contraction of the soil is experienced in a couple of seconds. Since the distance from the ground surface is the same in both cases, it is likely that the origin of these disturbances were due to the proximity to the structure.

Unlike the results received from the experiment at locations P3 and P4, important differences are observed between the outputs received from the locations P1 and P2. Although both are located at -0.5 m from the ground surface, the presence of the suction bucket avoid the liquefaction of the soil at the location P1, not being observed the same behaviour at the location of the sensor P2 where the value of $r_u = 1$ is reached between the second 7 and 14.

Regarding the trend of the r_u curve of the sensor P2, it can be observed how the numerical model constructed with $PDMY01$ material is able to replicate a similar behaviour, Figure 5.63c. Nonetheless, some deviations respect to the empirical results are observed during the strong shake phase, at the beginning of the simulation. The numerical model shows a dilative tendency that is not observed at the experiment and could not be corrected with any parameter combination. Besides, the permeability looks to be slightly higher in the numerical model after 20 second of shaking since the values of r_u are below the ones from the experiment.

However, the outputs received at the same location from $PM4Sand$ model are totally out of range. It looks that this numerical model is more sensitive to the fact of being closer to the surface so that it is not able to catch the trend of the experimental results at that depth.

Finally, the outputs received at the location of the sensor P1 are studied, see Figure 5.63a and b. In the case of $PDMY01$ model and in comparison with the rest of results, this curve is the one showing larger deviations respect to the experimental centrifuge test. The trend of the numerical model follows the same path than the experiment but great fluctuation of the value of r_u are observed which, as analyzed during the calibration process, only can be partially controlled by different parameter combinations.

The same is observed regarding the graph corresponding to $PM4Sand$ model, Figure 5.63b. Although the general trend of the experiment seems to be followed, important fluctuations of the value of r_u are observed, larger than in the case of $PDMY01$ model. Once again, similar to the curves of P3 and P4, dilative behaviour of the soil is experienced during the first 5 seconds, something that does not happen regarding the physical test.

The difficulties of the numerical model for fitting the experimental curve in the case of P1 might be related mainly with two events. On one hand, and already mentioned, the reason could be the proximity of this recorder to the ground surface. On the other hand, also observed at the recorder P3, see Figure 5.63e and 5.63f, the proximity of the structure makes larger these high and low peaks on the graph, specially, during the stage of the strongest shake, between the period of 2 and 8 seconds.

An important finding during the calibration process was that the correction of these fluctuations can be corrected by decreasing the masses of the structure and locating all the masses at the tip of the structure. This analysis is discussed in following sections.

5.3.2 Settlements

The value of the settlements is measured during the centrifuge reference test at the lid of the bucket as observed in Figure 3.1. For the same purpose, a recorder measuring the displacement along y is placed at the origin of coordinates, node x=0.0m y=0.0m in both numerical models, see Figures 4.4 and 4.5.

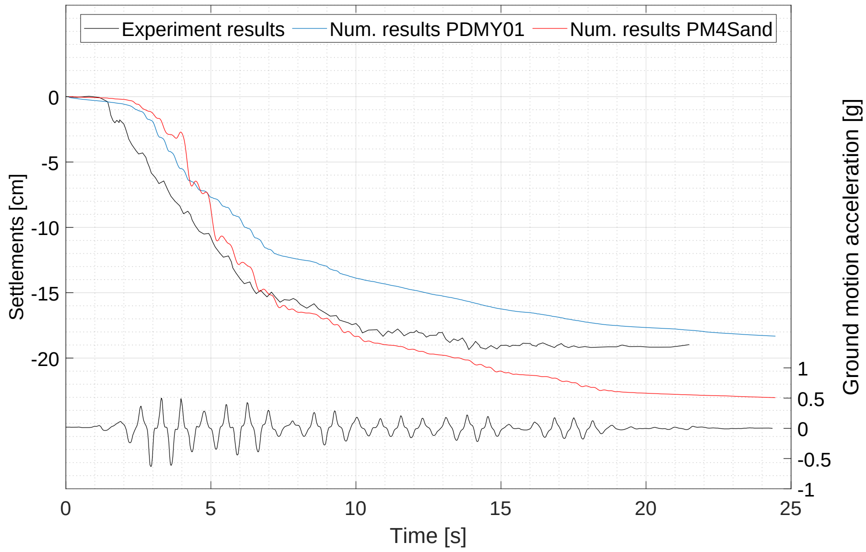

Figure 5.64. Comparison of settlements of the experiment with numerical results of $PDMY01$ and $PM4Sand$ models

If the results from the experiment are observed in Figure 5.64, it is noticed that the generation of settlements starts at the beginning of the shake and they stabilize after approximate 15 seconds. In the case of the numerical models, the settlement generation starts a few seconds later but the velocity of settling is approximately the same during the first 7 seconds for the case of $PDMY01$, being a little bit faster regarding the $PM4Sand$. After that point, both numerical curves seem to change the trend to a curve with less slope which in the case of $PM4Sand$, ends with a larger final value of vertical displacement.

In contrast to the experimental values, the numerical results do not reach a point of constant settlements but they continue being generated until the end of the shake although following a slower rate.

This fact can be explained regarding the limitation of the numerical models in general to simulate volumetric settlements. The first stage, from 0 to 10 seconds, when the settlements development is more critical, they are mainly caused by the shearing of the soil, an event that looks to be simulated properly by the virtual models. However, during the second stage, approximately after 10 seconds shaking, the type of settlements are mainly volumetric, whose simulation is not accurately carried by any available software. It has to be noted that in case of *PM4Sand*, the special command activating the reconsolidation strains, *PostShake*, in order to better simulate the development of the volumetric strains after strong shaking contributed to the overestimation of the settlements. During the process of calibration, more appropriate outputs were received with the adjustment of the secondary input parameters, but at the cost of the excess pore water pressure output. However, the delivered results in the report come as an suitable compromise in regard to the fitting curves.

5.3.3 Accelerations

As observed at the Figure 3.1, the nodal accelerations received from the experiment are located under the bucket, sensor A1, at the free field, sensor A2, and at the tip of the tower, sensor A3. The same locations are set at the numerical model for measuring the accelerations and comparing them with the experimental results.

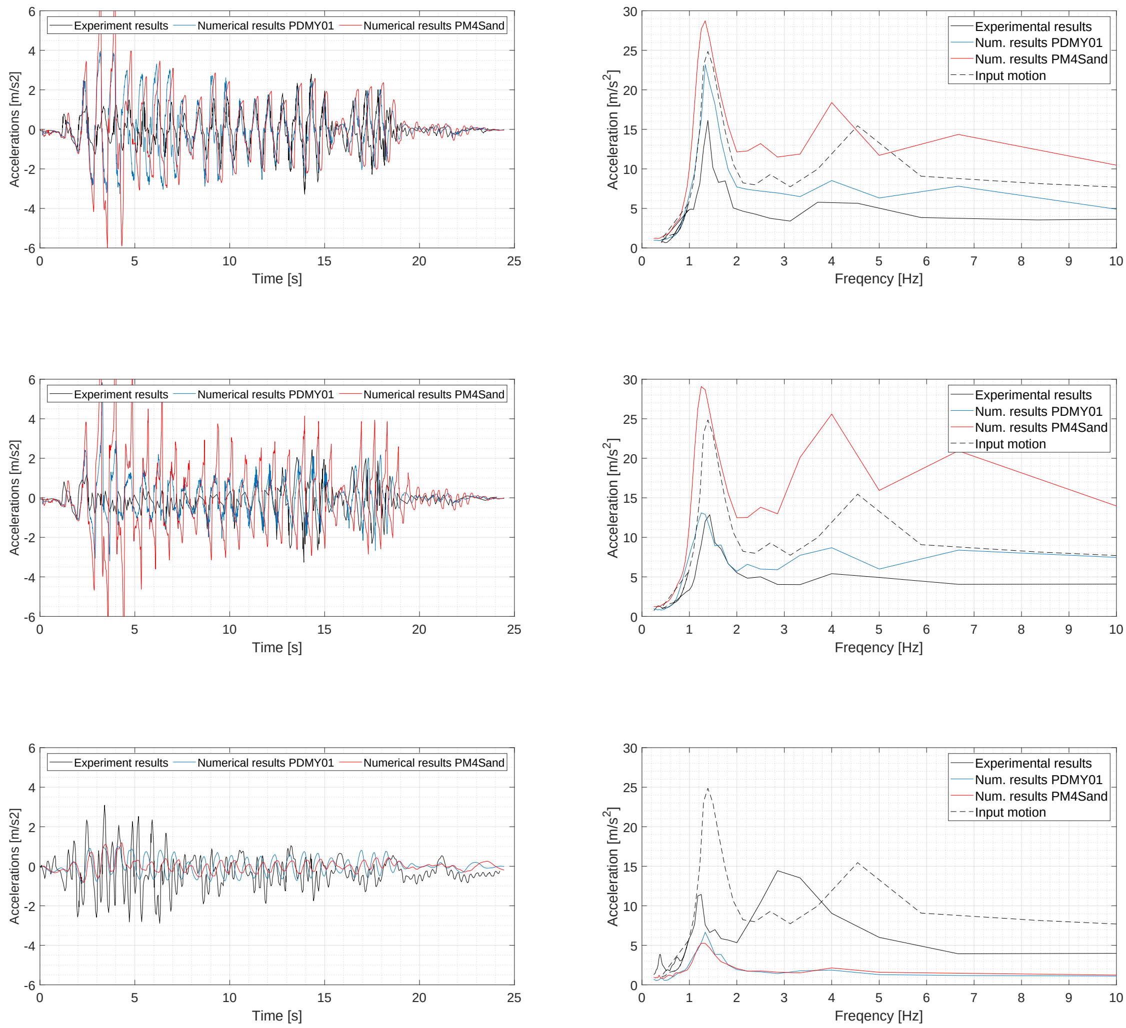

Figure 5.65. Comparison of nodal accelerations-time history and spectra accelerations of $PDMY01$ and $PM4Sand$ with experimental results, from left to right: (a) Nodal acceleration sensor A1 x=0m y=-0.5m $PDMY01$ and $PM4Sand$. (b) Spectral acceleration sensor A1 x=0m y=-0.5m $PDMY01$ and $PM4Sand$. (c) Nodal acceleration sensor A2 x=6m y=-0.5m $PDMY01$ and $PM4Sand$. (d) Spectral acceleration sensor A2 x=6m y=-0.5m $PDMY01$ and $PM4Sand$. (e) Nodal acceleration sensor A3 x=0m y=13m $PDMY01$ and $PM4Sand$. (f) Spectral acceleration sensor A3 x=0m y=13m $PDMY01$ and $PM4Sand$.

Analyzing the outputs received from the sensors A1 and A2 located within the soil domain in the case of $PDMY01$, Figures 5.65a and 5.65c, it is noticed that the model is able to catch perfectly the nodal accelerations after 10 seconds shaking. This fact is also reflected at the pore water pressure generation graph at the locations P1 and P2, where the fitting between experimental and numerical curves becomes more accurate after the same period of shaking, see Figures 5.63a and c. Nonetheless, larger records of acceleration are obtained before those 10 seconds, which might be the cause of the inaccuracies at the pore water pressure outputs before the mentioned period.

These inaccuracies become more evident in the case of $PM4Sand$ model which is able to catch precisely only the nodal accelerations at A1 after 10 second shaking, showing in the rest of the cases higher values in comparison with the experiment. The case of the curves received from the sensor A2 for this numerical model, located at the free field, needs to be specially mentioned. Figure 5.65c and Figure 5.65d show thus an important deviation respect to the outputs from the centrifuge test both regarding the nodal accelerations and the acceleration spectra. It is likely that these important inaccuracies were the cause of the difficulties for simulating also the generation of pore water pressure at this point, see Figure 5.63d. Nevertheless, any set of parameters tested has not been able to correct this problem, so it is concluded that further investigations are needed. It is important to point out again that the proximity of the sensor to the soil surface makes this task more complicated.

Regarding the spectral accelerations of these ground sensors, Figures 5.65b and 5.65d, it is observed that the same dominant frequencies than the experiment are obtained. However, the peak spectral accelerations of both numerical models measured by the recorder A1 are higher than the ones recorded empirically. As noticed during the calibration process, the influence of the variation of the input parameters for $PDMY01$ and $PM4Sand$ material is larger at the free field than under the bucket, presumably, due to the presence of the structure. Nevertheless, any of the tested set of parameters combinations cast better results. Thus, these larger peaks registered at A1 may be the principal reason provoking large fluctuations of the value of r_u at the recorders located at the vicinity of the structure, see Figures 5.63a,b,e and f.

Once again, it is noticeable the great amplification of the accelerations experienced at $PM4Sand$ numerical model by observing the spectral accelerations, see Figure 5.65d. In contrast to $PDMY01$, which is able to fit almost perfectly the experimental results, $PM4Sand$ casts values even larger than the induced input motion so it is evidenced one more time the issues of this constitutive model at that location.

As far as the values registered by the recorder of the numerical model and the sensor of the centrifuge experiment located at the position A3 are concerned, important deviations are observed in both numerical models. The nodal accelerations generated by the virtual simulations are much smaller than the outputs from the experiment in both cases, specially, during the first 8 second, see Figure 5.65e. This fact is also reflected at the spectral accelerations, see Figure 5.65f. The peaks registered are smaller than the one from the experiment at a frequency equal to 1.5 Hz. This comes as a cost of chosen modelling by placing all mass on the tip of the structure, which leads to the larger oscillations period.

However, this is not the only issue that can be noticed. As observed, the predominant frequency of the structure according to the experiment is located at a value of 3 Hz, being the mentioned peak at 1.5Hz just a local maximum. Nevertheless, this behaviour is not replicated by any of the numerical models since they are only showing a peak at the smaller frequency. Any changes in mass distribution or in the stiffness of the bucket or the tower tested were not able to solve this issue as evidenced in previous paragraphs.

Due to the lack of information about the characteristics of the structure at the reference document (Yu et al., 2014), the calibration of the recorder at A3 is totally carried by a trial and error process. Thus, the values of stiffness, distribution of masses and the magnitude of them are chosen prioritizing the best possible outputs regarding the generation of pore water pressure, Figure 5.63, and accelerations at the locations A1 and A2 since more data is available for the soil domain.

5.3.4 Stress Paths and Stress-Strains Relation

The closer look on the development of stress paths and stress-strain relation in the soil domain during the excitation are observed. The relation between mean effective and deviatoric stress and the relation between shear stress and shear strains are presented side by side graphically. Stress and strain components are recorded at Gauss points at an element level. The obtained values are then averaged between elements with mutual nodes of interest. The stresses and strains are recorded across particular points through depth in two specific areas in columns below the structure and the one in the free field.

The recorders are set at the same depth level for both areas, below the bucket structure and in the free-field. They all align with the points where recorders for excess pore water pressure and acceleration are set, P1, P2, P3, P4. The stresses and strains are recorded at depths of 0.5 (P1, P2), 1.0, 2.0, 2.5 (P3,P4), 3.0 and 4.0 meters. This can provide insight into model behaviour during the induced shaking and its response to it. First, the outputs below the structure regarding the *PDMY01* model are commented and thereafter comments on the free field are made.

PDMY

Below the structure

Examination of the stress paths below the bucket are mentioned first as illustrated on the Figure 5.66. The record obtained at the depth of 0.5 m shows an irregular pattern. It can be seen that the mean effective stresses degraded to some extent but that were far from zero. Observing the shear stress-shear strain relation, shear strains γ_{xy} developed quickly after initial shaking and accumulated at level of 0.1 % without further propagation. Shear stress τ_{xy} amplitude remained in the range of -20 to 20 kPa.

At depth of 1.0 m similar trend is noticed but with more regularity in the stress path pattern. Here as well, the degradation of mean effective stresses did not reach zero, meaning that liquefaction due to cyclic mobility did not occur. From the deviatoric stress-strain relation, it can be seen that the accumulation of shear strains ended at the level of 0.2 %, showing that soil 1 m under the bucket performed well.

Going deeper it can seen that, due to larger confinement, stress paths initiate at higher effective stresses. At depth of 2.0 and 2.5 m, degradation of effective confining stress reach value of approximately 20 kPa, avoiding liquefaction occurring. It seems that up to 2.5 m depth, skirt of the bucket is able to mitigate the larger generation of excess pore water pressure and liquefaction occurrence. Shear stress-strain relation at depth of 2.0 m illustrate the accumulation of shear strains in the negative part of the axis. They stabilize at the level of -1.0 % approximately.

At level of 2.5 m they propagate even further and after a few initial cycles they tend to stabilize in the range from -3 to -2 % and gradually regain in stiffness develops and the strains stabilize at level of -2.5 % approximately. With depth increase the accumulation of shear strains tends to increase with more noticeable strength loss during shaking as seen from the shear stress amplitude decrease. Moreover, after a few initial loading cycles strain-hardening occurs initially followed on by gradual strength degradation. Generally, after the degradation of the shear strength ends, in the later stages of the earthquake motion, the pattern of regain in shear strength manifests across all depth points. This can be seen as the amplitude of shear stress increases while the development of shear strain fixes to the specific range.

As proved, greater shearing occurs at larger depths. Regarding the stress paths, they develop in more regular manner at depths of 3.0 and 4.0 m. Stress paths evolve in a vertical pattern, indicating that the undrained condition is in act and the soil is experiencing more elastic properties at greater depths due to larger confinement. As the larger shearing occurs, the paths tend to bend shifting from contractive to dilative phase. Here for the change, it can be noticed that the strength loss reached really close to zero effective confinement compared to the stress paths at shallower points, ending in a more significant loss of confining pressure and liquefaction susceptible conditions. This effect could be due to interaction of the foundation structure and the surrounding soil. Due to the imposed ground motion, larger inertial effects induce rocking motion of the foundation to the surrounding soil. This leads to larger amounts of shear-induced strains.

As explained at Chapter 4, the model designed includes the whole structural weight as a lumped mass on top of the turbine tower. This could be a cause of inaccuracy as the inertial loads on the foundation are intensified with this kind of modelling. Regarding the shallower depths, it seems that bucket skirts mitigated this strength loss by providing higher confinement to the soil encased by the caisson. Generally, it can be noticed that according to the shear stress-strain relation and stress paths shown, the soil has a tendency toward contractive behaviour during stronger shaking motion. This judgement is deducted based on the pattern of the shear stress-strain which lacks any dilation peaks. Peaks occur at later stages due to regain in soil stiffness. Moreover, the lower friction and phase transformation angle contributes to such a behaviour, limiting the level of dilative response.

Free field column

Regarding the stress paths in the free-field, as shown on Figure 5.67 , some differences can be observed. The level of initial confinement is at the lower degree than below the bucket. This is due to the lack of confinement imposed by the structural presence. In terms of degradation of mean effective stresses, the loss of confining stress occurs at shallower depths and degrades to zero value, triggering the liquefaction occurrence.

With the depth increase, the level of confinement increases as well, so initial mean effective stresses are higher and the degradation of the confining pressure at 3.0 and 4.0 m depth do not approach zero value. Phase shift here is more noticeable. In terms of shear stress-strain relation, larger strains occur at shallower locations. Development of strains near the surface is followed by very low level shearing approximately ranging in 1 kPa amplitude. Shear strains accumulate alternatively in both sign directions.

With the depth increase, the accumulation tends to move toward the negative portion of axis.

Large shear strains accumulation remain until depth of 2.5 m whereafter decrease in shear strains accumulation is noticed, where at depth of 4 m reaches the lowest level in the column. At deeper levels, the shear stresses increase too. Similar pattern of regain in shear strength in later phases of earthquake motion is present here as well. After the strong shaking ends, a regaining in strength occurs with stabilization of the shear strain accumulation. Hereafter, it can be seen that the soil exhibits contractive behaviour in the free field, following the shape of the stress-strain. Generally, the trend toward strain-softening is observed after a few initial loading cycles, after which as stronger shaking ends regains in stiffness occurs as previously mentioned.

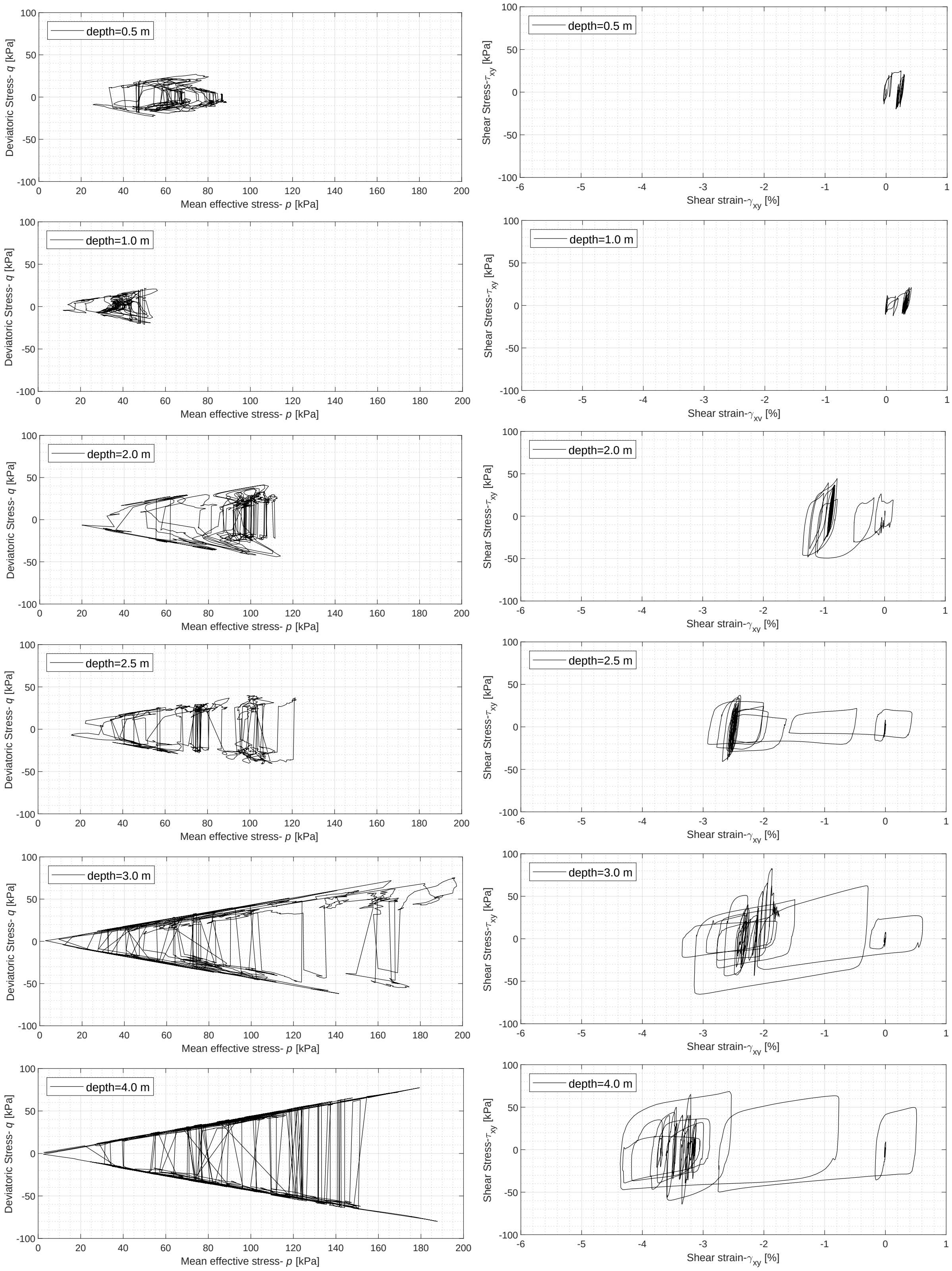

Figure 5.66. Stress paths and shear stress-shear strains relation recorded at nodes centered column below the bucket at depth of 0.5, 1.0, 2.0, 2.5 ,3.0 ,4.0 meter

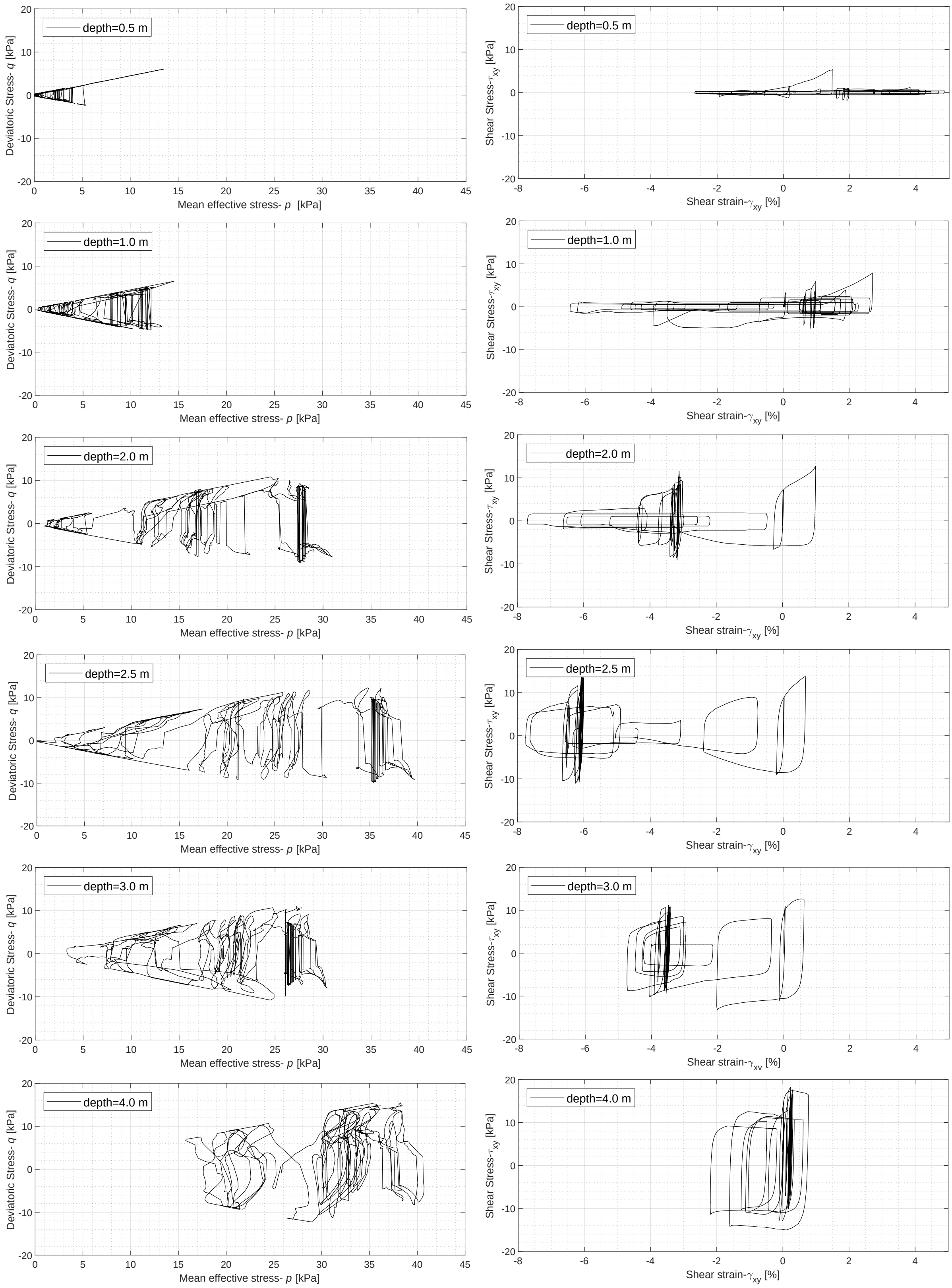

Figure 5.67. Stress paths and shear stress-shear strain relation recorded at nodes in free-field column at depth of 0.5, 1.0, 2.0, 2.5, 3.0, 4.0 meters

PM4Sand

Below the structure

In case of stress paths and strains following the *PM4Sand* constitutive model, the same order is applied, so the column below the bucket is mentioned first. At depth of 0.5 *m*, stress path follows the vertical pattern specific for the undrained condition. As loading progresses, stress path occurs in the limited range of shear stresses from approximately -10 to 10 *kPa* not reaching the critical state which can be seen at the lower level of accumulated shear strain, less than 1%. Stress path at this level initially diverge from the zero mean effective stress value, ending in a gain of effective confinement strength.

At the depth of 1 *m*, due to a bit higher magnitude in shear stress, the path slightly bended but nevertheless it remained at the approximately the same level of confinement and shear strain accumulation as for the depth of 0.5 *m*. Here is also noticed the trend with the initial divergence of effective confinement from zero value and convergence toward value of 80 *kPa*, after which stabilization of the confinement occurs at the level of approximately 50 *kPa*. Comparing to the shear stress-strain relation in *PDMY01* there is much resemblance in response of *PM4Sand* model. There is a distinction in the stress path response in the first two depth points, but the general conclusion is that at this stage overall both models showed similar response.

At depth of 2 *m*, after initial increase in effective confining pressure, a decrease in confinement unfolds, which after a few cycles ends in a progressive loss of mean effective confinement under a low level of shear stress magnitude. Looking at the shear stress-strain relation, initially a large shear stress develops leading toward greater strain evolution, which after a few initial cycles ends in stabilization ranging from -2 to 0.5 % under a low shear stress.

Similar trend is seen at depth point of 2.5 *m*, just that the confinement level increases due to the increase of the confining pressure with depth. Shear stress magnitude increases here as well, leading to a greater accumulation of shear strain, ranging from -3.5 to 2 %. This incide to the loss of effective confinement pressure and shear strength loss. At level of 3.0 *m*, initial confinement is larger, which prohibits the soil from loss of confinement and shear strength loss. Strain develops at higher values, ranging from -8 to 2%. The stabilization of strains ranges from -5 to -2% level. Again, the initial increase in shear led to an increase of effective confining stresses, after which gradual depression occurred which stopped at approximately 10 *kPa*.

Similar pattern is observed at depth of 4 *m*. Greater depth induced higher level of initial confinement which resisted strong shaking cycles, avoiding the total loss in confinement and shear strength. Although larger strain accumulation was recorded, this did not lead to a greater shear strength drop. It can be noticed that the model exhibited the initial gain in shear and effective confining strength which can be the reason of why the model did not reproduce the generation of the excess pore water pressure at early stage and responded more dilatively compared to the *PDMY01* and centrifuge test conducted by (Yu et al., 2014). Comparing the state of stresses and strains to ones reproduced by *PDMY01*, *PM4Sand* model shows better performance at greater depth, preventing the total loss of confinement at depth of 3.0 and 4.0 *m*. On the other hand, *PM4Sand* showed poorer performance at depth of 2.0 and 2.5 *m*. The shear strength loss at these two points is much bigger in case of *PM4Sand*. There is also a distinction in the stress ranges and level of strains but that could be prescribed to the difference between the two model outputs, since *PM4Sand* contains only two normal stress outputs, compared to the *PDMY01* which holds with three.

Free field column

When assessing the stress paths in the free field, the pattern developed resemble to the one shown in case of *PDMY01*. Loss in confinement occurs in the first two points near the surface. With the increase in depth, the initial effective confining pressure rises contributing to the increase in resistance to the liquefaction occurrence. Here is also noticed the trend toward an initial increase in confining and shear strength, followed by a sudden decrease.

Regarding the shear stress-strain relation in point P2(6,0.5) near the surface, large shear strains developed ranging from -6% to 2%, followed by the reduction in shear strength and effective confinement. At 1 m depth similar pattern is observed, just that the shear strains progressed to a greater amount until -14% leading toward strength loss and liquefaction. Going deeper, the limitation of shear strains accumulation is observable as a contribution of the higher initial effective stress. The progression limits to the level of -11% at depth of 2 m, then -10 % at 2.5 m and cease at level -6% and -4 % at levels of 3 m and 4 m. The pattern observed is expected and follows the similar trend seen in case of the model of *PDMY01*, except differences in the magnitudes of shear stresses and strains which can be explained due to the difference is stress outputs between two models, and difference in overall model performance.

Comparing the stress paths and shear stress-strain relation to the ones below the bucket at depth points of 2.0 and 2.5 m, it can be concluded that sudden strength loss that occurred below the bucket is not the result of the lower level of confinement since these points are not entrapped within the caisson skirts. At exact level in the free field, the soil is able to resist to the shear demand induced by strong shaking, which in case below the bucket is not the case. It could be that this drop in shear and effective strength is rather induced by the structural response and its mutual interaction with the soil caused by the inertial effects the structure is transferring to the surrounding ground which could lead to the strength loss. Modelling of the structure included all the lumped mass on top of the tower which could transfer bigger inertial forces on the foundation end, inducing larger rocking motions to the surrounding ground, the phenomenon is explained in the Section 2.2, see Figure 2.3c. Looking at the ranges of the shear stresses below the bucket, it can be seen that they are several-fold larger than the ones in the free field, validating the strong influence of the shearing near the structure. Also, when assessing the output of the recorder of excess pore water pressure P3, it can be seen that model response to the input motion leads to the liquefaction to occur, overreaching the threshold of the $r_u = 1$, thus, adding more credibility toward received results. Similar remarks was made for the case of *PDMY01* below the bucket but for the depths of 3.0 and 4.0 m.

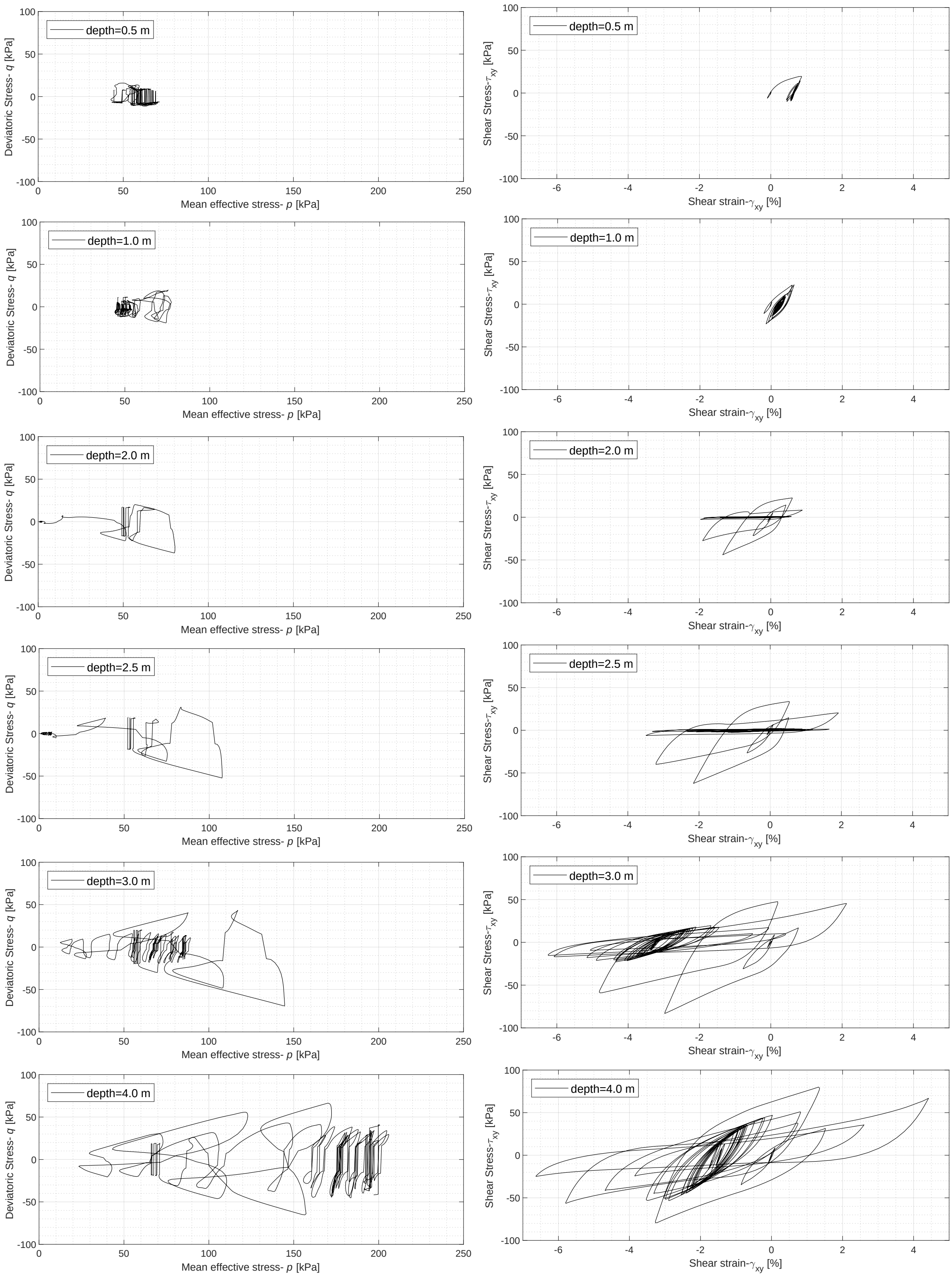

Figure 5.68. Stress paths and shear stress-shear strains relation recorded at nodes centered column below the bucket at depth of 0.5, 1.0, 2.0, 2.5 ,3.0 ,4.0 meter

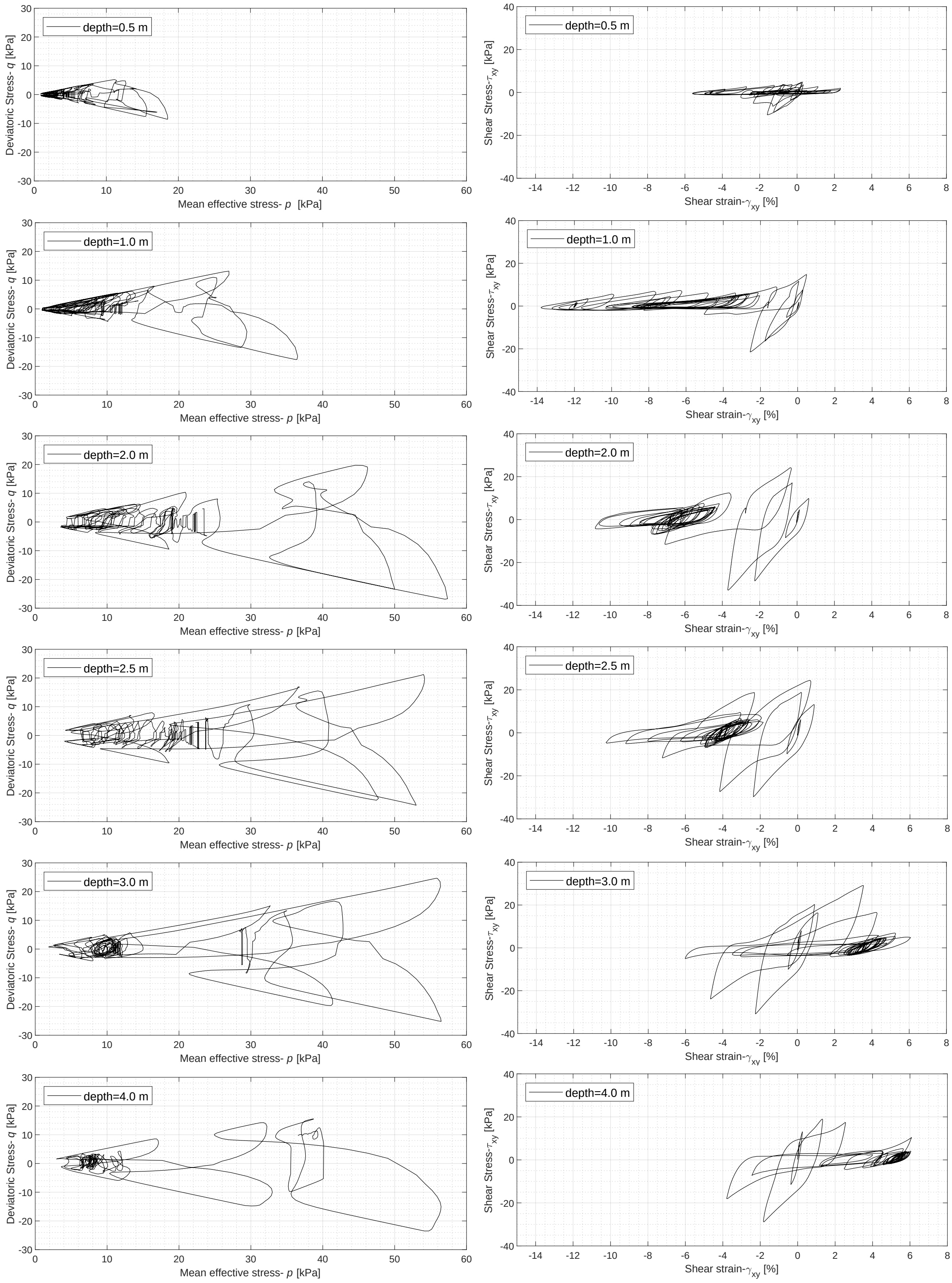

Figure 5.69. Stress paths and shear stress-shear strain relation recorded at nodes in free-field column at depth of 0.5, 1.0, 2.0, 2.5, 3.0, 4.0 meters

5.4 Comparison with lighter structure model and no structure model

Alternative models were tested during the calibration process with the intention of finding the source of errors of the final calibrated one. The main aspect taken into consideration in this section is to adjust the magnitude of the superstructure self-weight. for the two constitutive models studied ($PDMY01$ and $PM4Sand$).

Regarding $PDMY01$ constitutive model, the first alternative uses a lighter structure which counts with a lumped mass at the tip equivalent to 0.212 tons and a second mass of 0.374 tons at the foundation, concentrated at the node connecting the tower and the bucket, see Figure 5.70c. The second alternative tests the model without setting the structure, see Figure 5.70d. These two tests are compared with the final numerical model configuration shown at the Figure 5.70b and the experiment model presented the Figure 5.70a.

When it comes to $PM4Sand$ constitutive model, only one alternative model is tested, the one not considering the presence of the structure, Figure 5.70d.

In terms of providing a numerical model able to predict the performance of the actual centrifuge test presented in this report, both alternative models are not acceptable since they alter significantly the characteristics of the real prototype. However, as mentioned before, they are so useful for detecting the deviations of the final calibrated numerical simulations for both constitutive models tested.

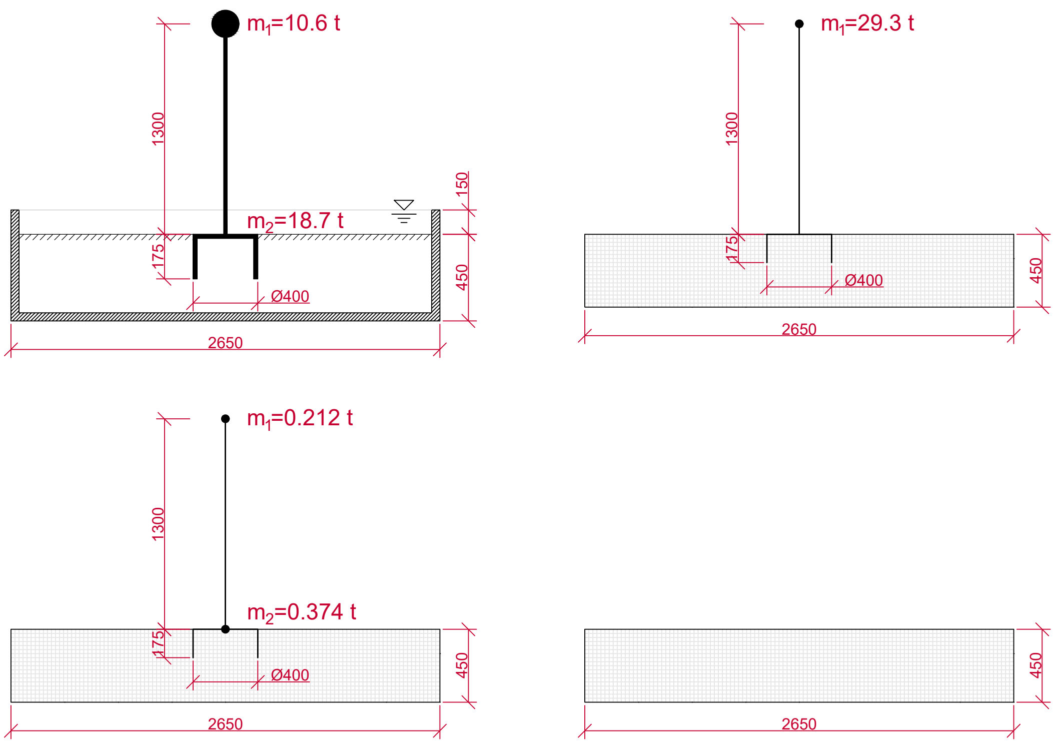

Figure 5.70. Alternative models tested, from left to right: (a)Prototype tested at laboratory (b) Calibrated final numerical model (c) Numerical model with lighter structure (d) Numerical model without structure

5.4.1 Pore water pressure ratio

PDMY01

Once again, the recorders from the sensors $P1$, $P2$, $P3$ and $P4$ of the experiment, located at the position indicated at Figure 3.1, are compared with the results obtained from the two numerical above mentioned alternative numerical models at the same locations.

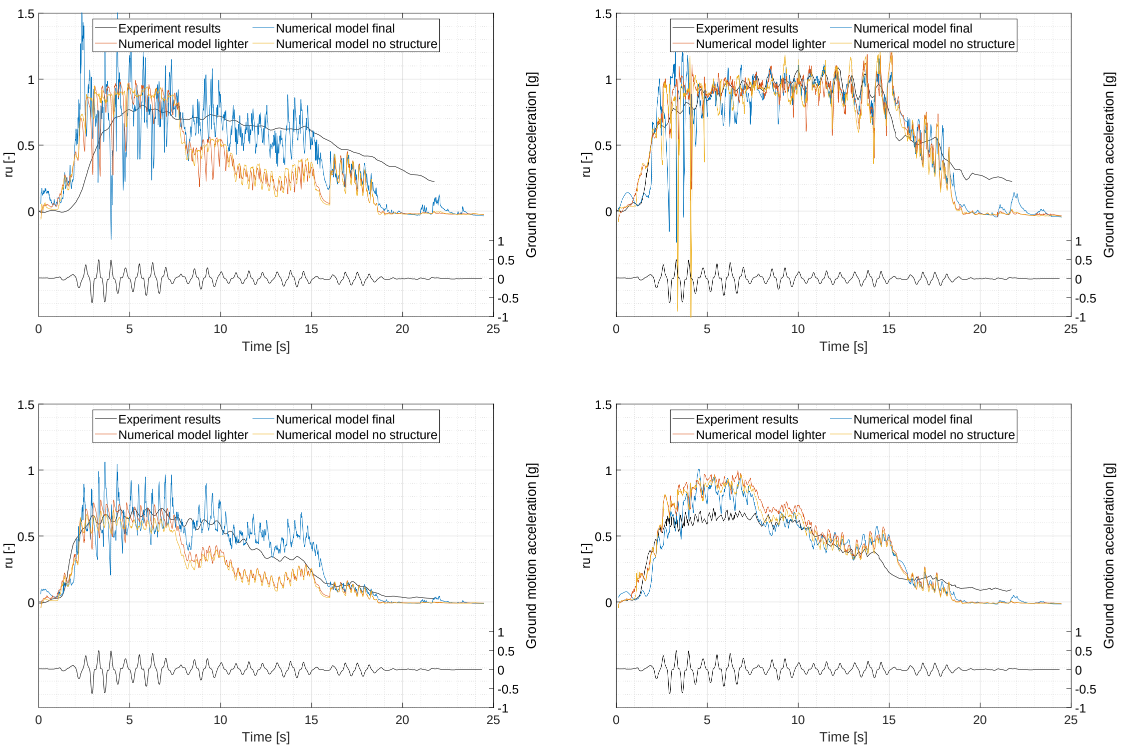

Figure 5.71. Pore water pressure ratio r_u time histories, from left to right: (a) Pore water pressure ratio sensor P1 x=0m y=-0.5m. (b) Pore water pressure ratio sensor P2 x=6m y=-0.5m. (c) Pore water pressure ratio sensor P3 x=0m y=-2.5m. (d) Pore water pressure ratio sensor P4 x=6m y=-2.5m.

Regarding the comparison between the results at the free-field, Figures 5.71b and d, it is observed that the curves in the three cases are virtually the same. Slightly higher fluctuations of r_u are observed in the graph corresponding to the final numerical model, especially during the first shaking. Also some extra dilation peaks are noticed in the model without structure at the sensor P2, however, after a couple of seconds, the trends of all curves join into a common path.

Nonetheless, the behaviours in the vicinity of the structure differ between the final considered model and the other two. At the locations P1 and P3, see Figures 5.71a and b, it is noticeable the increment of the fluctuations of r_u of the final model with respect to the models with lighter structure and no structure. Those fluctuations almost disappear when the weight of the structure is reduced or when the structure itself is totally removed. Thus, it can be concluded that the cause of the large fluctuations of r_u obtained close to the structure occurs as a consequence of the effects of mass on inertia of the structure.

Perhaps, one solution to this issue is to try to find an alternative connection between soil and structure instead of the current one which uses the command *equalDOF*. Nevertheless, any of the different tests carried out with the purpose of overcoming this problem succeeded.

Another observation of the recordings close to the structure is the different rate of dissipation of excess pore water pressure. As observed, the model considering the full masses of the structure keeps a higher value of r_u after the first shaking, which finishes after 8 seconds, being this excess of pore water pressure slowly dissipated. On the other hand, the model with reduced mass and the one without structure experience a larger drop after the first shaking. This behaviour is as expected since the presence of the bucket shall provide the mitigation of the immediate dissipation of the excess pore water pressure and more importantly the larger weight of the structure shall provide higher level of confinement contributing to the higher level of generations and thus slower rates of dissipation.

Thus, it seems that the larger shear forces of the structure in the case of the final calibrated numerical model contributes to a larger fluctuation of the excess pore water pressure, not observing this trend to the extent of the model without structure or with a lighter structure.

PM4Sand

As mentioned in the introduction paragraph of this section, $PM4Sand$ numerical model without the presence of the structure is conducted, with the main purpose of finding the possible source of error of the final calibrated numerical model. The outputs received from the 4 different sensors ($P1$, $P2$, $P3$ and $P4$) are shown in the Figure 5.72.

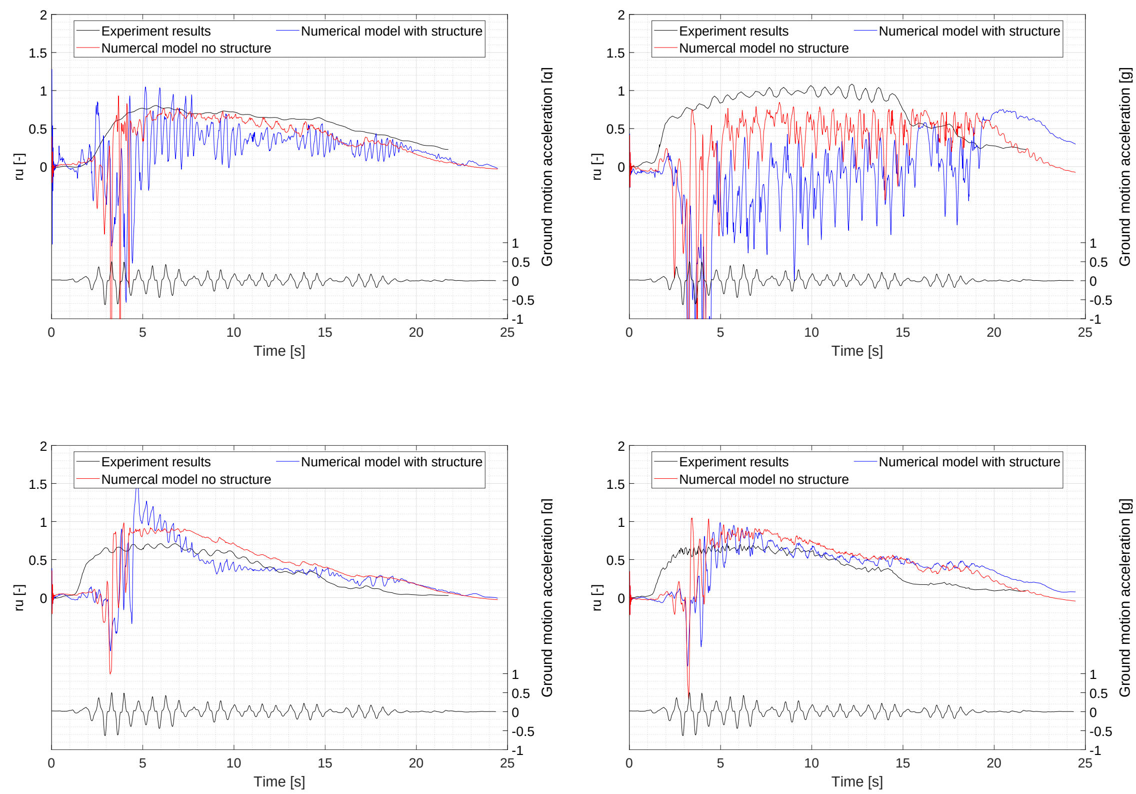

Figure 5.72. Pore water pressure ratio r_u-time histories, from left to right: (a) Pore water pressure ratio sensor P1 x=0m y=-0.5m. (b) Pore water pressure ratio sensor P2 x=6m y=-0.5m. (c) Pore water pressure ratio sensor P3 x=0m y=-2.5m. (d) Pore water pressure ratio sensor P4 x=6m y=-2.5m.

Regarding the sensors $P2$ and $P4$ located at the free field, the issue of predominant dilative soil responses in the first 4 seconds is witnessed in both cases of the considered numerical models. Thus, an important amount of negative pore water pressure is generated during the strong shaking of earthquake motion, specially in $P2$ located closer to the soil surface. However, after that period, the pattern trend of excess pore water pressure started to follow the trend of experimental results in the case of $P4$. Regarding $P2$, the deviations respect to the experiment are obvious but it is observed that the generation of negative pore water pressure is reduced significantly when the structure is removed.

Moreover, the generation of excess pore water pressure still shows , when the structure is removed, a few seconds delay compared with the experimental results at the beginning of the motion. The same issues are also captured in the sensors within and underneath the bucket as can be seen at the Figures 5.72a and 5.72c.

However, the consideration of $PM4Sand$ numerical model without structure brings out a significant affect on the noise problems in r_u curves. Taking an overview at the Figure 5.72, apparently, the alternative model shows outputs with smaller fluctuations. Thus, it can be concluded, as in the case of $PDMY01$, that the source of these fluctuations is the imprecise interaction between soil domain and superstructure. Consequently, in order to solve this problem, another method of simulating the interface between soil and structure need to be found out, alternative to the use of the command $equalDOF$.

5.4.2 Settlements

PDMY01

The settlements obtained at the experiment are compared with the ones from the numerical model and the other two alternative numerical models following the same procedure described in the previous section.

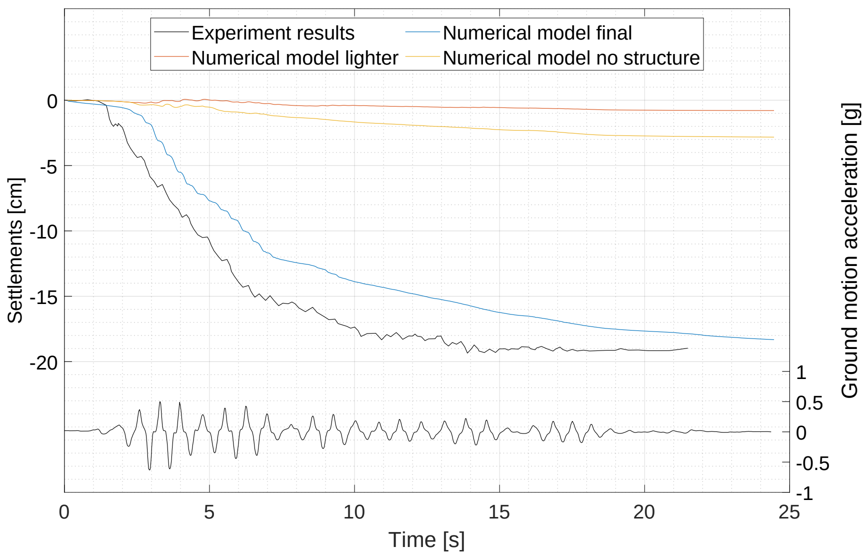

Figure 5.73. Calibrated values of settlements at the base of the tower, location x=0.0m y=0.0m

As expected, the settlements obtained from the model without structure and with a reduced value of masses do not fit the experimental results. The value of settlements is not only related with the self-weight of the structure but also with the inertia forces of the masses during the shaking process. If these masses are reduced, the value of settlements decreases drastically as can be observed at Figure 5.73 due to the reduction of shearing stresses. Thus, the conclusion is that settlements below the structure merely occur as a consequence of the deviatoric effects induced by soil-structure interaction.

Regarding the model without the structure, the type of settlements are hundred per cent volumetric due to the absence of any structural disturbance. The limitations of the numerical software to catch this kind of settlements are well known, so any extra conclusion can be done regarding this output.

PM4Sand

An identical process than the carried for $PDMY01$ is implemented for $PM4Sand$ numerical model. Thus, an alternative simulation without accounting for the structure is ran. The outputs received regarding the settlements are shown at Figure 5.74.

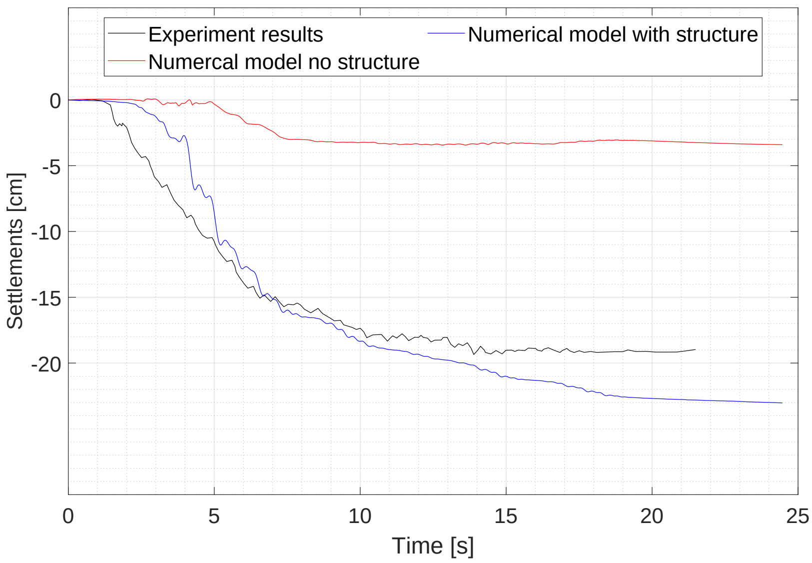

Figure 5.74. Calibrated values of settlements at the base of the tower, location x=0.0m y=0.0m

As expected, the settlement records decreased dramatically by removing the structure. The fact is that the settlement development is not only controlled by the contact pressure of the superstructure self-weight, but also significantly influenced by the inertia force of the masses during the applied shaking motion.

Theoretically, it means that the deformation of the soil domain after removing the superstructure is totally depended on the volumetric strains. However, as mentioned before, the numerical software counts with the limitation of not being capable of catching properly these volumetric deformations, so any further analysis or comparison is carried.

5.4.3 Accelerations

PDMY01

The outputs corresponding to the nodal and spectral accelerations at the locations A1, A2 and A3, see Figure 3.1, are compared with the physical centrifuge test and the three numerical models proposed in this section.

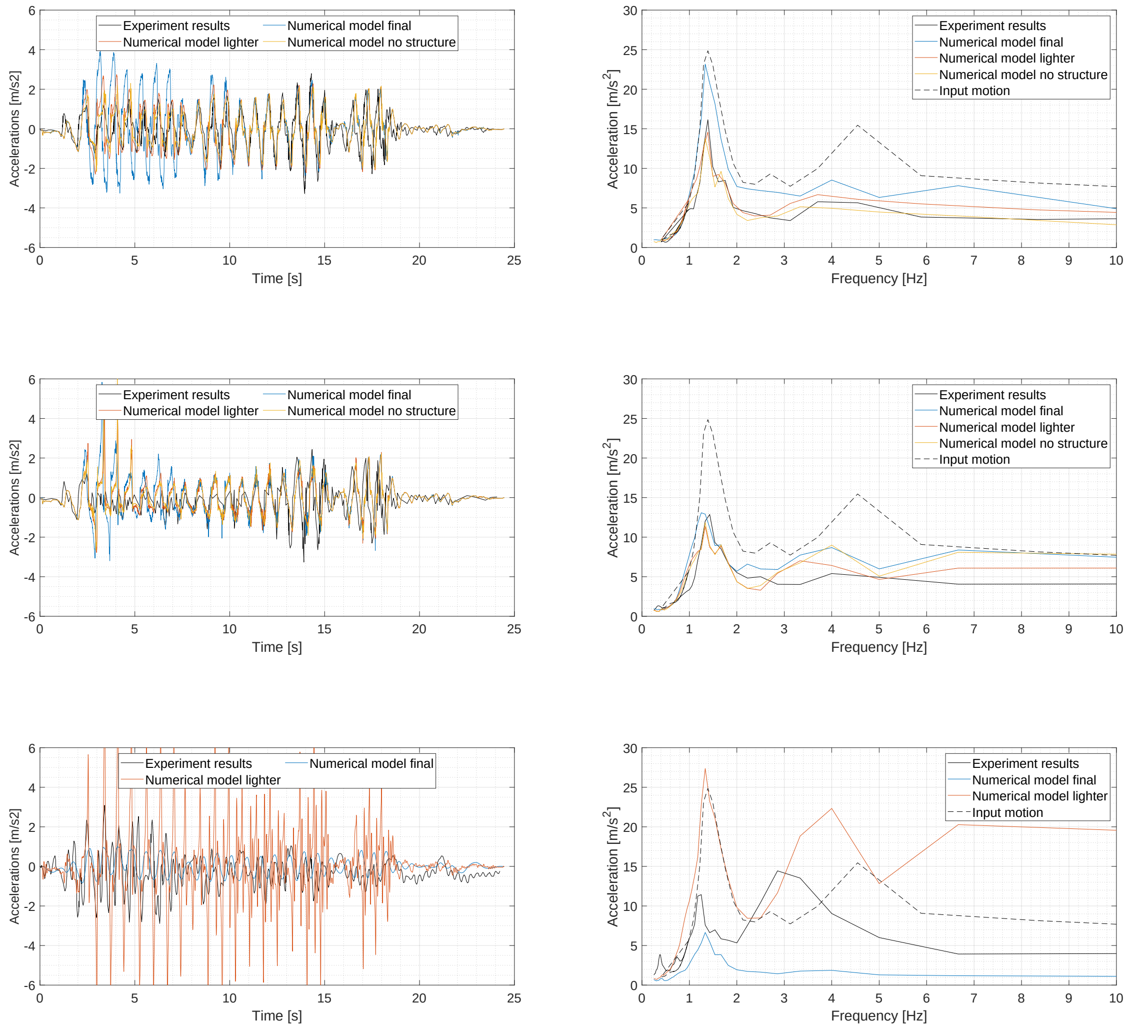

Figure 5.75. Nodal accelerations and acceleration spectra, from left to right: (a) Acceleration sensor A1 x=0m y=-0.5m. (b) Spectral acceleration sensor A1 x=0m y=-0.5m. (c) Acceleration sensor A2 x=6m y=-0.5m. (d) Spectral acceleration sensor A2 x=6m y=-0.5m. (e) Acceleration sensor A3 x=0m y=13m. (f) Spectral acceleration sensor A3 x=0m y=13m.

Firstly, if the Figure 5.76 d is observed, it can be checked that the nodal spectral accelerations of the three numerical models match with the experimental results in the free field. Thus, it can be concluded that any disturbance from the structure is not registered in this point since the model which does not include the wind turbine prototype follows the same trend than the rest.

However, the scenario is different if the outputs of $A1$ are regarded, Figures 5.76a and b. As observed, the numerical model free of structure and the one with lighter structure match with the experimental results obtained within the bucket foundation. Nevertheless, when the same masses of the experimental test are implemented to the numerical model, the nodal accelerations during the first shake, and the peak acceleration spectra increases. As observed at Section 5.1.4, some parameters like permeability, phase angle or contraction parameter are able to decrease this peak but the outputs from the pore water pressure generation would be less accurate.

On the other hand, as far as the accelerations at the tip of the tower are concerned, see Figures 5.76e and f, the high influence of the masses of the tower considered is observed. When the structure becomes lighter, the accelerations increase dramatically due to the increment of the vibration frequencies of the structure. This fact makes the spectral accelerations to match with the input motion so that an important amplification of the dynamic forces is observed. This is one of the main reasons behind modelling the total structural mass as the lumped mass at the tip of the tower. By adding a slight increment to the mass of the structure, the structural response triggers large amounts of noise in the acceleration record as well as in the ones of excess pore water pressure.

Another interesting feature observed when the masses are reduced is the appearance of a second mode of vibration at 4 Hz. This second mode is also observed at the experimental results but does not appear when the masses of the structure are increased, neither when the masses of the final numerical model are distributed following the guidelines of the experiment, i.e. considering a lumped mass of 10.6 tons at the tip and a mass of 18.7 tons at the foundation, see Figures 5.28 and 5.29.

PM4Sand

The same procedure followed during the last section is carried for $PM4Sand$ model. Therefore, the comparison between the alternative model, the calibrated numerical model and the experiment is shown regarding the accelerations. Specifically, the outputs from the sensors A1 and A2 are analyzed, with the main purpose of getting visually precise evaluation, as shown in the Figure 5.76.

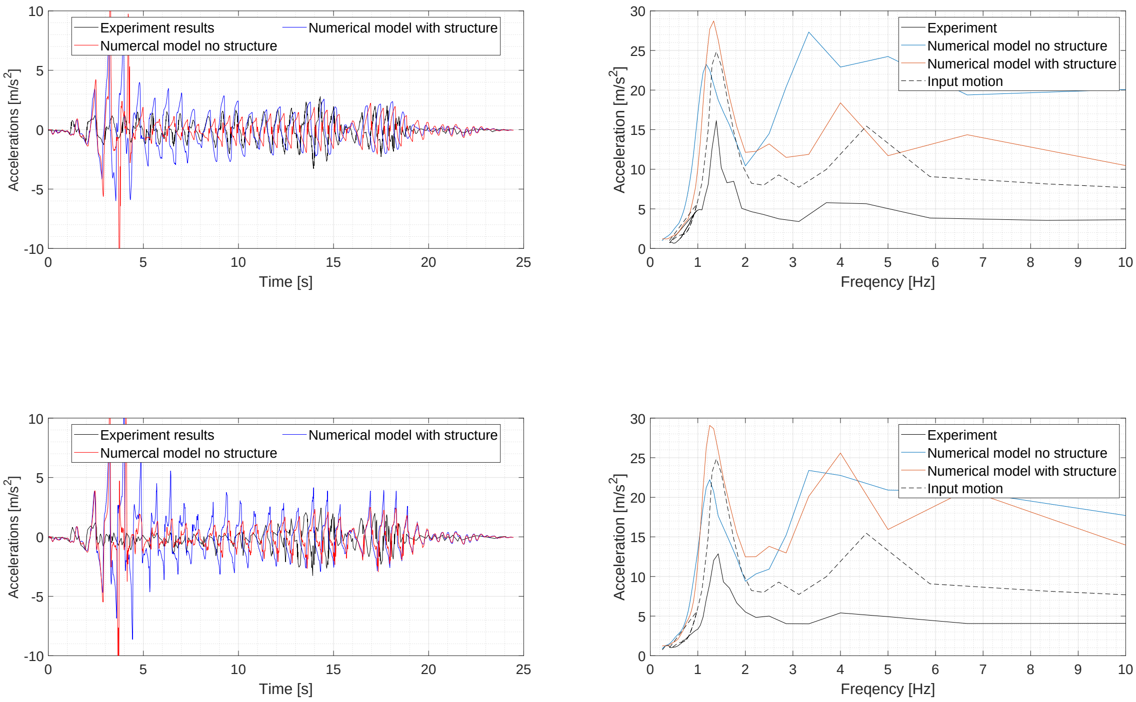

Figure 5.76. Nodal accelerations and acceleration spectra, from left to right: (a) Acceleration sensor A1 x=0m y=-0.5m. (b) Spectral acceleration sensor A1 x=0m y=-0.5m. (c) Acceleration sensor A2 x=6m y=-0.5m. (d) Spectral acceleration sensor A2 x=6m y=-0.5m.

Regarding the sensor $A1$ under the bucket, after removing the structure, the peak ground accelerations during the first 4 seconds are even larger than the ones from the numerical model with structure. Thus, the soil domain at this specific point without the presence of the contact pressure of the superstructure amplifies the accelerations more than the model with the structure during this first stage.

However, during the rest of the dynamic event, it is observed that the soil stiffness of numerical model with structure is higher than the alternative one, likely, due to the confinement phenomenon in the soil domain and the capacity of the bucket for controlling the generation of pore water pressure. Thus, the peak accelerations of the blue curve remain higher than the red curve, as the figure 5.76a.

When it comes to the spectral accelerations of sensor A1 observed at the Figure 5.76b, the value of the accelerations at the predominant frequency is higher in the case of the model with structure. However, different values of predominant frequencies are observed in both cases. Thus, when the structure is accounted the value of the predominant frequency is around 1.3 Hz, while the highest peak of the spectral accelerations without the presence of the structure occurs at the value of frequency of around 3.5 Hz.

In both cases the values of spectral accelerations at the position of A1 are greatly amplified and, as observed, the presence of the structure is not the reason. Thus, it can be concluded that the soil parameters need to be adjusted for overcoming this issue.

As regards the sensor in the free field $A2$, a similar trend pattern of acceleration as A1 is witnessed, see Figure 5.76c. Thus, it is noticed that the superstructure simulation not only brings out affect on the vicinity of the suction bucket, but also has some influence in the free field of the soil domain.

Interestingly, more clear evidence can be obtained by taking a look at the response spectra of the soil at the free field, see Figure 5.76d. Although more similar than in the case of the recorders under the bucket, see Figure 5.76b, the spectral accelerations of the model with and without structure at the free field do not match each other. Therefore, it is concluded that the structure is still having some influence on the recorders located at the free field.

This fact is not observed in the case of the model constructed in $PDMY01$, see Figure 5.76d, where the response spectra of all models match at the free field. The main difference between the models constructed using $PDMY01$ and $PM4Sand$ is the element size. Thus, it can be concluded that, probably, a refinement of the mesh might overcome this issue.

Numerical predictions 6

Once the numerical model is calibrated according to the parameters shown in the previous chapter, it can be used for predicting the outputs received from performances under different inputs conditions. Thus, in the current section, the characteristics of the structure of the original model as well as the input motion implemented are modified and the results obtained analyzed with the mentioned intention.

6.1 Influence of the characteristics of the structure

The numerical model is calibrated according to the outputs received from the *Test 1* showed at the Table 3.1 since values from all the recorders are available. Nonetheless, some other tests, named *Test 2*, *Test 3* and *Test 4*, with different features of the structure are presented on the same table whose outputs are partially showed, see (Yu et al., 2014).

In the current section, those extra tests are also constructed numerically, following the same process and characteristics presented at the Chapter 4. The features of each of them are shown at Table 6.1 and Figure 6.1. They are constructed for simulating as similar as possible the ones tested physically whose attributes are gathered at Table 3.1. The outputs obtained are compared each other and with the experimental results, if they are available, in order to study the influence of the new characteristics of the structure on the performance of these models.

Due to the limited time, all the extra numerical simulations explained are carried by the use of the constitutive model *PDMY01* since the computation time is shorter than in the case of $PM4Sand$.

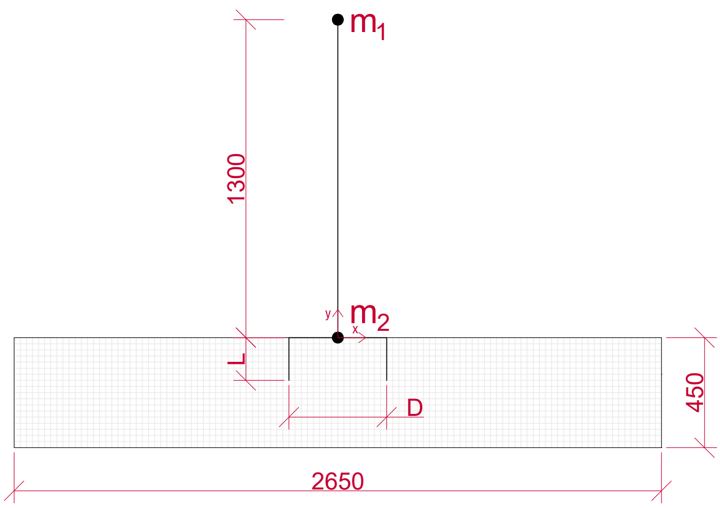

Figure 6.1. Configuration of the four extra numerical models studied

	Diameter D [m]	Skirt length L [m]	Mass foundation m_2 [ton]	Mass tower m_1 [ton]
Test 1	4	1.75	0.0	29.3
Test 2	6	1.75	0.0	29.3
Test 3	4	2.5	0.0	29.3
Test 4	4	1.75	0.0	38.8

Table 6.1. Parameters of the structure of additional numerical models

6.1.1 Settlements

The values of the settlements obtained during the centrifuge tests from the $LDVT_1$, see the Figure 3.1, are compared with the outputs corresponding to the vertical displacements of the structure at the connection of the tower with the foundation of the numerical models presented above, location x=0 y=0 of the Figure 6.1.

In the case of the settlements, the outputs of the four tests are available at (Yu et al., 2014), so that they can be compared with the ones obtained after the virtual simulations.

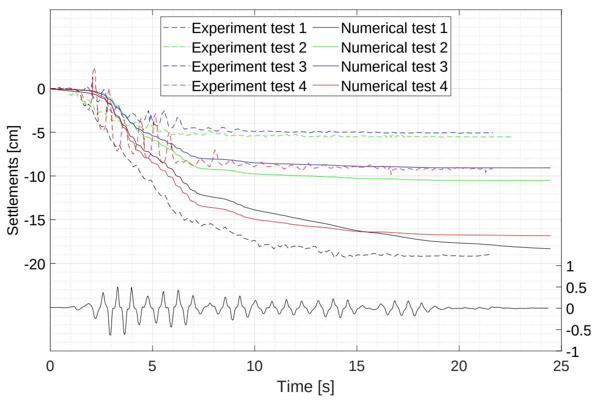

Figure 6.2. Comparison of settlements time history between experiment and numerical model for the four different tests performed

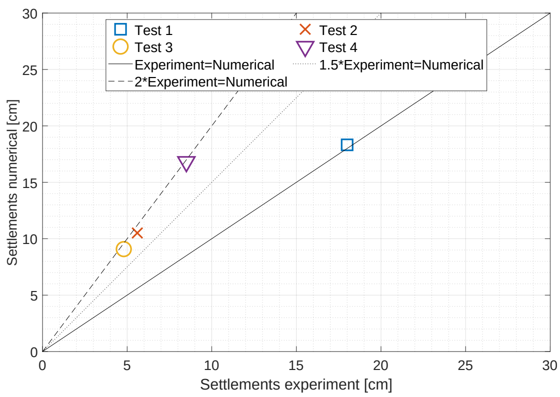

Figure 6.3. Comparison of total settlements between experiment and numerical model for the four different tests performed

	Sett. experiment [cm]	Sett. numerical [cm]	Deviation [%]
Test 1	18.00	18.32	+ 1.77 %
Test 2	5.60	10.51	+ 87.68 %
Test 3	4.80	9.08	+ 89.17 %
Test 4	8.50	16.82	+ 97.89 %

Table 6.2. Total amount of settlements and deviation between experiment and numerical models for the four tests performed

The general conclusion about the results obtained from the numerical models is that, as well as in the case of the experiment, any of the three modifications implemented to the structure, i.e., increasing the diameter of the bucket, increasing the length of the skirt of the bucket or increasing the mass of the foundation, supposes an improvement on the behaviour of the prototype in terms of settlements since the values become smaller, see the Figure 6.2.

Although the enlarging of the diameter of the suction bucket supposes a smaller vertical effective pressure induced by the structure at the $Test$ 2, the volume of soil confined is increased so that the stiffness of a larger area of the material is improved. The ability of this soil for resisting liquefaction is also increased so that a smaller value of induced settlements is expected. The same finding is achieved by (Wang et al., 2017) and (Yu et al., 2014). Moreover, according to (Dashti, Bray, Pestana, Riemer and Wilson, 2010), increasing the foundation width contributes to increase in drainage path, which mitigates the significant accumulation of volumetric strains due to dissipation and limits the influence of the *SSI*.

As far as the $Test$ 3 is concerned, in which the length of the skirt is augmented, also an important improvement of the value of the settlements is observed. One of the reason, also proved by (T.Olalo et al., 2016) and (Yu et al., 2014), is the increment of the friction between the soil and the structure. However, this feature is not accurately implemented to the numerical model, so probably the explanation is more related with the capacity of the bucket for minimizing the shear-induced displacements and volumetric strains due to the partial drainage during shaking. The water barrier induced by the bucket may reduce the shear stresses transmitted to the structure, reducing therefore the tendency for ratcheting. This improvement was also proved by (Dashti, D.Bray, M.Pestana, Riemer and Wilson, 2010) by the analysis of settlements in buildings, although it is also proved there that these mitigation techniques may induced a larger tilting of the structure.

Checking the values of the vertical displacements after increasing the contact pressure of the structure, $Test$ 4, an important improvement is observed in the case of the physically performed centrifuge test due to an improvement of the confinement of the soil under the bucket and the drastic reduction of the overturning moment of the structure induced by the lumped mass at the top (Yu et al., 2014). Nevertheless, this better performance is negligible in the case of the numerical simulation since the increment of the contact pressure of the structure is carried out by increasing the value of the mass at the tip of the tower. This procedure is followed with the aim of reducing the fluctuation of r_u at the recorders under the bucket, see the figures 5.30 and 5.31.

Despite of all the improvements observed, a considerable deviation between the experimental and the numerical outputs is noticed except for the $Test$ 1 as can be observed at the Figure 6.3 and Table 6.2. The reason that might explain that smaller deviation of the $Test$ 1 is that the calibration process has been carried according to the outputs received for that test, see Chapter 5, so that all the soil parameters are carefully adjusted.

Another key factor explaining the larger value of settlements in all the tests simulated numerically is the large fluctuations of r_u registered in all the cases under the bucket, location of the sensor P1, see Figure 6.4. As observed, liquefaction is triggered in all the tests in contrast to the experimental models, a fact that increases the strains of the soil due to more important looses of partial bearing failure.

6.1.2 Generation of excess pore water pressure

Once again, the generation of excess pore water pressure at the locations of the sensors P1, P2, P3 and P4, see Figure 3.1, is compared with the outputs obtained at the same locations of the four models presented in the current section.

The only outputs available regarding the generation of pore water pressure are the ones corresponding to the *Test* 1, for the four mentioned sensors, and for the *Test* 2, *Test* 3 and *Test* 4 for the location of the sensor P1.

Although the results obtained at the sensor location P1 are not quite accurate even after the calibration process due to its position close to the surface and inside the bucket, see the figure 5.63a, the curves corresponding to the four different tests are going to be compared to the ones from the experiment since some findings can be discussed.

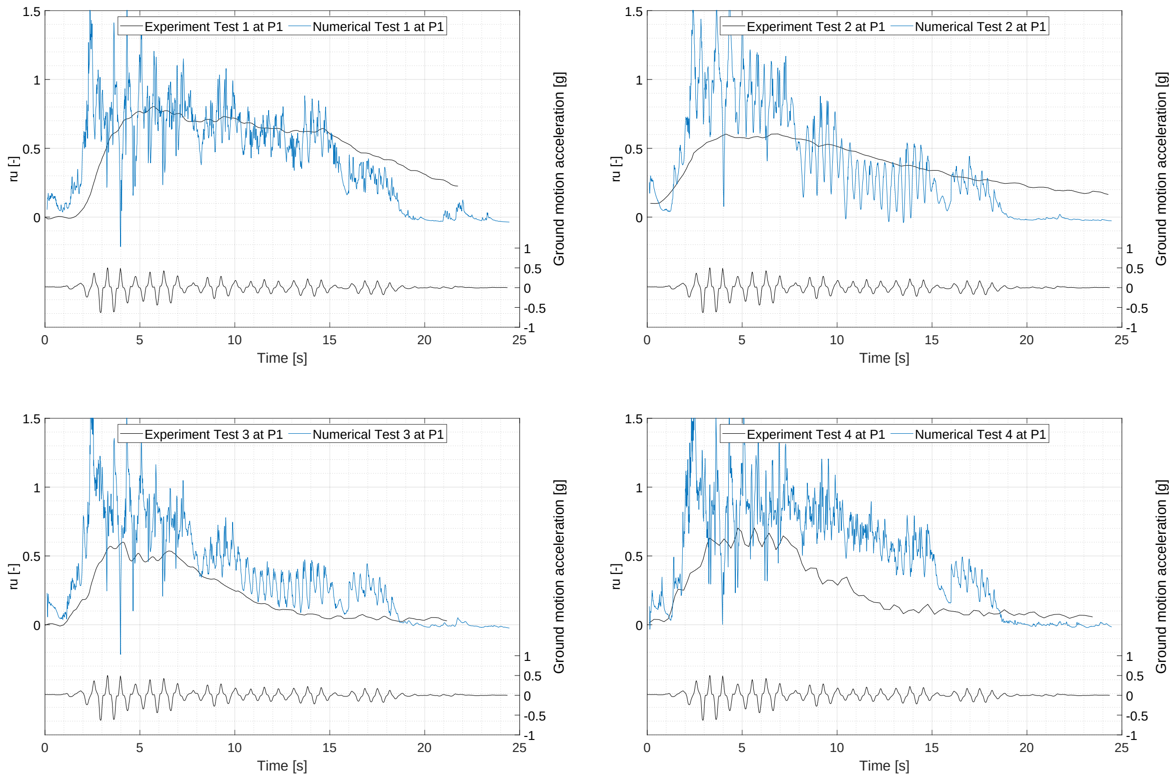

Figure 6.4. Comparison pore water pressure ratio at location P1 with experimental results, from left to right: (a) Pore water pressure ratio sensor P1 Test 1 (b) Pore water pressure ratio sensor P1 Test 2 (c) Pore water pressure ratio sensor P1 Test 3 (d) Pore water pressure ratio sensor P1 Test 4

The same issue observed after the calibration process of *Test* 1 is once again experienced in the results received from *Test* 2, *Test* 3 and *Test* 4. The modification of the characteristics of the structure do not avoid the recording of important fluctuations of the value of r_u, specially during the first 7 seconds, when the largest shake occurs. However, relevant conclusions are observed despite of these fluctuations.

For instance, when the diameter of the bucket, Figure 6.4b, or the length of the skirt, the Figure 6.4c, are increased, an important drop of the general trend of the curves is observed after the first 7 second shaking. Both mitigation techniques are effective since the reinforced area under the bucket is reduced in both cases, so the generation of pore water pressure is significantly reduced (Yu et al., 2014).

Nonetheless, this tendency is not observed at the *Test* 4, see the figure 6.4d. Once again, the reason might be because of the different distribution of masses between the numerical and the experimental model. When the weight of the foundation is increased, the overturning moment of the structure is drastically mitigated, which reduce the dynamic response of the tower (Yu et al., 2014). However, if the masses at the tip of the tower are increased, the model is contributing to the increment of the mentioned overturning moment, even though the enlarging of the confinement pressure is having a positive contribution.

This mentioned improvements are more easily noticed when the outputs at the location P1 from the four mentioned tests are plotted together in the same graph, see Figure 6.5a.

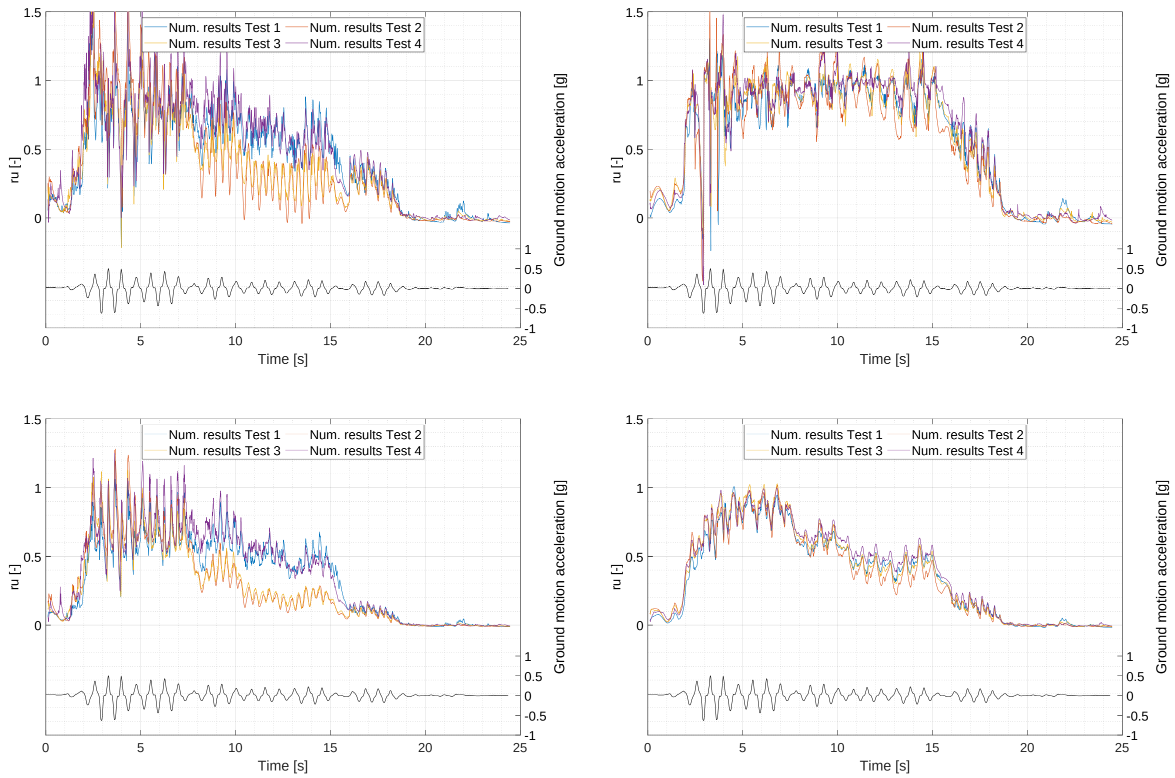

Figure 6.5. Comparison pore water pressure ratio for different values of skirt length, diameter of the bucket foundation and weight of the structure, from left to right:(a) Pore water pressure ratio sensor P1 x=0m y=-0.5m. (b) Pore water pressure ratio sensor P2 x=6m y=-0.5m. (c) Pore water pressure ratio sensor P3 x=0m y=-2.5m. (d) Pore water pressure ratio sensor P4 x=6m y=-2.5m.

Taking a look at the figures comparing the development of r_u at the position of the four sensors, see the Figure 6.5, it is noticed that the influence of the modification of the structure are mostly noticed at the recorders in the bucket and under the bucket, positions P1 and P3, so that P3 and P4 remain virtually unaltered.

This lower generation of pore water pressure near to the foundation after running the $Test$ 2 and $Test$ 3 is likely the cause of smaller vertical displacements of the structure as seen in the Figure 6.2.

The increment of the skirt length leads to a reduction of the tilting during the dynamic events and also to the confinement of a larger volume of soil (T.Olalo et al., 2016), so a mitigation of the peak levels of r_u-time history is expected. The same consequences has the increasing of the diameter of the bucket, so a similar improvement is experienced (Yu et al., 2014).

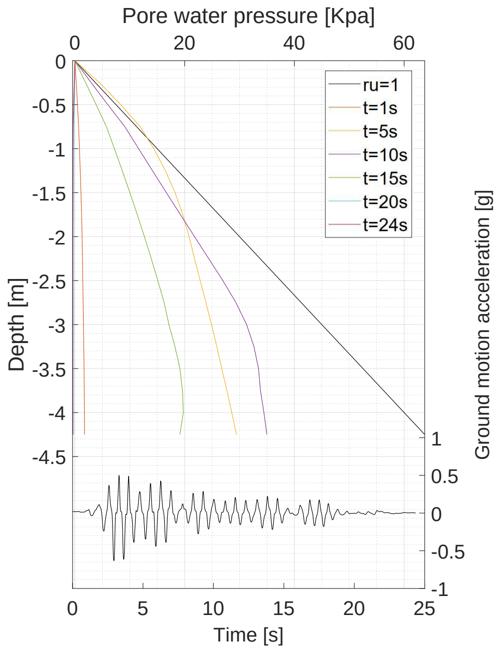

Figure 6.6. Test1-Representative isochronous excess pore water pressure with respect to depth.

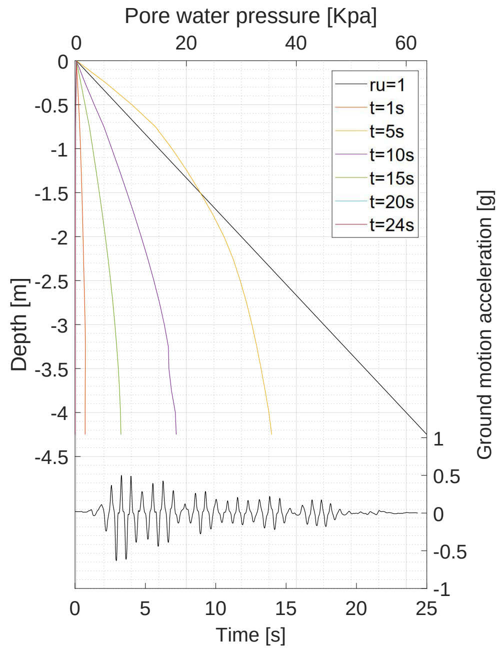

Figure 6.7. Test2-Representative isochronous excess pore water pressure with respect to depth.

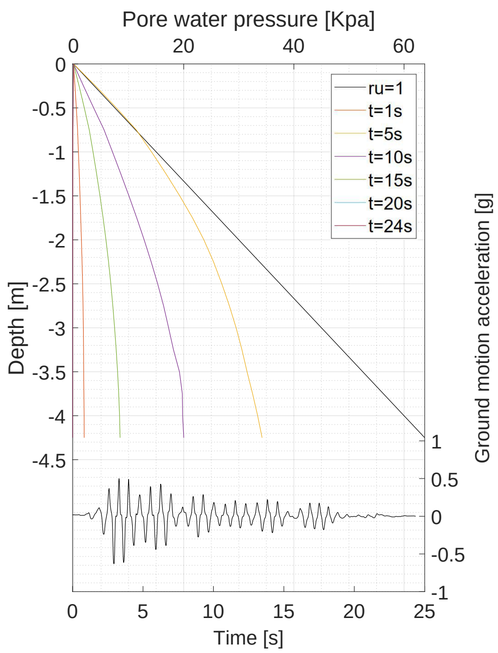

Figure 6.8. Test3-Representative isochronous excess pore water pressure with respect to depth.

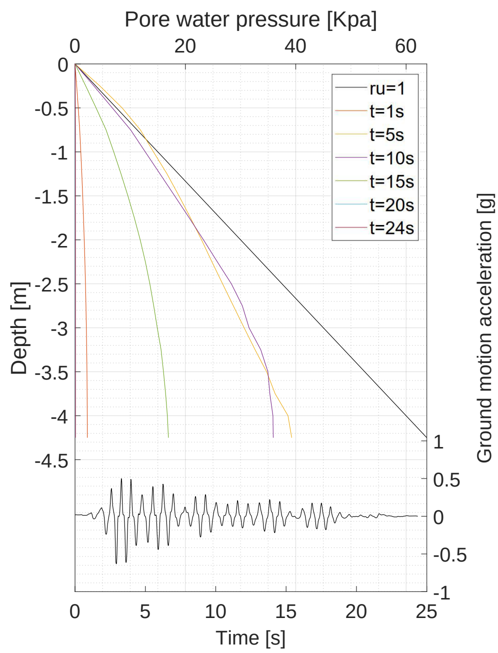

Figure 6.9. Test4-Representative isochronous excess pore water pressure with respect to depth.

The same trend observed at the recorders of pore water pressure ratio r_u inside and underneath the bucket, Figure 6.5a and c, is obtained when the isochronous curves of pore water pressure are plotted at different depths at the point x=0. Thus, as observed at the Figures 6.7 and 6.8 the level of pore water pressure after 10 seconds during the $Test$ 2 and $Test$ 3 is lower than the one measured during the $Test$ 1 and $Test$ 4, Figures 6.6 and 6.9, where the pore water pressure does not dissipate or is even larger.

Expectedly, the pore water pressure curves are further from $r_u = 1$ at deeper layers. However, according to the four numerical models presented in this section, liquefaction is occurring in all the tests approximately within the first meter depth. Nevertheless, this fact might not be totally accurate since the large fluctuations of r_u experienced in all the numerical models at shallow locations are creating high unreal peaks.

6.1.3 Accelerations

Both the nodal and the spectral accelerations obtained from the four numerical tests presented in this section are compared with the outputs from the experiment. Regarding the experimental results available at (Yu et al., 2014), only the nodal accelerations at the location A3 are presented on that research, see Figure 3.1, so only this comparison can be carried. Nevertheless, all the remain outputs cast by the numerical models at the locations A1 and A2 are also shown in this section.

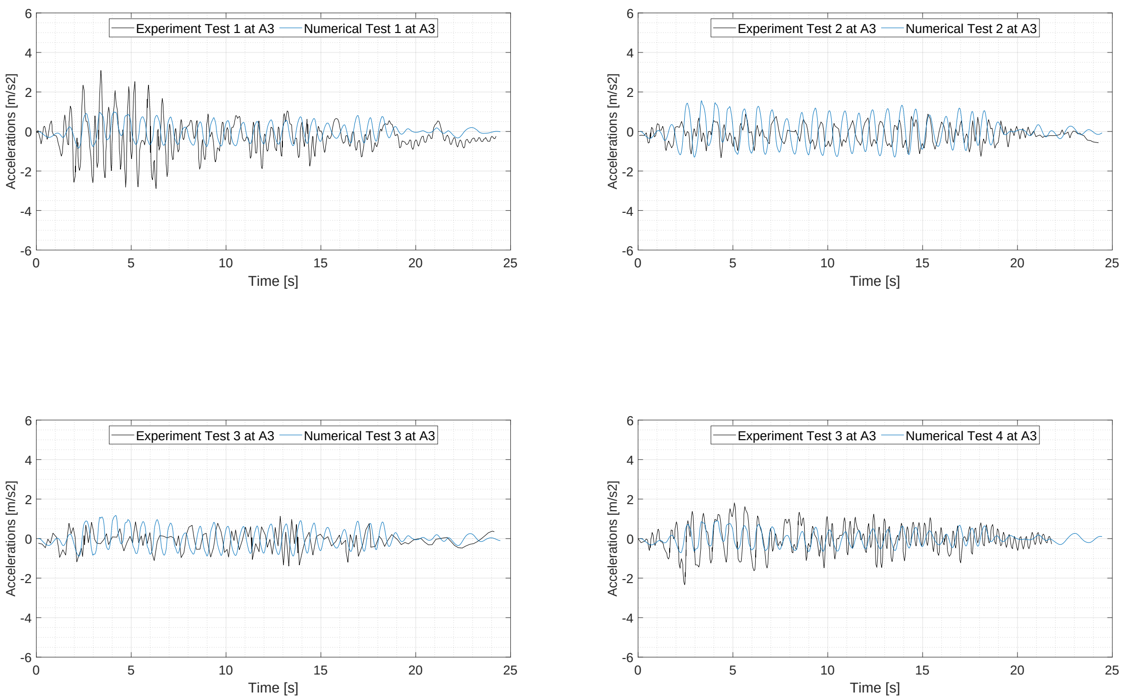

Figure 6.10. Comparison nodal accelerations at location A3 from numerical model with experimental results, from left to right: (a) Nodal acceleration sensor A3 Test 1 (b) Nodal acceleration sensor A3 Test 2 (c) Nodal acceleration sensor A3 Test 3 (d) Nodal acceleration sensor A3 Test 4

Despite of the modifications implemented on the structure of the different tests, the nodal accelerations shown a quite similar trend, see the figures 6.10a, b, c and d. However, this is not the behaviour observed at the experimental prototype where a drastic mitigation of the accelerations is observed when either the skirt length or the diameter of the bucket is enlarged (Yu et al., 2014).

Although those curves seems to match with the experimental results of the *Test* 2 and *Test* 3, the calibration process carried based on the experimental outputs of the *Test* 1 showed that the behaviour of the numerical model at the sensor A3 is not accurately simulated, see Figure 5.65e and f.

Thus, it is probably that this matching observed between the numerical models of the *Test* 2 and *Test* 3 do not come as a result of a proper simulation of the behaviour of the structure.

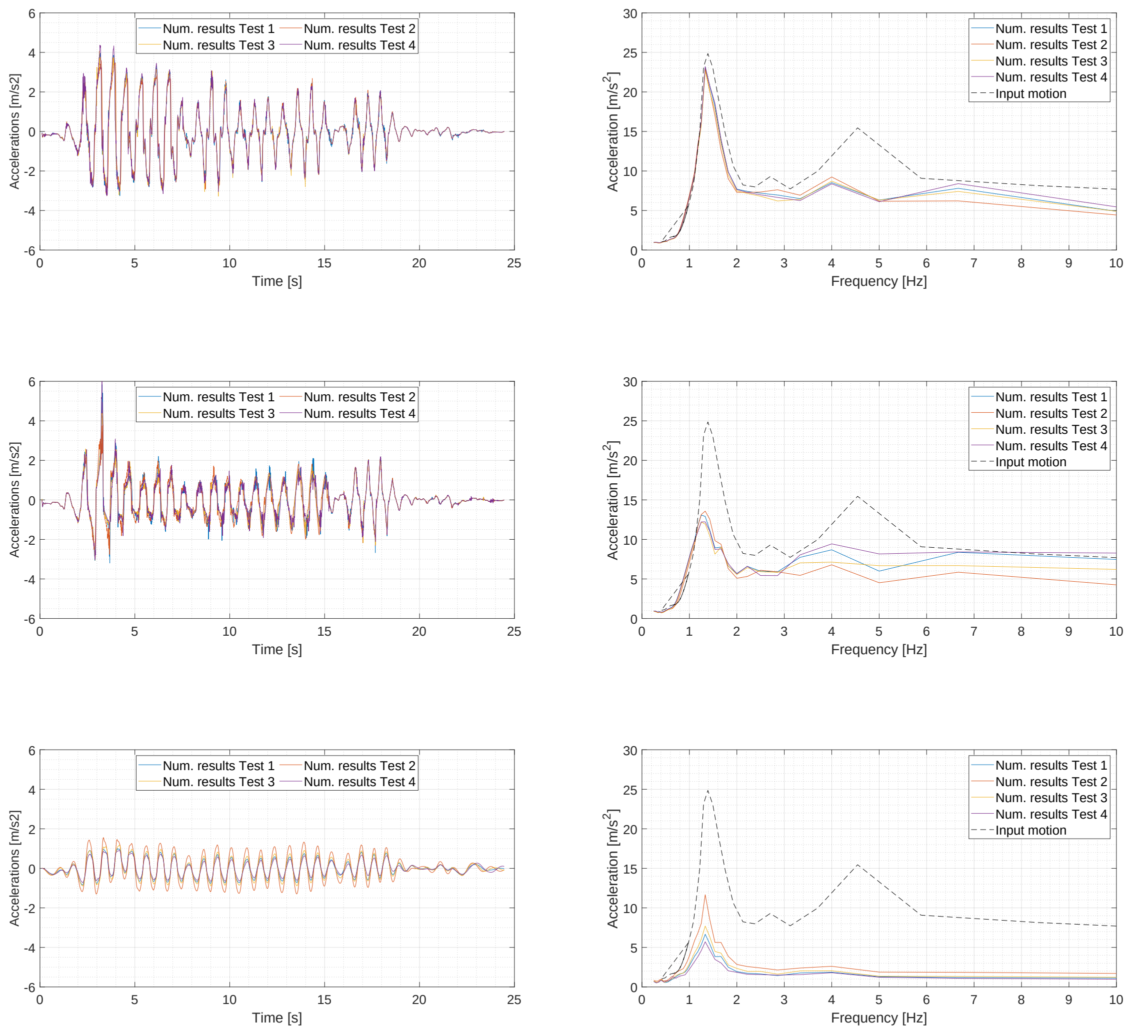

Figure 6.11. Comparison accelerations and spectral accelerations for different values of skirt length, diameter of the bucket foundation and weight of the structure: (a) Acceleration sensor A1 x=0m y=-0.5m. (b) Spectral acceleration sensor A1 x=0m y=-0.5m. (c) Acceleration sensor A2 x=6m y=-0.5m. (d) Spectral acceleration sensor A2 x=6m y=-0.5m. (e) Acceleration sensor A3 x=0m y=13m. (f) Spectral acceleration sensor A3 x=0m y=13m.

More evidences about the inaccurate behaviour of all numerical models at the location A3 is proved when all nodal accelerations are plotted together, see Figure 6.11e and f. As observed in these graphs, the $Test$ 2 and $Test$ 3 increases the nodal accelerations registered, a fact that goes in the opposite direction to the behaviour observed in the experiment. Regarding the amplification case of *Test* 2 of numerical model, according to (Dashti, Bray, Pestana, Riemer and Wilson, 2010) increasing the foundation depth provide better performance against *SSI*-induced rocking mechanism ensuring the larger reinforcement on the foundation end, thus altering the structural response. This could be the cause of increased acceleration of numerical model in *Test* 2.

As far as the recordings under the bucket and at the free field are concerned, any significant change is observed when the properties of the structure are modified as observed at the curves of the nodal accelerations, see Figures 6.11a and c, and acceleration spectra, the Figures 6.11b and d, corresponding to the recorders at the locations A1 and A2. As regards the $Test$ 3, in which the skirt length is increased, the same trend is proved by (T.Olalo et al., 2016), where any important alteration of the accelerations registered at the lid of the bucket is measured after the modification of this dimension.

6.2 Influence of the input motion

The numerical model calibrated during the last chapter by inducing the acceleration time history showed at the Figure 3.2a is tested under different input motions for five different values of masses at the tip of the tower $m = (10\ \ 20\ \ 29.3\ \ 40\ \ 50)\ tons$. Assuming the geometry of the foundation corresponding to $Test$ 1 at the Table 6.1, the contact pressures between the structure and the soil after computing the five different values of masses mentioned are $P = (7.80\ 15.61\ 23.41\ 31.22\ 39.02)\ kPa$.

All the tested input motions are obtained from (PEER library, 2021) and correspond to real earthquakes measured at different locations around the world whose characteristics are summarized in the Table 6.3. The input motion used for the calibration of the numerical model is also included at the same table under the name of event $R0$.

The acceleration time history of all of them can be observed at the Appendix F, and the one corresponding to the input motion used for the calibration of the numerical model can be checked at the Figure 3.2a.

ID	NGA No.	Name of event	Year	M_w	Mechanism	Arias Intensity $[m/s]$	R $[km]$	V_{s30} $[m/s]$	PGA $[g]$
R0	-	Original Input motion	-	-	-	6.30	-	1000.00	0.632
R1	934	Big Bear-01	1992	6.46	Strike Slip	0.10	35.41	659.09	0.060
R2	1245	Chi-Chi, Taiwan	1999	7.62	Reverse Oblique	0.10	37.72	804.36	0.041
R3	285	Irpinia, Italy-01	1980	6.90	Normal	0.40	8.18	649.67	0.130
R4	1111	Kobe, Japan	1995	6.90	Strike Slip	3.40	7.08	609.0	0.483
R5	1126	Kozani, Greece-01	1995	6.40	Normal	0.30	19.54	649.67	0.207
R6	801	Loma Prieta	1989	6.93	Reverse Oblique	1.30	14.69	671.77	0.276
R7	454	Morgan Hill	1984	6.19	Strike Slip	0.10	14.83	729.65	0.115
R8	497	Nahanni, Canada	1985	6.76	Reverse	0.20	4.93	605.04	0.182
R9	1041	Northridge-01	1994	6.69	Reverse	0.30	35.53	680.37	0.234
R10	71	San Fernando	1971	6.61	Reverse	0.90	13.99	602.10	0.382
R11	8158	Christchurch, New Zealand	2011	6.20	Reverse Oblique	5.70	2.52	649.67	0.910
R12	143	Tabas, Iran	1978	7.35	Reverse	11.80	1.79	766.77	0.854
R13	73	San Fernando	1971	6.61	Reverse	0.20	17.20	670.84	0.170
R14	6891	Darfield, New Zealand	2010	7.00	Strike Slip	0.40	43.60	638.39	0.089
R15	5685	Iwate, Japan	2008	6.90	Reverse	0.50	57.15	859.19	0.185
R16	897	Landers	1992	7.28	Strike Slip	0.10	41.43	635.01	0.080
R17	369	Coalinga-01	1983	6.36	Reverse	0.30	27.46	648.09	0.174
R18	501	Hollister-04	1986	5.45	Strike Slip	0.10	12.32	608.37	0.044
R19	4872	Chuetsu-oki, Japan	2007	6.80	Reverse	0.30	27.30	640.14	0.147
R20	1633	Manjil, Iran	1990	7.37	Strike Slip	7.50	12.55	723.95	0.515

Table 6.3. Identification and characteristics of the alternative input motions considered (PEER library, 2021)

The procedure used for implementing the new input motions to the model follows the same steps explained at the Chapter 4 in which the velocity time history is used for calculating equivalent forces applied to the boundaries, and the shear wave velocity is used as one of the variables for obtaining the dashpot coefficient.

The shear wave velocity considered in each case for running the calculation of the dashpot coefficient is observed at the column V_{s30} of the table above. This value is equivalent to the shear wave velocity at a depth of 30 meters which indicates the presence of a bedrock when it is larger than 600 m/s. In the case of the collected earthquakes, the shear wave velocity is always larger than this value so in all cases V_{s30} has been measured in a rock medium.

Thus, although the depth of the prototype is smaller than those 30 meters, see the figure 4.4, the assumption of a bedrock on the bottom and the lateral boundaries of the domain makes possible to use the value of V_{s30} observed at the table above, no matter the depth of the prototype.

6.2.1 Settlements

One of the most widely used parameters in order to evaluate the damaging level induced to a structure after an earthquake is the evaluation of the settlements. The measurement of the vertical displacements registered in the numerical model during each of the events presented are recorded at the node x=0, y=0 of the structure, exactly at the connection between the tower and the lid of the bucket, see Figure 4.4.

The settlements time story during an earthquake follows the shape of the Arias Intensity-time history of the induced motion (D.Bray and Dashti, 2014). The Arias Intensity I_a is an index which represents the energy of the ground motion and depend on the amplitude, the ground motion and the duration of the ground motion. Thus, this rate represents, in a roughly manner, the rate of earthquake energy build-up and its value can be obtained through the Equation 6.1 (D.Bray and Dashti, 2014).

$$I_a(T) = \frac{\pi}{2g} \int_0^T a^2(t)dt \tag{6.1}$$

g	Gravity acceleration
a	Measured acceleration values
T	Time period

For the sake of illustration, the settlement time history recorded at the numerical model for the before mentioned five different values of contact pressure after the implementation of the events $R4 - Kobe, Japan$ and $R10 - SanFernando$ are plotted together with its corresponding Arias Intensity-time history , see the figures 6.12 and 6.13. The plots after testing the rest of events observed at Table 6.3 are gathered in the Appendix F.

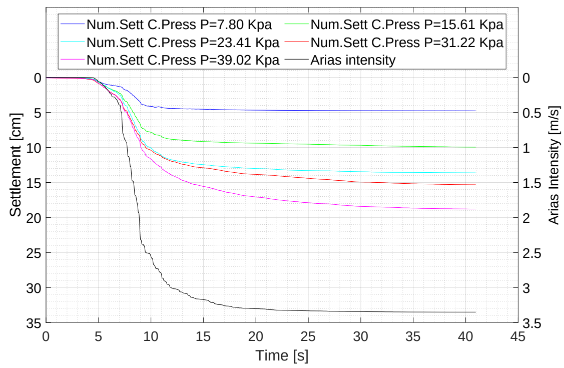

Figure 6.12. Settlements time history and Arias intensity time history of the event $R4 - Kobe, Japan$

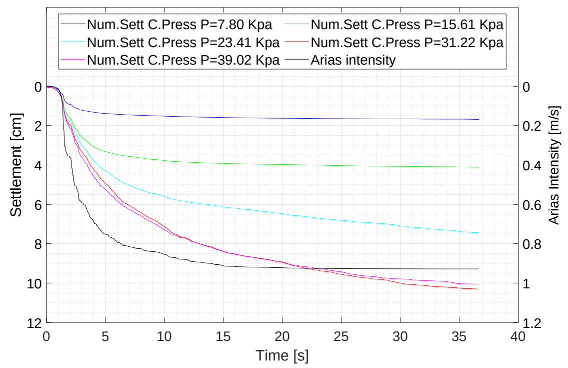

Figure 6.13. Settlements time history and Arias intensity time history of the event $R10 - SanFernando$

The same trend mentioned before is roughly replied by the numerical model constructed so that the shape of the Arias Intensity-time history follows the shape of the settlement-time history. Thus, it can be concluded that the development of vertical displacements is not only related with the weight of the structure or the thickness of the liquefiable layer, but there is also an obvious relation between the intensity of the earthquake I_a and the final value of settlements (Dashti, D.Bray, M.Pestana, Riemer and Wilson, 2010). Hence, all these inputs must be accounted for achieving an accurate prediction of the expected settlements of a structure in contrast to the empirical existing approaches based on records at the free-field.

Regarding the total value of vertical displacements calculated, for lower values of contact pressure, the following rule is valid; the bigger the pressure applied to the soil by the structure the larger the value of the settlements obtained, as evidenced in the Figures 6.12 and 6.13. Nevertheless, when higher pressures are tested, this behaviour seems not to be replicated in all the cases. In other words, the value of vertical displacements seems to reach a threshold after certain value of contact pressure of the structure, a fact also observed by (Macedo Escudero, 2017).

Thus, if the settlements calculated for a contact pressure equal to 31.22 kPa is compared with the model using 39.02 kPa at the tip of the tower, it can be checked that the lighter structure brings larger vertical displacements in the case of the event $R10 - San\ Fernando$, see the figure 6.13, something that is not occurring in the model tested under the event $R4 - Kobe, Japan$, in which the larger the pressure of the structure transfer to the soil surface, the larger the settlements.

However, this is not necessarily an inaccuracy of the behaviour of the numerical model since it is also observed in some more cases, see Appendix F. The increment of the contact pressure of the structure is simulated by increasing the mass at the tip of the tower which implies the reduction of the accelerations registered at this point as evidenced in previous analyses carried in this report, see the Figure 5.76e and f. This fact implies a reduction in the inertial forces induced by the structure to the soil, resulting in a possible reduction of the value of the vertical displacements.

Moreover, as proved by (Yu et al., 2014), the increment of the mass of the foundation, which is another way of increasing the contact pressure induced by the wind turbine, implies also a reduction in the value of the settlements due to the increasing of the confinement. Although the configuration of all the numerical models used in this section differs from the one mentioned, since all the masses are lumped at the tip of the tower, the larger masses might be also increasing the value of the confinement so that, together with lower values of accelerations, the value of the settlements is reduced.

Relation between settlements and contact pressure induced by structure

This phenomenon is further investigated with the intention of finding the possible existence of a threshold in the value of the contact pressure of the structure above which the growing of settlements stabilize so that the vertical displacements do not increment anymore respect to the value of the vertical pressure induced. This behaviour was proved numerically by (Macedo Escudero, 2017), a research in which $PM4Sand$ constitutive model was used in contrast to $PDMY01$ model used in this report.

For achieving this purpose, some extra values of contact pressure are tested, together with the ones mentioned previously, for all the input motions described at Table 6.3. These extra values are calculated by considering a mass at the tip of the tower of $m = (60\ 70\ 80\ 90\ 100)\ tons$ which provides a contact pressure of $P = (46.83\ 54.63\ 62.43\ 70.24\ 78.04)\ kPa$ obtained assuming, as previously, a diameter of the lid of the suction bucket equal to 4 meters.

The vertical displacements recorded are plotted against the contact pressure, and the points obtained on that locus, fitted by the use of a second degree-polynomial curve by the use of the software $Matlab$. This plot is divided into three different graphs so as to analyze the possible influence of the Arias Intensity and the Shake Intensity Ratio SIR.

This variable not only accounts for the intensity of the earthquake but also for the time employed by the dynamic events to release the energy so that a higher value of this ratio is expected when the same intensity is showed by an earthquake in a shorter period of time. The value of SIR is calculated by the Equation 6.2 (Yu et al., 2014).

$$SIR = \frac{I_{a5-75}}{D_{5-75}} \tag{6.2}$$

I_{a5-75}	Change in Arias intensity from 5% to 75% of its total value
D_{5-75}	Corresponding time duration

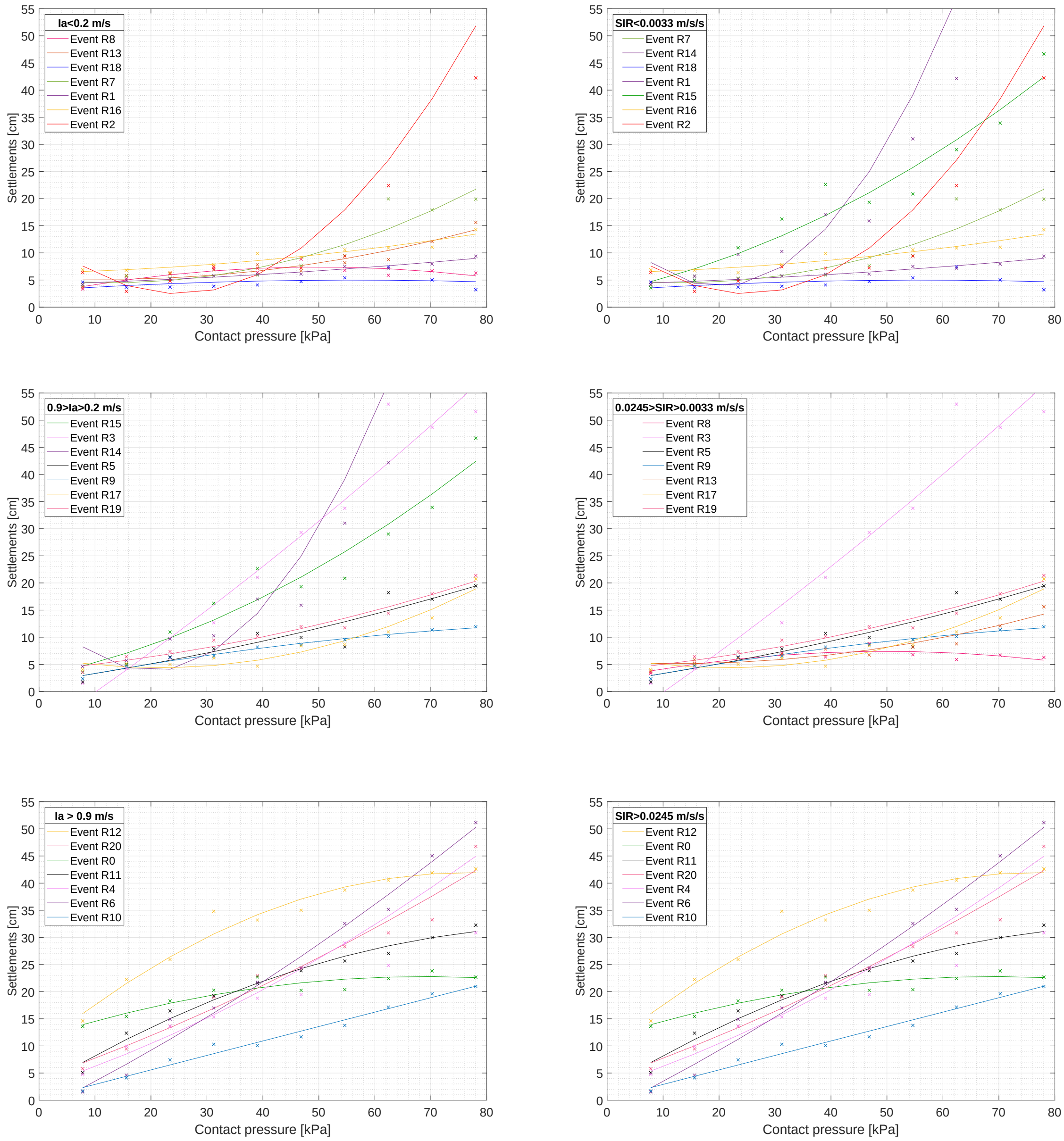

Figure 6.14. Relation between settlements and contact pressure of the structure, from left to right: a) Dynamic events with $I_a < 0.2$ m/s b) Dynamic events with $SIR < 0.0033$ $m/s/s$ c) Dynamic events with $0.9 > I_a > 0.2$ m/s d) Dynamic events with $0.0245 > SIR > 0.0033$ $m/s/s$ e) Dynamic events with $I_a > 0.9$ m/s f) Dynamic events with $SIR > 0.0245$ $m/s/s$

An overview to the figure 6.14 reveals that the existence of a threshold on the value of the settlements, when the contact pressure is increased, does not occur in all the cases, at least for all contact pressure values studied. Thus, although after implementing some of the dynamic events the mentioned threshold is observed, some other curves show a linear trend or even an increment in the rate of grow of settlements.

Nevertheless, even though a clear trend of the curves is not obtained, some observations are derived if a comparison between different intensities of the earthquakes is carried. Thus, it can be noticed that for the largest values of I_a and SIR, the Figure 6.14e and f, the trend of the settlements development is either linear or a threshold is observed. On the other hand, if the intermediate values of I_a or SIR are analyzed, the figures 6.14c and d, virtually only linear growing rates are observed in the case of SIR, whereas linear and exponential trends are recorded in the case of I_a. Finally, for the less intense earthquakes and lowest SIR, the figures 6.14a and b, mostly exponential trend are observed.

As a conclusion, although a threshold is not always observed when the contact pressure of the structure is increased, it seems that this occurrence is more likely when the Arias Intensity I_a or the Shake Intensity Ratio SIR are higher. This might be explained calling some of the findings mentioned at (Dashti, D.Bray, M.Pestana, Riemer and Wilson, 2010), where it is proved that the relative density of the soil increases during the shaking event. Thus, one hypothesis explaining this fact might be that the more intense events contribute to a higher densification of the soil, leading to a reduction of the effects of partial bearing failure of the material due to the increment of pore water pressure.

If this fact were confirmed, it would mean that, by adjusting properly the contact pressure of the structure, the mechanisms inducing the settlements might be controlled and, therefore, the total amount of vertical displacements of the structure expected. Anyway, further investigation are needed in order to confirm this phenomenon, since the simplifications and assumptions carried in order to construct the numerical model used for this report need to be considered.

Relation between settlements and intensity of the shake

In the current section, the total value of settlements of the structure obtained for each of the events presented at Table 6.3 and for the different values of contact pressure of the structure are compared with the corresponding value of Arias Intensity I_a and Shake Intensity Ratio SIR.

The influence of the distance parameter R, which measures the distance to the fault, is also studied so that the events with a value of R<15km are considered near-fault, whereas the ones with R>15km are known as far-fault. The value of this parameter for each of the earthquakes is also collected at the Table 6.3.

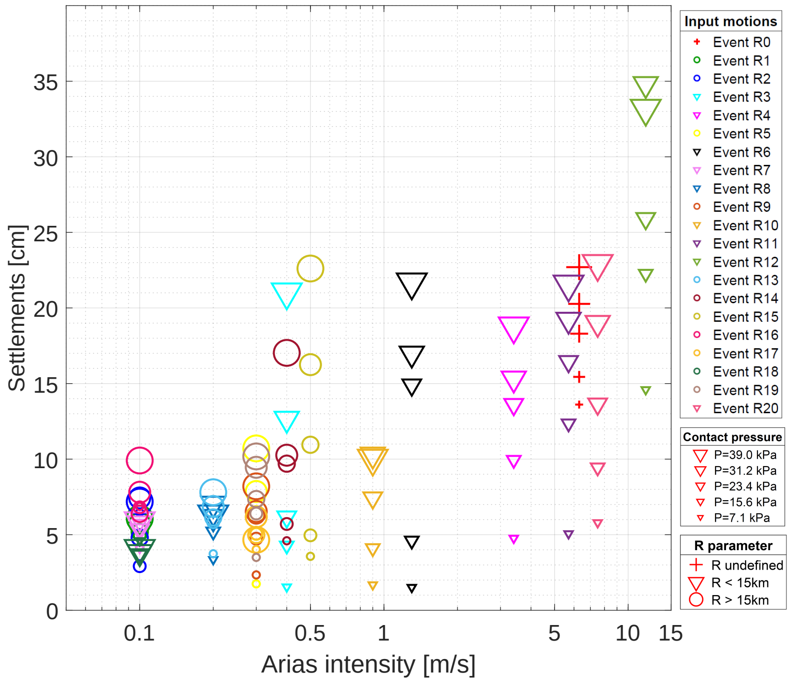

Figure 6.15. Relation between total value of settlements and value of Arias Intensity for each of the events and masses tested

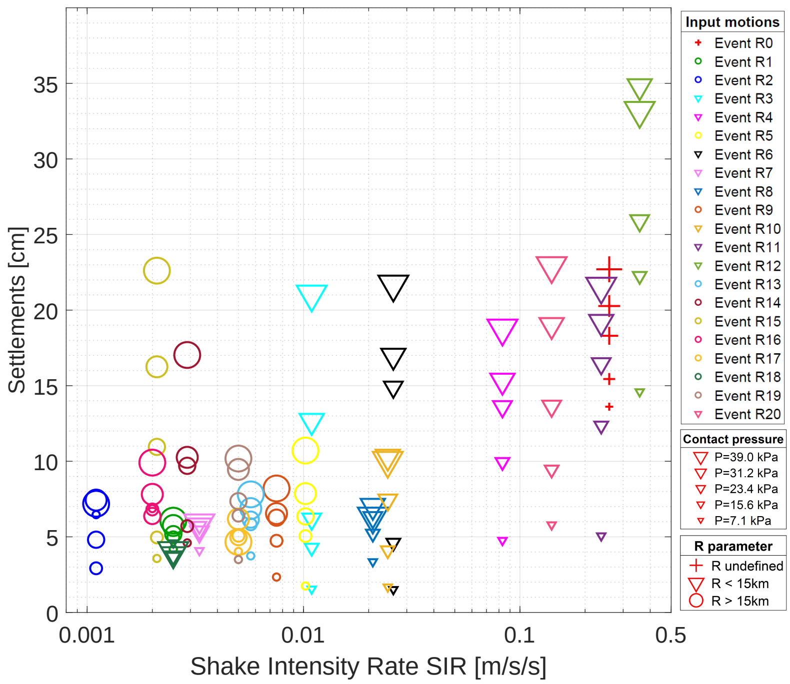

Figure 6.16. Relation between total value of settlements and value of Shake Intensity Rate SIR for each of the events and masses tested

Taking a look at the figure 6.15, it is observed that the events with larger values of Arias intensity usually correspond to near-fault events although some of them are also located on the left-hand side of the graph where $I_a < 1\ m/s$. The same observation arises when the relation between settlements respect to SIR is studied. Most of the near-fault events present a higher value of SIR.

As mentioned in previous paragraphs and evidenced at the figures 6.12 and 6.13, the general trend brought by most of the tests is that the larger pressure transmitted by the structure is, the larger value of the settlements obtained is. Nonetheless, as also mentioned previously, in some of the cases the vertical displacements of the structure are larger for 31.2 kPa than for a contact pressure equal to 39.0 kPa. However, as explained before, this fact can be occurring due to a drop of the accelerations of the tower together with a larger value of confinement of the soil underneath the suction bucket.

Despite of these observations, the most relevant one is the relation observed between the Arias Intensity and the total value of settlements registered. The graph above shows that the larger the value of I_a, the larger the value of vertical displacements of the structure. Thus, settlements no bigger than 12 centimeters are recorded for $I_a < 0.3\ m/s$, whereas values above 20 centimeters are in most of the cases measured when $I_a > 1\ m/s$.

This observation is less clear when the settlements are plotted against SIR, see the figure 6.16. If settlements corresponding to highest values of SIR are observed, it seems that the rule stated above is fulfilled. Nevertheless, for values of $SIR < 0.01$, this rule seems not to be accomplished anymore since large and small values of total settlements are observed with a same value of SIR.

Although due to the lack of time it is not performed, it would be interesting a comparison between SIR and the rate of settlement development during a certain period of time since, according to (Dashti, D.Bray, M.Pestana, Riemer and Wilson, 2010), a linear relation between them exist.

6.2.2 Fluctuations of r_u at pore water pressure recorders

If the calibrated curves corresponding to the generation of pore water pressure expressed in terms of r_u-time histories are observed, see Figure 5.63, it is noticed the important fluctuations of this parameter specially at the vicinity of the structure, recorders at the location P1 and P3, see Figure 3.1.

However, after performing the simulation of the numerical model using the different input motions collected at Table 6.3, it is observed that these fluctuations do not occur in all of the cases. For illustrating this fact, four pore water pressure ratio r_u-time histories at the location P1 are showed. Each of them are simulated under the following four different input motions, RO, $R1$, $R9$ and $R12$, with a value of contact pressure between structure and soil of $P = 23.4\ kPa$ equivalent to the setting of a mass of $m = 29.9\ tons$ at the tip of the tower. See Figure 6.17. The rest of pore water pressure ratio-time histories at locations P1, P2, P3 and P4 for all the input motions presented at this section are gathered at the Appendix F.

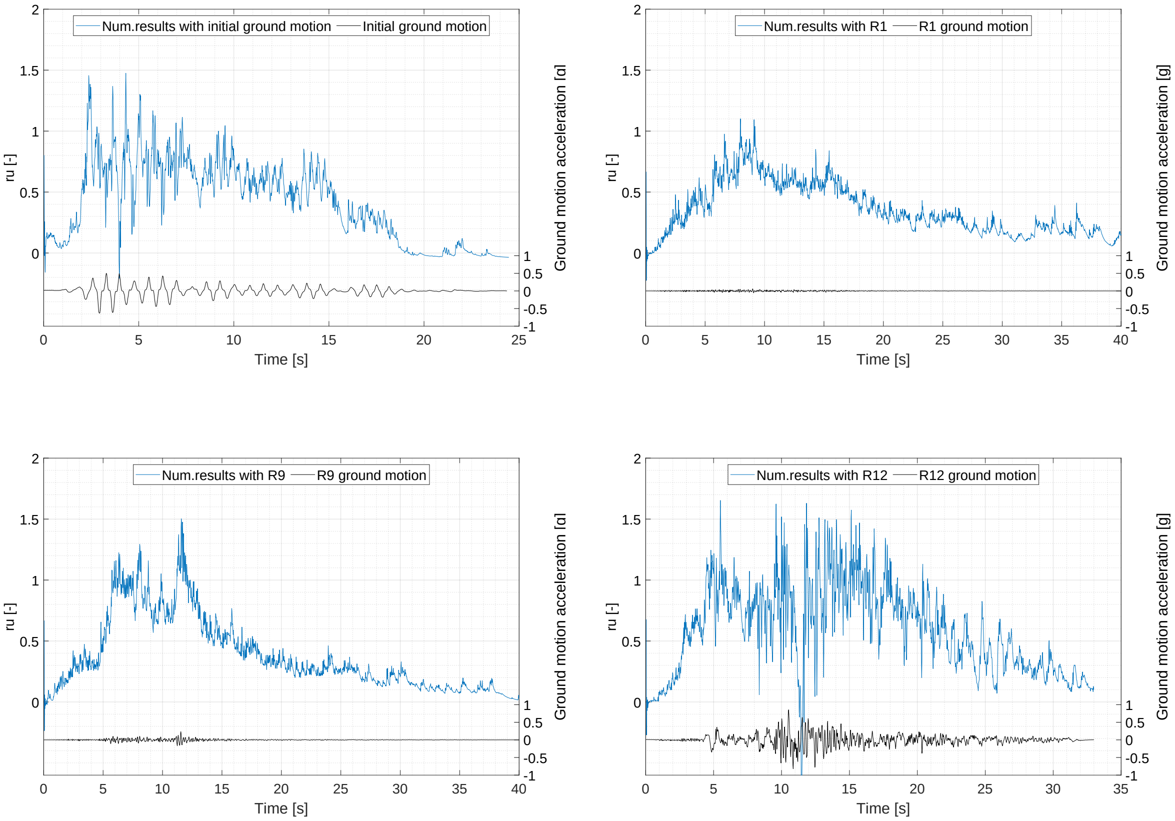

Figure 6.17. (a) Pore water pressure ratio sensor P1 event $R0$. (b) Pore water pressure ratio sensor P1 event $R1$. (c) Pore water pressure ratio sensor P1 event $R9$. (d) Pore water pressure ratio sensor P1 event $R12$.

As observed in the curves plotted above, important fluctuations of the value of r_u are observed when the input motions RO and $R12$ are used, the figure 6.17a and d, whereas smoother graphs are obtained for the events $R1$ and $R9$, the figure 6.17b and c.

Regarding these outputs, three different reasons might explain the generation of the mentioned fluctuations. The first one is related with the characteristics of the input motion. As observed in the Table 6.3, the value of Arias Intensity I_a, Shear Wave Velocity at a depth of 30m V_{s30} and Peak Ground Acceleration PGA, are larger for the earthquakes RO and $R12$ than for $R1$ and $R9$.

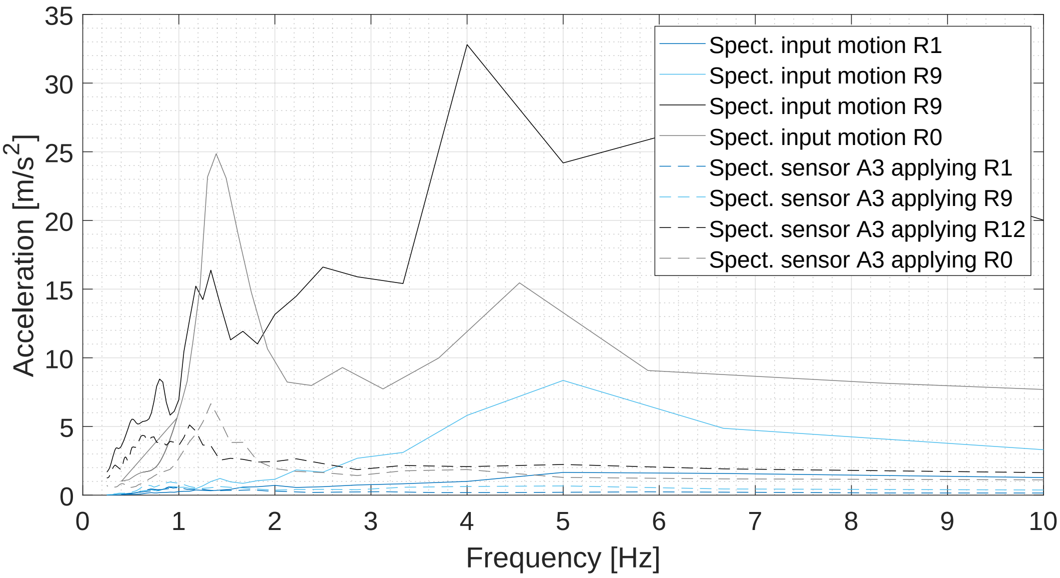

Figure 6.18. Comparison between input acceleration spectra of events RO, $R12$, $R1$ and $R9$ and acceleration spectra obtained at the location of the sensor A3 of the numerical model after applying those four events setting a mass m=29.3 tons at the tip of the tower

The second reason is a consequence of the first one. Due to the stronger shake characteristics, when the acceleration spectra of these input motions are plotted, see the figure 6.18, larger peaks of accelerations are obtained for the case of $R0$ and $R12$. These higher peaks of the input motions induce also larger accelerations at the tip of the tower where the sensor A3 is located, being this fact specially critical for the case of $R0$. These accelerations registered at the tip of the structure are transmitted to the soil provoking presumably the mentioned fluctuations at the sensor P1 located within the suction bucket.

The third possible reason of this noise observed at the time histories of pore water pressure ratio might be related with the matching between the dominant frequencies of the input motion and the natural frequency of the structure. If the figure 6.18 is seen, it is noticeable that, in all the cases, the frequency of the structure bringing larger values of accelerations is approximately 1 Hz. Thus, it is likely that the input motions showing peaks acceleration around this value of frequency, i.e. events RO and $R12$, are inducing some resonance on the structure, provoking thus larger fluctuations on the value of r_u at the location P1.

Conclusion 7

7.1 Construction of the numerical model

An overall look at the calibrated values with respect to the provided experimental results for both constitutive models studied in this report, $PDMY01$ and $PM4Sand$, leads to the conclusion that in both cases the numerical model is able to catch the behaviour of the physical performance of the centrifuge test in terms of generation of excess pore water pressure, accelerations and settlements.

Nonetheless, it is also known the shortcomings of the numerical models for simulating the performance of the outermost layers of the soil due to the lower values of confinement pressure and effective stresses. These difficulties are also observed in the case of this report, specially if the generation of pore water pressure captured at the location of the sensors P1 and P2 is checked, see Figure 3.1. They are found just 0.5 meters from the ground surface and, in both cases, large fluctuations of the value of r_u is registered no matter the constitutive model used.

This fact becomes specially critical at the locations of the sensor P1 in the case of the model $PDMY01$ presumably due to the proximity to the structure, and at the location P2 in the case of $PM4Sand$. Therefore, with the intention of overcoming this issue, some modifications of the configuration of the structure and some extra calibration of the value of the input parameters of the soil were carried. However, these adjustments led to some cases to solutions which do not fit totally with the real conditions.

Thus, regarding the distribution of masses along the structure, the experiment placed a lumped mass at the tip of the tower and a second mass at the lid of the suction bucket. However, it is demonstrated that if this configuration is adopted for the numerical model, higher values of fluctuations of r_u at superficial layers are recorded due to an important increment of the accelerations at the tip of the tower. Therefore, it was decided to concentrate all the masses at the top of the wind turbine prototype making weightless the foundation although much lower accelerations respect to the experiment at the tip of the tower were registered, sensor location A3.

On the other hand, it was observed that an effective way of decreasing the fluctuations of r_u when $PDMY01$ material is tested is by decreasing the value of the phase and the friction angle as well as increasing the density of the material. Nonetheless, the best results are obtained when these values are out of the range considered common for a medium dense sand, see Table 5.3. As far as $PM4Sand$ material is concerned, the fluctuations are corrected by decreasing dramatically the value of G_o respect to the recommended values of the Equation 4.3. However, this requirement is also observed at the element test in which lower values than the recommended ones are needed in order to calibrate properly the model, see Table 5.1.

As previously mentioned, concentrating the mass on the tip of the tower managed to decelerate the structural response, contributing to the larger rocking motions, thus limiting the influence of punching effects of the foundation on the surrounding soil. This probably led to a decrease in fluctuations of r_u output and reduced the noise and managed to reduce the settlements to a desirable level. This was more obvious, especially in the case of *PM4Sand* where placing the mass on the top of the tower contributed to the reduction of settlements substantially.

In order to identify more accurately the cause of the mentioned fluctuations of r_u, the numerical simulations of both constitutive model are also carried without the presence of the structure as well as under different input motions. As observed at the Chapter 5, both models are able to correct effectively this noise registered at the outermost layers, specially at P1, when the structure is not accounted. Thus, it can be concluded that the connection set between the structure and the soil by invoking the command *equalDOF* available in *OpenSees* is not totally effective in the case of the numerical simulation of the dynamic performance of a suction bucket founded wind turbine.

The frequency and characteristics of the input motion induced to the models seems to play also a relevant role on the reduction of the r_u fluctuations. Thus, it is observed how dynamic events which show a peak around the frequency of 1 Hz produce larger accelerations at the tip of the tower. Presumably, this behaviour is occurring due to the matching between the natural frequency of the structure and one of the predominant frequencies of the input motion. Besides, it is also noticed that this issue is more critical when the earthquakes count with a higher value of Arias Intensity I_a.

Taking into account all the points mentioned above, it is observed that, in general, both numerical models tend to overestimate the stiffness of the soil at the initial stages of the input motion, see Section 5.3. Thus, higher peaks at the nodal accelerations are observed at the first seconds in comparison with the experimental results, as well as dilative behaviour of the soil manifested through the generation of negative pore water pressure, and a delay of the generation of settlements.

7.2 Numerical predictions

Moving to the numerical predictions brought by the numerical model, it is important to point out again that all of them are carried by using the constitutive model $PDMY01$. Theoretically, $PM4Sand$ material is a more advance constitutive model but the computational time is larger and, due to the limited time, these predictions could not be carried by its use.

Having said that, the numerical simulations confirm the predictions cast by the experiment. Thus, the value of settlements is reduced drastically when the diameter of the suction bucket or the length of the skirt is increased, see Figure 6.2. A drop in the curve of generation of pore water pressure underneath the structure sensor P1, is observed in both cases, being presumably this reason the one explaining the reduction of vertical displacements, see Figure 6.4.

However, the provided outputs of the experiment state also that an increment of the value of the weight of the foundation reduces the total settlements registered (Yu et al., 2014). Nonetheless, this behaviour is not clearly observed in the numerical model constructed. The reason explaining this fact could be the different mass location setting if the experimental prototype and the numerical model are compared. As mentioned before, all masses in the numerical model are concentrated at the tip of the structure, whereas the tested prototype during the centrifuge test counts with masses located at both the tip and the foundation. The model accounted does not approximate the behaviour during vibration properly due to underestimation of the accelerations in structural response. Thus, the confinement pressure is the same in terms of the gravity loads but the behaviour is different during the shaking event since the inertia forces are larger if a larger mass is set at the tip of the structure.

In order to investigate more into detail that possible improvement of the values of vertical displacements after increasing the contact pressure induced by the structure to the soil, the numerical model is tested under twenty different dynamic events for different values of weight of the structure. The first finding is that the value of the settlements increases together with the Arias Intensity I_a so that the more intense the event is, the larger value of vertical displacements measured is. This relation also exist when the settlements are compared with the Shaking Intensity Ratio SIR, although for smaller values of this parameter, the mentioned relation is not totally proved.

From that set of tests it is also found that the vertical displacements recorded do not increase linearly when the contact pressure induced by the structure is enlarged so that, for some certain events, a kind of threshold on the value of settlements is observed which can not be surpassed even increasing the value of the masses located at the structure. This fact is studied by plotting the value of vertical displacements against the value of contact pressure induced by the structure in two different graphs, for $I_a < 0.9\ m/s$ and for $I_a > 0.9\ m/s$. In both graphs, some of the events show this behaviour so it can be concluded that it is not completely related with the value of the Arias Intensity of the earthquake. Moreover, there are also events whose increment of vertical displacements continues being linear or even some of them show a growing rate of increment of settlements. Therefore, it could not be found the reason why the mentioned threshold is observed in some of the cases, so further investigations are needed.

Discussion 8

8.1 Limitation of the model

Although the level of accuracy obtained by the numerical simulations constructed in this report can be considered satisfactory for both constitutive models, there are some uncertainties which might be playing a central role regarding the deviation between the outputs from the experiment and the virtual performances.

The main difficulty concerning the construction of the model is the lack of information about the physical characteristics of the structure tested during the centrifuge test presented at (Yu et al., 2014). Some data like the material used, the stiffness of both the foundation and the body of the wind turbine, or the section of the tower of the prototype is missed. Therefore, all these characteristics has been defined in the model by a process of trial and error, guessing a set of initial values and testing which parameters provide better output.

As a consequence of the before-mentioned point, the priority was to catch the recordings of the sensors located within the soil domain, P1, P2, P3, P4, A1, and A2, more than the ones coming from the accelerometer at the tip of the tower, A3, since all the data is available regarding the features of the sand. However, the measurements recorded at these locations might have been more precise if the structure characteristics had been totally defined.

In the previous section are discussed the strategies followed for reducing the large fluctuations of r_u experienced at recorders P1 and P2. In the case of $PDMY01$, as pointed out before, one effective way was by the reduction of the phase angle and the friction angle, as well as by the increasing of the soil density. However, the final set of values for these parameters, observed at Table 5.3, count with values that seem to be out of the range considered usual for a medium-dense sand. Since the numerical model constructed using $PDMY01$ material is the one used for the numerical predictions, these values might compromise the accuracy of the outputs received on that section.

Regarding the performance of *PM4Sand*, the model constructed showed flaws in simulating the early stage of the provided earthquake loading on the domain, responding in a quite dilative manner in the first few seconds of the strong shaking causing large spikes in the acceleration recorder. Thus, delaying the generation of the pore water pressure was captured in approximately the first 4 seconds. The exact cause of such a response is not resolved and could be due to an error in the code. Different input motions were applied to the domain and the same pattern was noticed. Thus, due to time limitation, the source of errors remained undetected.

Moving back to the large fluctuations of r_u at the sensors P1 and P2, one conclusion of the current report is that the connection established between the soil and the structure by the use of the command *equalDOF* available in *OpenSees* might be an improvable feature on the model. More complex connections are available in (Mazzoni et al., 2007) but, due to the lack of time, not further investigation are carried.

Another relevant point which may suppose an important source of error is the simplification made by considering valid simulations in 2 dimensions. In terms of the characteristics of the soil, boundary conditions and features of the structure, the model might be working similarly than a 3D model but, in the last case, an extra horizontal direction for the dissipation of pore water pressure is available so it might be having an important influence on the final results.

Finally, it is needed to be pointed out that the virtual simulations are constructed considering the water table at the same level than the seabed since following this solution accurate enough results are obtained and the soil continues behaving as fully saturated. Nevertheless, as observed in Figure 3.1, the water level at prototype scale is located 1.5 meters above the seabed, so some influence must be experienced on the final results. This simplification is carried due to the high increment observed in the computational time when the water mass is modelled, specially regarding the simulation of $PM4Sand$ material.

8.2 Future work

Due to the limited amount of time, several assumptions and simplifications of the numerical models are implemented, or a reduced number of tests are carried. However, if more accurate outputs or stronger evidences want to be obtained from the numerical simulations constructed in this thesis, the following points may be further investigated:

- Because of its complexity, $PM4Sand$ constitutive model requires a higher computational time, so its process of calibration is slower. The outputs received from that model in this report might be improved, for instance, studying more in detail the influences of the secondary parameters, stiffness of the structure, etc.
- In order to analyze the influence of the construction of the model in 2 dimensions, an alternative 3D model may be constructed. Thus it could be proved if the assumption of a 2D model is valid.
- As mentioned previously, all numerical predictions in this thesis are carried by the use of $PDMY01$ constitutive model. However, it would be convenient to perform the same simulations using $PM4Sand$ model to confirm if the behaviour of the soil observed is also replicated by alternative materials.
- The water above the seabed might be modelled so that the influence of this feature could be analyzed
- At the numerical predictions section, it is observed that when the contact pressure of the structure is increased, depending on the dynamic event, a threshold on the value of the total vertical displacements of the structure is observed in some cases. Further investigations are needed to conclude which factor is the one determining the occurrence of this fact.
- Although it is not mentioned in the current report, it would be interesting to study if a relation between the thickness of the liquefable layer and the amount of settlements exists.
- An important improvement of the numerical results might be experienced if a further investigation about the characteristics of the structure were carried. Thus, different locations of the masses could be studied or a more complex modelling might be considered due to the mentioned limitations of the existing model
- It is observed that the presence of the structure has an important influence on the creation of the large fluctuations of r_u observed at the recorders P1 and P2. It would be convenient

to study alternative connections between the structure and the soil, for instance, by testing the *Contact element* available in *OpenSees*.

- Focus of the report was mainly on analyzing the response of the soil domain and *SSI*, neglecting the effects on the structure in terms of stresses and whether the structure exhibited any plasticity
- Considering the tilting of the structure would provide more precise insight on overall performance of the model, since the current one included a lumped mass only on the tip of the tower, most likely deteriorating the structural response in terms of serviceability
- Mesh refinement in vicinity of the structure may be considered, especially in the case of the *PM4Sand* model
- Up-to-date constitutive models may be implemented in the numerical model simulation, such as $PDMY02$, etc.

Bibliography

Agaiby, S. and Ahmed, S. M. (2016), 'Learning from failures: A geotechnical perspective', *Proceedings of the International Conference on Forensic Civil Engineering, Nagpur, India 21, 22, 23 January 2016* pp. 1–24.

API-RP-2A-LRFD (1997), *Recommended Practice for Planning, Designing, and Constructing Fixed Offshore Platforms-Load and Resistance Factor Design*, American Petroleum Institute.

Asheghabadi, M., M.Sahafnia, A.Bahadori and N.Bakhshayeshi (2019), 'Seismic behaviour of suction caisson for offshore wind turbine to generate more renewable energy', *International Journal of Environmental Science and Technology. 16:2961-2972* .

Ayala, G. and Aranda, G. (1977), 'Boundary conditions in soil amplification studies', *Proceedings of the 6th World Conference on Earthquake Engineering, New Dehli, India* 6.

Bhattacharya, S. (2019), *Loads on the Foundations*, John Wiley Sons, Ltd, chapter 2, pp. 51–102.
URL: *https://onlinelibrary.wiley.com/doi/abs/10.1002/9781119128137.ch2*

Boulanger, R. W. and Ziotopuolou, K. (2017), *PM4SAND:A sand plasticity model for earthquake engineering applications*, version 3.1 edn, Department of civil and environmental engineering. College of Engineering. University of California at Davis.

Bray, J. D. and Dashti, S. (2010), Liquefaction-induced movements of buildings with shallow foundations, International Conferences on Recent Advances in Geotechnical Earthquake Engineering and Soil Dynamics. 4, Missouri University of Science and Technology.
URL: *https://scholarsmine.mst.edu/icrageesd/05icrageesd/session12/4*

Castro, G. (1969), 'Liquefaction of sands', *Harvard Soil Mechanics Series 87* .

Dafalias, Y. and Manzari, M. (2004), 'Simple plasticity sand model accounting for fabric change effects', *Journal of Engineering Mechanics* 130(6), 622–634. cited By 452.
URL: *https://www.scopus.com/inward/record.uri?eid=2-s2.0-2942552104doi=10.1061*

Dashti, S., Bray, J., Pestana, J., Riemer, M. and Wilson, D. (2010), 'Mechanisms of seismically induced settlement of buildings with shallow foundations on liquefiable soil', *Journal of Geotechnical and Geoenvironmental Engineering - J GEOTECH GEOENVIRON ENG* 136.

Dashti, S., D.Bray, J., M.Pestana, J., Riemer, M. and Wilson, D. (2010), 'Centrifuge Testing to Evaluate and Mitigate Liquefaction-Induced Building Settlements Mechanisms', *Journal of Geotechnical and Geoenvironmental Engineering, July 2010* 136(7).

D.Bray, J. and Dashti, S. (2014), 'Liquefaction-induced building movements', *Bulletin Earthquake Engineering* 12, 1129–1156.
URL: *https://doi.org/10.1007/s10518-014-9619-8*

DNVGL-OS-C201 (2017), *Offshore standards - Structural design of offshore units - WSD method*, DNV-GL.

DNVGL-ST-0126 (2018), *Standard - Support Structures for Wind Turbines*, DNV-GL.

DNVGL-ST-0437 (2016), *Standard - Loads and site conditions for wind turbines*, DNV-GL.

Dnv/Risø (2002), *Guidelines for Design of Wind Turbines*, Det Norske Veritas Wind Energy Department of Risø National Laboratory, Denmark.

Dobry, R., Ladd, R., Yokel, F., Chung, R. and Powell, D. (1982), 'Prediction of pore water pressure buildup and liquefaction of sands during earthquakes by the cyclic strain method', *NBS Building Science Series 138, National Bureau of Standards, Gaithersburg, Maryland, 150 pp* .

Elgamal, A., Yang, Z., Parra, E. and Ragheb, A. (2003), 'Modeling of cyclic mobility in saturated cohesionless soils', *International Journal of Plasticity* 19(6), 883 – 905.
URL: *http://www.sciencedirect.com/science/article/pii/S0749641902000104*

EN-1997 (2007), *Geotechnical Design*, European Committee for Standardization.

EN-1998-5 (2004), *Design of structures for earthquake resistance - Part 5: Foundations, retaining structures and geotechnical aspects*, European Committee for Standardization.

Energy, O. (2013), 'First Bucket Foundation Installed at Dogger Bank (UK)'.
URL: *https://www.offshore-energy.biz/first-bucket-foundation-installed-at-dogger-bank-uk/*

Hashash, Y. and Park, D. (2002), 'Viscous damping formulation and high frequency motion propagation in non-linear site response analysis', *Soil Dynamics and Earthquake Engineering* 22, 611–624.

Hill, R. (1950), *The Mathematical Theory of Plasticity*, Oxford engineering science series, Clarendon Press.
URL: *https://books.google.dk/books?id=EMDaAAAAMAAJ*

Huang, B., Chen, X. and Zhao, Y. (2015), 'A new index for evaluating liquefaction resistance of soil under combined cyclic shear stresses', *Engineering Geology* (199), 125–139.

IEC-61400-1 (2005), *Wind turbines - Part 1:Design requirements*, International Electrotechnical Commission.

Ishihara, K. and Yamazaki, A. (1984), 'Analysis of wave-induced liquefaction in seabed deposits of sand', *Soils and Foundations* 24(3), 85–100.

ISO-19900 (2019), *Petroleum and natural gas industries - General requirements for offshore structures*, International Organization for Standardization.

Iwan, W. D. (1967), 'On a Class of Models for the Yielding Behavior of Continuous and Composite Systems', *Journal of Applied Mechanics* 34(3), 612–617.
URL: *https://doi.org/10.1115/1.3607751*

Joyner, W. B. (1975), 'A method for calculating nonlinear seismic response in two dimensions', *Bulletin of the Seismological Society of America* 65(5), 1337–1357.

Joyner, W. B. and Chen, A. T. F. (1975), 'Calculation of nonlinear ground response in earthquakes', *Bulletin of the Seismological Society of America, October 1975* 65(5), 1315–1336.

K.Chopra, A. and McKenna, F. (2015), *Modeling viscous damping in nonlinear response history analysis of buildings for earthquake excitation*, Wiley Online Library (wileyonlinelibrary.com). DOI: 10.1002/eqe.2622.

Khosravifar, A., Elgamal, A., Lu, J. and Li, J. (2018), 'A 3d model for earthquake-induced liquefaction triggering and post-liquefaction response', *Soil Dynamics and Earthquake Engineering* 110, 43 – 52.
URL: *http://www.sciencedirect.com/science/article/pii/S0267726117308722*

Koteras, A., Ibsen, L. and Clausen, J. (2016), Seepage study for suction installation of bucket foundation in different soil combinations, *in* J. Chung and H. Wang, eds, 'The Proceedings of the Twenty-sixth (2016) International Ocean and Polar Engineering Conference', Vol. 2 of *Proceedings of the International Offshore and Polar Engineering Conference*, International Society of Offshore Polar Engineers, pp. 697–704. ISOPE: The 26th International Ocean and Polar Engineering Conference, ISOPE 2016 ; Conference date: 25-06-2016 Through 01-07-2016.

Kramer, S. L. (1996), *Geotechnical Earthqueake Engineering*, Prentice-Hall International Series in Civil Engineering and Engineering Mechanics.

K.Ueda, R.Uzuoka, S.Iai and T.Okamura (2020), 'Centrifuge model tests and effective stress analyses of offshore wind turbine systems with a suction bucket foundation subject to seismic load', *Soil and Foundations* 60(6), 1546–1569.
URL: *https://doi.org/10.1016/j.sandf.2020.08.007*

L.Kutter, B., T.Manzari, M., Zeghal, M. and Zeghal, M. (2017), *Model Tests and Numerical Simulations of Liquefaction and Lateral Spreading*, Springer Open.

Lloyd, G. (2010), *Guideline for the Certification of Wind Turbines*, Germanischer Lloyd Industrial Services GmbH, Hamburg, Germany.

Lysmer, J. and Kuhlemeyer, R. L. (1969), 'Finite dynamic model for infinite media', *Journal of the Engineering Mechanics Division, August 1969* 95(5), 859–877.

Macedo Escudero, J. L. (2017), Simplified Procedures for Estimating Earthquake-Induced Displacements, PhD thesis, University of California, Berkeley.

Mazzoni, S., McKenna, F., Scott, M. H. and Fenves, G. L. (2007), 'Opensees command language manual'. `https://opensees.berkeley.edu/wiki/index.php/Command_Manual`.

McKenna, F., Fenves, G. L. and Scott, M. H. (2000), 'Open system for earthquake engineering simulation'. `http://opensees.berkeley.edu`.

Mohamad, R. and Dobry, R. (1986), 'Undrained monotonic and cycli triaxial strength of sand', *Journal of Geotechnical Engineering, ASCE* 112(10), 941–958.

Mróz, Z. (1967), 'On the description of anisotropic workhardening', *Journal of the Mechanics and Physics of Solids* 15(3), 163 – 175.
URL: *http://www.sciencedirect.com/science/article/pii/0022509667900300*

Parra-Colmenares, E. J. (1996), Numerical modeling of liquefaction and lateral ground deformation including cyclic mobility and dilation response in soil systems, PhD thesis, Dept. of Civil Engineering, Rensselaer Polytechnic Institute.

PEER library (2021), 'Pacific earthquake engineering research center'. `https://peer.berkeley.edu/`.

Plaxis 2D Reference Manual (2020), *Plaxis 2D Reference Manual*, Bentley, (https://communities.bentley.com/products/geotech-analysis/w/plaxis-soilvision-wiki/46137/manuals—plaxis).

Prevost, J. H. (1985), 'A simple plasticity theory for frictional cohesionless soils', *International Journal of Soil Dynamics and Earthquake Engineering* 4(1), 9 – 17.
URL: *http://www.sciencedirect.com/science/article/pii/0261727785900300*

Theocharis, K.-K. (2020), *Gid+OpenSees User manual 2020*, School of Civil Engineering Aristotle University of Thessaloniki, Greece.

T.Olalo, L., Choo, Y. W. and Bae, K.-T. (2016), 'Influence of the skirt on the seismic response of bucket foundations for offshore wind tower using dynamic centrifuge model tests', *Proceedings of the ASME 2016 35th International Conference on Ocean, Offshore and Arctic Engineering, June 19-24* OMAE2016-54739.

Vaid, Y. and Chern, J. (1958), 'Cyclic and monotonic undrained response of saturated sands', *Advances in the Art of Testing Soils under Cyclic Conditions, ASCE, New York* pp. 120–147.

Wang, X., Yang, X. and Zeng, X. (2017), 'Seismic centrifuge modelling of suction bucket foundation for offshore wind turbine', *Renewable Energy* 114, 1013–1022.

Yang, Z. (2000), Numerical modeling of earthquake site response including dilation and liquefaction, PhD thesis, Columbia University.

Yang, Z., Elgamal, A. and Parra, E. (2000), 'Computational model for cyclic mobility and associated shear deformation', *Journal of Geotechnical and Geoenvironmental Engineering* 129(12), 1119–1127. Cited By :257.
URL: *www.scopus.com*

Yu, H., Zeng, X. and Lian, J. (2014), 'Seismic Behaviour of Offshore Wind Turbine with Suction Caisson Foundation', *Geo-Congress 2014 February 23-26, 2014, Atlanta, Georgia* pp. 1206–1214.

Zhang, Y., Conte, J. P., Yang, Z., Elgamal, A., Bielak, J. and Acero, G. (2018), 'Two-dimensional Nonlinear Earthquake Response Analysis of a Bridge-Foundation-Ground System', *Earthquake Spectra* 24(2), 343–386.

Ziotopoulou, K. (2018), 'Seismic response of liquefiable sloping ground: Class a and c numerical predictions of centrifuge model responses', *Soil Dynamics and Earthquake Engineering* 113, 744–757.
URL: *https://www.sciencedirect.com/science/article/pii/S0267726117300908*

Appendices

Dynamic soil response

A

A.1 Seismic waves

The earthquake motion is transmitted by seismic waves which can be divided into two main groups, body waves and surface waves. Body waves are able to travel through the interior of the earth and they are also divided into two different types.

- *Primary waves (P-waves).* They are known as compressional waves and induce a successive compression and rarefactions of the material which they pass so that the motion induced is parallel to the direction of the wave propagation. They are able to travel through solid and fluids. The velocity of propagation can be calculated following the Equation A.1 (Kramer, 1996).

$$v_p = \sqrt{\frac{G(2-2\nu)}{\rho(1-2\nu)}} \tag{A.1}$$

where,

v_p	Velocity propagation of P-waves
G	Shear modulus
ρ	Density of the soil
ν	Poisson's ratio

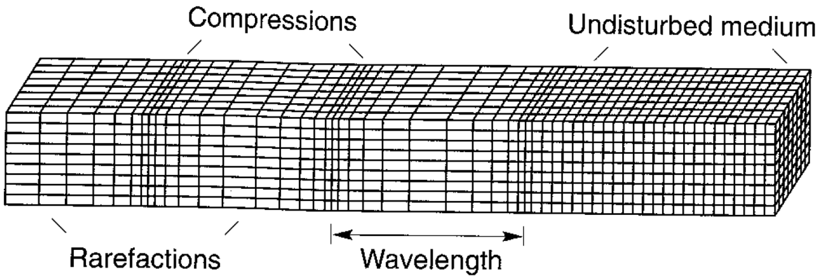

Figure A.1. Primary seismic waves, P-waves. (Kramer, 1996).

- *Secondary waves (S-waves).* Also known as shear waves, they are able to cause shearing deformation as they travel through a material so that the motion induced to a particle is perpendicular to the direction of the wave propagation. Due to its characteristics, they are able to travel just through solid bodies. This fact explains the smaller response of the soil particles after the liquefaction. The velocity of propagation can be calculated following the Equation A.2 (Kramer, 1996).

$$v_s = \sqrt{\frac{G}{\rho}} \tag{A.2}$$

where,

v_s	Velocity propagation of S-waves
G	Shear modulus
ρ	Density of the soil

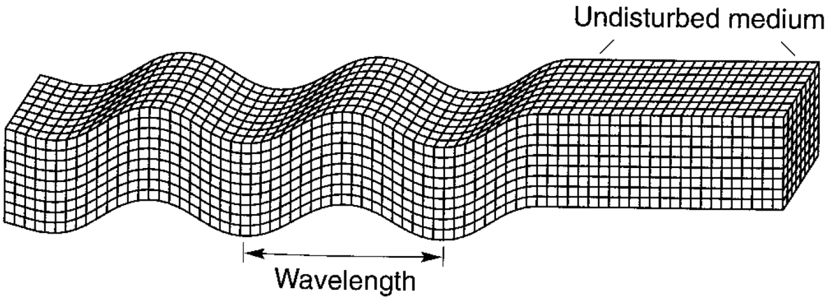

Figure A.2. Secondary seismic waves, S-waves. (Kramer, 1996).

As far as the surface waves are concerned, they are produced due to the interaction between body waves and superficial layers of the earth. The most important surface waves to take into consideration for civil structures are the Rayleigh waves and the Love waves.

- *Rayleigh waves.* They are generated by the interaction between *Primary waves* and the vertical component of the *Secondary waves* with the surface of earth. Thus, they involve both vertical and horizontal particle motion.

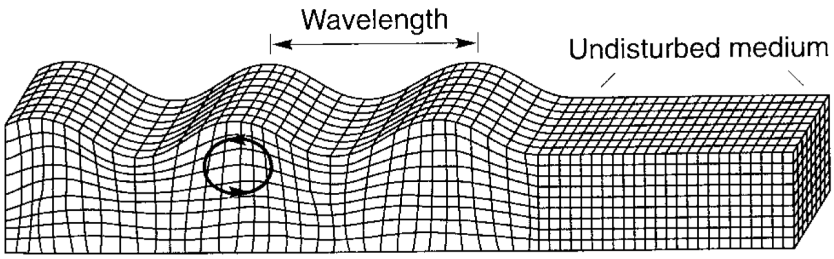

Figure A.3. Surface waves, Rayleigh waves. (Kramer, 1996).

- *Love waves.* By the interaction of the horizontal component of *Secondary waves* and the soft superficial soil layers, this waves are induced. They do not count with vertical component of particle motion.

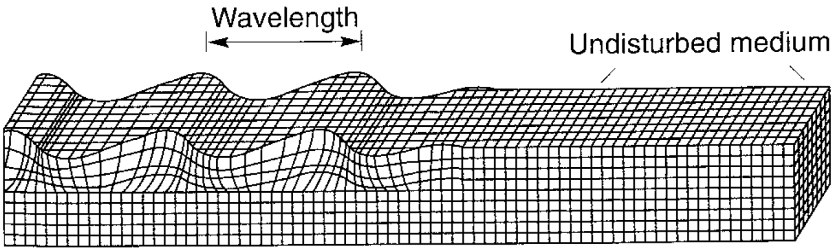

Figure A.4. Surface waves, Love waves. (Kramer, 1996).

A.2 Liquefaction mechanism

A.2.1 Phenomena susceptibility

The event of an earthquake does not involves necessarily the triggering of liquefaction. The susceptibility to liquefaction of a certain soil can be addressed according to some criteria which may include historical, geological, compositional and state features. In some cases, these criteria may be different from flow liquefaction to cyclic mobility.

Historical criteria

Most of the knowledge about liquefaction comes from the post-earthquake field observations. In order to find if a specific site may be prone to liquefy, its case histories need to be studied. Therefore, if historical investigations show the triggering of liquefaction in a certain area, it needs to be taken into consideration that this site is likely to liquefy again during the performance of future earthquakes.

Geologic criteria

The depositional processes, hydrological environment and the age of the deposit contribute to the tendency to liquefy of the soil.

Processes which involves an uniform grain distribution with loose states, like fluvial deposit, present a high liquefaction susceptibility. Moreover, since liquefaction occurs only in saturated soils, the depth of the groundwater becomes also a key feature so that the deeper is the water level, the smaller is the tendency to liquefaction of a deposit. Thus, this phenomena is more likely observed where the water table is within a few meters of the surface.

Compositional criteria

The composition characteristics related with the volume changes of the soil influence the liquefaction susceptibility of it since this phenomena is related with the generation of excess pore water pressure. Therefore, it is usually assumed that liquefaction is an event occurring mainly in sandy soils although it has been also observed in nonplastic cohesionless silts.

Another features as the gradation and the particle shape can also influence liquefaction susceptibility. Thus, poorly graded soils and rounded particle shapes are more prone to trigger this phenomena.

State criteria

The liquefaction susceptibility of the soil also depend on the initial state of the soil, in other words, the state of stresses and density characteristics at the time of the earthquake. The state of a soil can be evaluated in *e-p-q'* space and its tendency to liquefaction according to its position respect to the so-called *steady-state line* (SSL) at mentioned space. This line is constructed by the locus of points describing the relationship between void ratio, effective confining pressure and shear strength in the steady state of deformation as observed in Figure A.5.

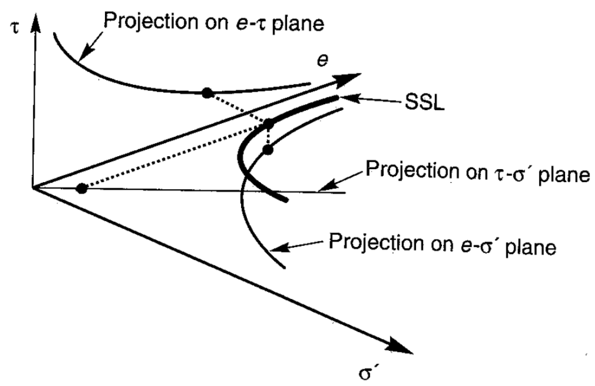

Figure A.5. Three dimensional steady state line represented on *e-p-q'* space. (Kramer, 1996)

The steady state of deformation is defined as *"the state in which the soil flows continuously under constant shear stress and constant effective confining pressure at constant volume and constant velocity"* (Kramer, 1996). This event was well illustrated by (Castro, 1969) after the performing of several static and cyclic triaxial tests on isotropically consolidated specimens and some static tests on anisotropically consolidated specimens.

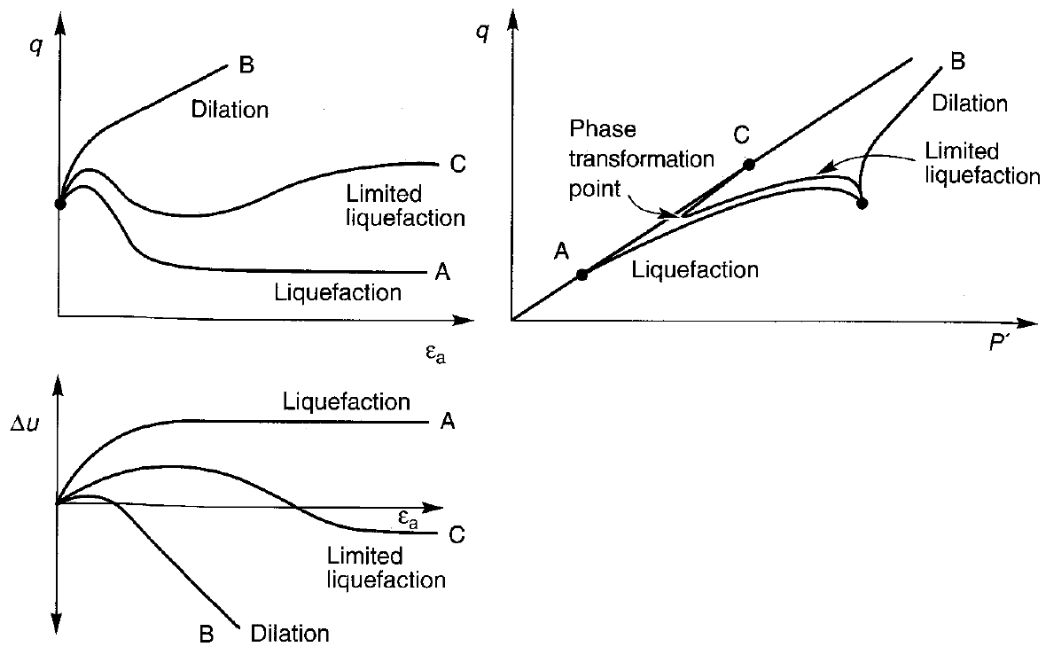

Figure A.6. Results obtained after monotonic loading test by (Castro, 1969). (Kramer, 1996)

As observed in Figure A.6, very loose specimens, characterized with the letter A, reached a peak of strength at a small shear strain before collapsing and developing large shear strains together with a high value of pore water pressure which made the effective confining pressure to drop significantly.

On the other hand, dense specimens, named with the letter B, showed contractive behaviour during the very initial stage, but then dilated until reaching a high constant effective confining pressure while great strain-strength was acquired. Moreover, was observed a negative generation of pore water pressure due to the "vacuum effect".

Intermediate dense specimens, letter C, reached also a peak strength at low axial strains which was followed by a strain-softening behaviour similar to the one observed at specimen A. The cause of this behaviour, as in the case of the loose specimen, was the generation of positive pore water pressure. Nevertheless, a dilative phase followed that stage which made the pore water pressure to decrease again. This change from contractive from dilative occur at the so-called *phase transformation point.*

The conclusion after the test performed was the finding of an unique relationship between void ratio e and effective confining pressure p' which would be used later for defining the locus of points known as *steady-state line (SSL)*, illustrated above, Figure A.5. Thus, the *SSL* establishes the conditions under which a certain soil is susceptible or not to trigger flow liquefaction as observed in Figure A.7.

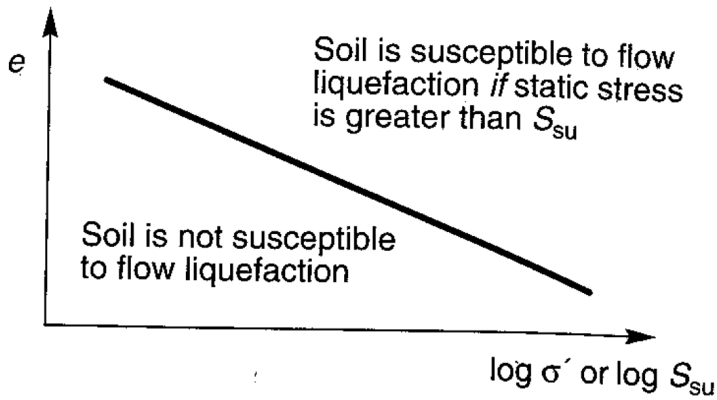

Figure A.7. Flow liquefaction susceptibility. (Kramer, 1996)

Despite of the showed relationship, liquefaction might be triggered even in a soil located below the *SSL* due to the effects of cyclic mobility, which can be triggered in both loose and dense soils. Prior to explain this phenomena, the *Flow Liquefaction Surface* need to be introduced.

Five different specimens with the same void ratio but with different effective confining pressure are considered. Since all of them count with the same density, the same effective stress conditions at steady state are reached but following different paths. As observed in Figure A.8, due to the location of A and B below the *SSL*, a dilative behaviour is observed on them during shearing. The opposite performance is observed on the specimens C, D and E whose behaviour is contractive.

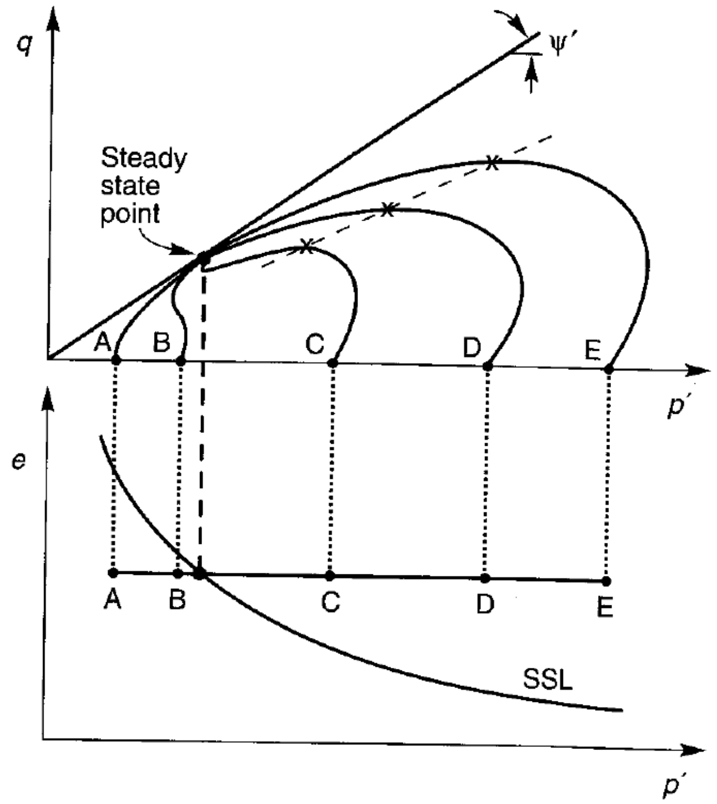

Figure A.8. Response of five specimens with similar void ratio at different initial effective confining pressures. (Kramer, 1996)

Specimens C, D and E reach a peak undrained strength after which they experience a sudden decrease of effective confining pressure due to the generation of pore water pressure which leads them toward the steady state. The line which joins the observed peak shear strengths is known as *Flow Liquefaction Surface (FLS)*, see Figure A.8, proposed with a different name by (Vaid and Chern, 1958). This line establishes the boundary between stable and unstable states during undrained shear and it is truncated below the steady-state point since flow liquefaction can not occur at that level, see Figure A.9.

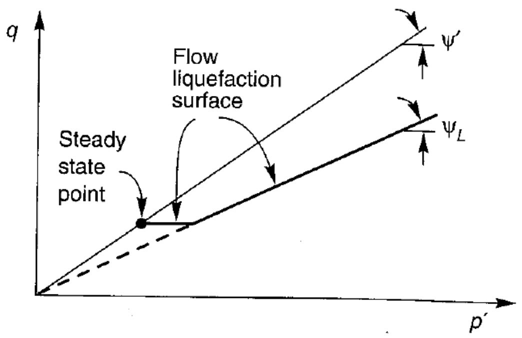

Figure A.9. *Flow Liquefaction Surface* in stress path space. (Kramer, 1996)

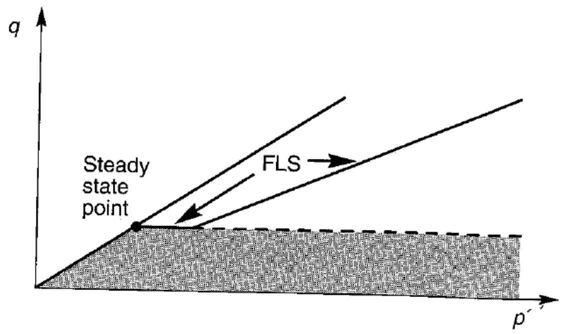

Figure A.10. Zone of susceptibility to cyclic mobility.(Kramer, 1996)

Nonetheless, liquefaction can be triggered due to cyclic mobility even when the static shear stress is smaller than steady-state shear strength, see Figure A.10. Three different scenarios are usually observed.

- **First scenario** ($\tau_{static} - \tau_{cyc} > 0$ $\tau_{static} + \tau_{cyc} < S_{su}$). The effective stress path moves to the left due to the generation of positive pore water pressure until the drained failure envelope is reached. Figure A.11a.
- **Second scenario** ($\tau_{static} - \tau_{cyc} > 0$ $\tau_{static} + \tau_{cyc} > S_{su}$). Once again, due to the generation of pore water pressure, the stress path moves to the left but, in this case, the FLS is momentary touched provoking periods of instability. Important permanent strains can develop during these periods but straining will cease when the loading returns to τ_{static}. Figure A.11b.
- **Third scenario** ($\tau_{static} - \tau_{cyc} < 0$ $\tau_{static} + \tau_{cyc} < S_{su}$). In this case, each cycle includes compression and tension loading. Due to this fact, the generation of pore water pressure is quicker so the stress path reaches faster the drained failure envelope (Dobry et al., 1982)(Mohamad and Dobry, 1986). Figure A.11c.

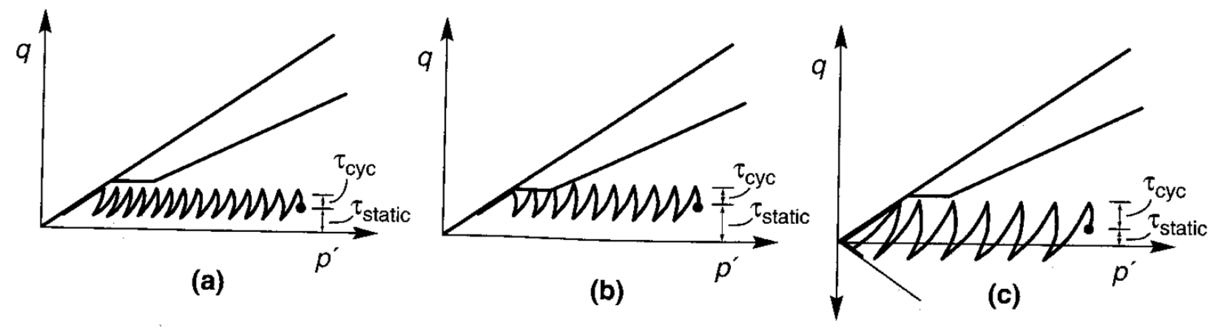

Figure A.11. Three common scenarios of cyclic mobility a) no stress reversal and no exceedance of steady-state strength, b) no stress reversal and exceedance of steady-state strength, c) stress reversal and no exceedance of steady-state strength. (Kramer, 1996)

Code construction guidelines B

In the present chapter of the Appendix, the construction of the code for generating the numerical model described at Section 4 is explained in detail.

B.1 Geometry of the model

B.1.1 Geometry of the soil domain

As mentioned in that section, the construction of the geometry of the model has been carried by the use of the software *Gid+OpenSees* due to the large amount of nodes of the soil domain. This program defines in the *.tcl* code every single node with lines similar to the following ones.

```
node 1 -13.25 -4.5

node 2 -13 -4.5

node 3 -13.25 -4.25

node 4 -13 -4.25
```

For instance, the first line showed creates a node tagged as 1 with x-coordinate equal to -13.25 and y-coordinated equal to -4.5.

Once the nodes are created, the restraints defining the boundary conditions of the model are set according to the Figure 4.15.Thus, for the gravity analysis, the nodes at the bottom are set as fixed for displacements along x and y, and free for generating pore water pressure. As an example, observe the following line of the *.tcl* code which fix the node tagged as 1, located at the bottom, according to the mentioned restraints.

```
fix 1 1 1 0
```

On the other hand, the lateral boundaries are set as fixed for displacement along x direction but free along y, allowing also the generation of pore water pressure. See the code line corresponding to the node tagged as 3.

```
fix 3 1 0 0
```

Finally, the boundaries of the surface are set as free for displacements along x and y directions, but the generation of pore water pressure is not allowed. The restraints of the node 277 located a the surface shows then as follow.

```
fix 277 0 0 1
```

Before creating the elements which compose the soil domain, the material establishing the constitutive behaviour of the elements need to be defined. In the case of the current report, as mentioned in the Chapter 4, two different materials are tested, *PressureDependentMaterialMultiYield* (*PDMY01*) and Plastic Model for Sands (*PM4Sand*). In the case of the first mentioned, the *.tcl* line for invoking it looks as follow.

```
nDMaterial PressureDependMultiYield $tag $nd $rho $refShearModul $refBulkModul
$frictionAng $peakShearStra $refPress $pressDependCoe $PTAng $contrac $dilat1
$dilat2 $liquefac1 $liquefac2 $liquefac3 <$noYieldSurf=20 <$r1 $Gs1 ...> $e=0.6
$cs1=0.9 $cs2=0.02 $cs3=0.7 $pa=101 <$c=0.3»
```

All the variables preceded by the symbol $ are substituted by numerical values defining the tag, number of dimensions and the inputs parameters of the material whose calibrated values are presented at Table 5.3. The definition of each of the variable is showed at the Table 4.4.

In the case of *PM4Sand*, the code looks as follow.

```
nDMaterial PM4Sand $matTag $Dr $G0 $hpo $rho $Patm $h0 $emax $emin $nb $nd $Ado
$zmax $cz $ce $phicv $nu $Cgd $Cdr $ckaf $Q $R $m_m $Fsed_min $p_sedo
```

Following the same logic than the previous material, the variables preceded by the symbol $ are used for tagging the material and for defining the input parameter of it. The definition of each of the variable is presented at the Chapter 4 and summarized in the Table B.1. The calibrated parameters of *PM4Sand* are collected in the Table 5.4.

Definition	Symbol
Integer tag identifying material	$matTag
Relative density	$Dr
Shear modulus constant	$G0
Contraction rate parameter	$hpo
Mass density of the material	$Den
Atmospheric pressure	$P_atm
Ratio plastic modulus to elastic modulus	$h0
Maximum void ratio	$emax
Minimum void ratio	$emin
Bounding sourface parameter	$nb
Dilatancy surface parameter	$nd
Dilatancy parameter	$Ado
Fabric-dilatancy tensor parameter	$z_max
Fabric-dilatancy tensor parameter	$cz
Adjusting of rate of strain accumulation	$ce
Critical state effective friction angle	$phic
Poisson's ratio	$nu
Adjusting of degradation of elastic modulus	$cgd
Control of rotated dilatancy surface	$cdr
Control effect of static shear stress on plastic modulus	$ckaf
Critical state line parameter	$Q
Critical state line parameter	$R
Yield surface constant	$m
Control reduction factor of elastic modulus during reconsolidation	$Fsed_min
Mean effective stress up to which reconsolidation strains are enhanced	$p_sedo

Table B.1. Parameters used for characterization of PM4Sand material in *.tcl* code.

An important feature after defining the materials of the model is invoking the command *nDMaterial InitialStateAnalysisWrapper*. This command allows to set an initial state of stress of the soil defined by any *nDMaterial* not inducing any deformation on it. Otherwise, the initial geometry of the soil domain would be altered just by the application of the self-weight of the soil. The following code was used in the numerical model for creating a *nDMaterial InitialStateAnalysisWrapper* tagged with the number 3034, associated with another *nDMaterial* tagged as 1001, which can be *PDMY01* for instance, and for a 2 dimension analysis.

```
nDMaterial InitialStateAnalysisWrapper 3034 1001 2
```

Once all the nodes, the corresponding restraints and the material of the model are set, the elements composing the soil domain can be defined. The type of elements used is *element quadUP* which is illustrated at Figure 4.3 and whose characteristics are explained in detail at the Chapter 4.

As is explained also there, the size of it depends on the kind of material used so that its dimensions are 0.25m x 0.25m for *PDMY01* and 0.5m x 0.5 for *PM4Sand* in order to reduce the calculation time. Thus, the whole soil domain counts with 1908 *quadUP elements* in the case of *PDMY01* material, and 486 *quadUP elements* in the case of *PM4Sand*. Thus, the general form of the code defining this kind of element in *OpenSees* language shows as follow.

```
element quadUP $eleTag $iNode $jNode $kNode $lNode $thick $matTag $bulk $fmass
$hPerm $vPerm <$b1=0 $b2=0 $t=0>
```

In order to take a deeper overview in such command of *quadUPelement*, one specific element applied for our model is mentioned below. Particularly, this element contains four nodes connected to each other from the left to the right (*node* 282, *node* 273, *node* 276 and *node* 286 respectively). This element was tagged as 1 with the thickness considered as 1. Moreover, the material tag of 3034 was included in the *quadUPelement* command, with the main purpose of transferring all of soil constitutive model features to the element. When it comes to the next step, the undrained bulk modulus of $2.20E+06$ was defined for the element, which pointed out the changing in pore pressure and volumetric strain. After that, in this specific case, fluid mass density, horizontal and vertical permeability were defined as 1. Another important factor needed to be assigned as gravitational acceleration, particularly, -9.81 was applied for this element for the gravitation analysis in the proceeding task of analysis.

```
element quadUP 1 282 273 276 286 1 3034 2.20E+06 1 1 1 0 -9.81 0
```

B.1.2 Geometry of the structure domain

After finishing the works related to the soil model aspects, the structure domain (wind turbine and suction bucket) was defined through 4 main parts as follows structural nodes, masses, elements and connection between soil and structure.

Structural nodes defining

The same code mentioned before defining soil nodes was used for the structural node defining illustrated as the command below.

```
node 868 -2 -1.75
```

the soil node at the location of -2 in x-axis and -1.75 in y-axis was defined according to such command. The process continued to be conducted with such command until finishing defining all nodes of superstructure.

Structural masses defining

After finishing the structure node defining, the weight of the superstructure was defined through the lumped-masses applying for a specific node at the top of the wind turbine as shown in the figure . In order to interpret the defining command, one realistic example of this task is shown as in the command below.

```
set mass1 29.3

mass 3047 mass1 mass1 1e-9

pattern Plain 21 Constant

load 3047 0 [expr ((-1*((1*mass1)*9.81)))] 0
```

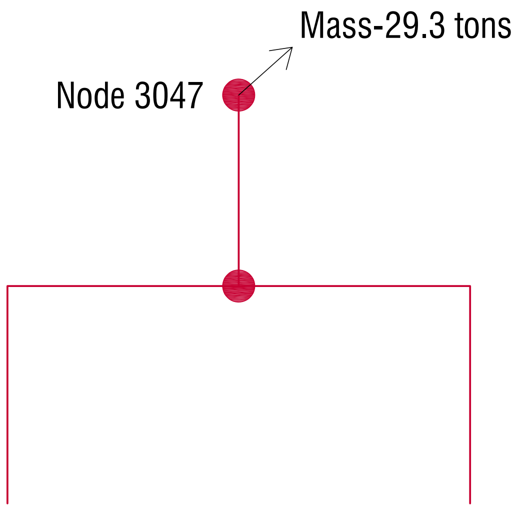

Figure B.1. Relative state parameter index ζ_R in terms of relative density D_R and mean effective stress (Boulanger and Ziotopuolou, 2017)

The function of those commands above is to define the mass as $29.3 - ton$ at the node 3047, with the multiplication factor as the gravitational acceleration of 9.81.

Structural element defining

Regarding the following step, the element defining of the structure is taken into account. One example mentioned below is useful to take an overview of this task.

```
element elasticBeamColumn 1909 868 874 0.25 2.1e+12 0.00520833 1 -mass 0 ;
```

The structure of the command above is similar to the command defining *quadUP* element. Particularly, the element was tagged as 1909 connecting 2 different structure nodes (868 and 874). The section of this element was defined as 0.25. Besides, the Young modulus of this element was defined as $2.1e + 12$ which is approximately equivalent to the steel Young modulus. After that, the inertia moment was invoked for being assigned as 0.00520833. Another important factor defined for the next step was the geometric transformation tag, which governed the working mode of the structure elements, particularly, linear system was used according to the tag of 1. The last step is to define the mass of the element. In this case, it was defined as 0 with the main purpose of avoiding the automatic mass computation in Opensees software.

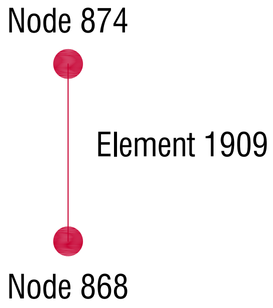

Figure B.2. Relative state parameter index ζ_R in terms of relative density D_R and mean effective stress (Boulanger and Ziotopuolou, 2017)

Connection between soil and structure nodes

In order to transfer the shaking motion of the earthquake from the soil nodes to the superstructure, the movement of the structure nodes was technically depended on the responses of the soil nodes. Specifically, one command as shown below was used for conducting such sake.

```
equalDOF 317 874 1
```

Taking a look at the command above, the soil node of 317 was connected with the structural node of 874 through the first degree of freedom - tag number one (horizontal displacement). In this report, all of the nodes at the sharp of the suction bucket were linked with the soil nodes through the first degree of freedom and the rest ones on the surface were connected with soil nodes through the second degree of freedom - tag number two (vertical displacement).

Besides, the structure nodes at the both sides of suction bucket were also connected with each other through the first degree of freedom, with the main purpose of getting the same horizontal movement of the suction bucket.

B.2 Analysis

B.2.1 Gravity analysis

Gravity analysis is the first fundamental analysis in any numerical simulation model. By implementing the flow paths of dead loads, this analysis brings out the determination how vertical loads are transmitted from the top to the foundation of the model. In this report, two components of dead load were taken into account such as self-weight of the model and the lumped-mass defined in the previous section. Interestingly, in this analysis, there are two kinds of soil behaviour taken into consideration, particularly elastic and elasto-plasitic standpoints. The command combination of gravity analysis assigning is shown as below.

```
integrator Newmark gamma beta

constraints Penalty 1.e20 1.e20

test EnergyIncr 1.0e-3 100 1

algorithm KrylovNewton

numberer RCM

system ProfileSPD

analysis Transient

analyze x y
```

First of all, the integrator object of the model was defined as Newmark controlled by two factors *gamma* and *beta*. After that, the constrain handler object was determined with the main purpose of implementing a specified value of a DOF, or a relationship between DOFs. When it comes to the test system of the model, energy increment was applied, being such that the convergence test provides the solution vector and the right hand side norm of the computation matrix equation when the convergence has been achieved.

In the following step, one important assignment was taken into account, which is the algorithm of the system. In this case, $KrylovNewton$ was used for solving the non-linear equation of the gravity analysis. $Numberer$ aspect of the model subsequently needed to be defined for controlling the mapping between the degree of freedom and the considered computational equation. The last feature of the gravity analysis was defined for the system, particularly $ProfileSPD$. The significant purpose of using such system is to store and compute the equation system in the analysis.

After assigning all of the characteristics of the analysis system, the command of specifying the performance of analysis type was used. In particular, transient analysis was applied for both elastic and elasto-plastic analyses. Finally, the number of steps and time-step were defined by the command *analyze* x y, in which x is the number of time step and y is the time step between each iteration.

Moreover, there is one important thing taken into account in the gravity analysis. That is the creation of the stress state. The fact is that during the gravity analysis, the self-weight of the soil brought the modification in the geometry, in terms of deformation, and the stress state also. Thus, with the idea of avoiding the affect of such problem in the proceeding analysis - dynamic analysis, the two commands mentioned below were used in this analysis.

```
InitialStateAnalysis on

InitialStateAnalysis off
```

Regarding the first one, the command was used to turn on the affect of the soil self-weight on the stress state and the geometry deformation as well in the elasto-plastic analysis. Subsequently, before going to dynamic analysis, the second command above was applied for deactivating such affect with the main purpose of avoiding the initial results of pore water pressure generated in the dynamic analysis.

It has to be mentioned that in case of *PM4Sand*, command *FirstCall* is used to set the back-stress ratio history terms equal to the current state and to erase all fabric terms. This command is activated after switching the analysis from elastic to elastic-plastic one and it will also consider that all secondary parameters assigned to a negative value in the code, e.g. $A_{do} = -1$, are determined with a default value following the guides of (Boulanger and Ziotopuolou, 2017). The *FirstCall* is assigned to value of zero. In case of dropping this term, the memory of the loading during static analysis would remain influencing the accuracy of the dynamic analysis. The command of assigning the *FirstCall* to a single element is presented below.

```
setParameter -value 0 -ele $i FirstCall 3034
```

Assigning the command to a whole domain is done by constructing the loop where all elements are considered. Another,very important command is considered in case of *PM4Sand*, termed *PostShake*. The command is responsible for improving the modelling of the post-liquefaction reconsolidation strains. The command is activated prior to shaking, and is assigned to value of zero, so that the modelling of reconsolidation strains is neglected during the intense motion. After the strong shaking period is gone, the command is activated by assigning the value of one to it. Again, the command is looped in order to consider the whole domain.

```
setParameter -value 0 -ele $i PostShake 3034
```

B.2.2 Dynamic analysis

Before the dynamic analysis is performed, the time domain is reset to zero and all loads are set as constant. Furthermore, all previous analysis objects are removed before employing dynamic ones. The commands are shown below.

```
loadConst -time 0.0
```

```
wipeAnalysis
```

Next step in code development consists in substituting the boundaries of the domain. This step is needed to construct boundaries according to (Lysmer and Kuhlemeyer, 1969). First, the lateral and bottom horizontal supports are removed following the command presented.

```
remove sp 100 1
```

The command removes the restrain at the node tagged 100 for the DOF of 1, meaning removing the horizontal restrains for the tagged node.

In order to apply viscous dashpots in form of *ZeroLength* elements at the nodes at the domain boundaries, a supplementary pack of nodes needs to be defined in the domain. Extra nodes are defined following the same command presented previously in Section B.1.1. Nodes added to the domain share the same coordinates as the ones placed at the domain boundaries. Basically, two packs of nodes are added to the temporary ones. One pack of nodes are considered fixed for all 3 DOFs and are assigned to be a master nodes. The other pack of nodes, termed as intermediate ones are fixed for rotational and vertical DOF, while for horizontal remain unrestrained. Intermediate are considered as slave nodes. *ZeroLength* element is defined between the fixed master node and the intermediate slave node. Intermediate slave nodes are then connected to the nodes of the already defined boundary nodes in domain via *equalDOF* command, which prescribe the same horizontal DOF on the boundaries as for the slave node. This way the geometrical part in modelling of dashpots according to (Lysmer and Kuhlemeyer, 1969) are handled in *OpenSees* software. This is well illustrated in Section 4.5, Figure 4.17. For further implementation, the material properties needs to be assigned to dashpots, here modelled by *ZeroLength* elements. The viscous material type introduced for this purpose is arranged with command *uniaxialMaterial*. Material type prescribed to *ZeroLength* is *Viscous* with damping coefficient calculated based on the Equation 4.6 and 4.5, depending on whether the material is prescribed on lateral or bottom side of the boundaries. The whole command is handled in *OpenSees* following next script.

```
uniaxialMaterial Viscous 15 [expr $dashpotCoeffbottom*$Area] 1

uniaxialMaterial Viscous 16 [expr $dashpotCoeffbottom*$Area] 1
```

The command tagged with 15 is assigned to the bottom while the tagged with 16 is assigned to the lateral boundaries. The value of 1 at the end of the script stands for power factor, in this case means linear damping is employed. Finally, the dashpot is modelled with *ZeroLength* type of the element, following the next command.

```
element zeroLength 99900 10000 20000 -mat 15 -dir 1
```

Here the element is tagged with 99900, using a node tagged with 10000 as a master node and the one tagged with 20000 as a slave node. The case presented uses a material tagged 15, meaning at the bottom boundary. Material direction is assigned to 1, meaning the horizontal DOF is prescribed.

After the implementation of viscous boundaries to the domain, the application of horizontal reaction forces to the boundary nodes are put in effect. The reaction forces are recorded during the gravity analysis and then substituted instead of removed restraints to attain confinement within the domain during the performance of the dynamic analysis. Load pattern command is enforced on all nodes of interest. Plain type pattern is used. This pattern incorporates a time series object, here defined as a constant, meaning it is independent of time. Constant load factors are prescribed to the nodes of interest. The example of the extracted script is presented as follows.

```
pattern Plain 22 Constant {

.

.

load 100 -0.694344 0 0

load 110 -0.858344 0 0

.

.

}
```

Load pattern Plain tagged 22 is applied as a constant time series. Reaction forces are introduced on the nodes of 100 and 110 in the horizontal direction in the form of a load factor of values of -0.694344 and -0.858344.

Before applying the earthquake loads, the permeabilities were updated before the dynamic analysis has started. Since the domain has been structured of 4 subdomains with different sets of permeabilities for each, an example of Domain 3 is shown.

```
set ctr 330000.0

set vPerm3 2.5e-4

set hPerm3 2.5e-4

for {set i 109} {$i <= 192} {incr i 1} {

    parameter [expr int($ctr+1.0)] element $i vPerm

    parameter [expr int($ctr+2.0)] element $i hPerm

    updateParameter [expr int($ctr+1.0)] $vPerm3

    updateParameter [expr int($ctr+2.0)] $hPerm3

    set ctr [expr $ctr+2.0]

}
```

The general tag base is created and assigned to a value of 330000.0, which is pulled through a loop in order to appoint to each element the corresponding parameter tag with specific values of permeability defined. Horizontal and vertical permeabilities are set to $2.5e-4$. Then command *updateParameter* is used to assign the defined permeability values to each element of the domain by invoking an appointed tag to it.

Three recorder objects are set to record the outputs of acceleration, excess pore water pressure, and settlement in the specified nodes of interest already mentioned in Section 3.2.

```
recorder Node -file $fileName -node $node# -time -dT 0.01 -dof 1 accel

recorder Node -file $fileName -node $node# -time -dT 0.01 -dof 2 disp

recorder Node -file $fileName -node $node# -time -dT 0.01 -dof 3 vel
```

Finally, the input motion of the synthetic earthquake is introduced before the dynamic analysis is executed. Input acceleration is translated in to the set of forces applied at the bottom and lateral boundaries following the expression presented in Equation 4.6 and 4.7. Using the special software *SeismoSignal* input acceleration record is converted to a velocity measure. To implement the converted motion into the domain following steps are conducted.

First, the timestep duration of the interval is defined. Then constant scaling factor for the applied velocity is set.

```
set Dt 0.01

set cFactor [expr $dashpotCoeffbottom*$Area]
```

Velocity timeseries is introduced and the the timeseries object is defined.

```
set mSeries "Path -dt $Dt -filePath $velocityFile -factor $cFactor"
```

At the end, loading is initiated by *Plain* loading pattern object associated with defined timeseries.

```
pattern Plain 10 $mSeries {
.
.
load 500 1 0 0
load 520 1 0 0
.
.
}
```

At the end the analysis object is defined specially for the dynamic part. Here different convergence test is used, *EnergyIncr*, and constraints handler object is operated by *Transformation* command. *Penalty* constraint handler is avoided for convergence issues and as recommended in (Mazzoni et al., 2007). Also different γ and β were applied for dynamic analysis in *Newmark* integrator. Applied γ equals 0.6 while β is calculated via built-in code expresseion.

```
integrator Newmark $gamma [expr pow($gamma+0.5, 2)/4]
test EnergyIncr 1.0e-3 100 1
constraints Transformation
algorithm KrylovNewton
numberer RCM
system ProfileSPD
rayleigh $a0 $a1 0.0 0.0
analysis Transient
analyze 2436 0.01
```

Obtaining of dynamic equivalent forces C

The approximation used for prescribing the input motion to the both boundaries of the model, see Section 4, allows the wave energy to not be radiated back into the soil medium.

The process for the obtaining an expression for the shear stress in the underlying medium at the bottom boundary is explained at (Joyner, 1975). For the case of this report, the same force obtained at the bottom is also applied to the lateral boundaries assuming that the centrifuge test is ran in a rigid box whose lateral boundaries are also transmitting seismic forces.

$$U_I = U_I(x + v_s t) \tag{C.1}$$

U_I	Particle displacement for the incident wave
x	Depth
v_s	Shear velocity of the underlying medium
t	Time

Following the same approach, the particle displacement of the reflected wave follows

$$U_R = U_R(x + v_s t) \tag{C.2}$$

U_R	Particle displacement for the reflected wave

The shear stress at the bottom boundary can be then computed as

$$\tau_B = \mu_E \left(\frac{\partial U_I}{\partial x} + \frac{\partial U_R}{\partial x} \right) \tag{C.3}$$

μ_E	Rigidity of the underlying medium

The partial differentiation of the particle displacement for the incident and the reflected wave respect to x can be rewritten as

$$\frac{\partial U_I}{\partial x} = \frac{1}{v_s} V_I \tag{C.4}$$

$$\frac{\partial U_R}{\partial x} = \frac{1}{v_s} V_R \tag{C.5}$$

V_I	Particle velocity for the incident wave
V_R	Particle velocity for the reflected wave

Thus, the particle velocity on the boundary can be expressed as the sum of the velocity of the incident and the reflected waves

$$V_B = V_R + V_I \tag{C.6}$$

Isolating the variable V_R and substituting in the Equation C.3, the following expression is obtained

$$\tau_B = \frac{\mu_E}{\nu_s}\,(2V_I + V_B) \tag{C.7}$$

or,

$$\tau_B = \rho_E\ \nu_s(2V_I + V_B) \tag{C.8}$$

ρ_E	Density of the underlying medium

This expression multiplied by the tributary area of each node is the one used for obtained the equivalent dynamic forces applied to the numerical model, see Equation 4.6.

Performance of numerical Cyclic Direct Shear Simple Test D

The general performance of the Cyclic Direct Simple Shear Test (CDSS) is explained at section 2.3. In order to simulate the same behaviour of a specimen but following a numerical approach, the following considerations are taken into account so as to carrying properly the element test of Toyoura Sand by the use of the software *OpenSees*.

D.1 Element implemented

The model domain counts with one single *SSPquadUP* element which is defined by four nodes and a single point of integration (Mazzoni et al., 2007), in contrast to *quadUP* element which count with four integration points, see Figure D.1 . This kind of element is indicated for dynamic analysis of fluid saturated porous media. As mentioned in the main report, it counts with three degree of freedom (DOF). The first two degrees of freedom, 1 and 2, account for the translations along x and y axis respectively, while the degree of freedom 3 controls the generation of pore water pressure.

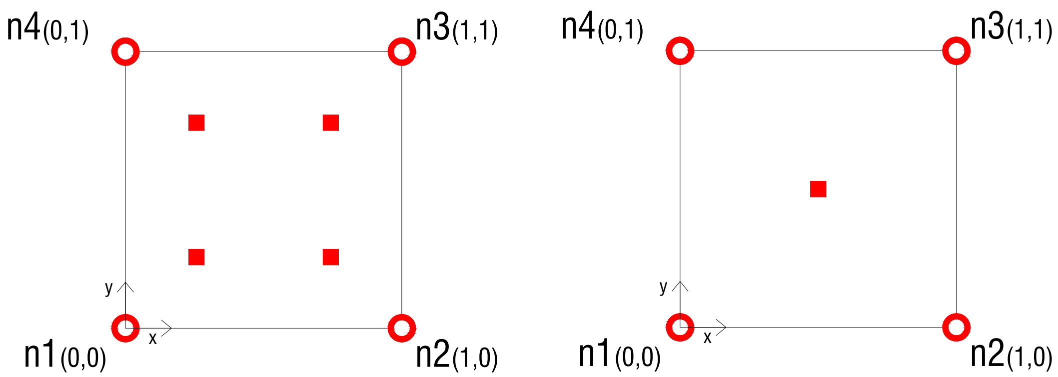

Figure D.1. (a) quadUP element (b) SSPquadUP element

D.2 Boundary conditions

A simple shear displacement mode is be implemented to the top nodes which allow the displacements along x and y axis. Regarding the bottom nodes, the translations along both axis is constrained. The generation of pore water pressure is restricted during the elastic phase of the analysis but it is switched on for the plastic stage.

D.3 Load pattern

Once the model is constructed, the load pattern follows the trend observed at Figure D.2a and it is applied according to the Figure D.2b . Thus, it can be observed that an initial value of vertical stress is implemented σ_{yy} and a certain shearing loading along the time with an amplitude equal to σ_{xy} and a predetermined number of cycles.

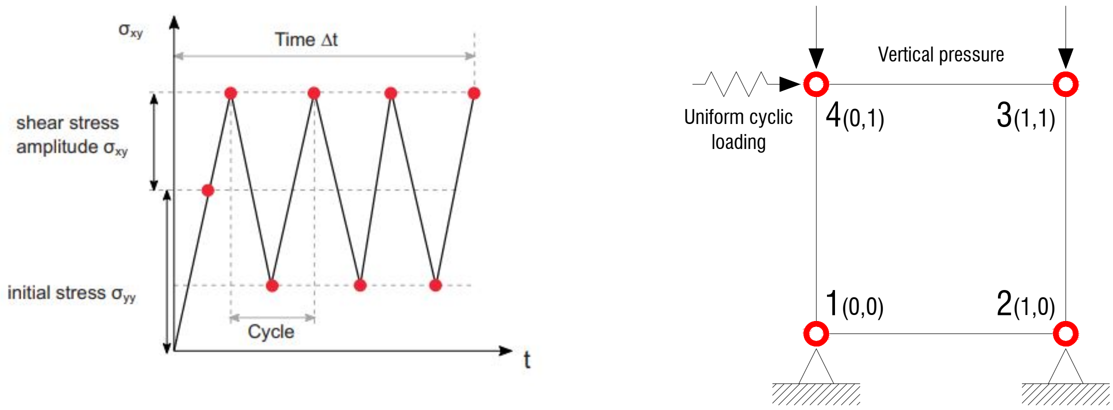

Figure D.2. (a) Load pattern applied to *SSPquadUP* element (Plaxis 2D Reference Manual, 2020) (b) Location of forces applied to *SSPquadUP* element

All the mentioned inputs together with the ones showed at Table D.1 can configured by the modification of the provided *.tcl* code. After setting the values of them, the calibration of parameters corresponding to the constitutive model *PM4Sand* can be initiated.

Parameter	Definition
Inital Vertical Stress σ'_{vo} *sigvo*	Initial effective overburden pressure. If any consolidation process is carried, its value correspond to the atmosphericpressure.
Cyclic Stress Ratio *CSR*	Ratio between the cyclic shear stress induced (τ_{cyc}) normalized to the initial effective overburden pressure (σ'_{vo}).
Maximum Number of Cycles *maxCycles*	Defines the number of load cycles performed during the test.
Strain Increment *strainIncr*	Increment of strain in term of volumetric and deviatoric components
At-rest coeffcient *K0*	Coefficient showing the ratio of horizontal to vertical effective stress
Poisson's ratio ν *nu*	Value of Poisson's ratio of the specimen tested.
Cutoff shear strain *devDisp*	Cutoff shear strain is the function of dilation angle showing the predicted dilatancy soil possibility
Permeability *perm*	Property of the soil which defines its capacity to transmit water through its voids. Also known as hydraulic conductivity.

Table D.1. Test parameters implemented in *OpenSees*.

Model calibration

E

E.1 Calibration based on PDMY01

E.1.1 Generation of pore water pressure at the free field

Contraction parameter

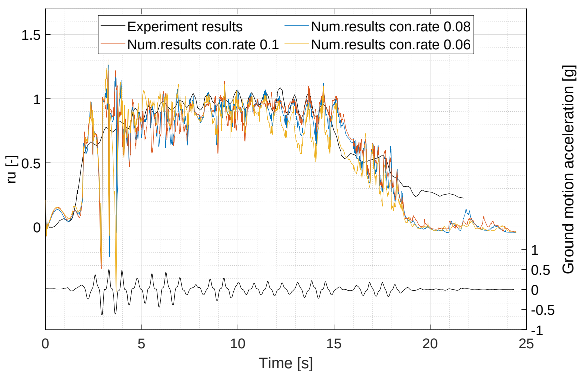

Figure E.1. Pore water pressure ratio of sensor P2 at the location of x=6m and y=-0.5m.

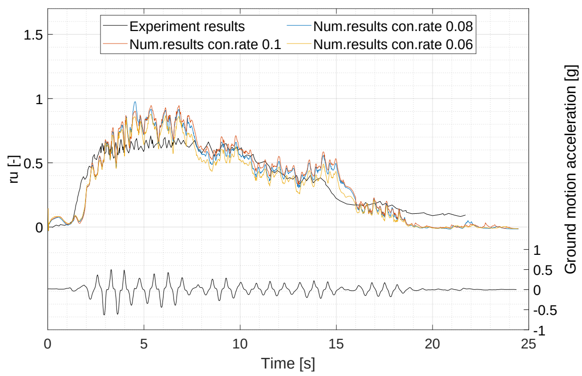

Figure E.2. Pore water pressure ratio of sensor P4 at the location of x=6m and y=-2.5m.

Permeability

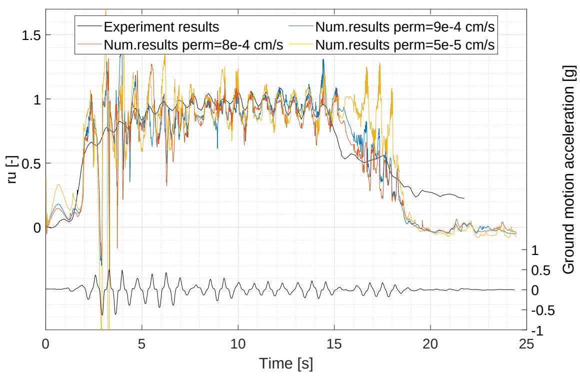

Figure E.3. Pore water pressure ratio of sensor P2 at the location of x=6m and y=-0.5m.

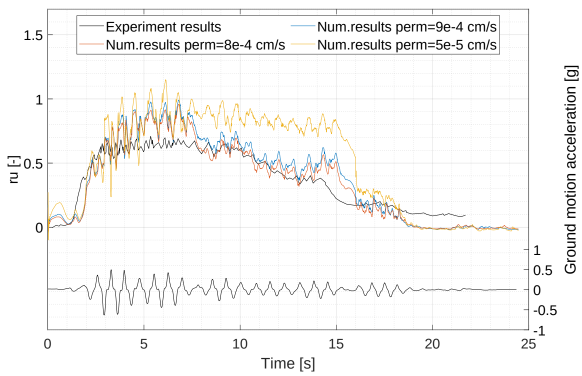

Figure E.4. Pore water pressure ratio of sensor P4 at the location of x=6m and y=-2.5m.

Density

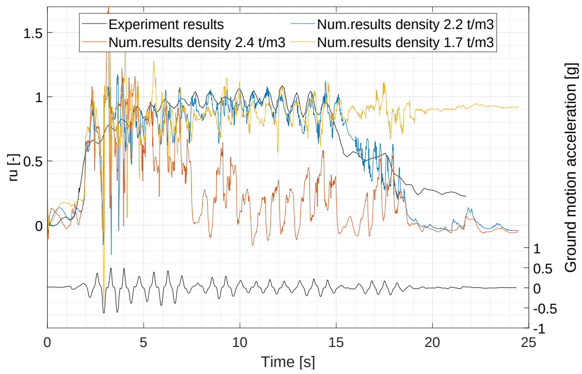

Figure E.5. Pore water pressure ratio of sensor P2 at the location of x=6m and y=-0.5m.

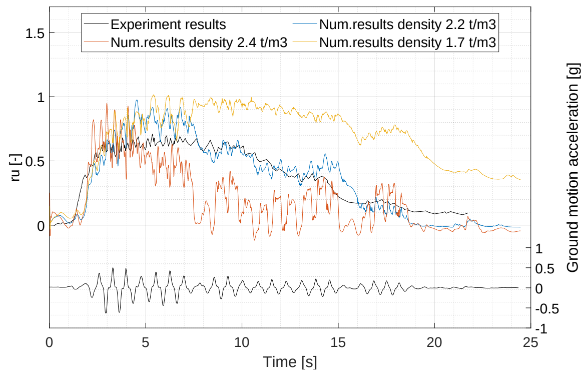

Figure E.6. Pore water pressure ratio of sensor P4 at the location of x=6m and y=-2.5m.

E.1.2 Settlement

Shear modulus

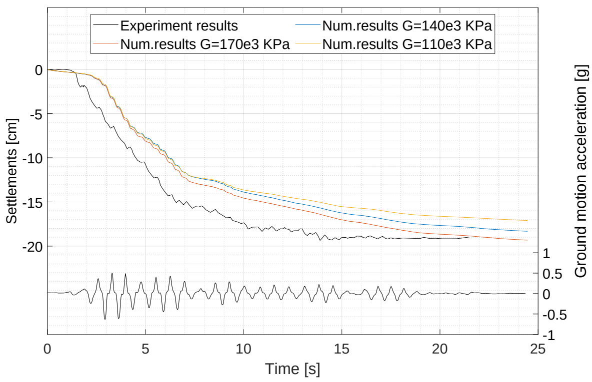

Figure E.7. Settlement with different values of density.

Friction angle

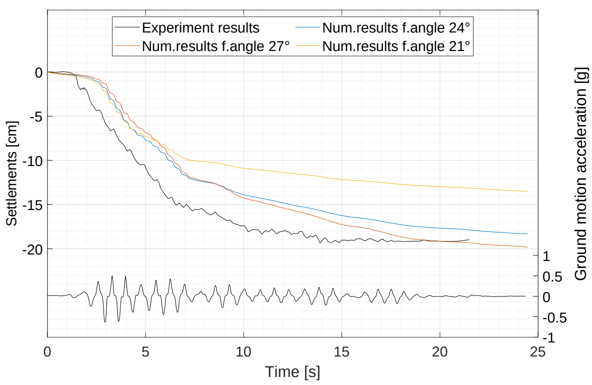

Figure E.8. Settlement with different values of friction angle.

Density

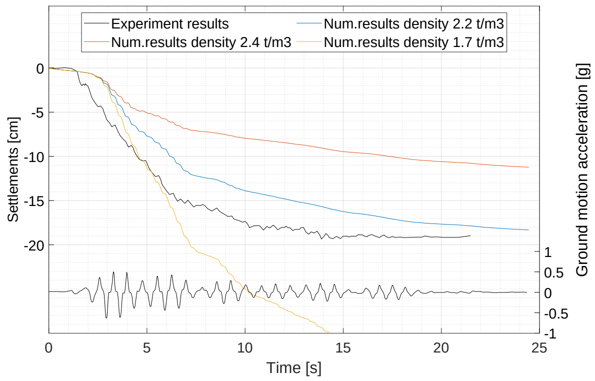

Figure E.9. Settlement with different values of density.

E.1.3 Generation of pore water pressure at the vicinity of the structure

Friction angle

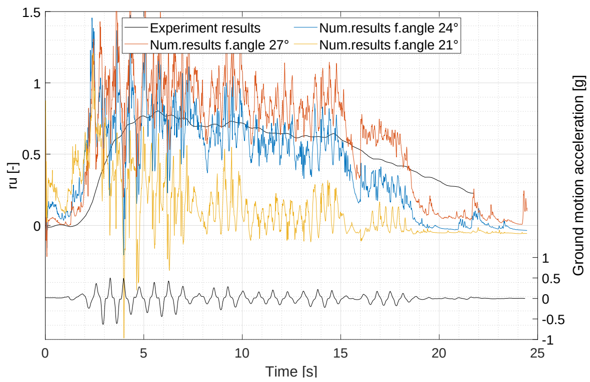

Figure E.10. Pore water pressure ratio of sensor P1 at the location of x=0m and y=-0.5m.

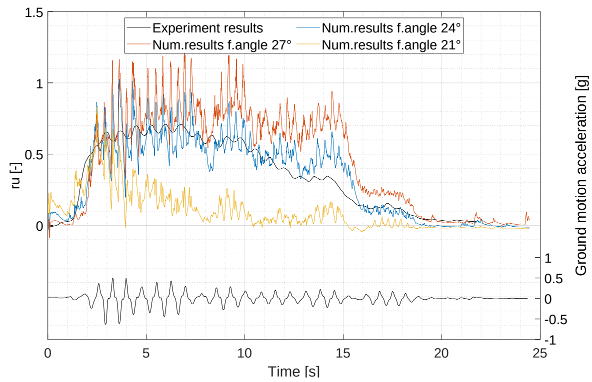

Figure E.11. Pore water pressure ratio of sensor P3 at the location of x=0m and y=-2.5m.

Phase angle

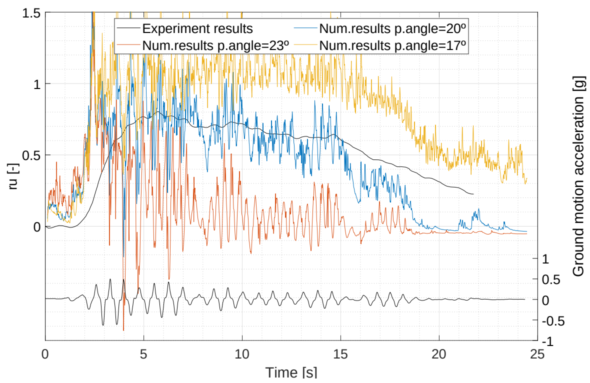

Figure E.12. Pore water pressure ratio of sensor P1 at the location of x=0m and y=-0.5m.

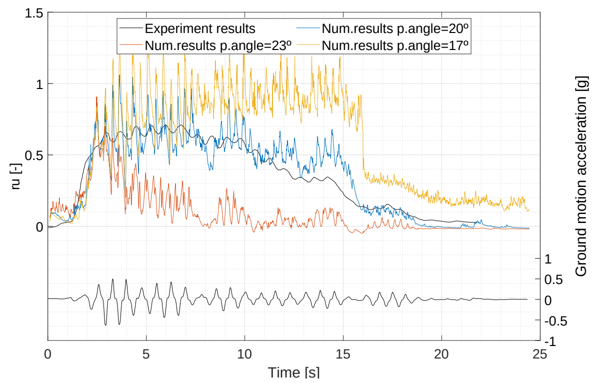

Figure E.13. Pore water pressure ratio of sensor P3 at the location of x=0m and y=-2.5m.

Bulk modulus

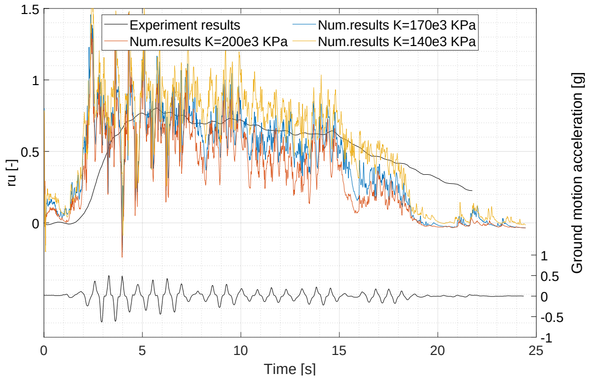

Figure E.14. Pore water pressure ratio of sensor P1 at the location of x=0m and y=-0.5m.

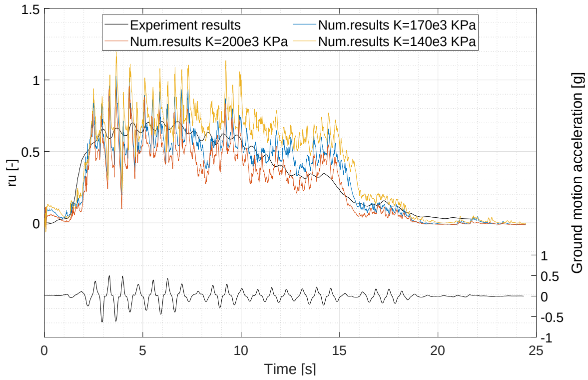

Figure E.15. Pore water pressure ratio of sensor P3 at the location of x=0m and y=-2.5m.

Shear modulus

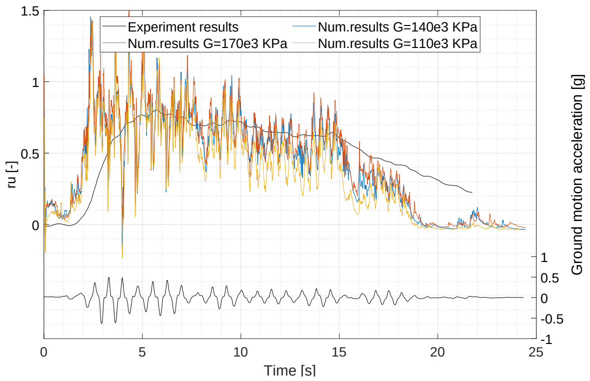

Figure E.16. Pore water pressure ratio of sensor P1 at the location of x=0m and y=-0.5m.

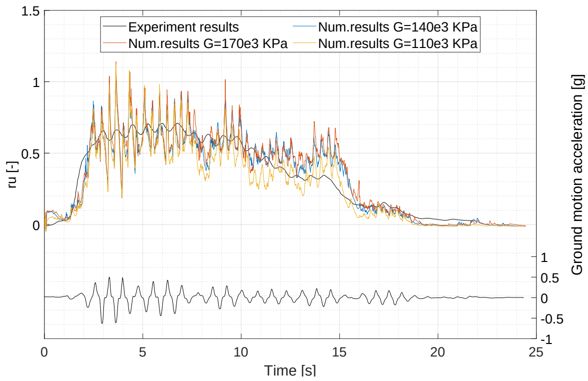

Figure E.17. Pore water pressure ratio of sensor P3 at the location of x=0m and y=-2.5m.

E.1.4 Acceleration recorders

Accelerations at the soil domain

Bulk modulus

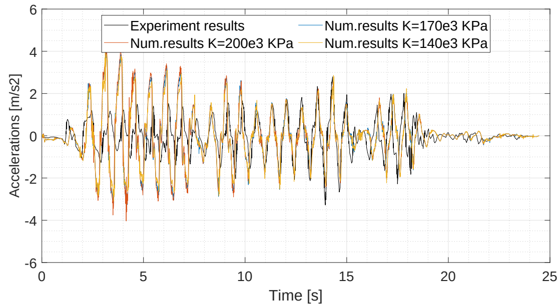

Figure E.18. Analysis nodal accelerations sensor A1 x=0m y=-0.5m.

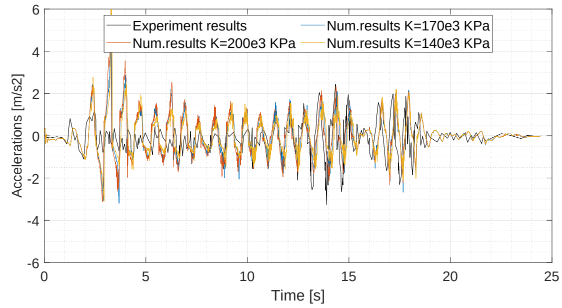

Figure E.19. Analysis spectral accelerations sensor A2 x=6m y=-0.5m.

Shear modulus

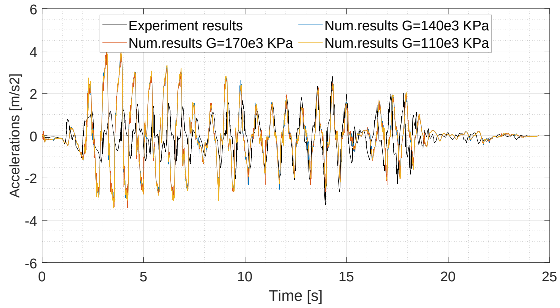

Figure E.20. Analysis nodal accelerations sensor A1 x=0m y=-0.5m.

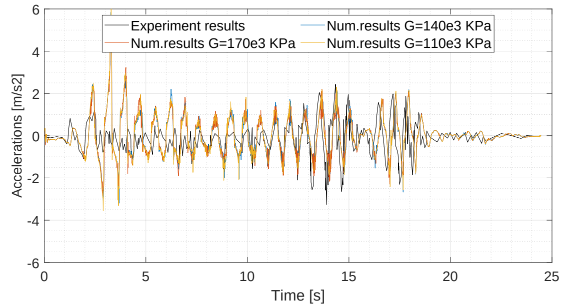

Figure E.21. Analysis spectral accelerations sensor A2 x=6m y=-0.5m.

Friction angle

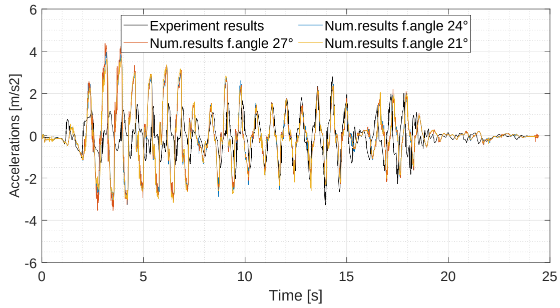

Figure E.22. Analysis nodal accelerations sensor A1 x=0m y=-0.5m.

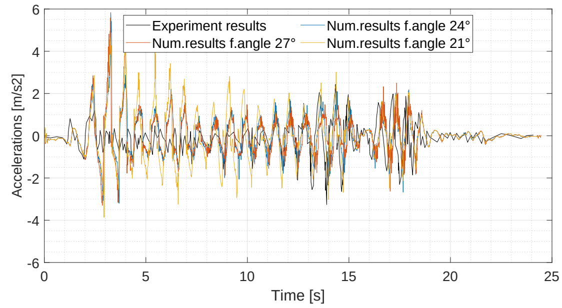

Figure E.23. Analysis spectral accelerations sensor A2 x=6m y=-0.5m.

Density

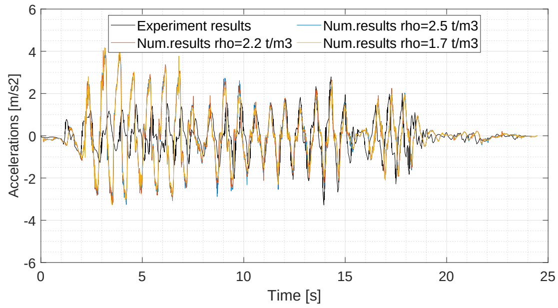

Figure E.24. Analysis nodal accelerations sensor A1 x=0m y=-0.5m.

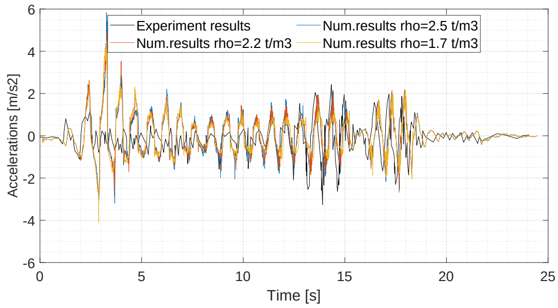

Figure E.25. Analysis spectral accelerations sensor A2 x=6m y=-0.5m.

Accelerations at the tip of the structure

Bulk modulus

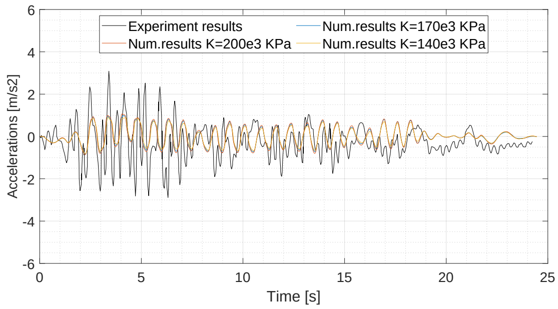

Figure E.26. Analysis nodal accelerations sensor A3 x=0m y=13.00m

Shear modulus

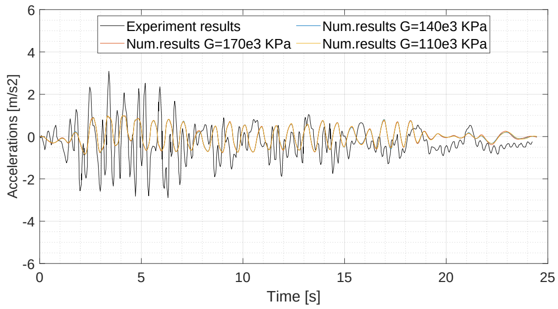

Figure E.27. Analysis nodal accelerations sensor A3 x=0m y=13.00m

Friction angle

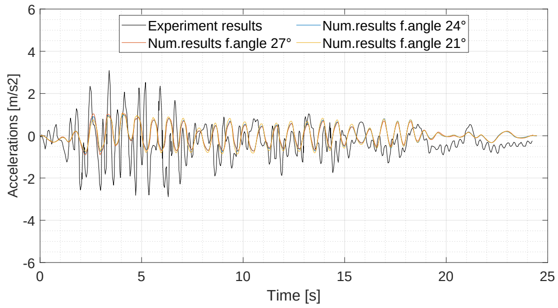

Figure E.28. Analysis nodal accelerations sensor A3 x=0m y=13.00m

Phase angle

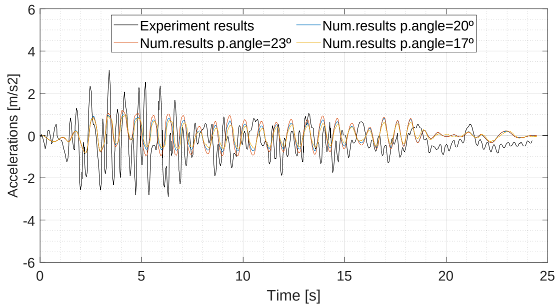

Figure E.29. Analysis nodal accelerations sensor A3 x=0m y=13.00m

Density

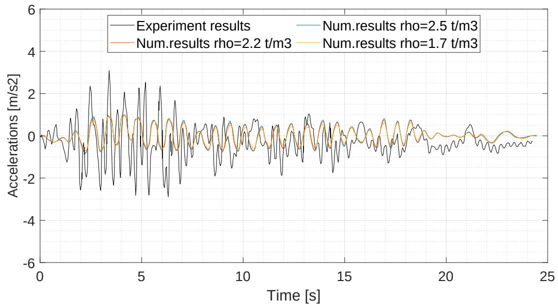

Figure E.30. Analysis nodal accelerations sensor A3 x=0m y=13.00m

Contraction parameter

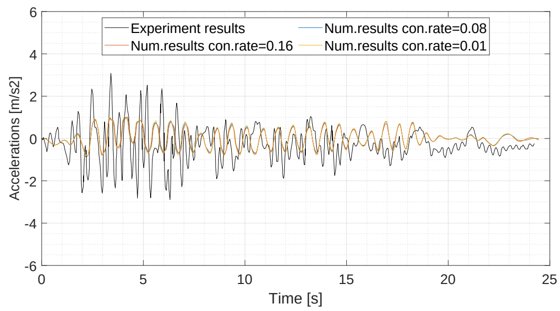

Figure E.31. Analysis nodal accelerations sensor A3 x=0m y=13.00m

Permeability

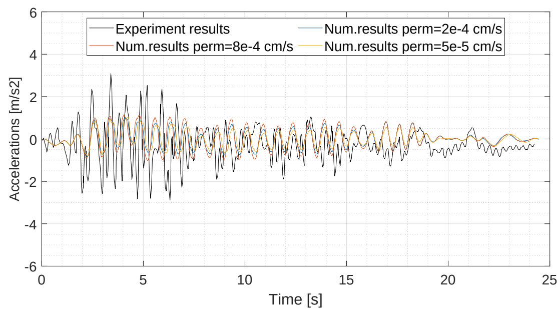

Figure E.32. Analysis nodal accelerations sensor A3 x=0m y=13.00m

E.2 Calibration based on PM4Sand

E.2.1 Generation of pore water pressure at the vicinity of the structure

The effects of three primary input parameters on the generation of excess pore water pressure in the free field are elaborated briefly in the main part of the report. Here, the findings during the calibration process regarding the sensors placed below the structure are presented and commented.

After catching the adapted curves of pore water pressure ratio versus experimental results in the free field, immediately, the identical requirement continues to be taken into account near the superstructure. Particularly, two sensors (P1 and P3) are invoked for the experimental comparison in terms of pore water pressure ratio. In addition, the locations of two such sensors were mentioned in the previous chapter.

Regarding the kind of considered parameters, three primary parameters are continued to be applied for the calibration assessment. However, the general pattern of soil responses remained unchanged, irrespective of any adjustment of up-mentioned parameters. Particularly, the generation of excess pore water pressure starts to occur around the third second, thereafter three seconds from that point, the immense spike of excess pore water pressure triggers and lasts for approximately two seconds. Additionally, at the end of the observed period, the excess pore water pressure dissipation initiates at around the seventeenth second.

Overall, the work of such three-parameter calibration is to capture the proper trends of excess pore water pressure in several crucial periods, for instance, the induced liquefaction or dissipation occasions.

Relative density D_R

As mentioned in the subsection of the free field calibration, the effect of volumetric strain is profoundly substantial on the changing of pore water pressure ratio. Especially for the domain under the bucket, such effect is even more interesting from the soil behaviour standpoint. In general, the soil under the bucket is subjected to the confinement pressure from the weight of the superstructure that leads to different soil responses and excess pore water pressure generation. Thus, the influence of relative density in this case is supposed to be altered by that fact. Consequently, three different values of relative density from the subsection of the free field calibration are again applied for getting the graphical evaluation in this subsection.

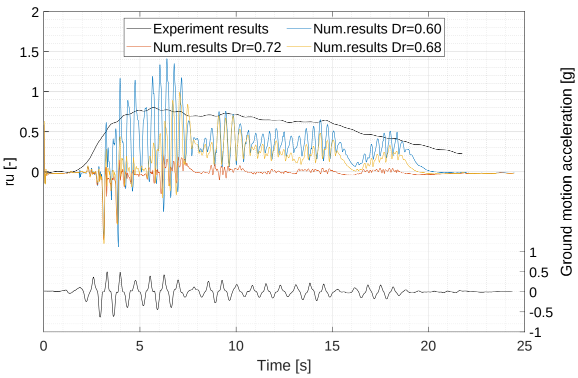

Figure E.33. Pore water pressure ratio of sensor P1 at the location of x=0m and y=-0.5m.

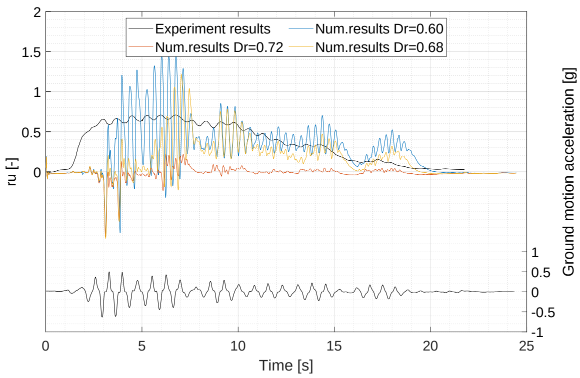

Figure E.34. Pore water pressure ratio of sensor P3 at the location of x=0m and y=-2.5m.

To achieve a visual understanding of D_R calibration affects in the vicinity of the bucket, taking a look at the two Figures E.33 and E.34 is required. Seemingly, the trend of 3 illustrated curves at P1 and P3 are almost identical to the curves at P2 and P4 in the free field. Particularly, the adjustment of relative density is still inversely proportional to the changing of pore water pressure ratio, due to the alteration mechanism of soil stiffness mentioned in the subsection of the free field calibration. For example, with the highest considered value as 0.72, the pore water pressure ratio still fluctuate around the zero value and remain unchanged trend until the end of the given period. However, apparently, the outputs of pore water pressure ratio near the structure are witnessed the less noise plotting curves, probably due to the effect of the soil confinement.

Besides, one more crucial distinction between the free field and near bucket is the dissipation phenomenon. It is evident that there is not any plummet part in the output plotting curves in terms of excess pore water pressure dissipation , with three values of relative density. This phenomenon implies that the excess pore water pressure are dissipated slower out of the soil particles in the domain under the bucket, compared to the domain in the free field. Moreover, the magnitude of excess pore water pressure recorders under the bucket are higher than those recorders in the free field, with the same depth level, due to the contact pressure between the soil and the structure.

Generally, the effects of relative density on calibration is significantly useful for getting the proper trend of pore water pressure ratio versus experimental results, in terms of generation and dissipation aspects.

Shear modulus coefficient G_0

As mentioned above in the subsection of the free field domain, the elastic soil behaviour is governed by controlling the magnitude of shear modulus coefficient. Thus, the dilative or compressive responses of the soil are also affected that leads to the changing in pore water pressure ratio. In order to get the visual overview of such influences,three different G_0 values as mentioned in the free field domain continue to be taken into account in the vicinity of the suction bucket as the Figures E.35 and E.36.

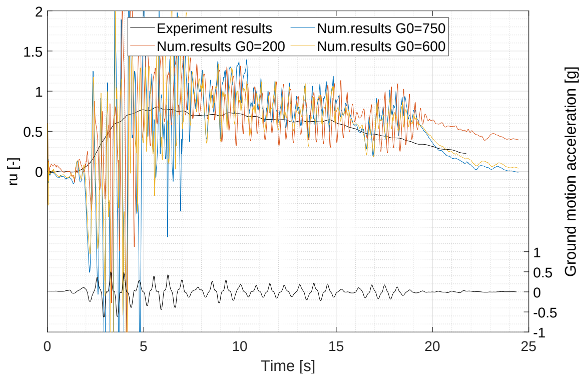

Figure E.35. Pore water pressure ratio of sensor P1 at the location of x=0m and y=-0.5m.

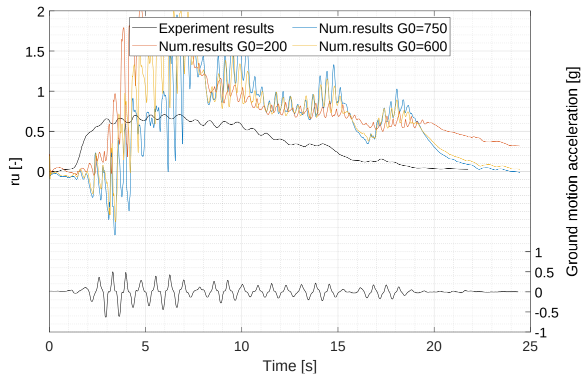

Figure E.36. Pore water pressure ratio of sensor P3 at the location of x=0m and y=-2.5m.

Taking a look at the two above figures, apparently, the adjustment of G_0 is inversely proportional to the updating of pore water pressure, theoretically the same as the operation mechanism of the soil in the free field under the calibration of shear modulus coefficient. For example, with the smallest considered value of G_0 as 200, the biggest peak point is witnessed that results in the favourable tendency of liquefaction triggering. Moreover, with smaller value of shear modulus coefficient, the pattern trend of pore water pressure ratio is lifted up slightly with much less noise in approximately the first 12 seconds. Another effect of decreasing G_0 is to suppress the dissipation phenomenon of excess pore water pressure. Therefore, the last part of the red curve is illustrated with the milder slopping compared to the two rest ones. Regarding the results with the highest considered value of G_0 as 750, the dilative soil behaviour is shown as more dominant than the others, evidently, the negative pore water pressure and dramatical fluctuation was depicted in the blue curve.

Overall, the work of shear modulus coefficient calibration can be used for controlling the soil response behaviour under the bucket effectively, in terms of the dilation behaviour aspects. Moreover, the manage of the excess pore water pressure dissipation is also operated by manipulating the shear modulus coefficient.

Contraction rate parameter h_{po}

Contraction rate parameter plays an indispensable role in actuating the liquefaction phenomenon due to the adjustment of the target cyclic resistance ratio (CRR). Consequently, the pore water pressure magnitude is influenced significantly undergone the calibration of h_{po}. For getting the graphical evaluation of such affect, three different values of h_{po} (0.05, 0.15 and 0.3 respectively) are defined in the PM4Sand constitutive model and they provides the outputs as the Figures E.37 and E.38.

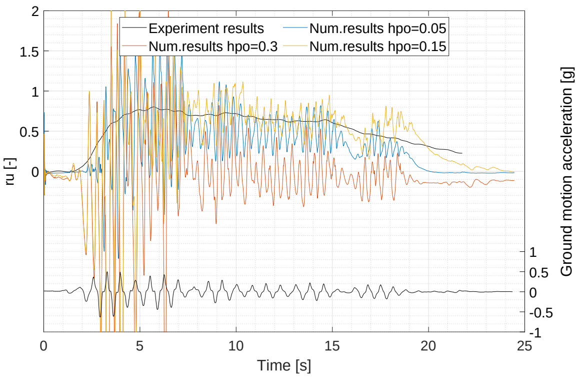

Figure E.37. Pore water pressure ratio of sensor P1 at the location of x=0m and y=-0.5m.

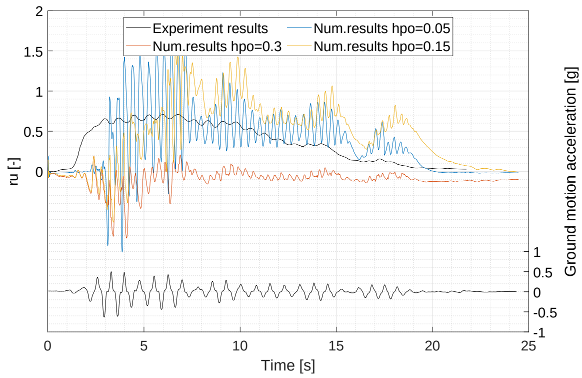

Figure E.38. Pore water pressure ratio of sensor P3 at the location of x=0m and y=-2.5m.

Taking an overview at the two figures above, it is obvious that the tendency of liquefaction triggering is suppressed significantly by increasing the value of contraction rate parameter. For example, in the red curve in the both Figures E.37 and E.38 of P1 and P3 with the highest considered value of h_{po} as 0.3, the peak value of pore water pressure ratio is around 0.7 and 0.2 respectively , which means that the liquefaction could not be triggered. Therefore, the regular prediction trend of pore water pressure ratio according to the h_{po} calibration could be obtained that the pore water pressure was generated more by reducing the value of the contraction rate parameter.

In addition, with the smallest considered value as 0.05, the pore water pressure ratios of sensor P3 are witnessed a wider fluctuation than the rest ones in the 4 first seconds. However, the trend was totally reversed in the sensor P1, particularly, the plot shows less noise curve with the value of h_{po} as 0.05. Besides, the dissipation of excess pore water pressure in case of calibrating h_{po} was not affected linearly. The fact is that there is not any regular prediction dissipation trend derived by adjusting the value of contraction rate parameter. Overall, the effect of h_{po} calibration is mostly to adjust the generation of excess pore water pressure and the noise of graphical output plots, instead of controlling the dissipation of excess pore water pressure at the end of given period.

Influence of the input motions F

F.1 Accelerations time histories

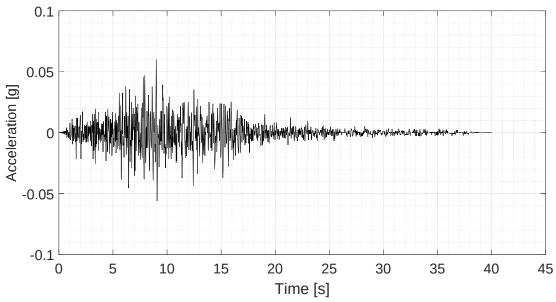

Figure F.1. R1 - Big Bear-01.

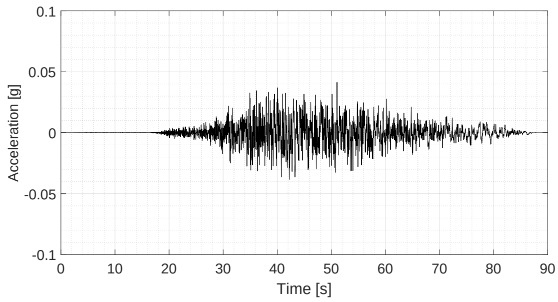

Figure F.2. R2 - Chi-Chi, Taiwan.

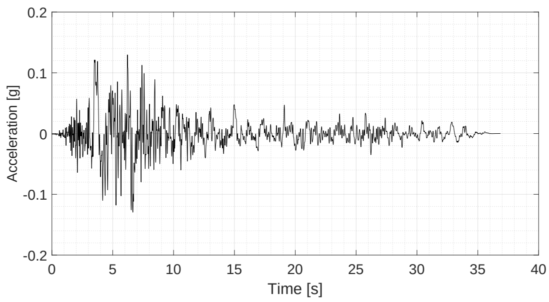

Figure F.3. R3 - Irpinia, Italy-01.

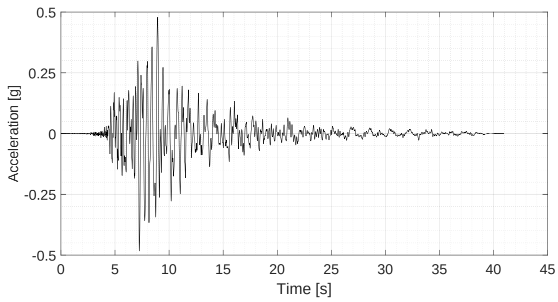

Figure F.4. R4 - Kobe, Japan.

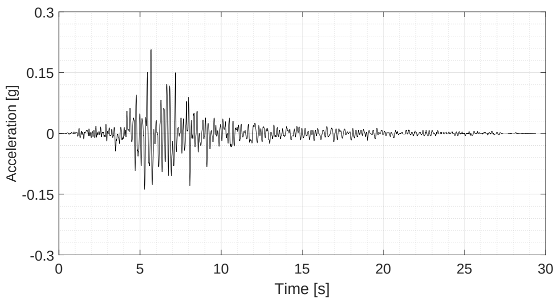

Figure F.5. R5 - Kozani, Greece-01.

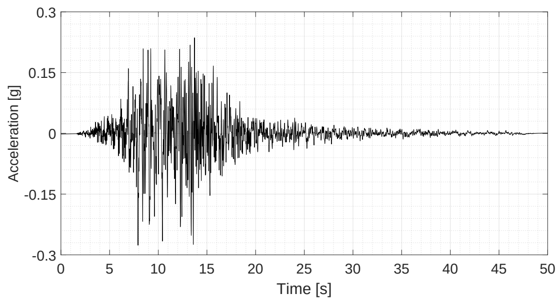

Figure F.6. R6 - Loma Prieta.

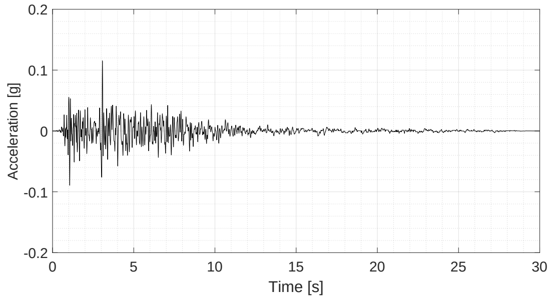

Figure F.7. R7 - Morgan Hill.

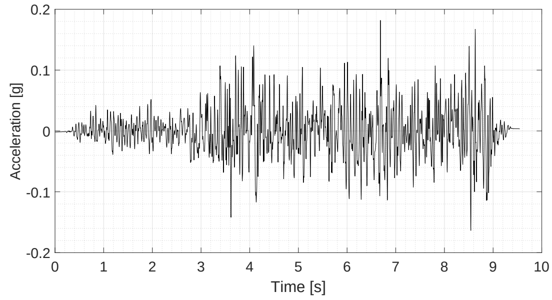

Figure F.8. R8 - Nahanni, Canada.

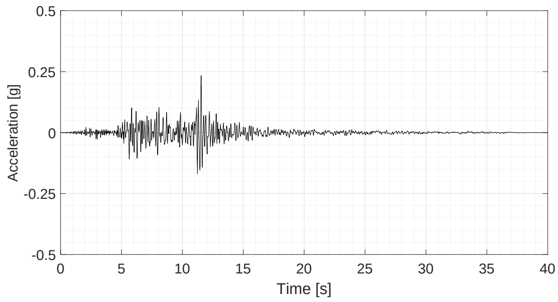

Figure F.9. R9 - Northridge.

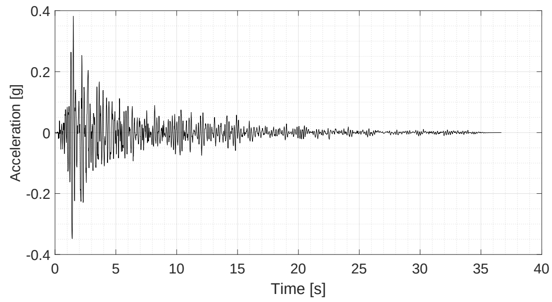

Figure F.10. R10 - San Fernando.

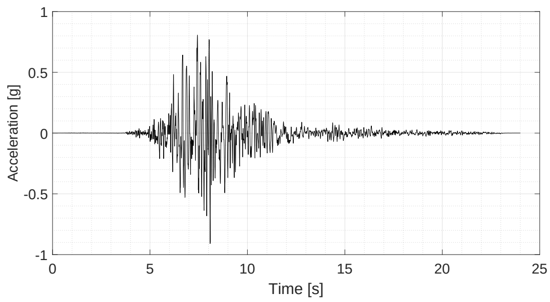

Figure F.11. R11 - Christchurch, New Zealand.

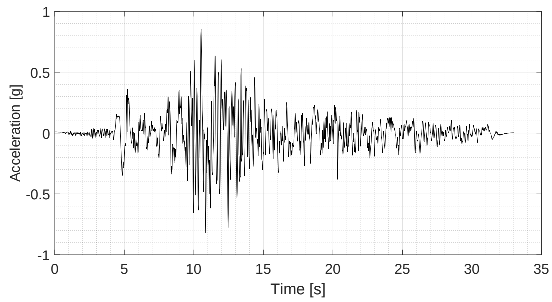

Figure F.12. R12 - Tabas, Iran.

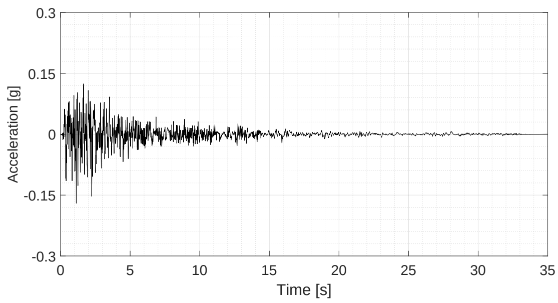

Figure F.13. R13 - San Fernando.

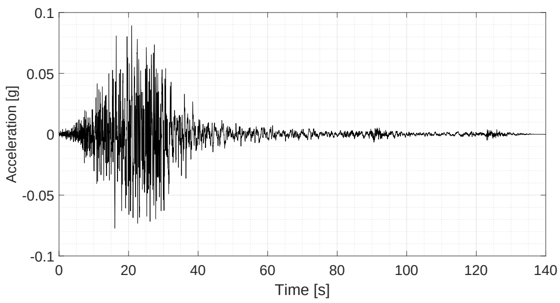

Figure F.14. R14 - Darfield, New Zealand .

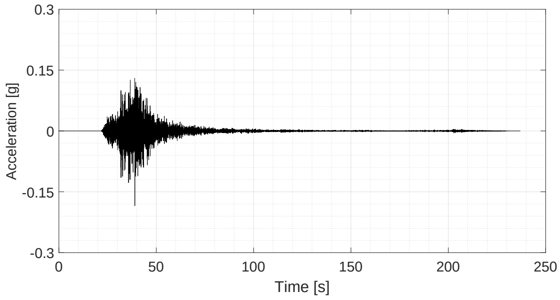

Figure F.15. R15 - Iwate, Japan.

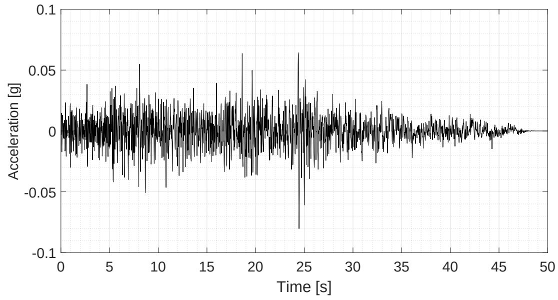

Figure F.16. R16 - Landers.

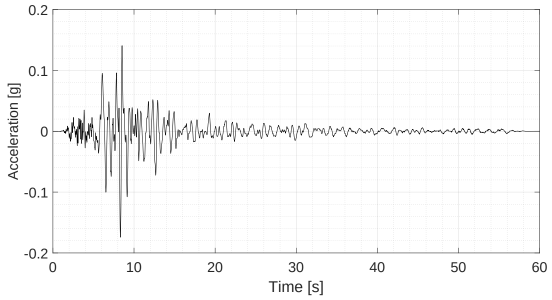

Figure F.17. R17 - Coalinga-01.

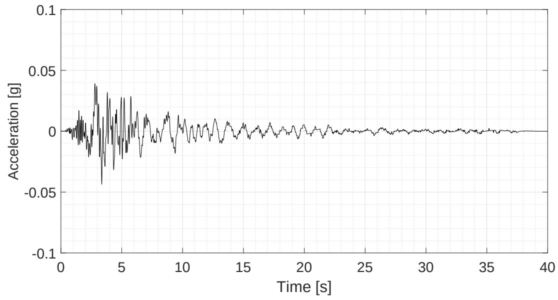

Figure F.18. R18 - Hollister-04.

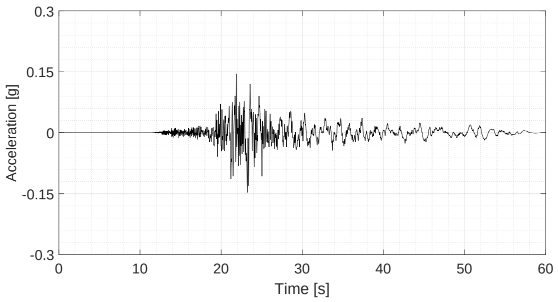

Figure F.19. R19 - Chuetsu-oki, Japan.

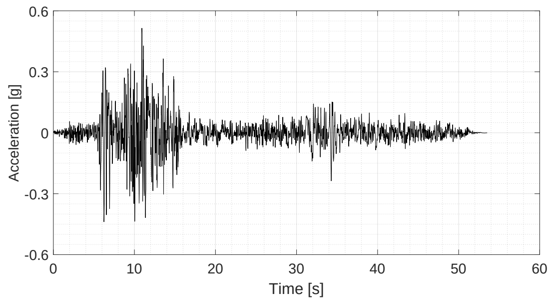

Figure F.20. R20 - Manjil, Iran.

F.2 Outputs data of input motions

F.2.1 Event R1

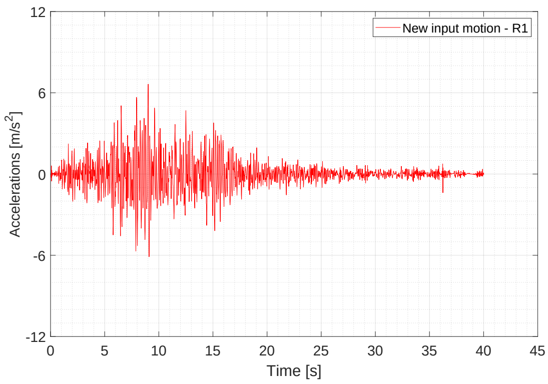

Figure F.21. R1-Accelerations at A1.

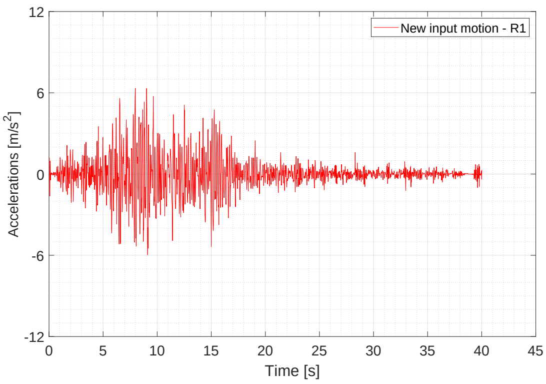

Figure F.22. R1-Accelerations at A2.

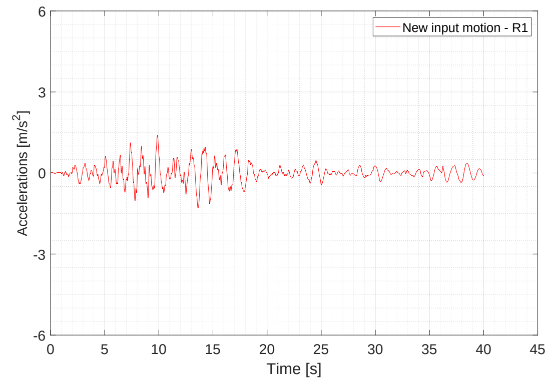

Figure F.23. R1-Accelerations at A3.

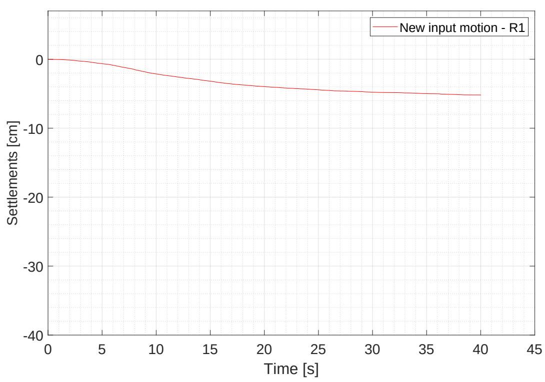

Figure F.24. R1-Settlement.

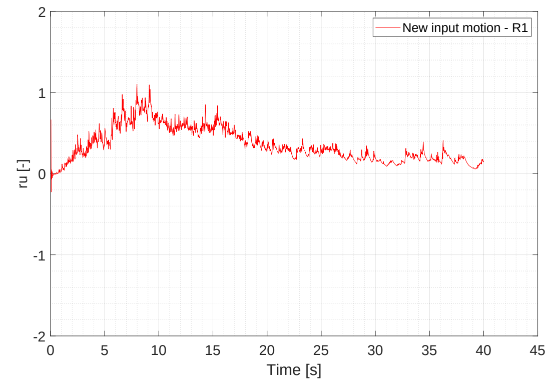

Figure F.25. R1-Pore water pressure ratio at P1.

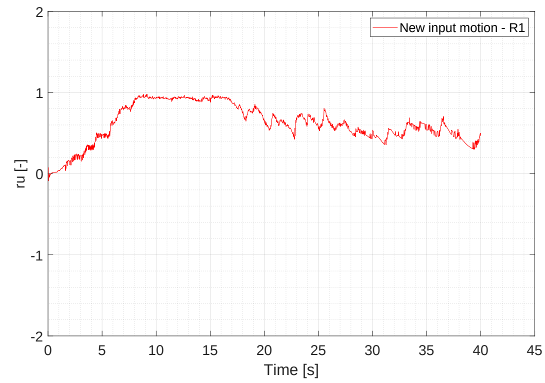

Figure F.26. R1-Pore water pressure ratio at P2.

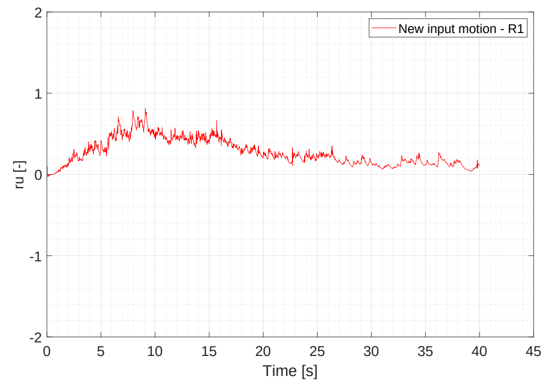

Figure F.27. R1-Pore water pressure ratio at P3.

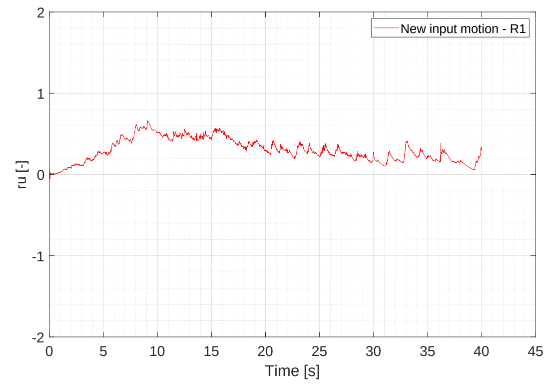

Figure F.28. R1-Pore water pressure ratio at P4.

F.2.2 Event R2

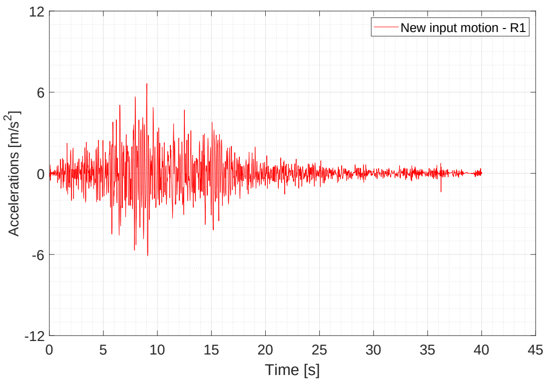

Figure F.29. R2-Accelerations at A1.

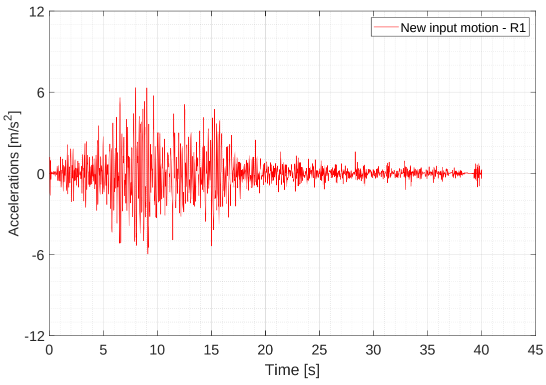

Figure F.30. R2-Accelerations at A2.

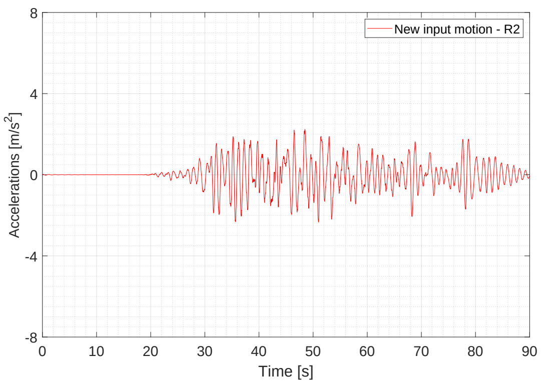

Figure F.31. R2-Accelerations at A3.

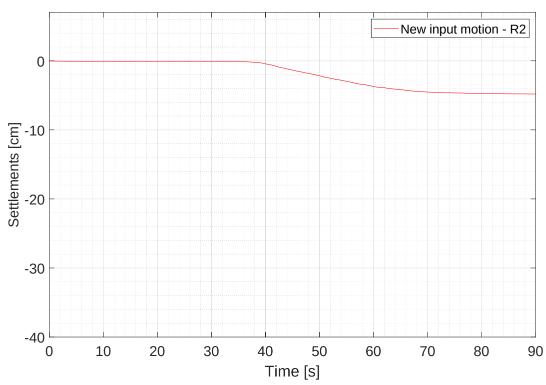

Figure F.32. R2-Settlement.

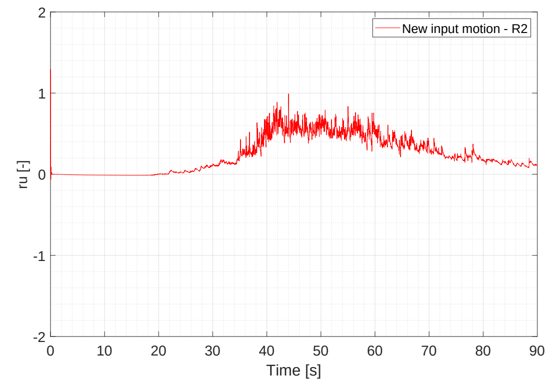

Figure F.33. R2-Pore water pressure ratio at P1.

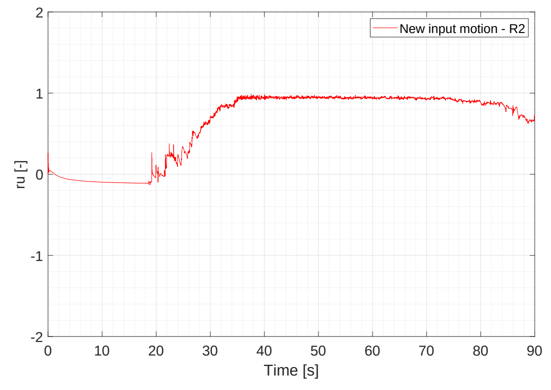

Figure F.34. R2-Pore water pressure ratio at P2.

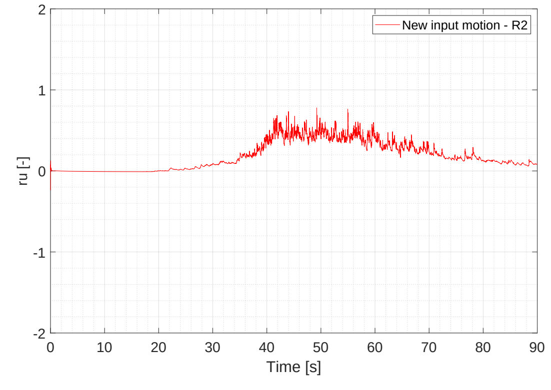

Figure F.35. R2-Pore water pressure ratio at P3.

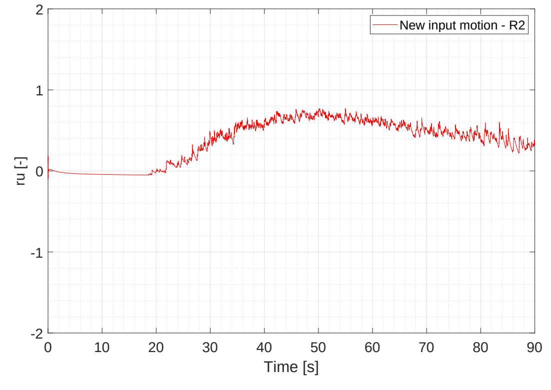

Figure F.36. R2-Pore water pressure ratio at P4.

F.2.3 Event R3

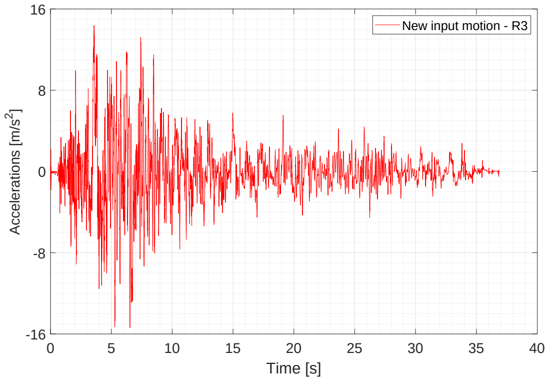

Figure F.37. R3-Accelerations at A1.

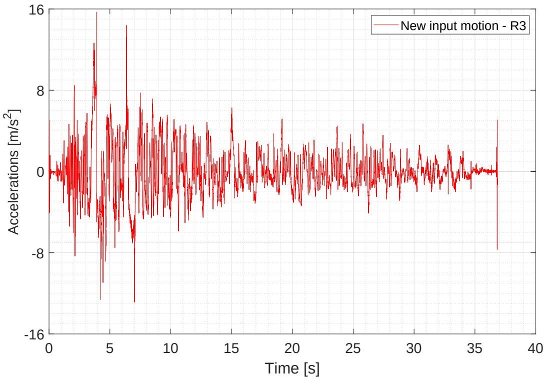

Figure F.38. R3-Accelerations at A2.

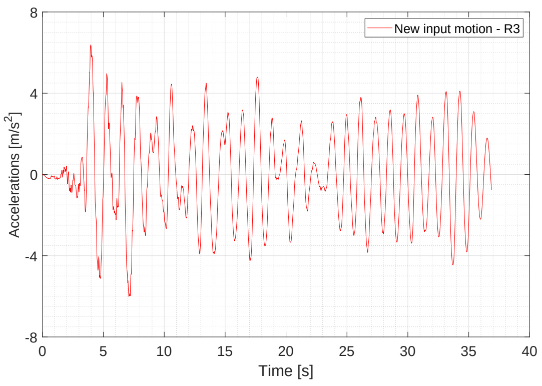

Figure F.39. R3-Accelerations at A3.

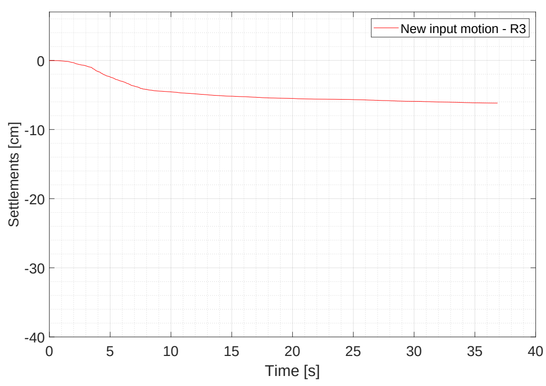

Figure F.40. R3-Settlement.

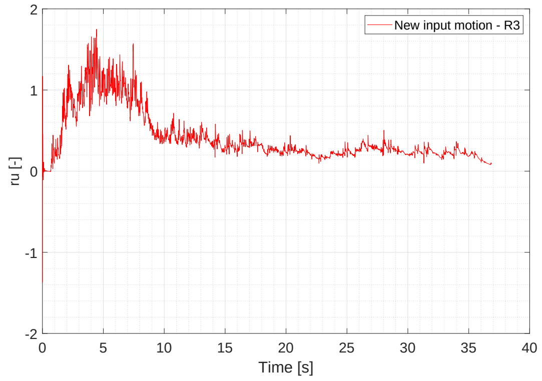

Figure F.41. R3-Pore water pressure ratio at P1.

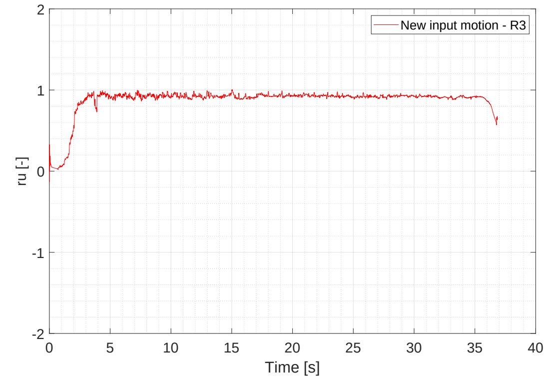

Figure F.42. R3-Pore water pressure ratio at P2.

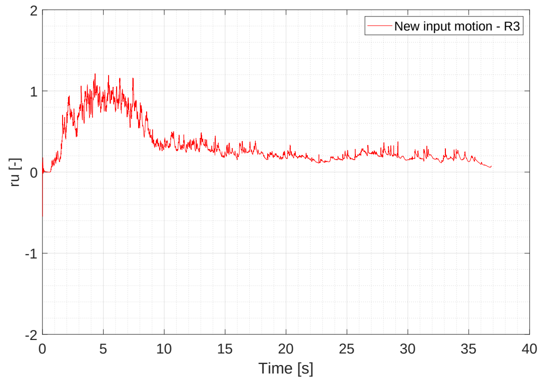

Figure F.43. R3-Pore water pressure ratio at P3.

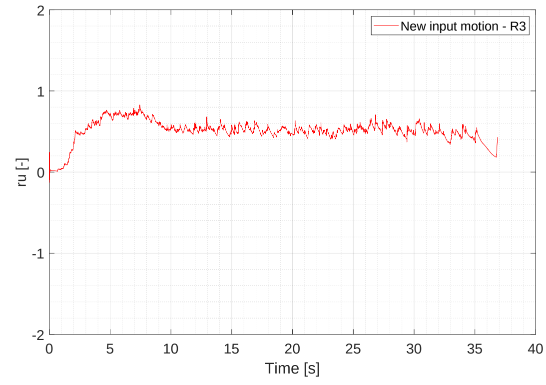

Figure F.44. R3-Pore water pressure ratio at P4.

F.2.4 Event R4

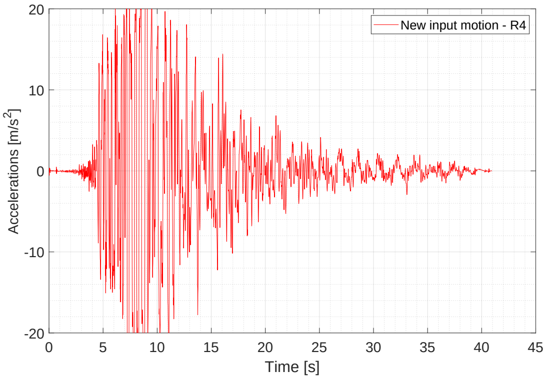

Figure F.45. R4-Accelerations at A1.

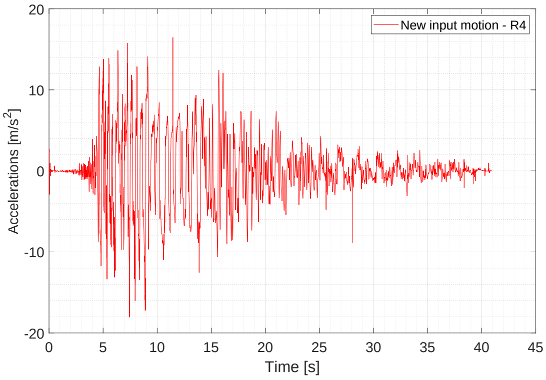

Figure F.46. R4-Accelerations at A2.

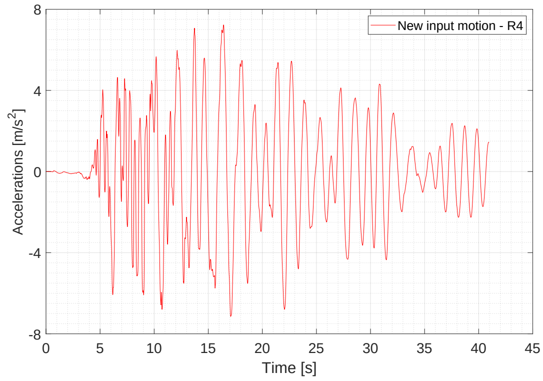

Figure F.47. R4-Accelerations at A3.

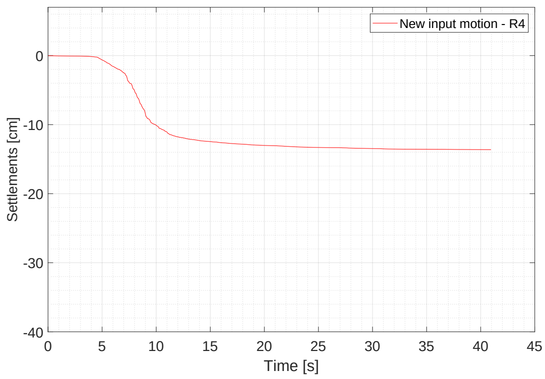

Figure F.48. R4-Settlement.

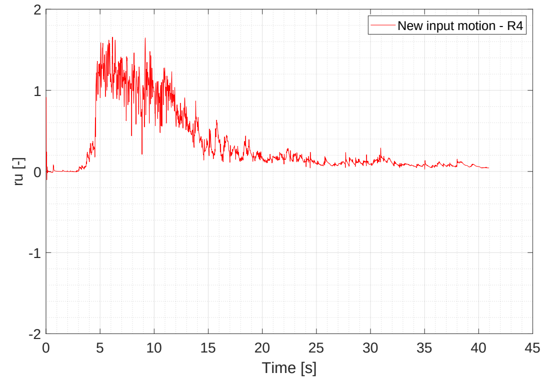

Figure F.49. R4-Pore water pressure ratio at P1.

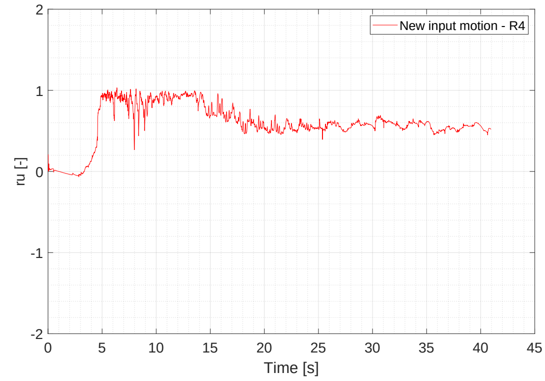

Figure F.50. R4-Pore water pressure ratio at P2.

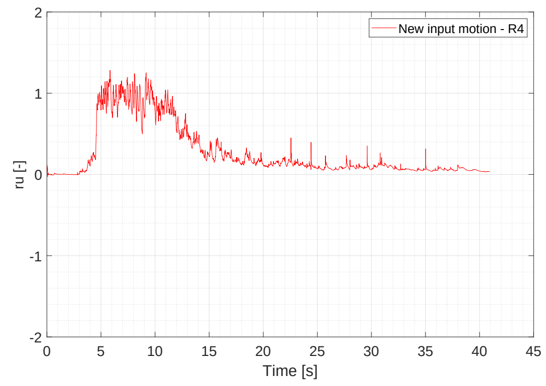

Figure F.51. R4-Pore water pressure ratio at P3.

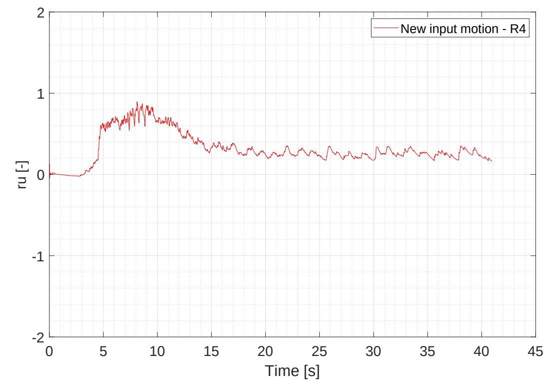

Figure F.52. R4-Pore water pressure ratio at P4.

F.2.5 Event R5

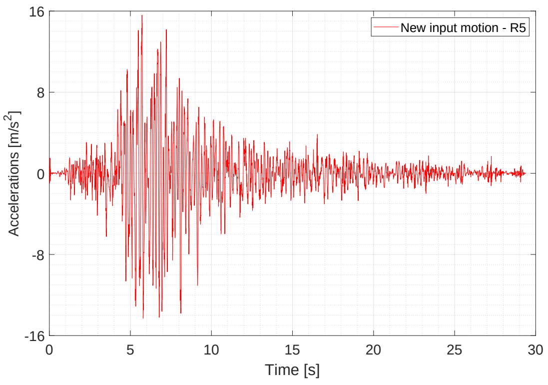

Figure F.53. R5-Accelerations at A1.

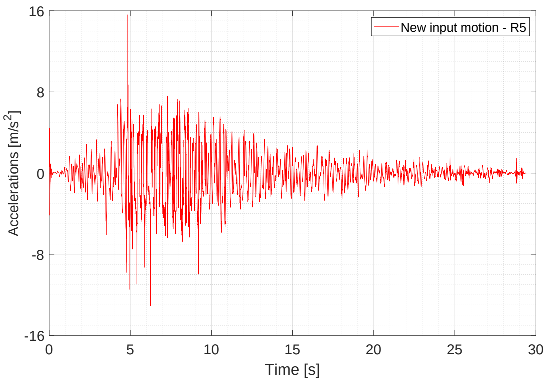

Figure F.54. R5-Accelerations at A2.

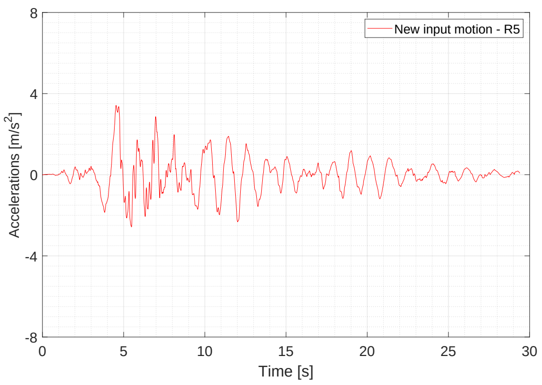

Figure F.55. R5-Accelerations at A3.

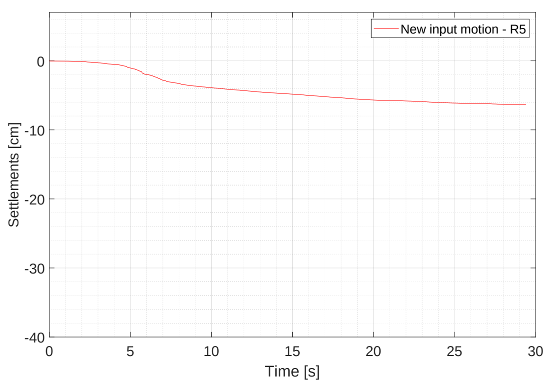

Figure F.56. R5-Settlement.

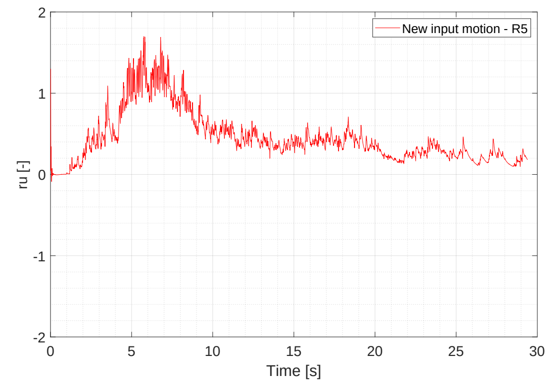

Figure F.57. R5-Pore water pressure ratio at P1.

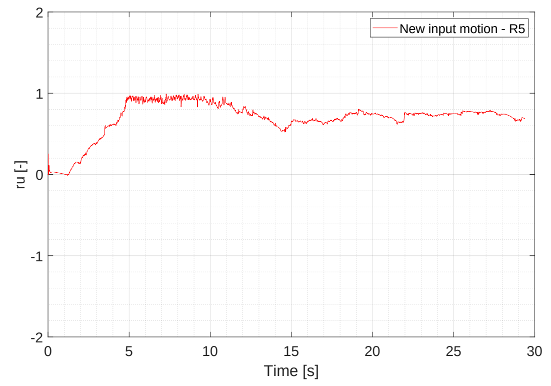

Figure F.58. R5-Pore water pressure ratio at P2.

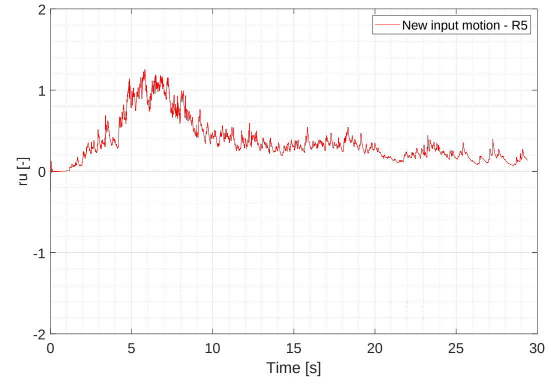

Figure F.59. R5-Pore water pressure ratio at P3.

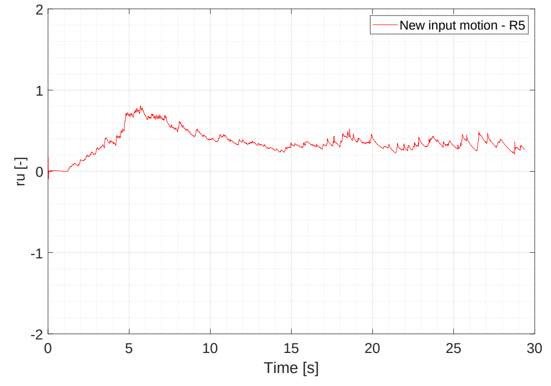

Figure F.60. R5-Pore water pressure ratio at P4.

F.2.6 Event R6

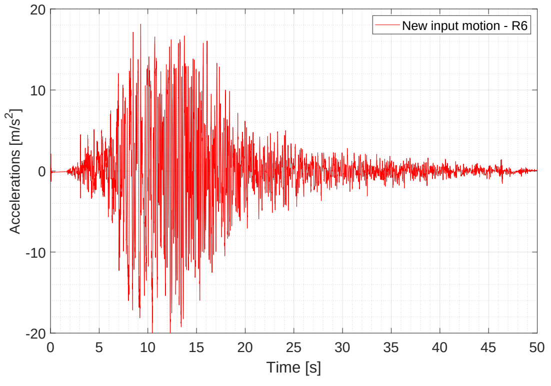

Figure F.61. R6-Accelerations at A1.

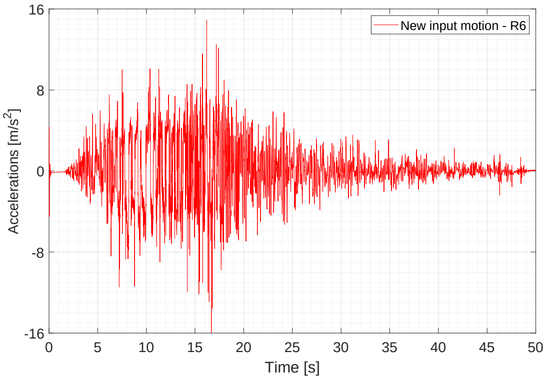

Figure F.62. R6-Accelerations at A2.

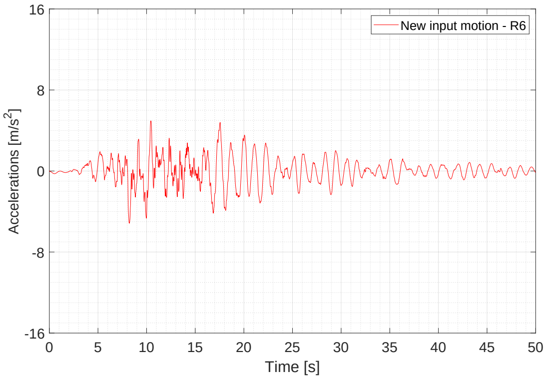

Figure F.63. R6-Accelerations at A3.

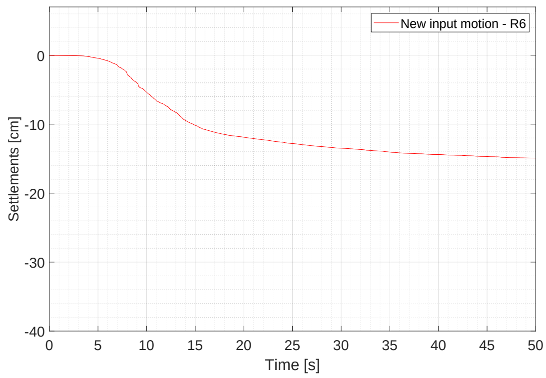

Figure F.64. R6-Settlement.

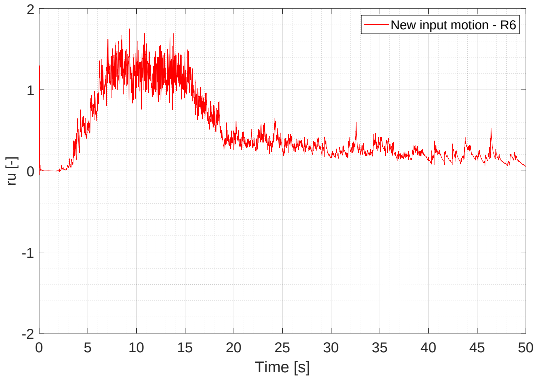

Figure F.65. R6-Pore water pressure ratio at P1.

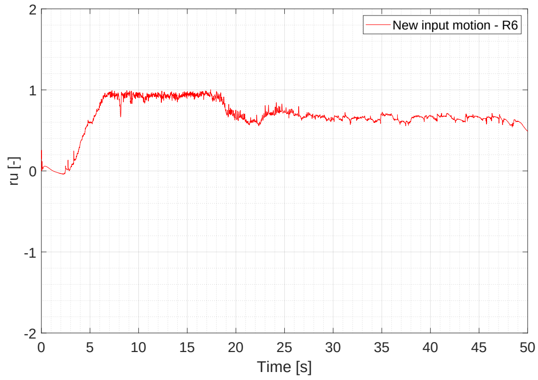

Figure F.66. R6-Pore water pressure ratio at P2.

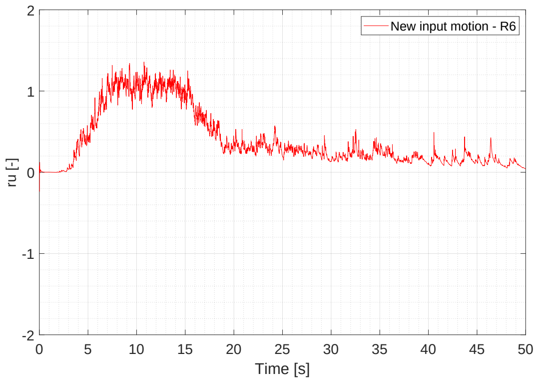

Figure F.67. R6-Pore water pressure ratio at P3.

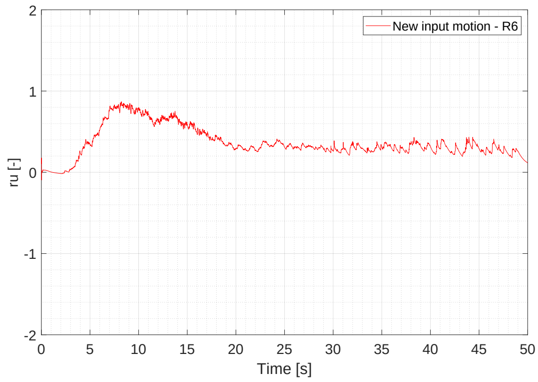

Figure F.68. R6-Pore water pressure ratio at P4.

F.2.7 Event R7

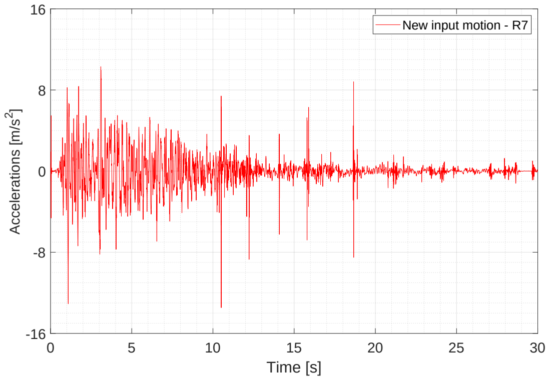

Figure F.69. R7-Accelerations at A1.

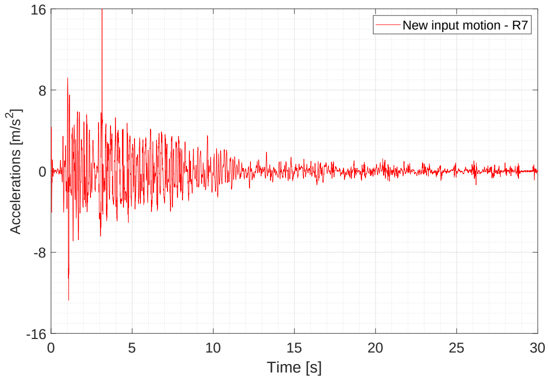

Figure F.70. R7-Accelerations at A2.

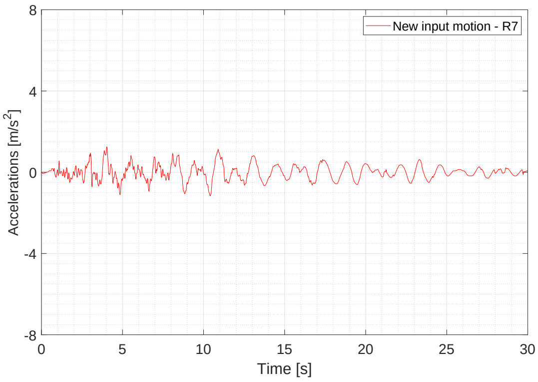

Figure F.71. R7-Accelerations at A3.

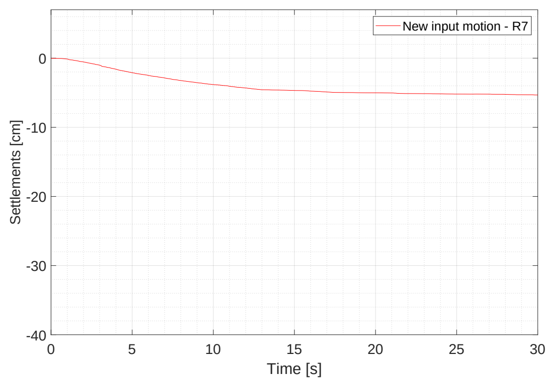

Figure F.72. R7-Settlement.

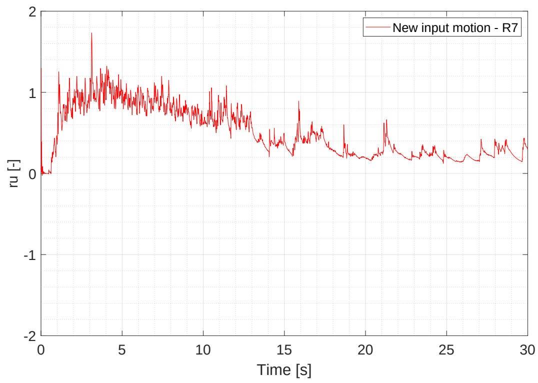

Figure F.73. R7-Pore water pressure ratio at P1.

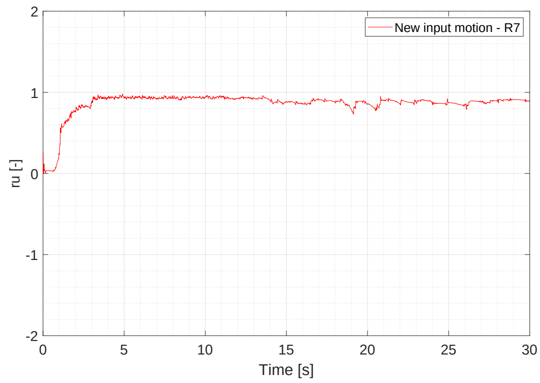

Figure F.74. R7-Pore water pressure ratio at P2.

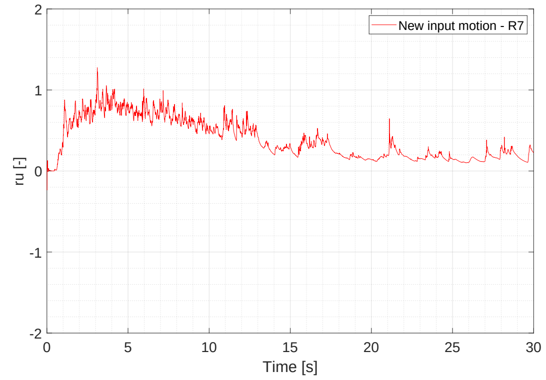

Figure F.75. R7-Pore water pressure ratio at P3.

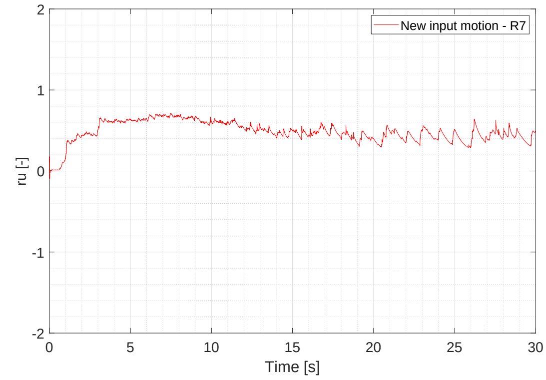

Figure F.76. R7-Pore water pressure ratio at P4.

F.2.8 Event R8

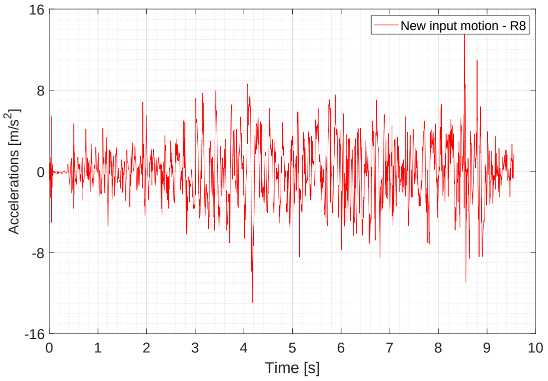

Figure F.77. R8-Accelerations at A1.

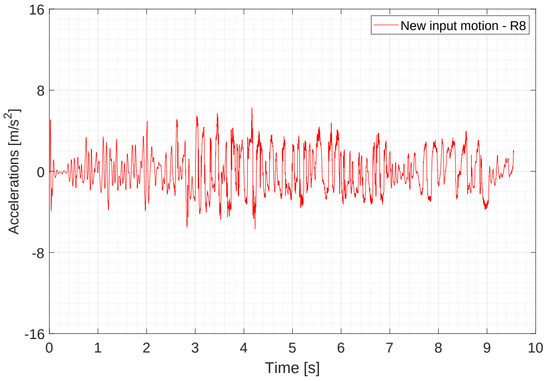

Figure F.78. R8-Accelerations at A2.

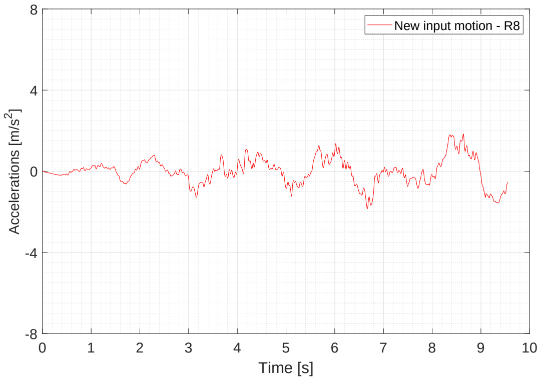

Figure F.79. R8-Accelerations at A3.

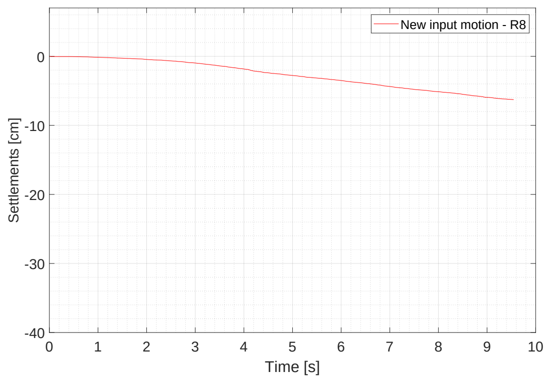

Figure F.80. R8-Settlement.

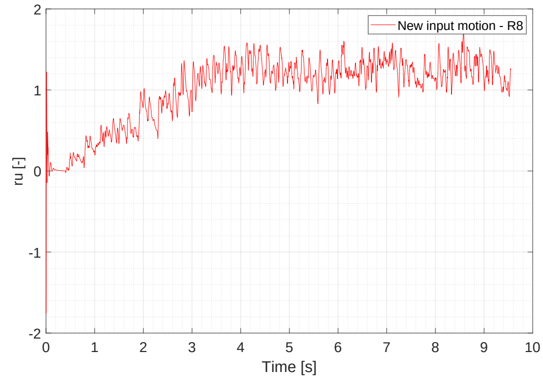

Figure F.81. R8-Pore water pressure ratio at P1.

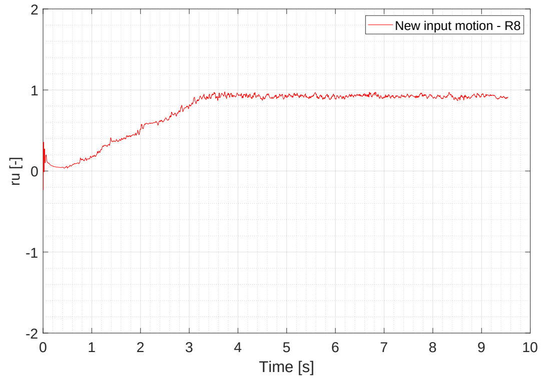

Figure F.82. R8-Pore water pressure ratio at P2.

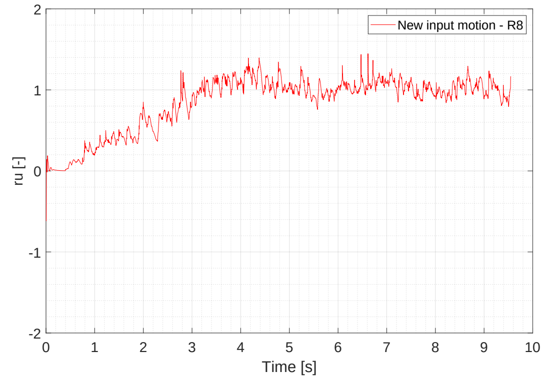

Figure F.83. R8-Pore water pressure ratio at P3.

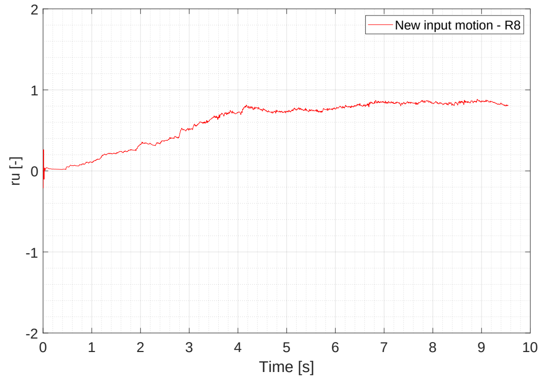

Figure F.84. R8-Pore water pressure ratio at P4.

F.2.9 Event R9

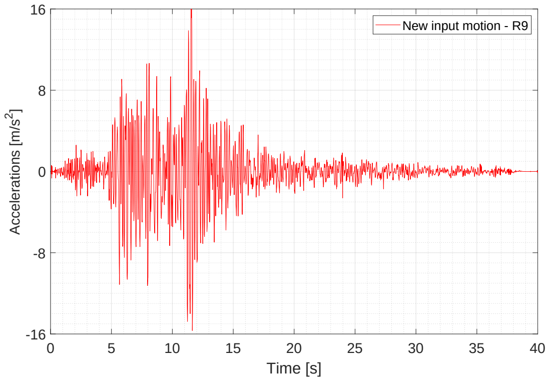

Figure F.85. R9-Accelerations at A1.

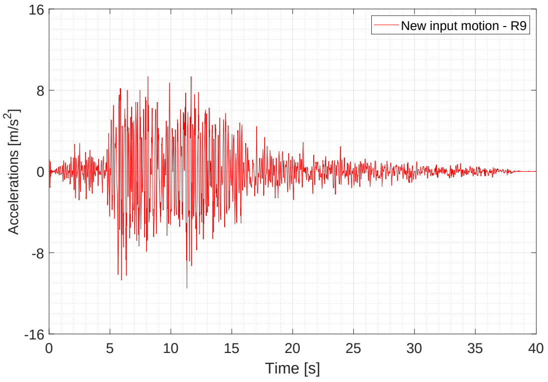

Figure F.86. R9-Accelerations at A2.

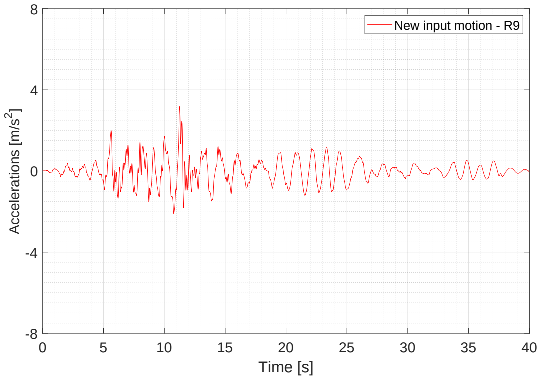

Figure F.87. R9-Accelerations at A3.

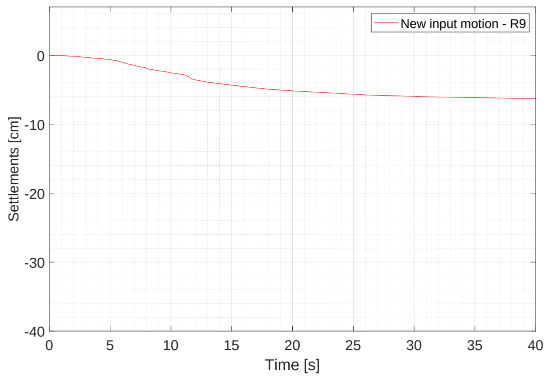

Figure F.88. R9-Settlement.

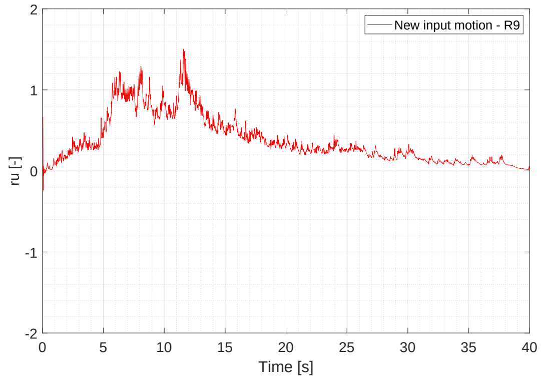

Figure F.89. R9-Pore water pressure ratio at P1.

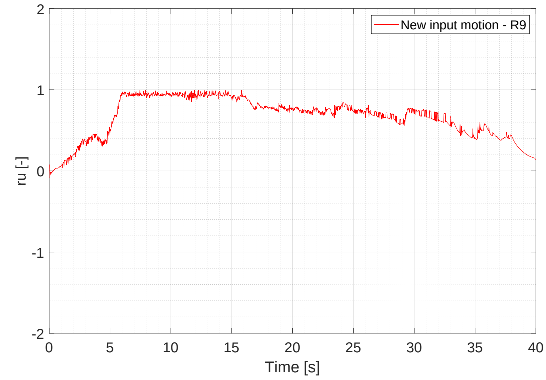

Figure F.90. R9-Pore water pressure ratio at P2.

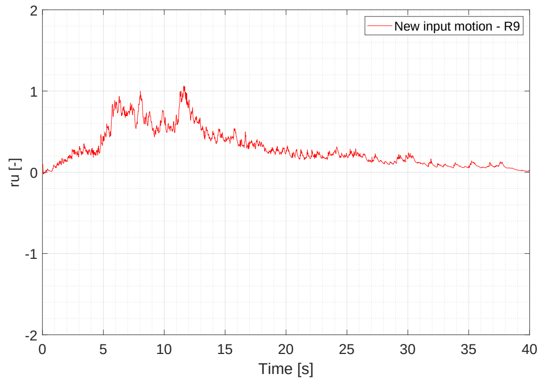

Figure F.91. R9-Pore water pressure ratio at P3.

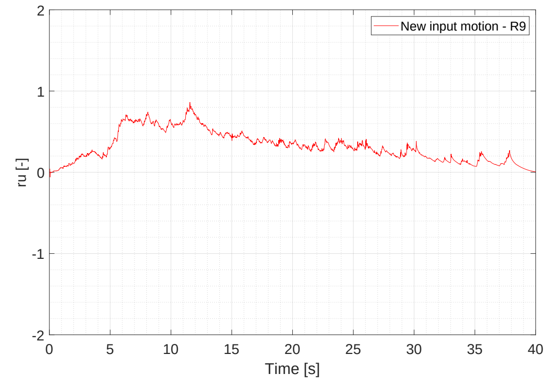

Figure F.92. R9-Pore water pressure ratio at P4.

F.2.10 Event R10

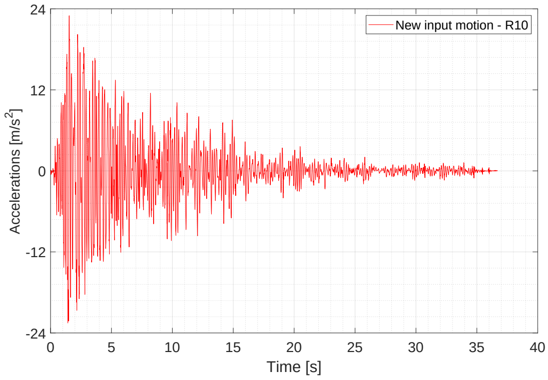

Figure F.93. R10-Accelerations at A1.

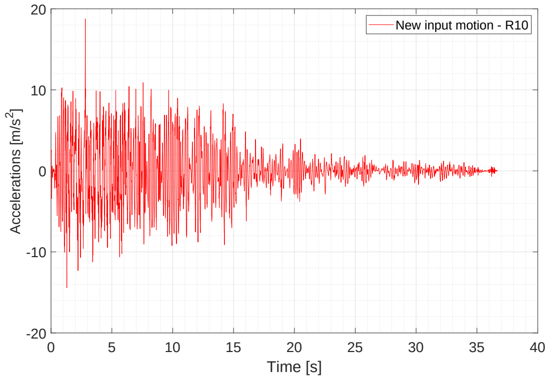

Figure F.94. R10-Accelerations at A2.

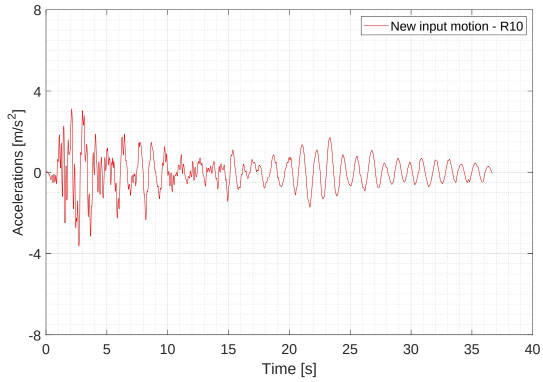

Figure F.95. R10-Accelerations at A3.

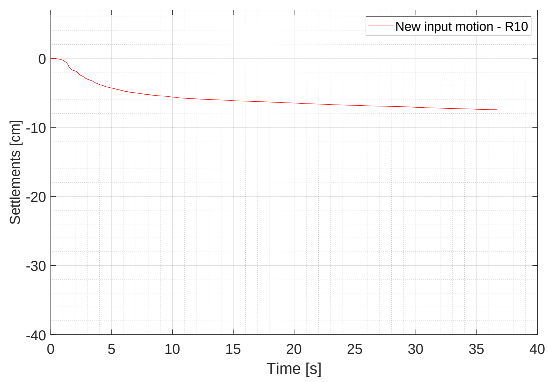

Figure F.96. R10-Settlement.

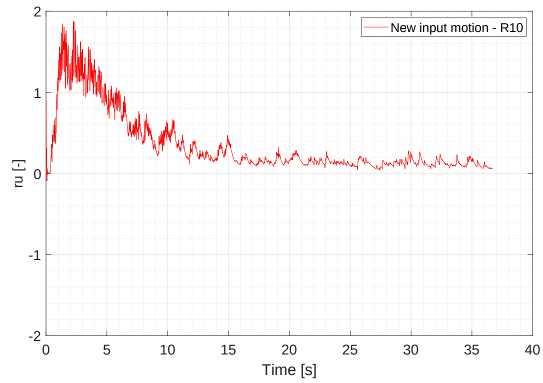

Figure F.97. R10-Pore water pressure ratio at P1.

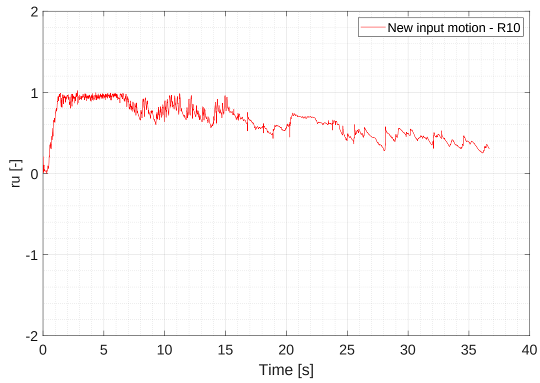

Figure F.98. R10-Pore water pressure ratio at P2.

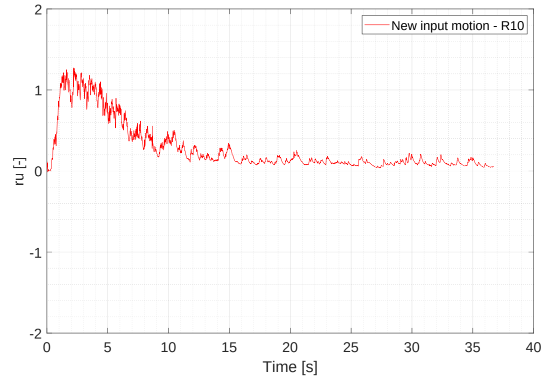

Figure F.99. R10-Pore water pressure ratio at P3.

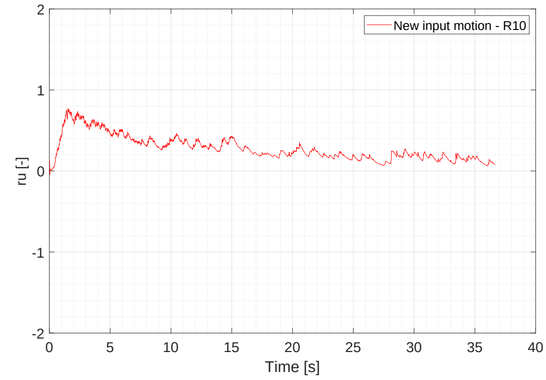

Figure F.100. R10-Pore water pressure ratio at P4.

F.2.11 Event R11

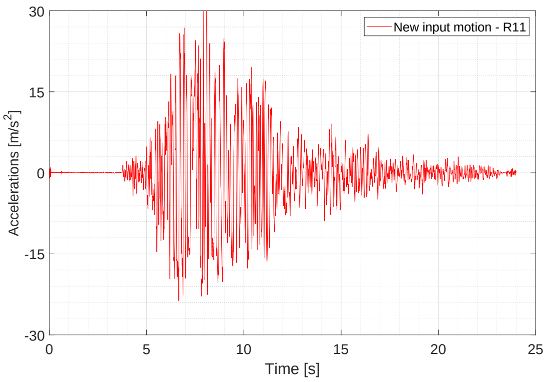

Figure F.101. R11-Accelerations at A1.

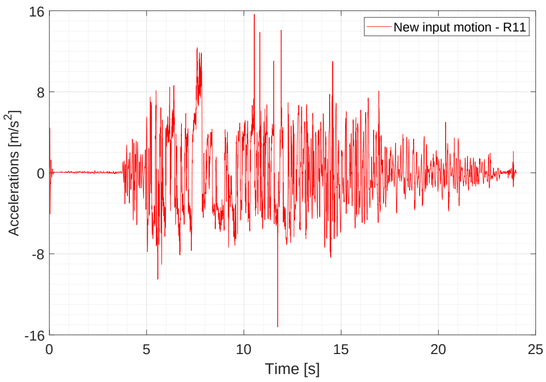

Figure F.102. R11-Accelerations at A2.

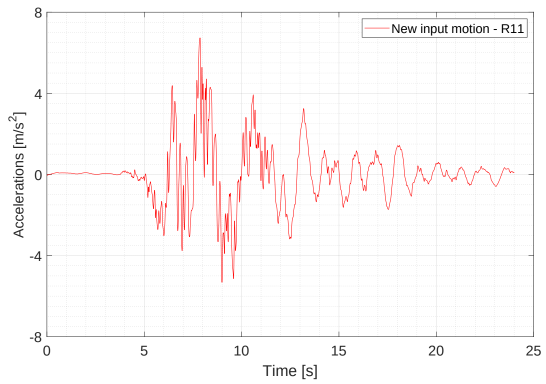

Figure F.103. R11-Accelerations at A3.

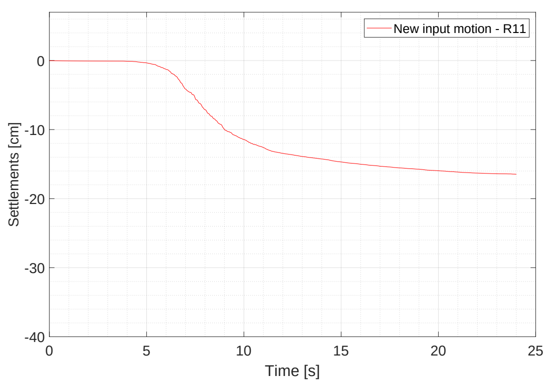

Figure F.104. R11-Settlement.

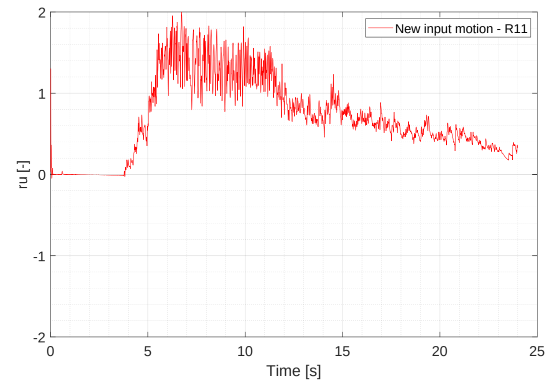

Figure F.105. R11-Pore water pressure ratio at P1.

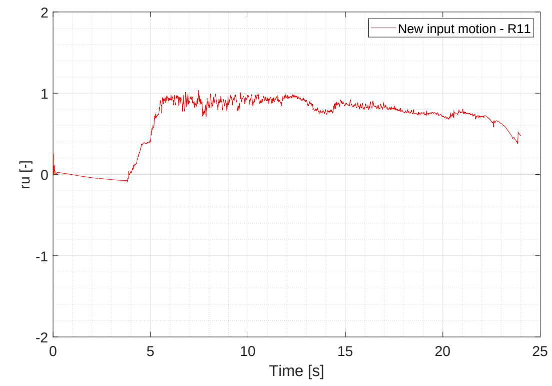

Figure F.106. R11-Pore water pressure ratio at P2.

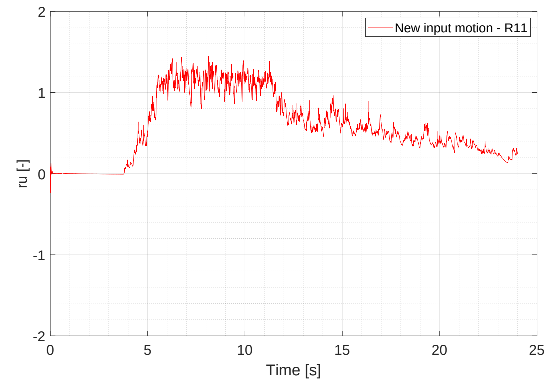

Figure F.107. R11-Pore water pressure ratio at P3.

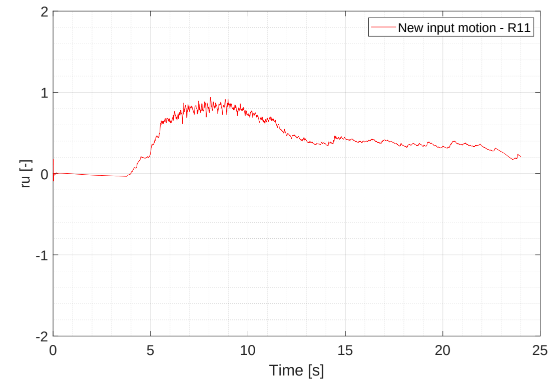

Figure F.108. R11-Pore water pressure ratio at P4.

F.2.12 Event R12

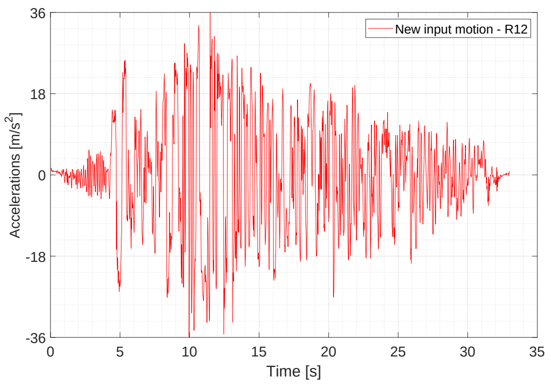

Figure F.109. R12-Accelerations at A1.

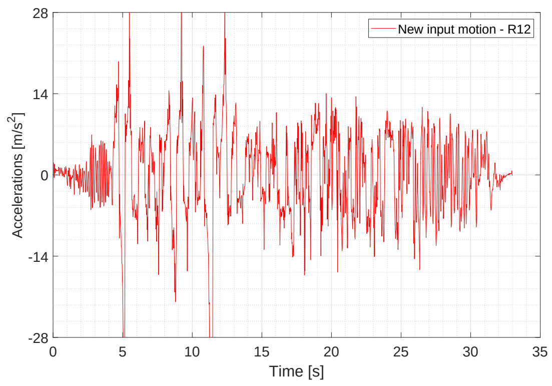

Figure F.110. R12-Accelerations at A2.

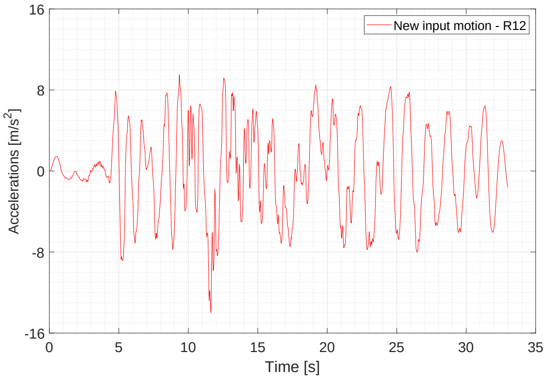

Figure F.111. R12-Accelerations at A3.

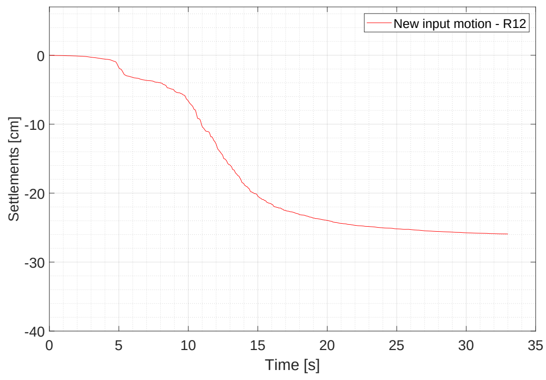

Figure F.112. R12-Settlement.

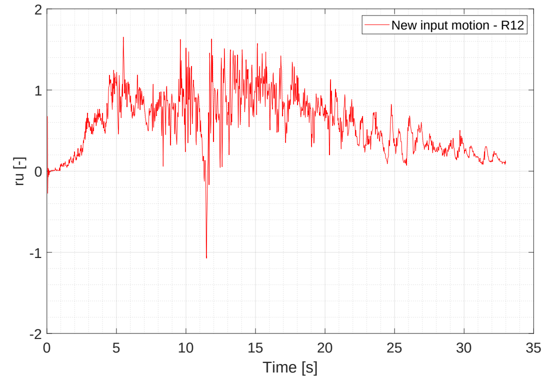

Figure F.113. R12-Pore water pressure ratio at P1.

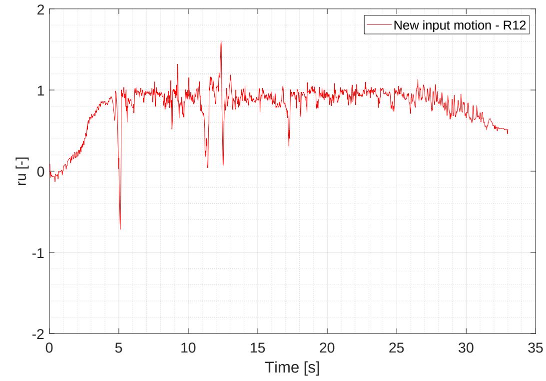

Figure F.114. R12-Pore water pressure ratio at P2.

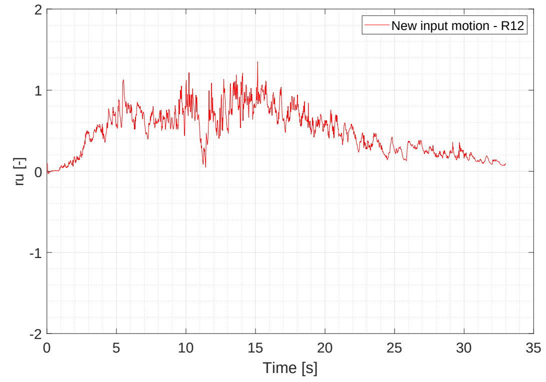

Figure F.115. R12-Pore water pressure ratio at P3.

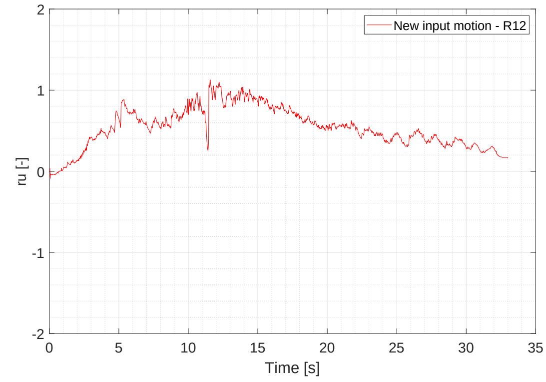

Figure F.116. R12-Pore water pressure ratio at P4.

F.2.13 Event R13

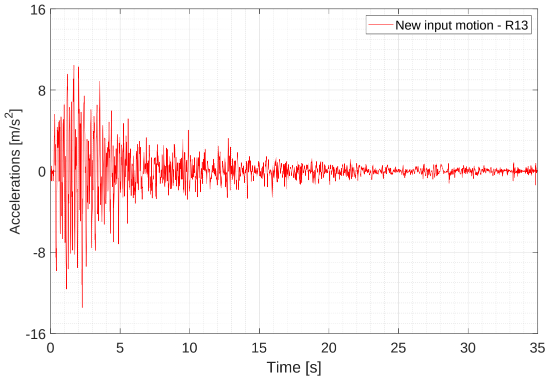

Figure F.117. R13-Accelerations at A1.

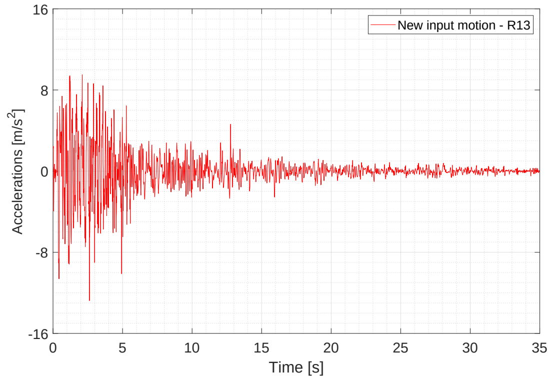

Figure F.118. R13-Accelerations at A2.

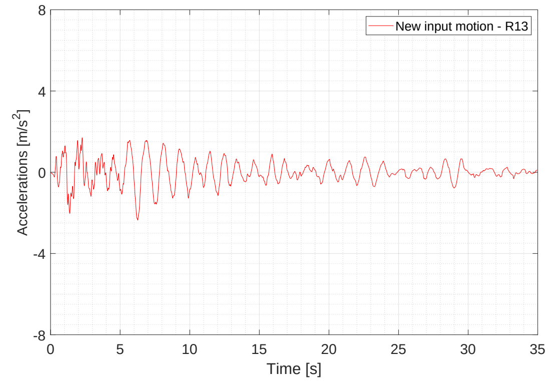

Figure F.119. R13-Accelerations at A3.

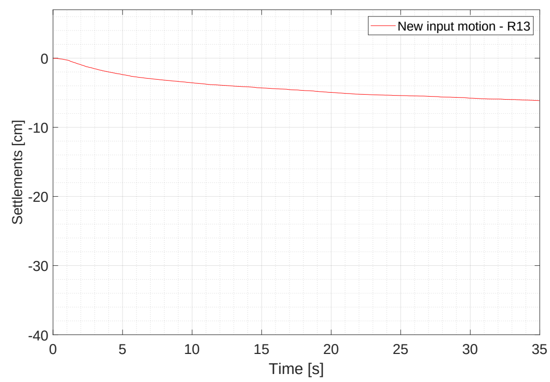

Figure F.120. R13-Settlement.

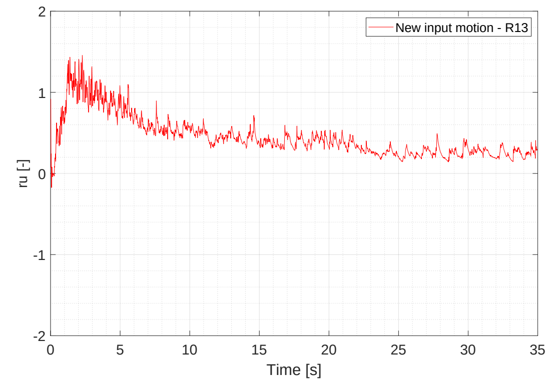

Figure F.121. R13-Pore water pressure ratio at P1.

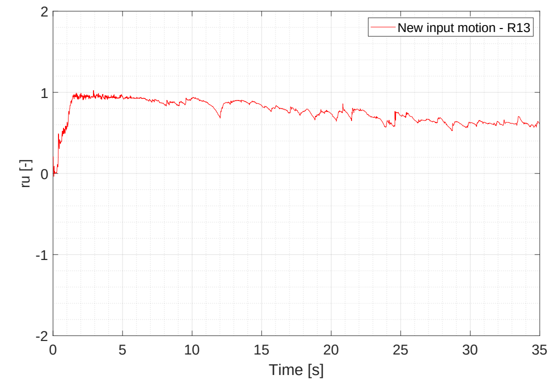

Figure F.122. R13-Pore water pressure ratio at P2.

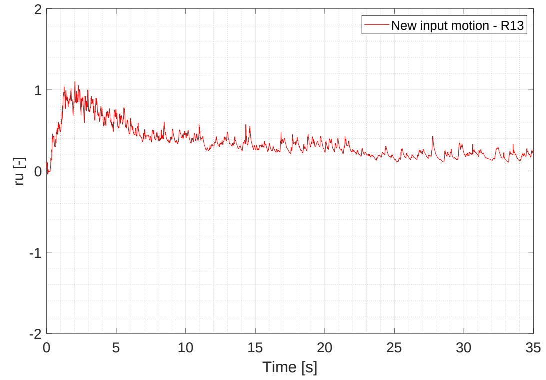

Figure F.123. R13-Pore water pressure ratio at P3.

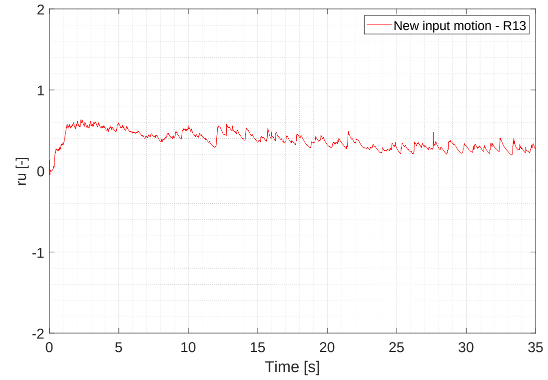

Figure F.124. R13-Pore water pressure ratio at P4.

F.2.14 Event R14

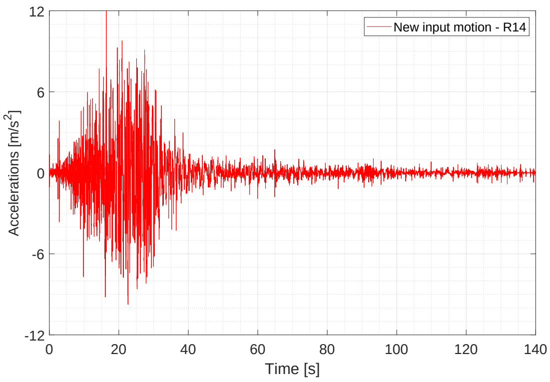

Figure F.125. R14-Accelerations at A1.

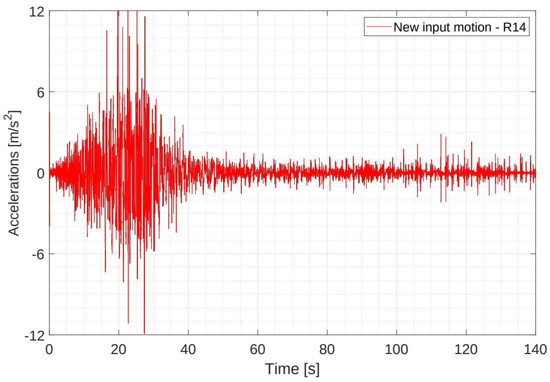

Figure F.126. R14-Accelerations at A2.

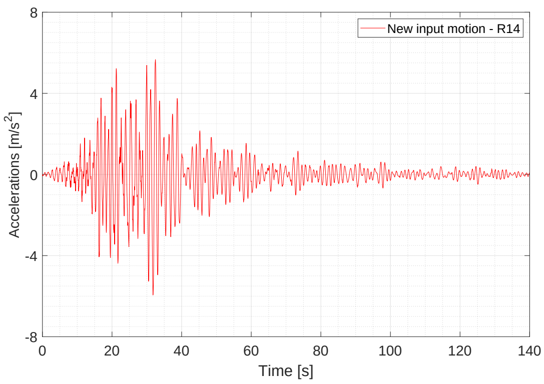

Figure F.127. R14-Accelerations at A3.

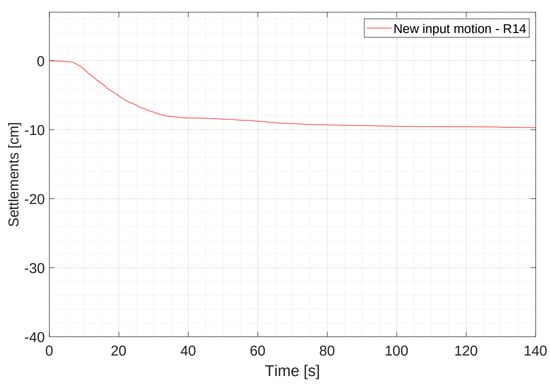

Figure F.128. R14-Settlement.

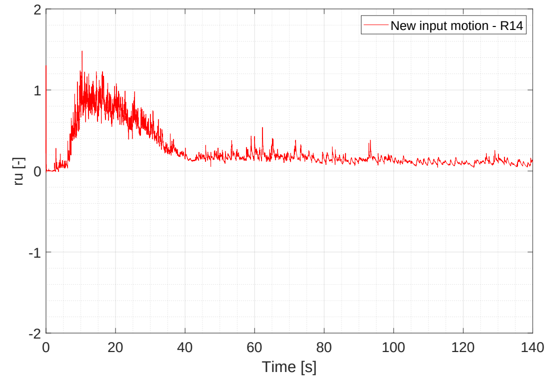

Figure F.129. R14-Pore water pressure ratio at P1.

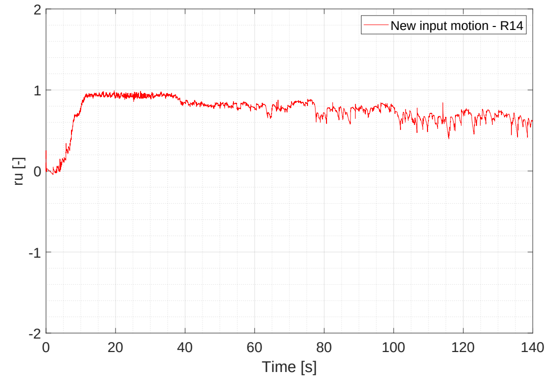

Figure F.130. R14-Pore water pressure ratio at P2.

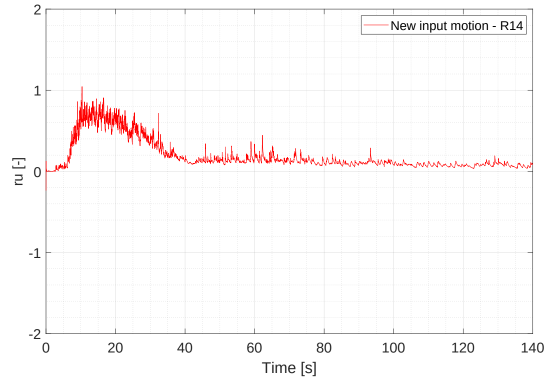

Figure F.131. R14-Pore water pressure ratio at P3.

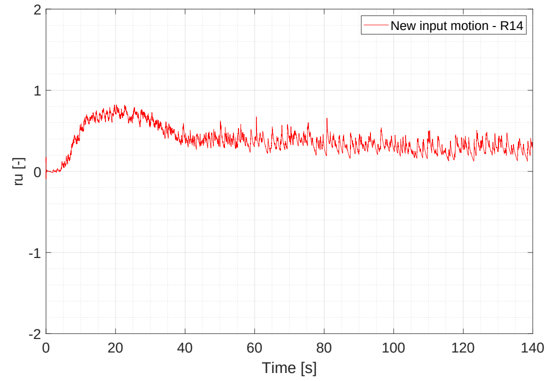

Figure F.132. R14-Pore water pressure ratio at P4.

F.2.15 Event R15

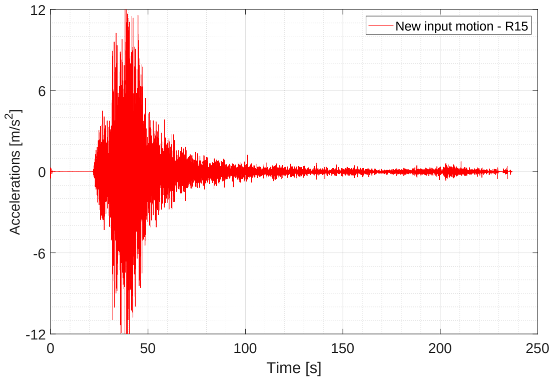

Figure F.133. R15-Accelerations at A1.

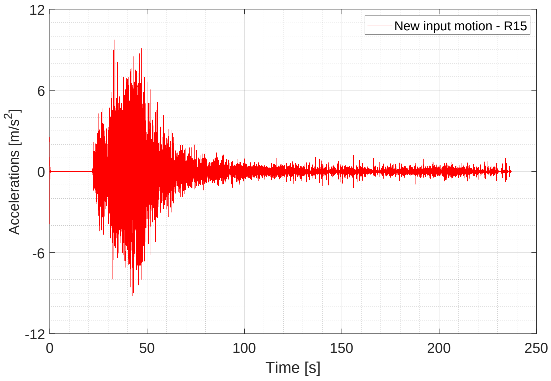

Figure F.134. R15-Accelerations at A2.

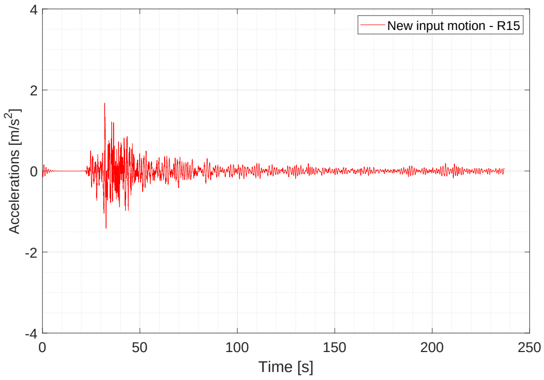

Figure F.135. R15-Accelerations at A3.

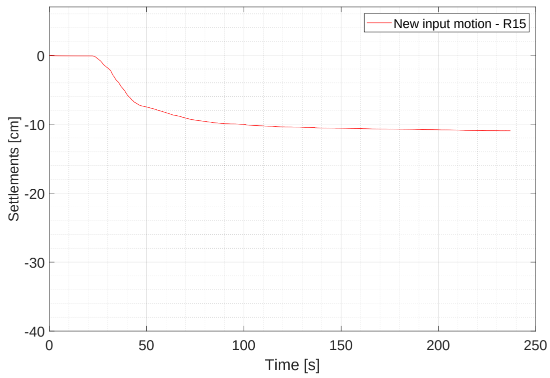

Figure F.136. R15-Settlement.

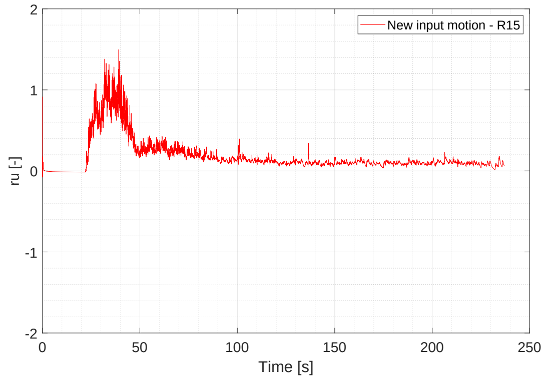

Figure F.137. R15-Pore water pressure ratio at P1.

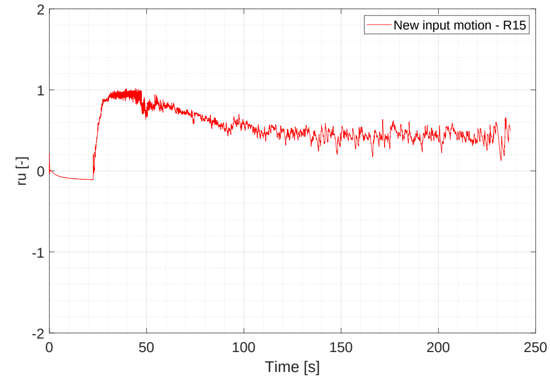

Figure F.138. R15-Pore water pressure ratio at P2.

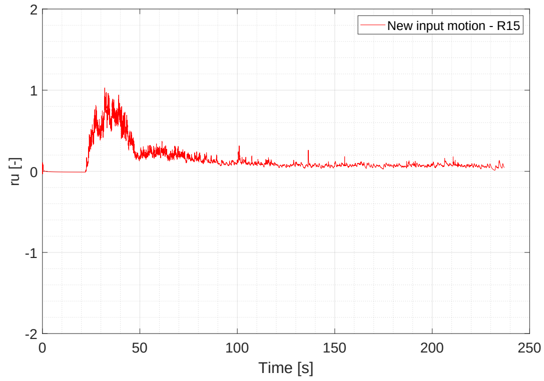

Figure F.139. R15-Pore water pressure ratio at P3.

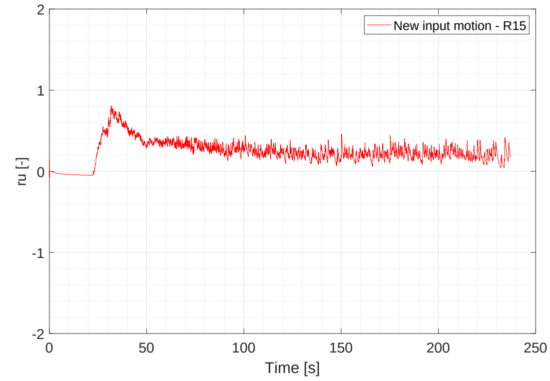

Figure F.140. R15-Pore water pressure ratio at P4.

F.2.16 Event R16

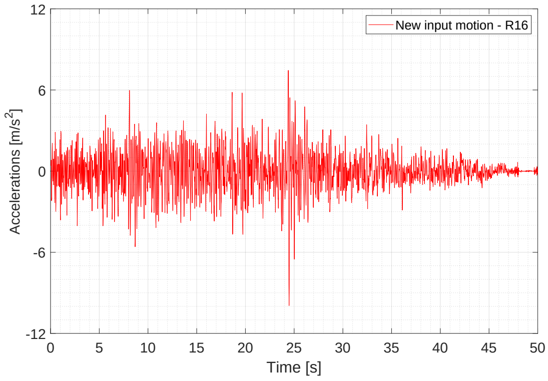

Figure F.141. R16-Accelerations at A1.

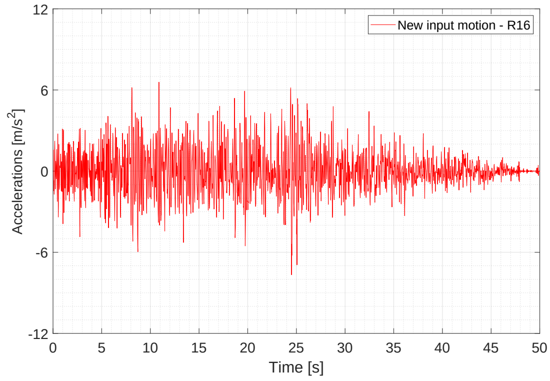

Figure F.142. R16-Accelerations at A2.

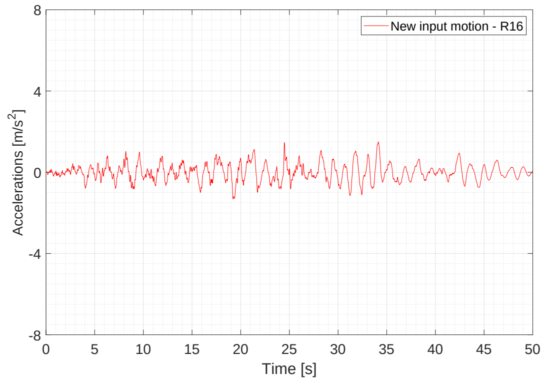

Figure F.143. R16-Accelerations at A3.

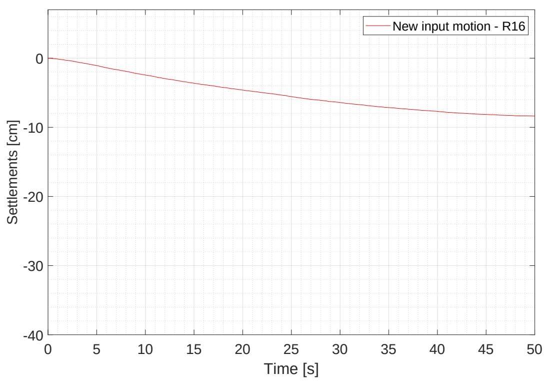

Figure F.144. R16-Settlement.

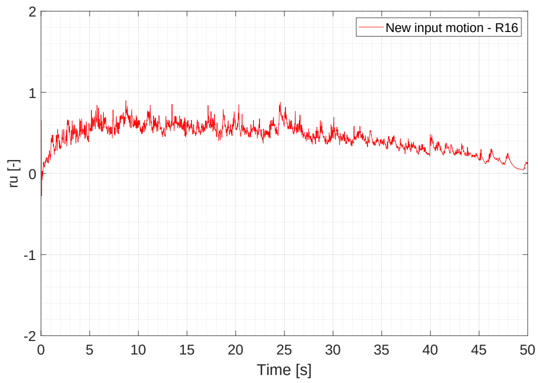

Figure F.145. R16-Pore water pressure ratio at P1.

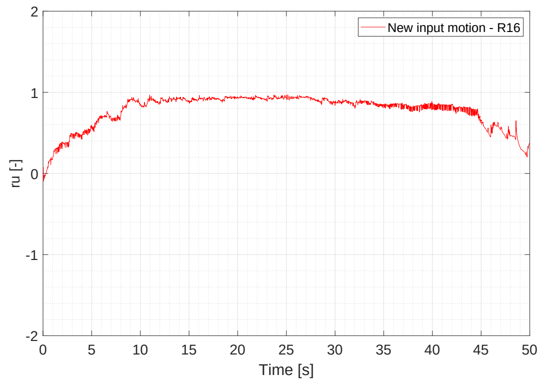

Figure F.146. R16-Pore water pressure ratio at P2.

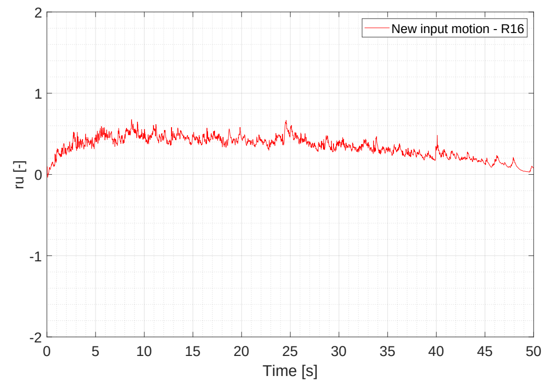

Figure F.147. R16-Pore water pressure ratio at P3.

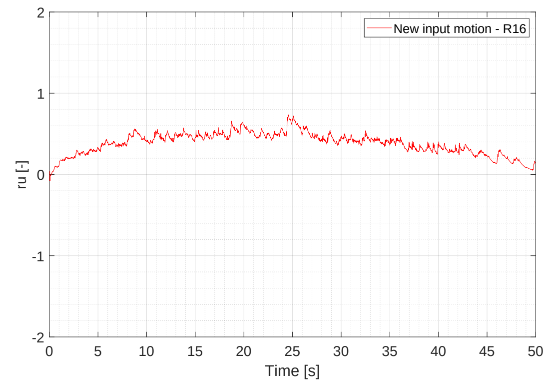

Figure F.148. R16-Pore water pressure ratio at P4.

F.2.17 Event R17

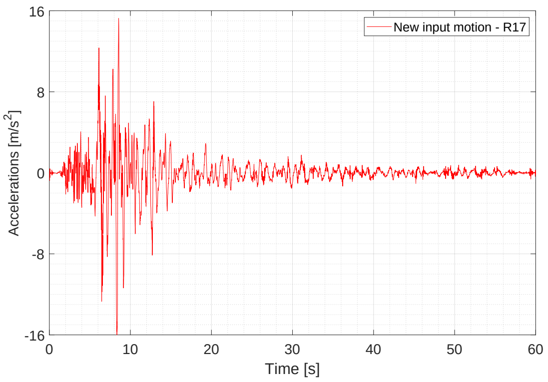

Figure F.149. R17-Accelerations at A1.

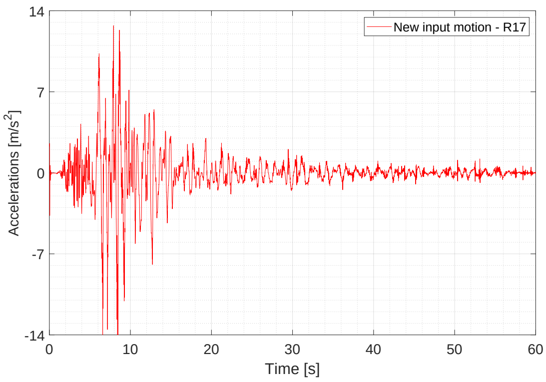

Figure F.150. R17-Accelerations at A2.

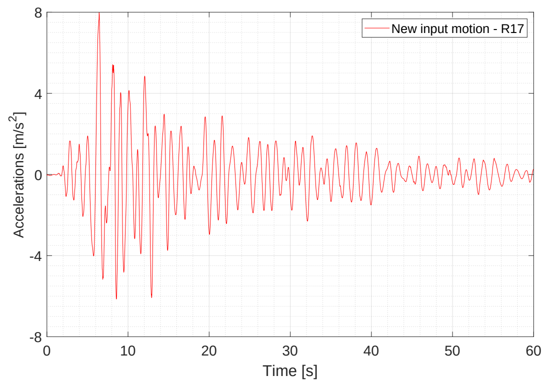

Figure F.151. R17-Accelerations at A3.

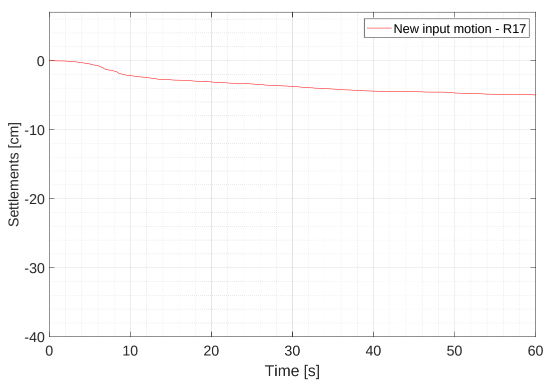

Figure F.152. R17-Settlement.

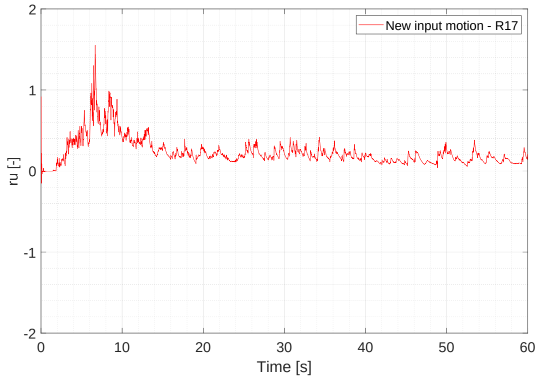

Figure F.153. R17-Pore water pressure ratio at P1.

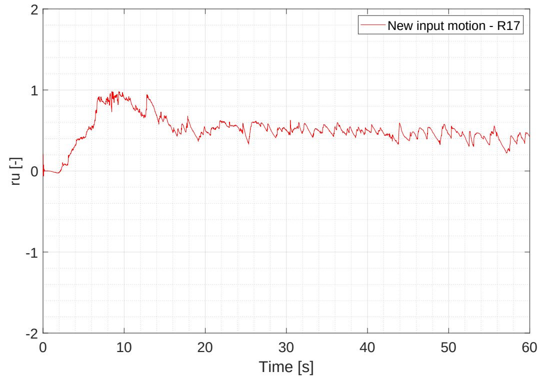

Figure F.154. R17-Pore water pressure ratio at P2.

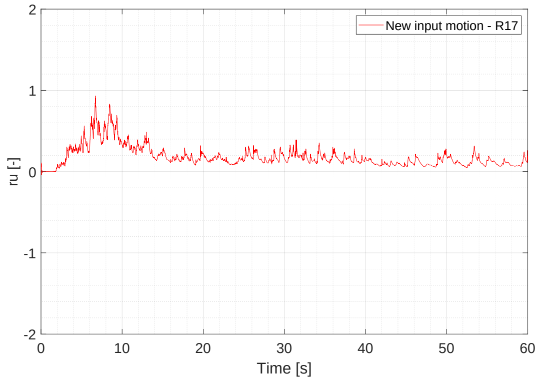

Figure F.155. R17-Pore water pressure ratio at P3.

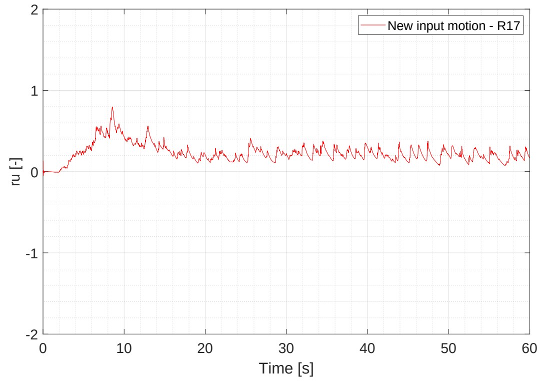

Figure F.156. R17-Pore water pressure ratio at P4.

F.2.18 Event R18

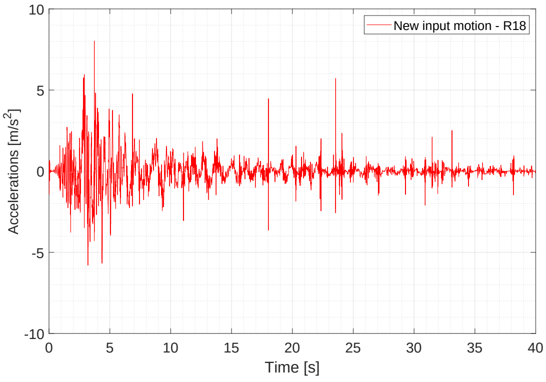

Figure F.157. R18-Accelerations at A1.

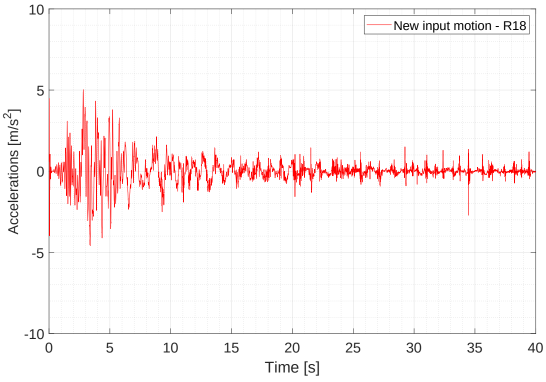

Figure F.158. R18-Accelerations at A2.

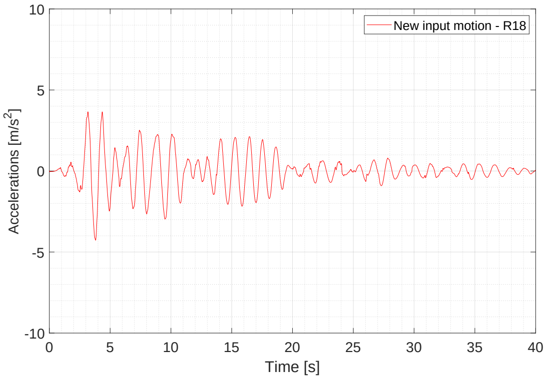

Figure F.159. R18-Accelerations at A3.

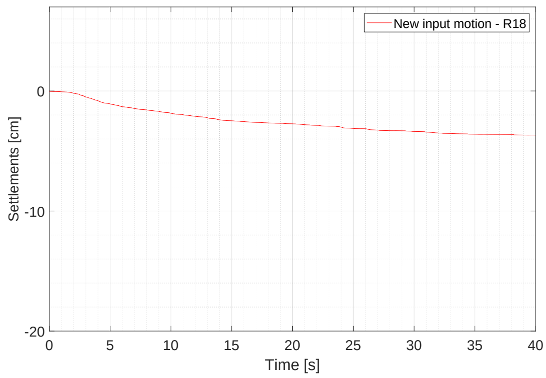

Figure F.160. R18-Settlement.

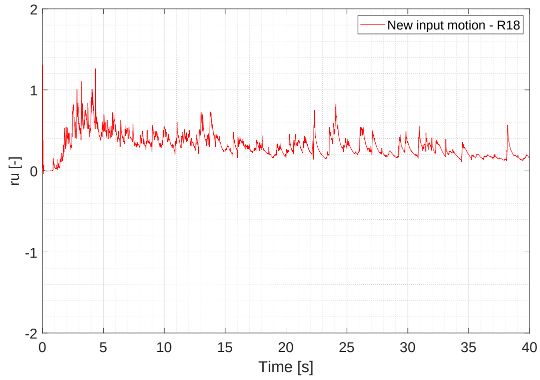

Figure F.161. R18-Pore water pressure ratio at P1.

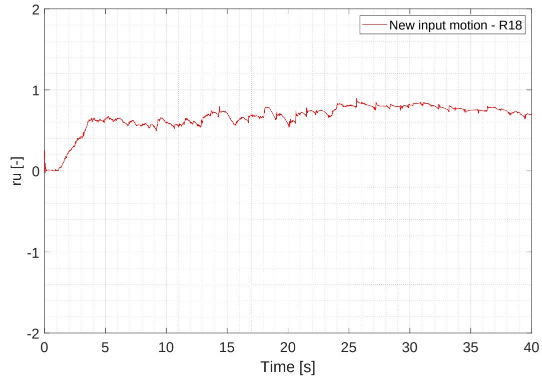

Figure F.162. R18-Pore water pressure ratio at P2.

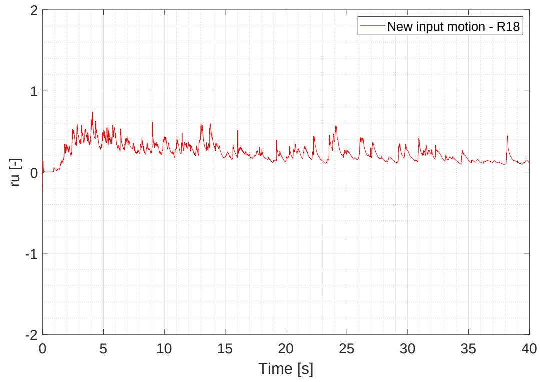

Figure F.163. R18-Pore water pressure ratio at P3.

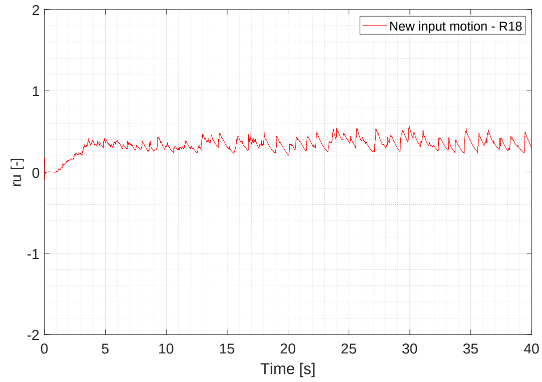

Figure F.164. R18-Pore water pressure ratio at P4.

F.2.19 Event R19

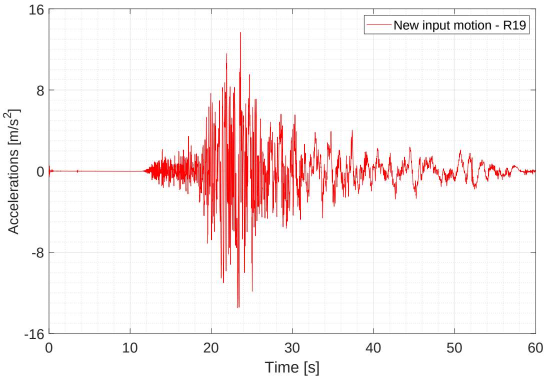

Figure F.165. R19-Accelerations at A1.

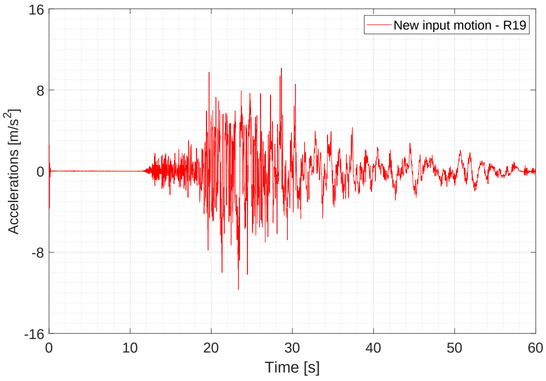

Figure F.166. R19-Accelerations at A2.

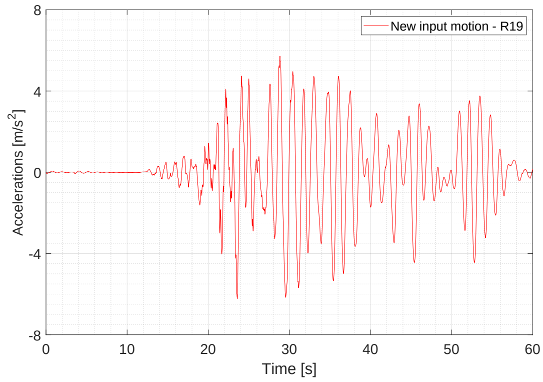

Figure F.167. R19-Accelerations at A3.

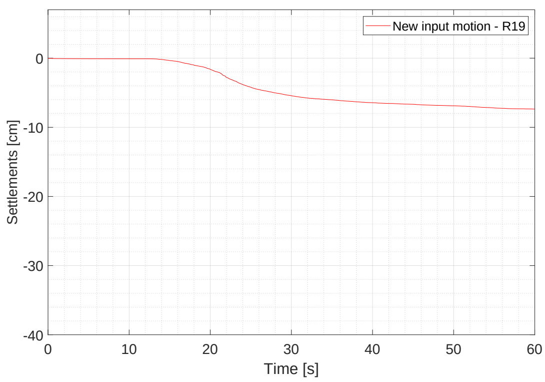

Figure F.168. R19-Settlement.

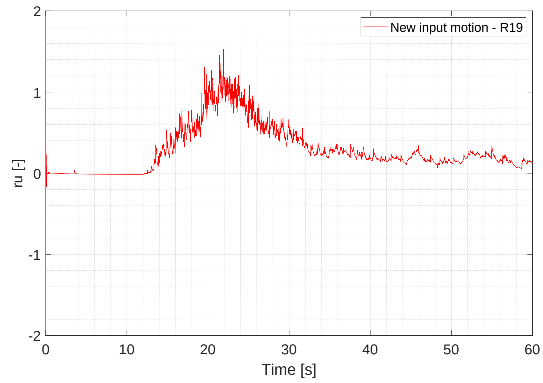

Figure F.169. R19-Pore water pressure ratio at P1.

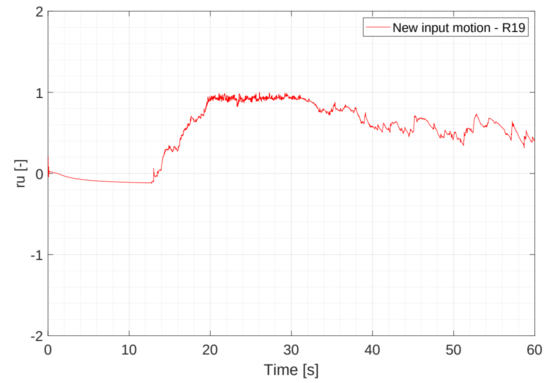

Figure F.170. R19-Pore water pressure ratio at P2.

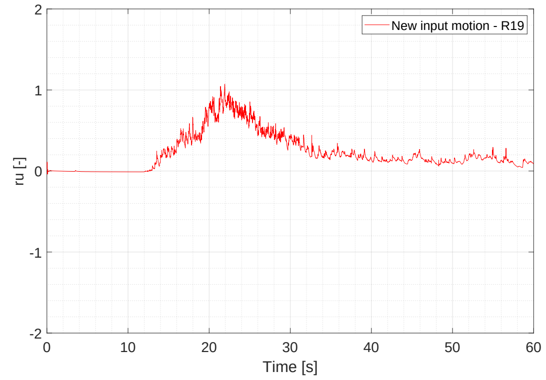

Figure F.171. R19-Pore water pressure ratio at P3.

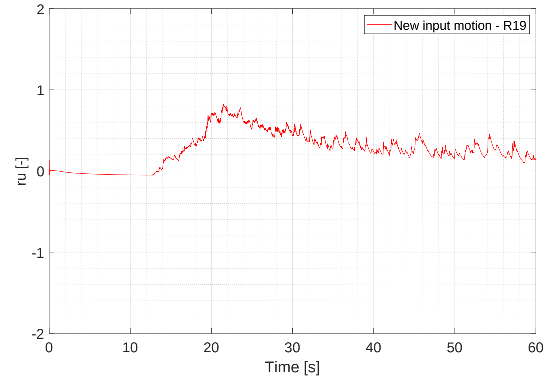

Figure F.172. R19-Pore water pressure ratio at P4.

F.2.20 Event R20

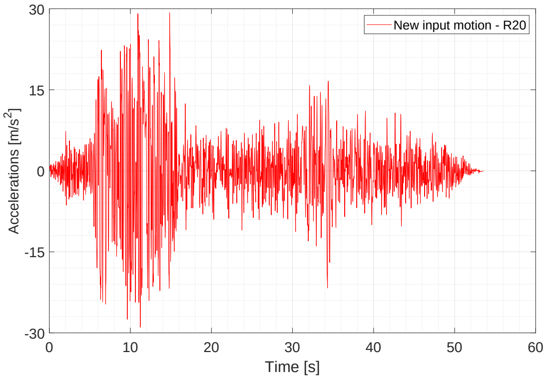

Figure F.173. R20-Accelerations at A1.

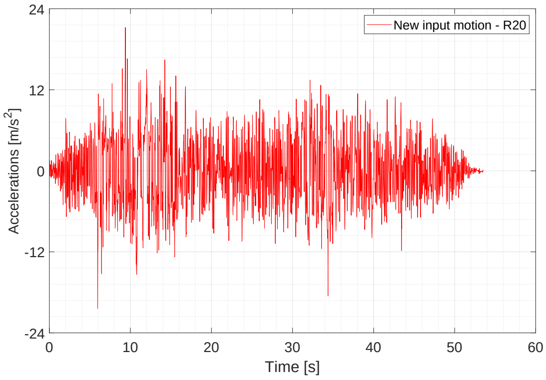

Figure F.174. R20-Accelerations at A2.

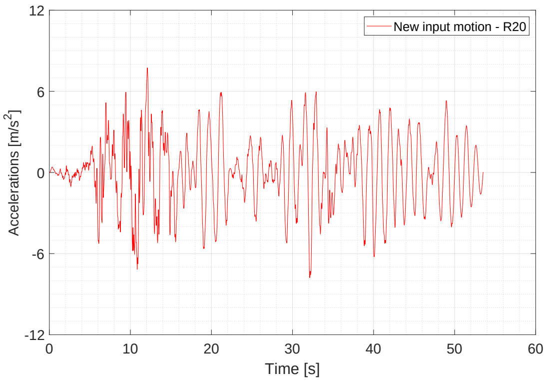

Figure F.175. R20-Accelerations at A3.

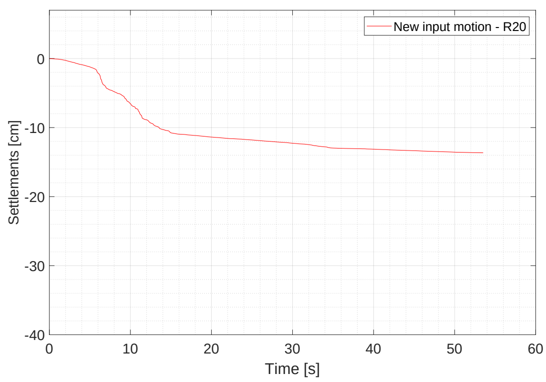

Figure F.176. R20-Settlement.

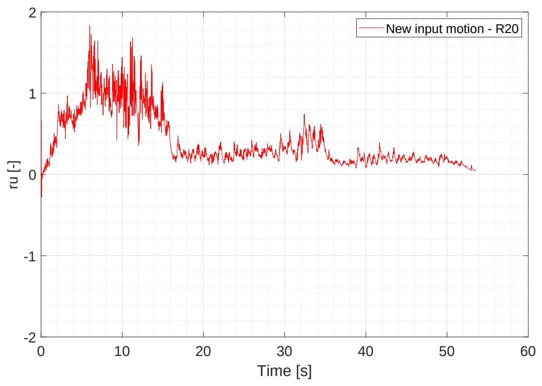

Figure F.177. R20-Pore water pressure ratio at P1.

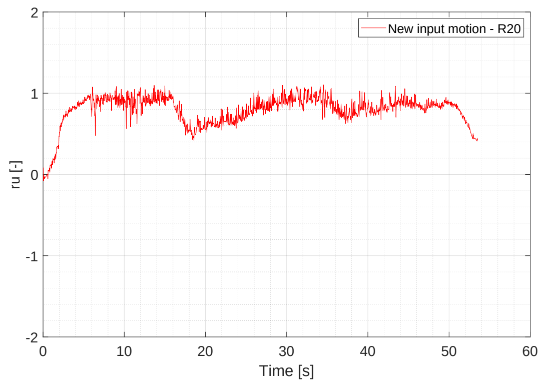

Figure F.178. R20-Pore water pressure ratio at P2.

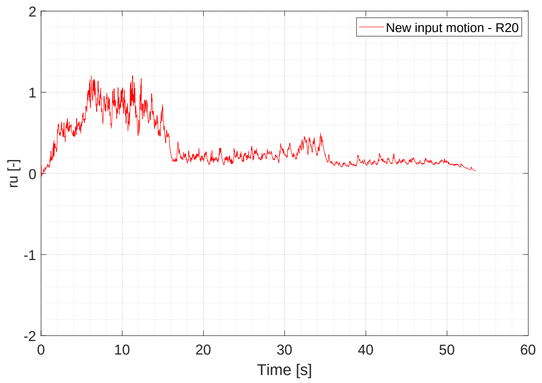

Figure F.179. R20-Pore water pressure ratio at P3.

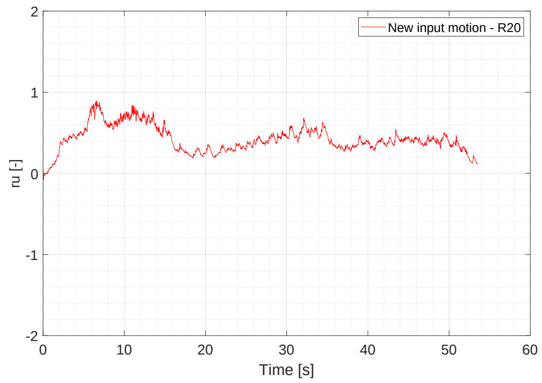

Figure F.180. R20-Pore water pressure ratio at P4.

F.3 Comparison of settlements-time histories and Arias Intensity curves for different values of contact pressure

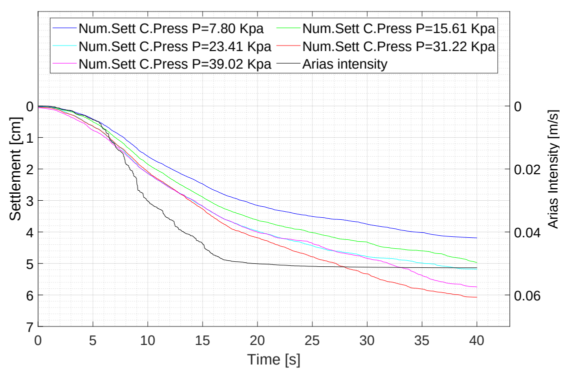

Figure F.181. Settlements time history and Arias intensity time history of the event $R1 - BigBear - 01$

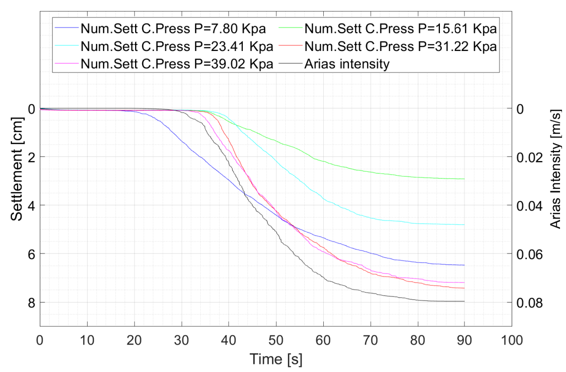

Figure F.182. Settlements time history and Arias intensity time history of the event $R2 - Chi - Chi, Taiwan$

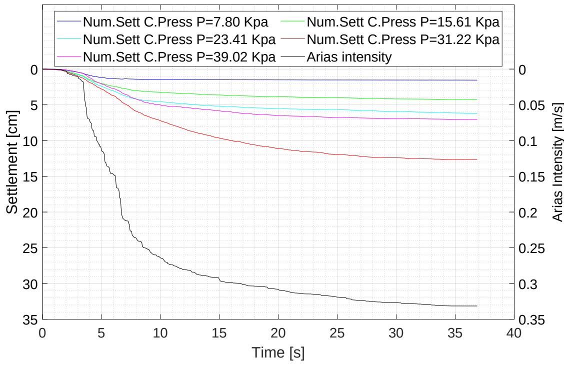

Figure F.183. Settlements time history and Arias intensity time history of the event $R3 - Irpinia, Italy - 01$

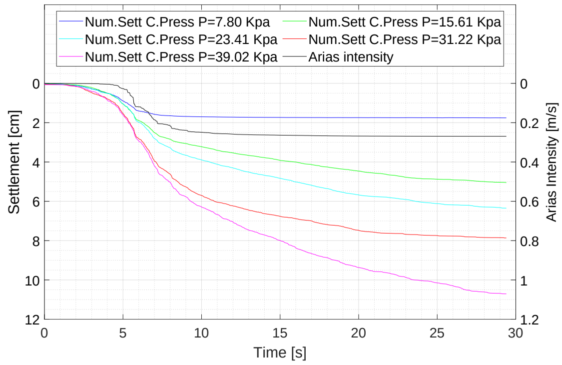

Figure F.184. Settlements time history and Arias intensity time history of the event $R5 - Kozani, Greece - 01$

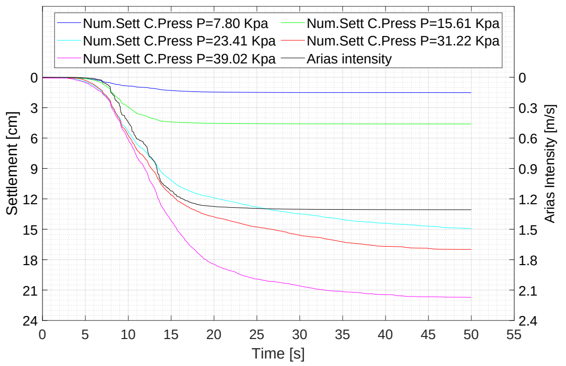

Figure F.185. Settlements time history and Arias intensity time history of the event $R6 - LomaPrieta$

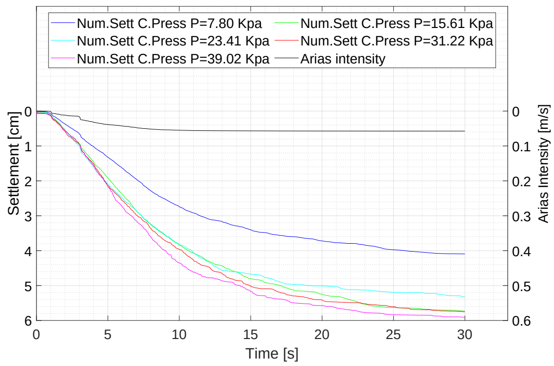

Figure F.186. Settlements time history and Arias intensity time history of the event $R7 - MorganHill$

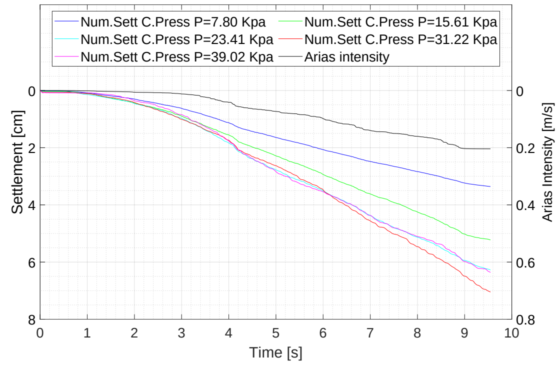

Figure F.187. Settlements time history and Arias intensity time history of the event $R8 - Nahanni, Canada$

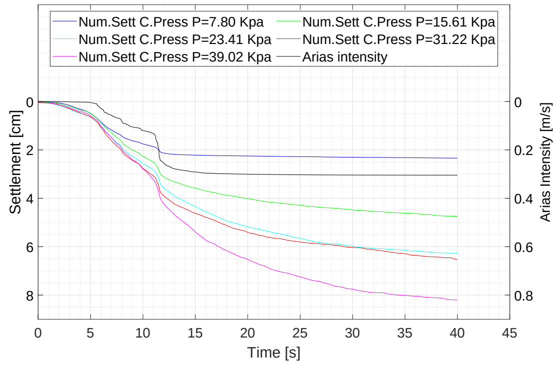

Figure F.188. Settlements time history and Arias intensity time history of the event $R9 - Northridge - 01$

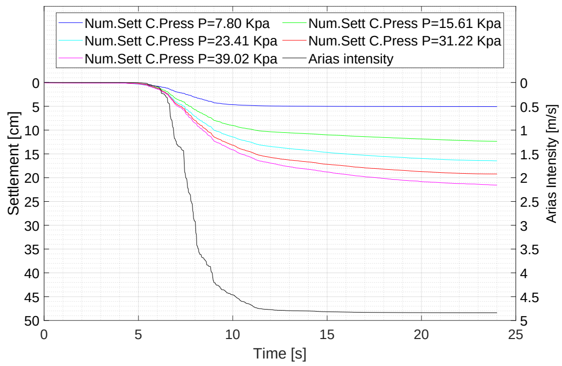

Figure F.189. Settlements time history and Arias intensity time history of the event $R11{-}Christchurch, NewZealand$

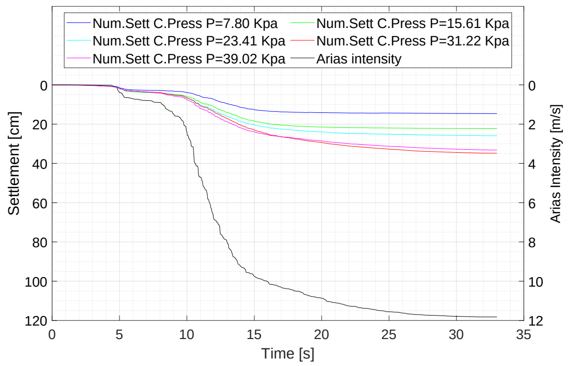

Figure F.190. Settlements time history and Arias intensity time history of the event $R12 - Tabas, Iran$

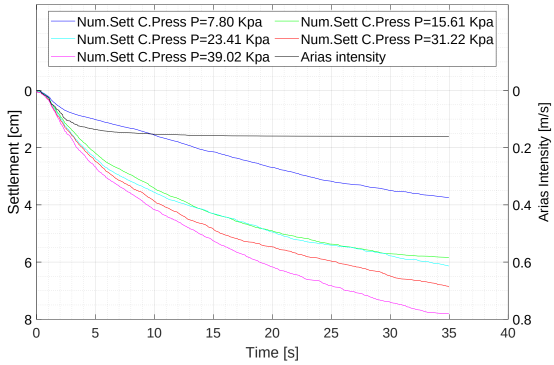

Figure F.191. Settlements time history and Arias intensity time history of the event $R13 - SanFernando$

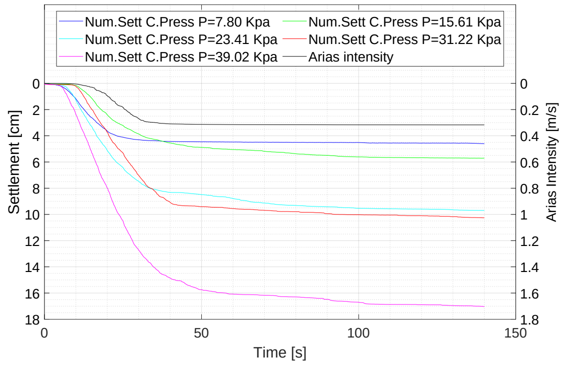

Figure F.192. Settlements time history and Arias intensity time history of the event $R14 - Darfield, NewZealand$

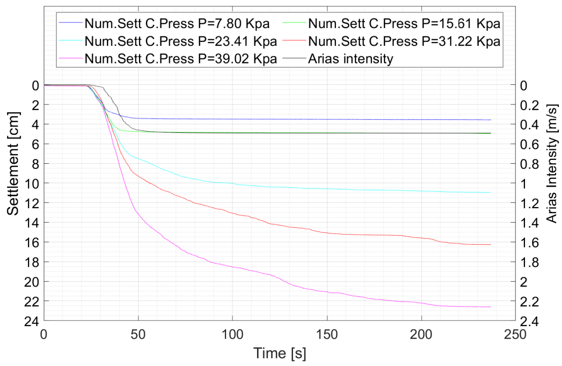

Figure F.193. Settlements time history and Arias intensity time history of the event $R15 - Iwate, Japan$

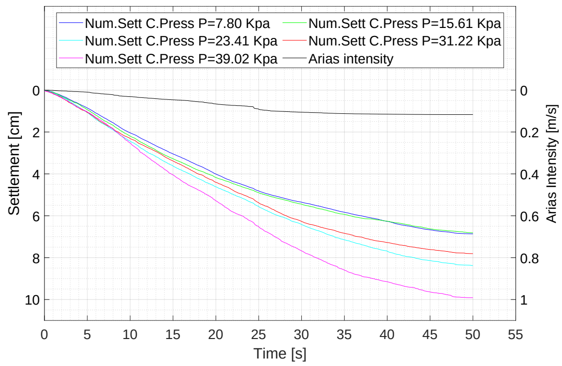

Figure F.194. Settlements time history and Arias intensity time history of the event $R16 - Landers$

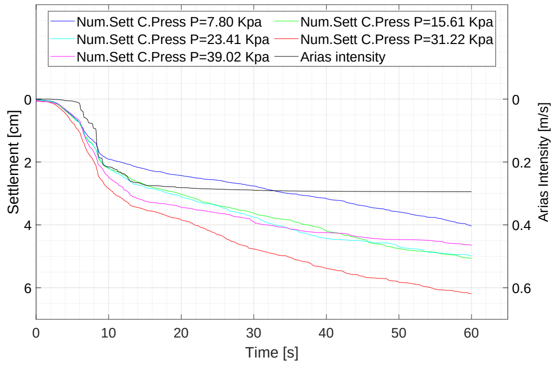

Figure F.195. Settlements time history and Arias intensity time history of the event $R17 - Coalinga - 01$

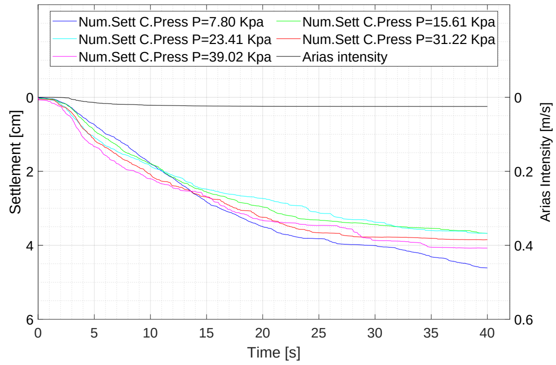

Figure F.196. Settlements time history and Arias intensity time history of the event $R18 - Hollister - 04$

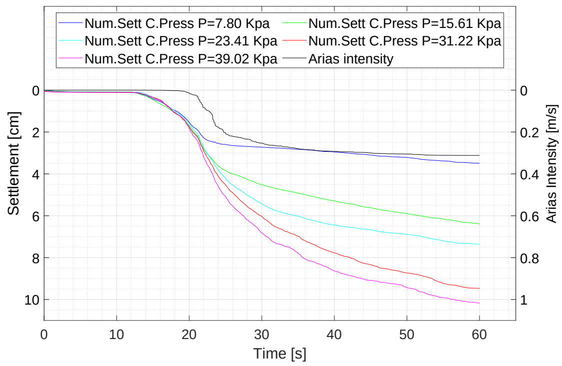

Figure F.197. Settlements time history and Arias intensity time history of the event $R19 - Chuetsu - oki, Japan$

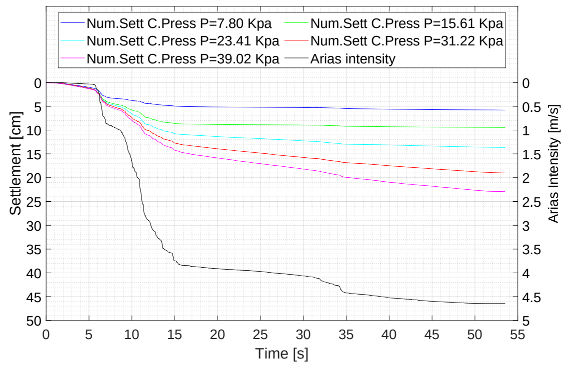

Figure F.198. Settlements time history and Arias intensity time history of the event $R20 - Manjil, Iran$